The Effects of Gold Nanoparticles on Isobutane Oxidation by Phosphopolyoxomolybdates and Metal Oxides

A Thesis Presented for the Degree of Master of Philosophy

at

The University of Newcastle

by

Hanadi Almukhlifi

B.Sc.

Discipline of Chemistry

School of Environmental and Life Sciences

The University of Newcastle

Callaghan, New South Wales

Australia, 2308

March, 2012

Declaration

I hereby certify that the work embodied in this thesis is the result of original research and has not been submitted for a higher degree to any other university or institution.

_____

Hanadi Almukhlifi

Dedication

To my mum and dad.

Acknowledgment

Foremost, I would like to express my sincere gratitude to my supervisor Dr. Robert Burns for his support, motivation and enthusiasm through this course of the project. His guidance and patience helped me during the research and in the writing of this thesis. I am grateful to have had the opportunity to work and learn from him a lot. I would like to extend my thanks to my co-supervisor Dr. Warwick Belcher for his support and assistance.

My sincere thanks go to Dr. Glenn Bryant for help in recording the X-ray photoelectron spectra, Mr. David Phelan for help in recording the scanning electron microscopy and transmission electron microscopy images, and Ms. Jennifer Zobec for help in recording the X-ray powder diffraction data. I would also like to thank A/Prof. Scott Donne for performing the surface area measurements I would like also to acknowledge the technical and academic staff members in the Faculty for their kind assistance and warm support.

Most importantly, my deepest gratitude goes to my mum and dad and my sisters and brothers. Thank you so much. You have been a constant source of love, encouragement and support. For them I will be forever grateful.

Last, but not least, I would like to thank the Ministry of Higher Education in Saudi Arabia and the Cultural Mission of Royal Embassy of Saudi Arabia in Canberra for their funding, support and encouragement.

Abstract

This thesis describes a new approach for the preparation of oxidation catalysts that contain pure gold nanoparticles on their surfaces and within their pore structures. The prepared gold nanoparticles were loaded onto phosphopolyoxomolybdate and metal oxide surfaces and the resulting catalysts were used for the partial and complete oxidation of isobutane. The process involved the initial formation of *n*-hexanethiol-stabilised gold nanoparticles, followed by addition of a solution of the stabilised gold nanoparticles in *n*-hexane to the solid catalyst and allowing adsorption to occur. Following this, thermolysis converted the *n*-hexanethiolate-stabilised gold nanoparticles to pure gold nanoparticles loaded on the catalyst surface by decomposition of the thiolate ligand from the gold nanoparticle surface.

The *n*-hexanethiolate-stabilised gold nanoparticles were prepared using the Brust-Schiffrin method. Alkanethiol (in this work *n*-hexanethiol) was used as the ligand to prevent agglomeration of the gold nanoparticles. The produced *n*-hexanethiolate-stabilised gold nanoparticles were easily isolated from solution and stored in the form of a black powder. More importantly, for this work, the stabilised gold nanoparticles could be simply redissolved in an organic solvent (*i.e.* hexane) for future applications, in the present case heterogeneous catalysis.

In this study, two types of catalysis have been studied, partial oxidation of isobutane over phosphopolyoxomolybdate Keggin-type $[PMo_{12}O_{40}]^{3-}$ catalysts, and complete oxidation (combustion) over the mixed oxidation state spinel-type metal oxides Mn_3O_4 and Co_3O_4. A fixed-bed flow reactor was constructed as part for this study. Gas chromatography and infrared spectroscopy were used to analyse the products of both partial and complete oxidation, which included methacrolein,

methacrylic acid, acetic acid, isobutyric acid, CO and CO_2 for the former, and CO_2 and CO for the latter. Infrared spectroscopy was used to analyse the CO and CO_2.

For the partial oxidation of isobutane three series of compounds were synthesised with varying counter-cations: $(Cs^+)_{3-x}H_x[PMo_{12}O_{40}]$ (where x = 0, 0.5, 1 and 2), $(Ag^+)_{3-x}H_x[PMo_{12}O_{40}]$ (x = 0, 1 and 2) and $(Cu^{2+})_{3-2x}H_{2x}[PMo_{12}O_{40}]_2$ (x = 0, 1 and 2). These compounds, and the parent acid $H_3[PMo_{12}O_{40}]$, were studied as selective oxidation catalysts for isobutane, along with analogous catalysts with a loading of 5 wt % gold nanoparticles. The size of the gold nanoparticles was estimated to be 6.0 nm using the Scherrer equation from X-ray powder diffraction studies. The series of catalysts, with and without gold nanoparticles, were characterised by a range of techniques including infrared spectroscopy, scanning and transmission electron microscopy, thermogravimetric and differential thermal analysis and X-ray photoelectron spectroscopy (XPS).

The catalytic activities of the phosphopolyoxomolybdate compounds for the partial oxidation of isobutane were examined before and after the addition of gold nanoparticles. The addition of gold nanoparticles affected both the % conversion and % selectivities to the products of the catalysts. This depended on the presence or not of H^+ in the catalyst makeup of the counter-cations. In some cases it is likely that the gold nanoparticles blocked the surfaces of the catalysts, thereby reducing the effective surface area for isobutane adsorption. In other cases this was not the case, and this appeared to depend on the surface area of the catalysts. The presence of Au(I), likely as AuO^-, was observed by XPS examination of the spent catalysts, and it likely that this species plays a significant role in the oxidation process.

In the complete oxidation studies, the spinel-type metal oxides Mn_3O_4 and Co_3O_4 (Fe_3O_4 was oxidised under the catalysis conditions to Fe_2O_3) in the form of

powders and nano-powders were used as supports for the gold nanoparticles (5 wt %). In this case the calculated sizes of supported gold nanoparticles ranged from 48 to 71 nm, respectively. Aggregation occurred on the surfaces of these metal oxides. The reason for this is not immediately obvious, and requires further study. The catalytic activities of Mn_3O_4 and Co_3O_4 gave apparent activation energies of 76 ± 7 and 95 ± 5 kJ/mol, respectively, which were lowered by the addition of the gold nanoparticles. Again the presence of Au(I) was observed in the spent catalysts and likely plays a role in the oxidation process.

List of Contents

List of Tables

List of Figures

Chapter 1

Introduction and Review of the Literature

1.1 Introduction

Throughout history gold has been known as a fascinating element. It is a component of some of the most beautiful pieces of artwork ever produced because of its qualities of being both an attractive and lustrous material, it doesn't corrode under normal conditions, and it keeps its beauty over millennia. In chemical terms, however, metallic gold has been considered to be chemically inert and thus of relatively little interest, although like any element there is a considerable chemistry displayed by its oxidation states, which range from -1 to +5. Thus until some 40 years ago, heterogeneous catalysis involving gold did not exist.

In 1972 Bond [1] stated "Although the catalytic properties of gold are surpassed by those of Group VIII metals [*i.e.* Groups 8 to 10], especially palladium and platinum, possible applications of gold in catalytic processes have been widely studied". However, the belief about gold at that time was that no one would have thought of gold as the logical first choice as a catalyst for any kind of reaction.

In 1985, Schwank [2] noted "In spite of its low intrinsic activity, gold can influence the activity and selectivity of [a] group VIII metal". This key paper was just the start of investigations of catalysis by gold. Bond and Thompson published two reviews written in 1999 and 2000 [3, 4]. By that time, catalysis using gold and gold compounds was a vibrant research field in both the areas of heterogeneous and homogeneous catalysis. Catalysis by gold was reinvigorated by two key discoveries:

- Application to the hydrochlorination of acetylene [5].

- Supported gold nanoparticles were shown to be very active for CO oxidation at low temperatures [6].

After these two discoveries, gold was established as a highly effective catalyst for both selective oxidation and hydrogenation reactions.

In 1982, the composite oxides of gold were discovered to be actually composed of gold nanoparticles with a diameter of 2-4 nm dispersed on metal oxides, *i.e.* on larger particles of Fe_2O_3, Co_3O_4 or NiO. Following this discovery, Haruta and co-workers attempted to prepare composite gold oxides with a variety of transition metals by co-precipitation methods, with the expectation that the materials formed might be as catalytically active as platinum and palladium metals for the oxidation of hydrogen, based on a volcano-type plot as shown in Figure 1 [7].

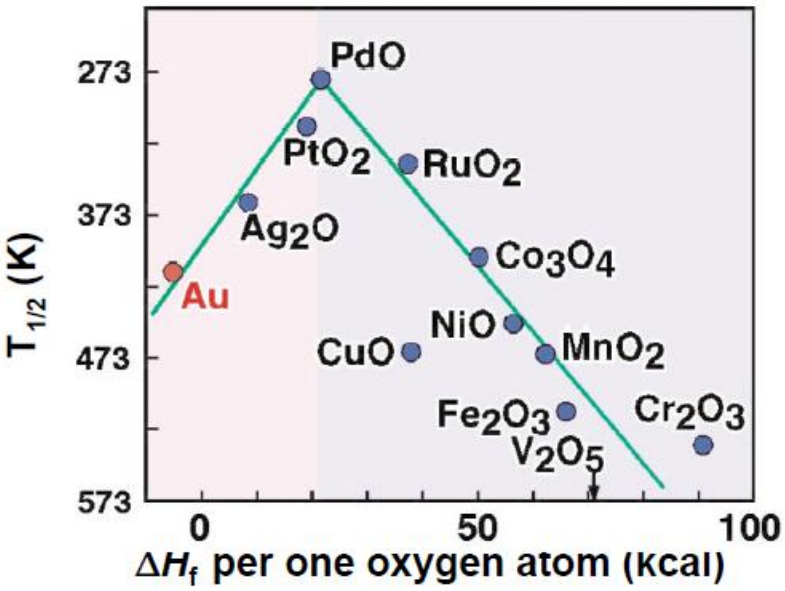

Figure 1. The catalytic activity correlation for the oxidation of hydrogen with the heat of formation of metal oxides per one oxygen atom [8].

Subsequently, Haruta and coworkers found that ‘composite’ gold oxides with 3d transition metals of Groups 8-10 (Fe, Co, and Ni) were much more active for CO oxidation than for hydrogen oxidation, and that they were also active at -75oC [9]. Moreover, they reported that gold remained active when stabilised in the form of nanoparticles connected to metal oxides and active carbon supports [10-12].

Gold nanoparticles dispersed on various metal oxides are beginning to make an important contribution to the field of heterogeneous catalysis. Indeed, their application in this area may be one of the oldest areas of ‘nanotechnology’. The unique properties and activity of gold nanoparticles supported on metal oxides have been widely investigated for various applications such as selective low-temperature CO oxidation, hydrogenation of unsaturated hydrocarbons, NO reduction with hydrocarbons, the water-gas shift reaction, liquid-phase reactions involving halogens, and both complete (*i.e.* combustion) and partial oxidation of hydrocarbons. The properties and activities are sensitive to the size of the gold particles, to the type of metal oxide support, and to the contact structure of the gold/metal oxide support. For all of these purposes, catalysts have been synthesised as gold nanoparticles deposited on such high-surface area and stable metal oxides as Al_2O_3, Fe_2O_3, SiO_2, TiO_2, *etc*.

Gold nanoparticle-metal oxide catalysts can be synthesised and characterised easily using different techniques. Some of the preparative methods that have been used to prepare gold nanoparticles dispersed on metal oxides are co-precipitation, deposition precipitation, and impregnation. After preparation, the gold particle catalysts are characterised by various instrumental methods including X-ray powder diffraction (XRD), scanning electron microscopy (SEM) and X-ray photoelectron microscopy (XPS), all of which are used to determine the structure, size distribution of gold nanoparticles and oxidation states on the support surface that are responsible for the activity (or enhanced activity) of the catalysts.

The present study covers the synthesis and characterization of gold nanoparticle-metal oxide and gold nanoparticle-phosphopolyoxomolybdate catalysts, and their applications to the total oxidation (*i.e.* combustion) of carbon-containing compounds, in particular isobutane, as well as the partial oxidation of isobutane to produce commercially important materials, such as unsaturated organics (*e.g.* methacrolein and methacrylic acid) suitable for poly(methyl methacrylate) formation, *i.e.* Perspex or Plexiglass.

Of course gold nanoparticles find applications in many areas, not just as heterogeneous catalysts, and there have been many reviews of fundamental studies as well as applications in these areas over the past 20 years. For example, Daniel and Astruc [13] reviewed the applications of gold nanoparticles in different areas. In this review, they discussed several methods of synthesis gold nanoparticles of different sizes and shapes, and the techniques that can be applied to characterise these nanoparticles. Also, they reviewed the chemical and physical properties of the gold nanoparticles and their applications in biology and other different fields. Moreover, they noted that the reasons for the increasing interest in gold nanoparticle research are related to their stability, the extraordinary diversity of their modes of preparation together with ceramics, glasses, polymers, ligands, surfaces, films, oxides, zeolites, biomolecules and bioorganisms, and their properties and roles in nanoscience and future nanotechnology. Also, Eustis and El-Sayed [14] have reviewed the history of interest of gold nanoparticles over the years and have discussed some of the newer applications of noble metal, in addition to gold, nanoparticles.

1.2 Gold nanoparticles

Historically, gold has been known as the most inert metal, which would appear to make it ineffective as a catalyst. However, in the form of nanoparticles this metal has been shown to be surprisingly active, and not just in the area of heterogeneous catalysis.

Consequently, gold nanoparticles have received much attention as a result of their properties and promising applications. Gold particles are regarded as colloidal or a nanoparticle dispersion if they consist of particles within a typical size range of 10 µm-1 nm [15].

Gold particles are stable at the nanoscale size, while other nanoscale metal particles mostly oxidise when exposed to air. For this reason, gold nanoparticles are preferred in most applications that involve colloidal metals [16]. In 2002, Haruta compared the catalytic performance of nanosized gold particles with other catalytically active metals such as platinum and palladium. The study showed that gold was more active for the oxidation of CO than other metals at low temperatures (300 K), while at room temperature they also exhibit other reactions, such as the epoxidation of propene. Moreover, gold nanoparticles may show unexpected activity when supported on metal oxides. Therefore, many studies have focused on gold nanoparticles that are supported on metal oxides with a high surface area and high adsorption capacity [11].

1.2.1 History of gold nanoparticles

Colloidal gold was used for a long time as a colorant before attracting Faraday's attention in 1857. Thus from at least the 5th century B.C., colloidal gold has been used in making ruby glass and to provide a reddish tinge to ceramics. According to Ostwald, "This colloidal gold was prepared even in the days of the alchemists by the reduction of gold salts by all kinds of organic substances including urine." [15].

The colour of gold nanoparticles in solution varies from red to blue depending on the shape and size of the particles [15]. It is red if the particles are small, and blue when the particles are larger [17]. In describing the colour of these particles, in 1917 Zsigmondy [18] noted "The color of colloidal gold solution in transmitted light may be red, violet, or blue, and occasionally yellowish brown, or brown. The ultramicrons of red solution are green;

those of blue solution are yellow to reddish brown; violet solution contains both. We have to do with green, yellow, or brown ultramicrons". He also added, "With regard to brown color of very small particles a large number of experimental facts point to the assumption that the ultramicrons are not composed of massive gold. The assumption that the particles are spherical in form is made solely for the purposes of calculation, and a number of facts would seem to discredit the hypothesis, the very great independence of the color on the diameter makes it seem plausible that ultramicrons in red hydrosols are not necessarily spherical when the size is 40 μm and under" [15].

In 1857, Faraday prepared colloidal gold by reducing gold chloride either by heating alone or by reaction with many different reagents including organic matter, phosphorus, tartaric acid, and many others [15]. However, after nearly forty years, Faraday's study was all but forgotten, when Zsigmondy, who developed a different synthetic protocol, became aware of it by combining his synthesis with Faraday's method [18]. He reduced a dilute, slightly alkaline solution of gold chloride with boiling formaldehyde. This method was referred to in the contemporary literature as the 'nuclear method', and the gold nanoparticles were described as ultramicroscopic particles, with ultramicrons used as a unit! Also, Zsigmondy managed to design an ultramicroscope to view the mobility of the gold particles [15].

Svedberg, who followed on from Faraday and Zsigmondy, made an important contribution to the synthesis of colloidal gold [19, 20]. He pioneered the use of an electrochemical method of synthesis. According to his text, he used every reducing agent available at that time to produce colloidal gold from chloroauric acid. He stated, "The best known reduction process is the reduction of chloroauric acid [$HAuCl_4$] to gold. Almost every conceivable reducing agent has been studied, *viz.*, hydrogen, hydrogen peroxide, hydrogen sulphide, carbon monoxide, carbon disulphide, nitric oxide, phosphorus, phosphorus tertoxide, hypophosphoric acid, sulphur disoxide, sodium thiosulphate, sodium bisulphate,

ferrous sulphate, tin, stannous chloride, acetylene, terpenes, alcohols, glycerine, aldehydes, acrolein, oxalic acid and oxalates, hydrochinones, hydrazines, hydroxylamines, protaldic acid, electric sparks (formation of nitric acid), alpha, beta, gamma-rays, *etc*." [15]. Today, there are many procedures that are used for the synthesis of gold nanoparticles. These will be discussed in the following section.

1.2.2 Synthesis of gold nanoparticles

In 1951, Turkevitch [21] generated spherical gold nanoparticles in aqueous solution by the citrate reduction method. This method was improved by Frens [22] in 1973. Essentially, an aqueous reaction mixture of gold chloride, $HAuCl_4$, and sodium citrate are heated with stirring. The size of the particles in this synthesis depends on the ratio of gold to citrate, the stirring rate and the temperature. Another synthesis that can be applied to form large spherical and non-spherical nanoparticles is called the 'seeding' technique. In this method, small gold nanoparticles are first created by using a strong reducing agent such as sodium borohydride. The next step involves adding a growth solution containing the metal ions to the seed solution. Following this, a weaker reducing agent such as ascorbic acid is added to the growth solution. Surfactant may be added to induce anisotropic growth. Also, very small nanoparticles can be generated by using a two-phase method in the presence of an organothiol. Moreover, electrochemical, sonochemical, thermal and photochemical reduction methods may be used to generate gold nanoparticles of different shapes [13, 23, 24].

Figure 2 outlines the general approach to the preparation of gold nanoparticles. Effectively, one starts with a Au(III) solution, and uses various reductants to reduce the oxidation state in the presence of ligands to stabilize the gold nanoparticles. Gold nanoparticles have been synthesised over a range of sizes using the two main methods shown in Figure 3, which details the advantages and disadvantages of each method.

1- Growth solution:

$HAuCl_4$ + TOAB (tetraoctylammonium bromide) $\longrightarrow$ $AuCl_4^-$. TOA^+

TOAB = this acts as a phase-transfer reagent.

2- The first reduction:

Au(III) $\xrightarrow{A}$ Au(I)

[A = usually a ligand source such as a phosphine, thiol, amine, *etc.*]

3- The second reduction:

Au(I) $\xrightarrow{R}$ Au^0

[R = a reducing agent such as $NaBH_4$ (the ligand is thiolate)]

Figure 2. The general steps in the preparation of gold nanoparticles.

The first synthetic approach is known as the 'one-phase' method and involves the preparation of gold nanoparticles in water and in non-polar organic solvents. This method was developed by Yee *et al*. [25] and involves reduction of an aqueous solution of a gold salt in a single step. The second method is known as the 'two-phase' method and involves the preparation of gold nanoparticles in an organic solution such as toluene. This method was developed by Brust *et al*. [26] and requires several steps. The first step involves the transfer of Au(III) ions (generally from chloroauric acid, $HAuCl_4$) into toluene using a phase transfer reagent, after which the Au(III) ions are reduced using a reducing agent, initially to Au(I), and then to gold nanoparticles which are stabilized by a ligand on the periphery of the nanoparticles [27].

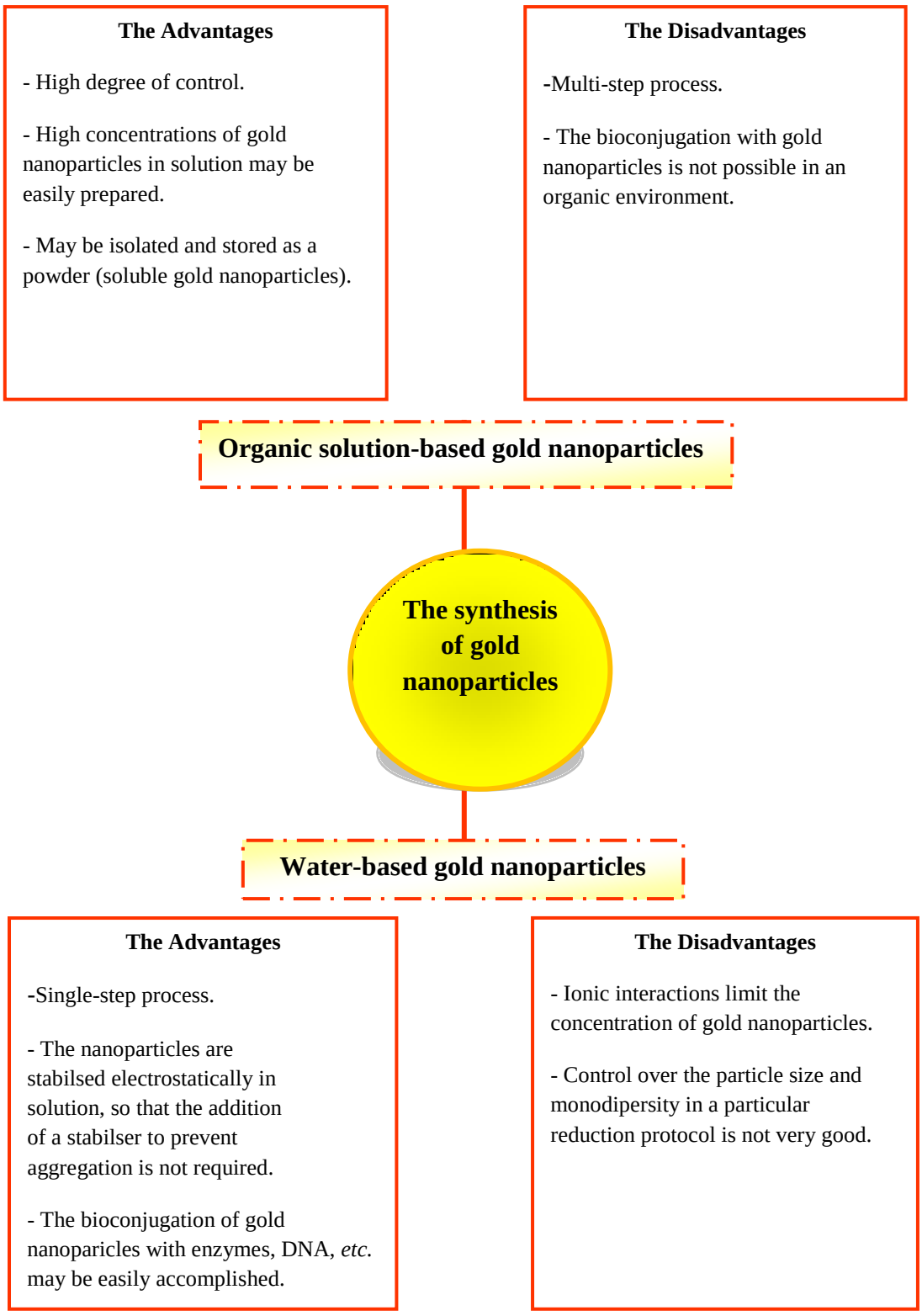

Figure 3. A comparison of the advantages and disadvantages of the different methods that can be used to prepare gold nanoparticles.

The particles so-formed can be stabilised by employing different ligands that are added following the phase-transfer process to bind to the surface of the particles strongly and thus control their growth during reduction of the gold, thereby avoiding aggregation [28]. Attracting the stabilising ligands is dependent on active sites on the surface of the gold particles [29]. Figure 4 illustrates the range of different ligands that can be used to bind to the surface of the gold nanoparticles. If one compares a thiol with other stabilising ligands, such as a disulfide, citrate, phosphine, phosphine oxide, amine, carboxylate, or isocyanide, it is found that none are as good as thiolate (RS^-), as these are strong electron-releasing ligands capable of high polarisation, and are known to strongly bond to gold [28-31]. When using thiolate as a ligand, it is possible to precipitate the gold nanoparticles out of the toluene solution using *n*-hexane, and thus obtain a solid powder containing the thiolate-stabilised gold nanoparticles. It is then possible to reconstitute them in toluene (or other solvent) at a future date. This increases enormously our ability to use gold nanoparticles for applications such as in the area of heterogeneous catalysis.

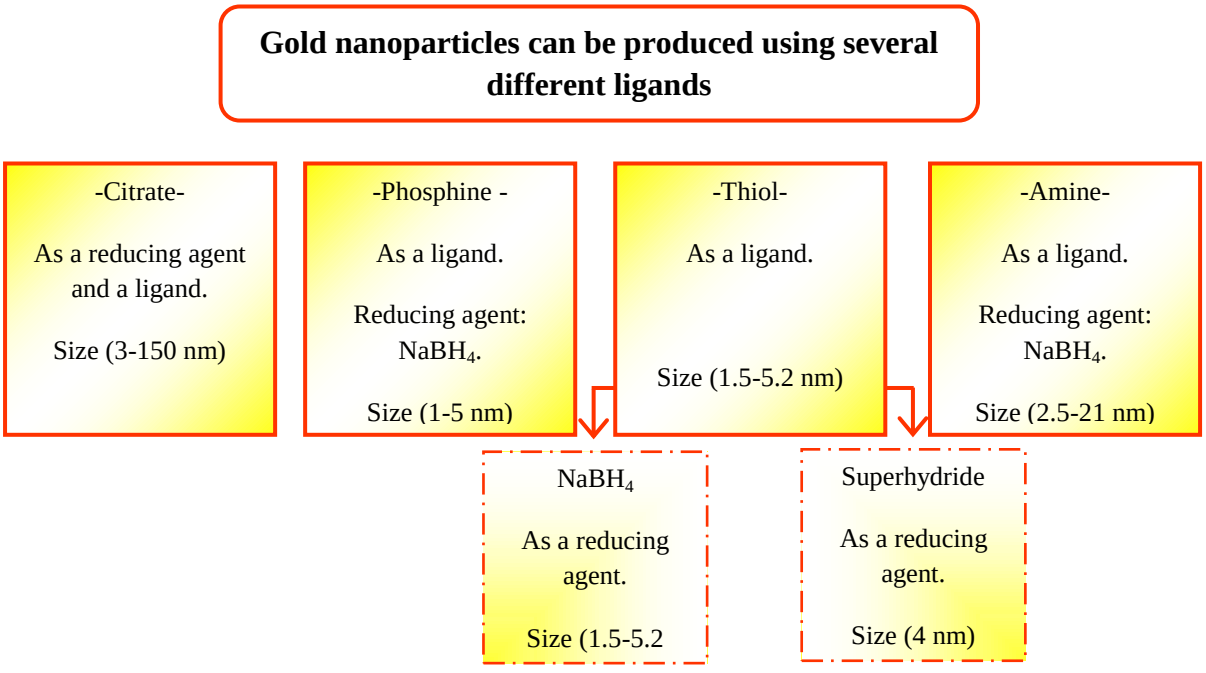

Figure 4. Examples of the different kinds of ligands that can bind with the gold nanoparticle surface.

1.2.3 Characterisation of gold nanoparticles

Gold nanoparticles can be characterised using several different physical techniques. One of the simplest techniques is UV-visible spectroscopy which can be used to determine the approximate size of the gold nanoparticles in solution. An indicated by Hostetler *et al.*, [32] the surface plasmon resonance band (SP band) at about 500 nm depends on the particle size. Furthermore, the SP band intensity decreases with decreasing particle size, and it may become difficult to detect in nanoparticles of less than ~2 nm in diameter. A typical series of spectra are shown in Figure 5, along with the relevant particle sizes, which illustrates this trend.

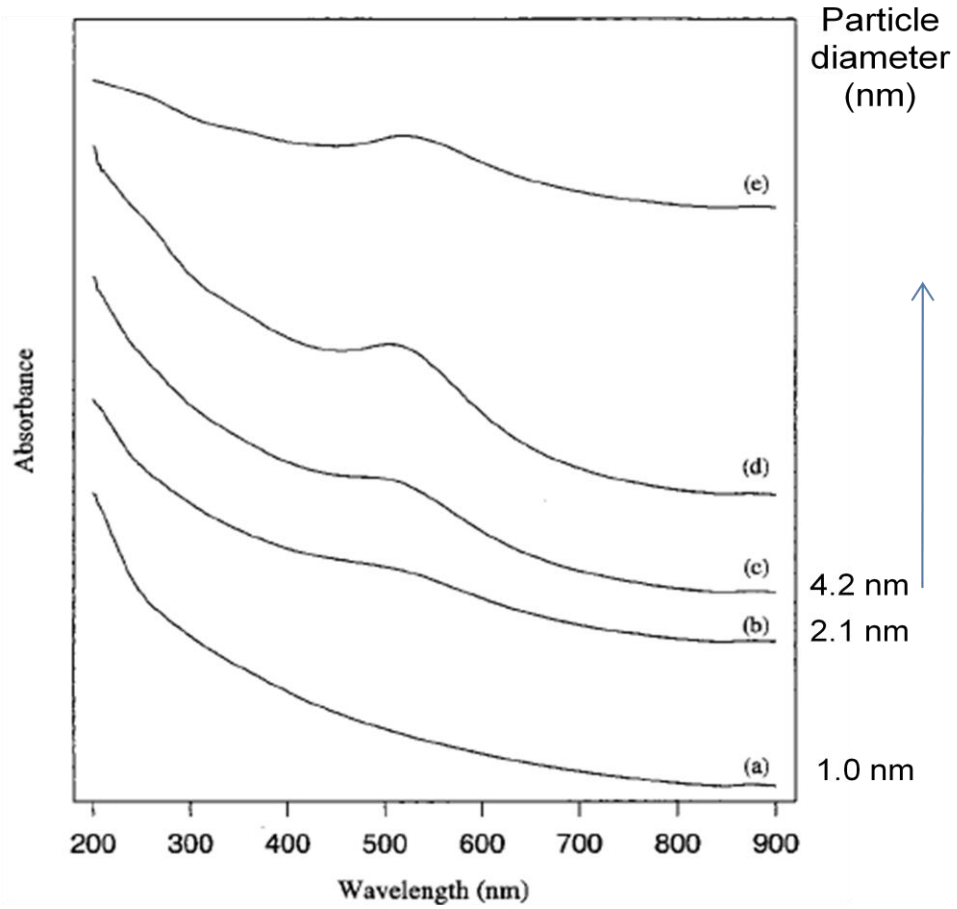

Figure 5. The UV-visible spectra of gold nanoparticles with different sizes [32].

Another technique used to characterize the size of gold nanoparticles is transmission electron microscopy (TEM), which can be used to directly image the nanoparticles. This technique provides more details about the sizes and shapes of the individual particles. Figure 6 shows a TEM image of gold nanoparticles that have been stabilized by dodecanethiol ($C_{12}H_{25}SH$). The sample was prepared by evaporation of two drops of a toluene solution of gold nanoparticles onto a carbon film supported on a standard copper grid. It shows a mixture of particle shapes and particles sizes in the range of 1-3 nm [26].

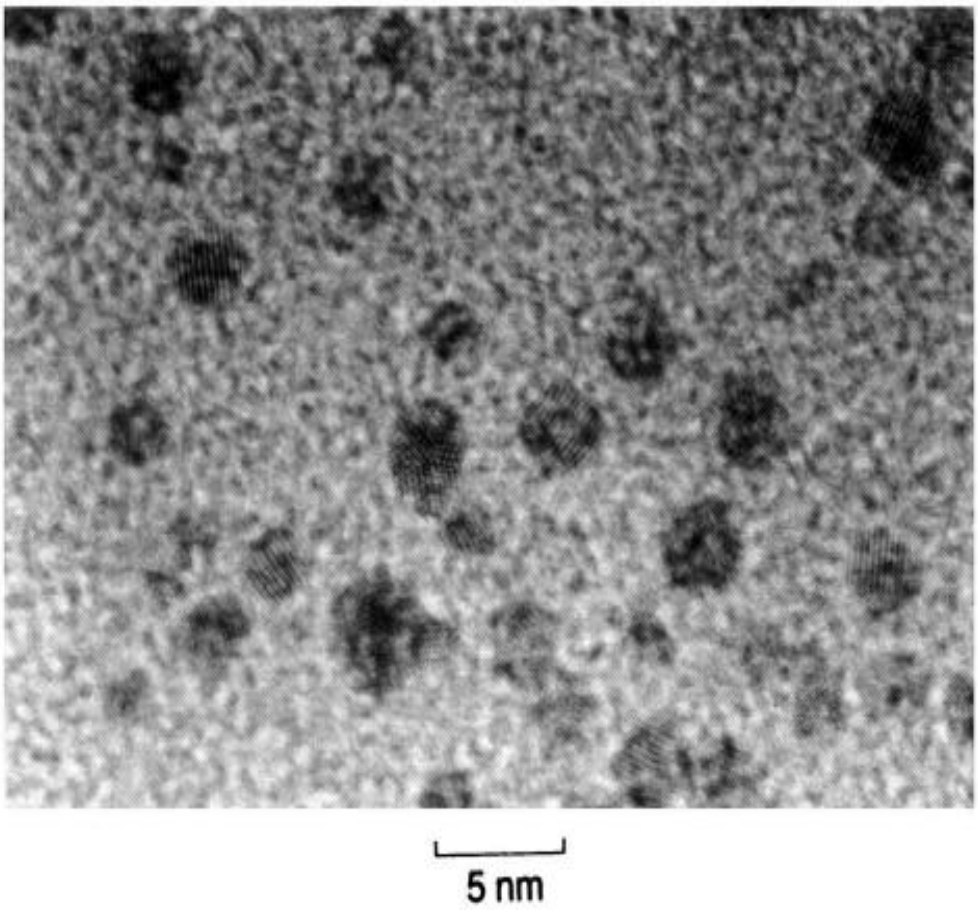

Figure 6. TEM image of dodecanethiolate-stabilised gold nanoparticles at high magnification (accelerating voltage = 200 kV; point resolution = 0.21 nm) [26].

Powder X-ray diffraction (XRD) may also be used to characterise the structures, while the sizes of the particles may be obtained using the Scherrer equation.

This equation is:

$$(\mathrm{MCD})_{hkl} = \frac{K\lambda}{\beta\cos\theta}$$

In this equation K is the constant (0.9×57.3), λ is the wavelength of the X-ray radiation (*e.g.* Cu $K_{\alpha 1}$ radiation, 1.54060 Å), β is the line width (in degrees), and θ is the Bragg angle of diffraction (in degrees).

Also, this technique may be used to provide structural information on unknown materials that contain gold nanoparticles, such as gold nanoparticle-supported metal oxides used for catalysis studies. Figure 7 shows four different sized samples of dodecanethiolate-stabilised gold nanoparticles [33].

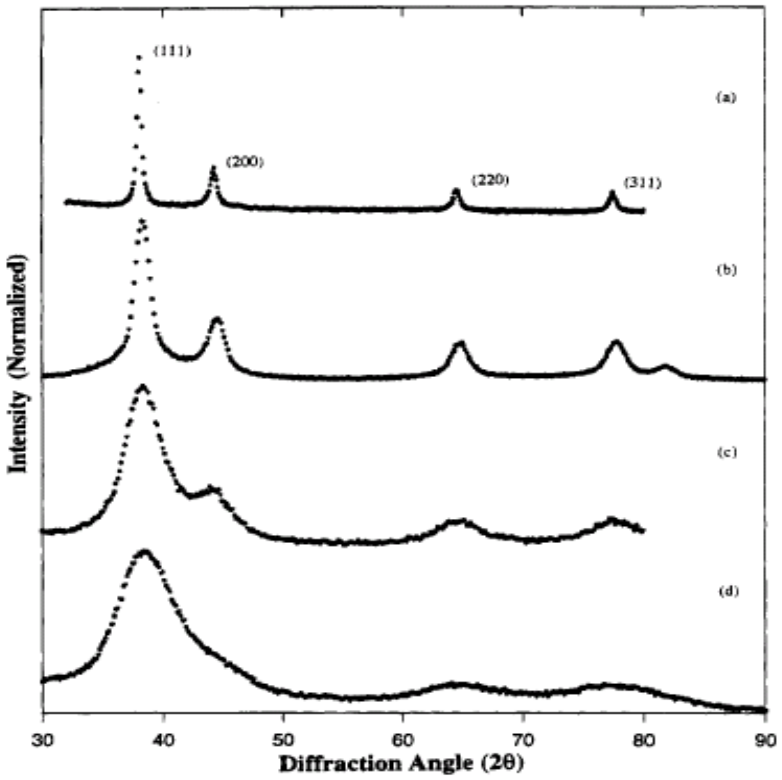

Figure 7. The XRD patterns of dodecanethiolate-stabilised gold nanoparticles containing different sizes of nanoparticles. The sizes are (a) 201.6 ± 38.3 Å, (b) 68.3 ± 3.8 Å, (c) 29.5 ± 2.0 Å, and (d) 15.5 ± 3.0 Å (see text for a discussion) [33].

The average particle size decreases from top to bottom in Figure 7 (*i.e.* progressively from 201 ± 38.3 Å to 15 ± 3.0 Å). It can be seen that the gold diffraction lines with Miller indices (111), (200), (220) and (331) all broaden as the particle size decreases, and estimates of the sizes of the particles may be obtained using the Scherrer equation. For this purpose the (111) line is best, as it is the most intense diffraction line. The sizes of the gold particles are (a) 201.6 ± 38.3 Å, (b) 68.3 ± 3.8 Å, (c) 29.5 ± 2.0 Å, and (d) 15.5 ± 3.0 Å [33].

Another important technique is X-ray photoelectron spectroscopy (XPS) which can be used to analyse the surface of the gold particles and also to detect any different species such Au^{+} and/or Au^{3+} that may be produced as a result of catalytic reactivity. Figure 8 shows the XPS spectra of dodecylamine-capped gold nanoparticles. It shows signals for gold ($5p_{3/2}$, $4f_{7/2}$, $4f_{5/2}$, $4d_{5/2}$, $4d_{3/2}$ and $4p_{3/2}$ at ~59, 84, 87, 336 and 548 eV, respectively), oxygen (1s at 531.8 eV), carbon (1s at 285.3 eV) and a weak signature of Br ($3p_{3/2}$ and $3p_{1/2}$ at 183.5 and 189.5 eV, respectively) from the phase transfer reagent [(n-$C_8H_{17})_4NBr$] [34].

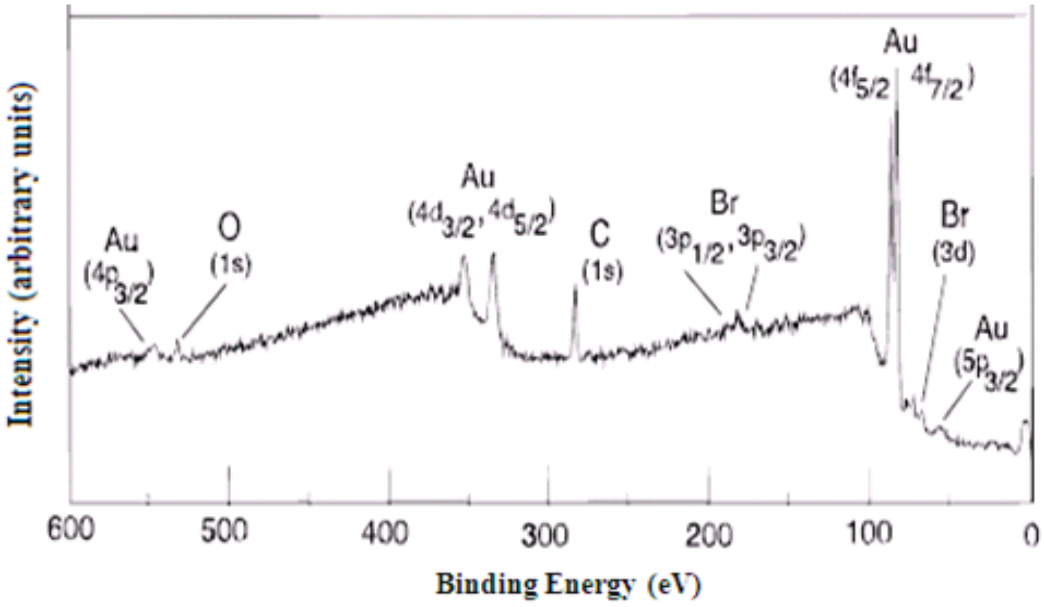

Figure 8. The XPS of dodecylamine-capped gold nanoparticles [34].

1.3 Heterogeneous catalysis

Heterogeneous catalysts have received wide attention because of their reusability and high efficiency. Moreover, they are easily separated from the input materials as they are in a different phase (gas, but can also be in the liquid phase). As a result, about 90% of chemical products of our current commercial processes have some involvement with a heterogeneous catalytic process. Furthermore, there are many other applications, such as in the pharmaceutical, automobile and food industries. In general, the activity and selectivity of a catalyst depends on several important properties, such as particle size, shape, and surface structure of the active species [35].

Heterogeneous catalysis can be classified according to the nature of the catalyst. Thus catalysis is commonly performed on metals, metal oxides, and metal sulfides, as well as other substrates such as phosphates. Metal oxides are usually applied in the reduction of NO_x with NH_3, as well as for the oxidation of hydrocarbons, while metals are applied in many reactions such as hydrogenation, the partial and complete oxidations of hydrocarbons, and NO_x reduction with hydrocarbons. Finally, for example, metal sulfides are applied in the hydrodesulfurisation of petroleum [11].

1.3.1 Heteropolyoxometalates; heterogeneous oxidative dehydrogenation and oxidation reactions

1.3.1.1 Introduction

There are many different types of polyoxometalates, including the so-called Keggin, Dawson, Anderson, lacunary (which have one or more missing Mo=O or W=O units), transition metal-substituted lacunary, and sandwich heteropolyoxometalates. These will be discussed in more detail below. Only the Keggin-type structures and some Dawson-based

structures are known to be active in heterogeneous catalysis, and this review will focus mainly on the Keggin-type heteropoly compounds, which are compounds used in the present study.

Heteropoly compounds have received wide attention because of their variety and high potential as heterogeneous catalysts. These species consist of large polyoxoanions containing molybdenum, tungsten or vanadium in their highest oxidation states, one (or more) central heteroatoms (*e.g.* phosphorus or silicon), counter-cations, and (generally) water of crystallisation. The last is generally easily removed at high temperatures. Partial substitution of H^+ in, for example, the Keggin-type acids $H_3[PMo_{12}O_{40}]$ or $H_3[PW_{12}O_{40}]$, using different counter-cations of different sizes influences their catalytic activity, thermal stability, and their surface areas. In general, only molybdenum-based Keggin-type species are used for heterogeneous catalysis, because of the ease of reduction of the (formal) Mo(VI), as opposed to the less reducible W(VI). Moreover, Keggin-type heterogeneous catalysts are generally built around P(V) heteroatoms, as opposed to other heteroatoms, as heteropoly compounds containing P(V) are generally the most thermally stable. For the Keggin-type species, the counter-cation sizes can be classified into small metal ions such as Na^+ and Cu^{2+} that have low surface areas (about 1-15 $m^2\ g^{-1}$), and large metal ions such as Cs^+ and NH_4^+ that have high surface areas (50-200 $m^2\ g^{-1}$) [36].

The protons in the free acid $H_3[PM_{12}O_{40}]$ (where M = Mo and W) can be substituted with cations such as the alkali and alkaline earth metals, NH_4^+, main group metal cations from Groups 13 and 14, the transition metals and lanthanides. As noted above, only Keggin anions built with molybdenum are active in heterogeneous (oxidation) catalysis, while those built with tungsten can be used in acid catalysis. In particular, the Keggin anion $[PMo_{12}O_{40}]^{3-}$ with transition metals as counter-cations that have the general formula $M_nH_{3-n}[PMo_{12}O_{40}]$ (M = Cs^+, K^+, NH_4^+, *etc.*) can be very efficient catalysts for the oxidation of alkanes [37].

Keggin anions built with molybdenum can be applied to the oxidation and oxidative dehydrogenation of organic compounds, such as hydrocarbons, aldehydes and carboxylic acids. Commercially, these compounds are used for the oxidation of methacrolein to methacrylic acid, which yields methyl methacrylate by esterification [36]. This can then be polymerized to yield poly(methyl methacrylate), which is known under the trade names Perspex and Plexiglass. In 2009, nearly 2.7 million tones of methyl methacrylate were produced worldwide. Poly(methyl methacrylate) is used in highly transparent optical devices, for the manufacture of CDs and DVDs, as a spinal cement, and as additives to resins and paints [38].

Currently, the acetone-cyanohydrin (ACH) process is one of the main methods that is used to produce methyl methacrylate in industry. Unfortunately, this process suffers from several drawbacks that makes it environmentally unfriendly. For example, HCN, which is a very toxic reactant, is used in this process to give acetone-cyanohydrin as an intermediate. Moreover, large quantities of impure ammonium bisulfate are formed as a co-product, which is very difficult to dispose of in an environmentally friendly way. All of these factors have contributed to the development of alternative commercial processes for the industrial production of methyl methacrylate, such as [38, 39]:

i. A two step approach to the direct catalytic oxidation of isobutene or *tert*-butanol (TAB) to methacrylic acid.
ii. The production of methacrylonitrile (MAN) by TAB ammoxidation.
iii. The BASF route that uses ethene, carbon monoxide and formaldehyde as raw materials.
iv. A modified ACH approach by Mitsubishi Gas Chemical Co., Inc., that eliminates acid waste.
v. The direct oxidative esterification of methacrolein by Asahi Chemical Co. Ltd.

In 1981, the Roham and Hass company [40] discovered a one-step oxidation of isobutane to methacrolein and methacrylic acid. The oxidation of isobutane to yield methacrylic acid, which is an intermediate in methyl methacrylate synthesis, is interesting because of the low cost of the raw material, and it has a very low environmental impact. Methacrylic acid synthesis is shown in Figures 9 and 10, including other pathways, and the proposed mechanism for the partial oxidation is given in Figure 11[41]. Note that in this mechanism, both methacrolein and methacrylic acid are produced through a common intermediate, and the methacrylic acid is not produced as a result of further oxidation of the methacrolein. For this kind of reaction, Keggin-type polyoxometalates containing phosphorus and molybdenum as the main components are the most active catalysts [39].

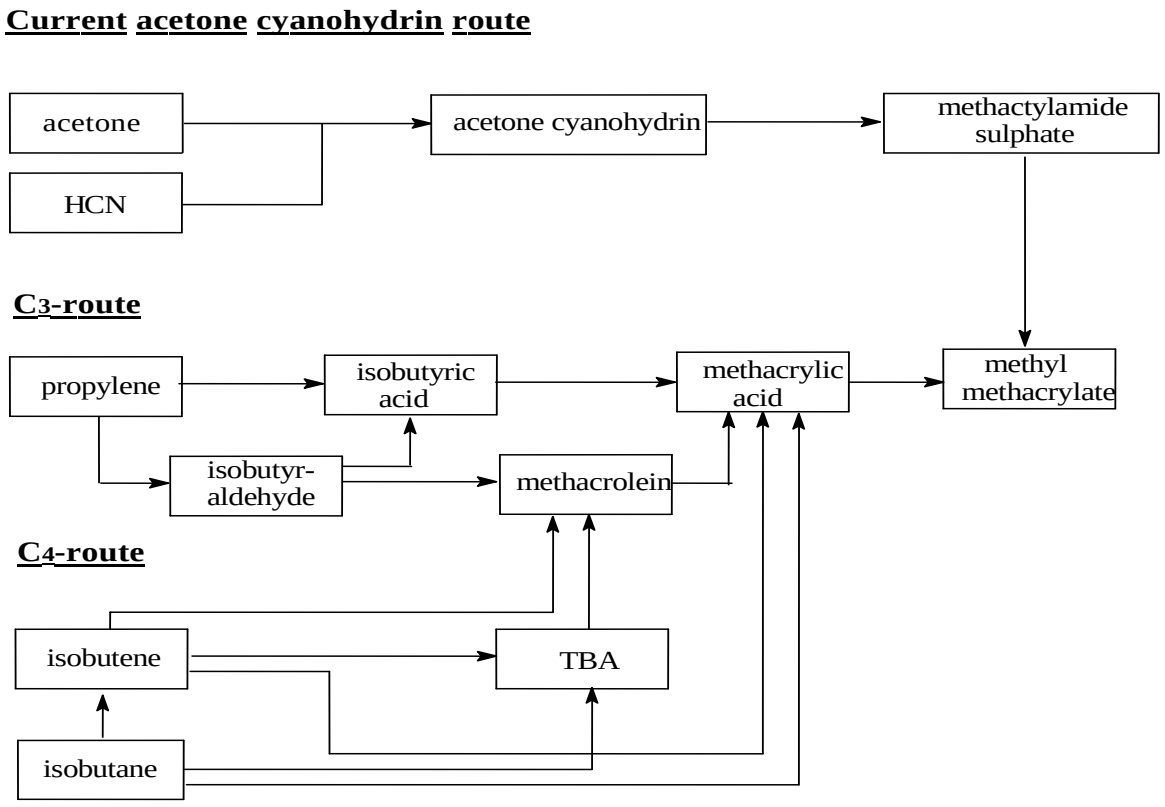

Figure 9. The conversion of C_3 and C_4 to acyrlic monomoers [42].

(TBA = t-butyl alcohol)

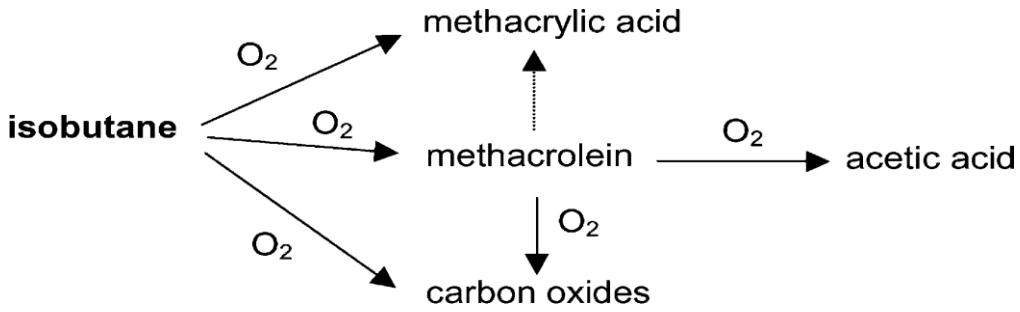

Figure 10. The scheme of isobutane oxidation [41].

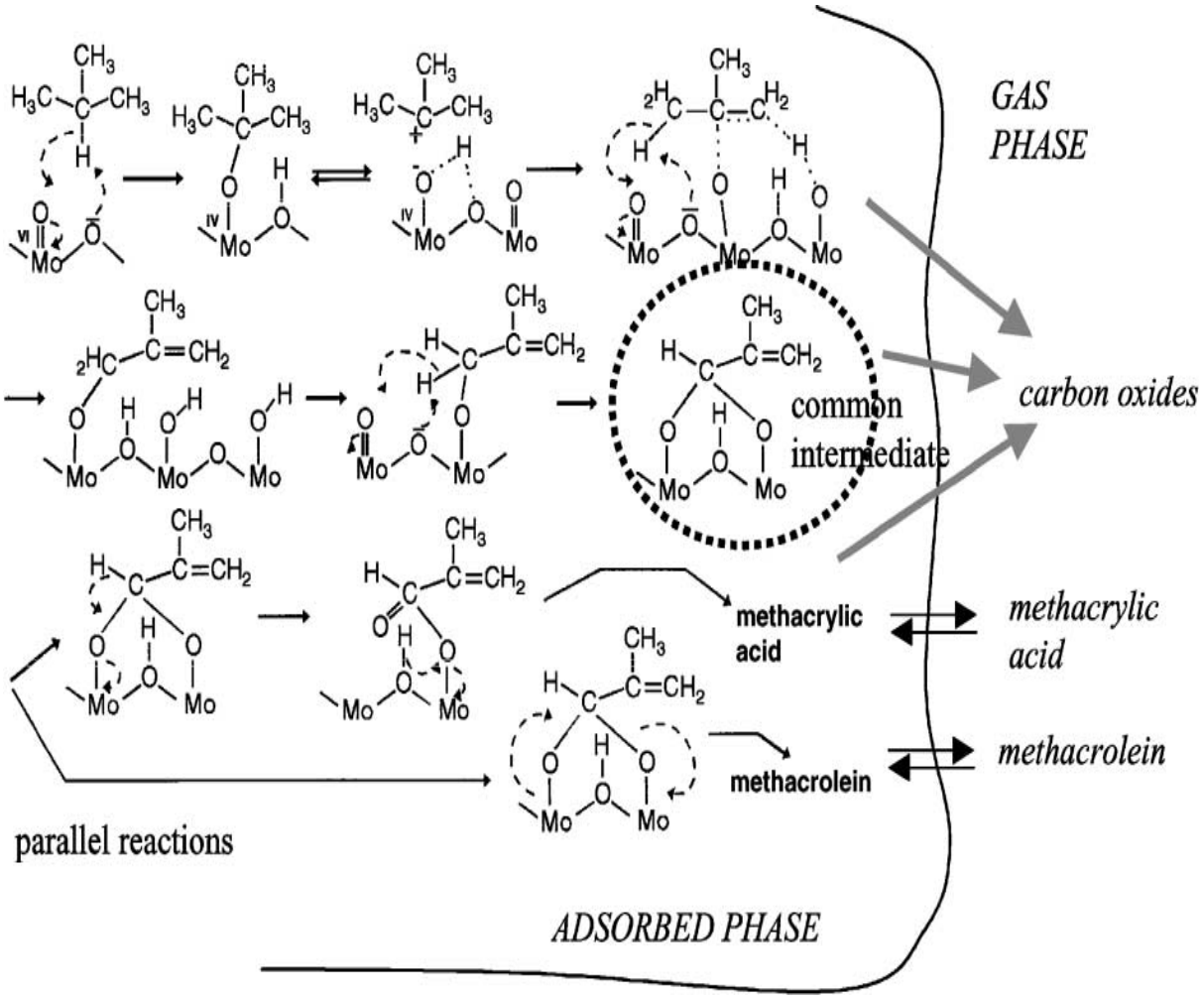

Figure 11. The proposed mechanism of partial oxidation of isobutane over Keggin-type polyoxometalates [41].

1.3.1.2 Structures of heteropoly compounds

Heteropoly compound have received much attention in heterogeneous catalysis because of their unique properties. The structures of these compounds can be examined at three levels, all of which are important to their catalytic nature. These involve their primary, secondary and tertiary structures.

1.3.1.3.1 Primary structure

As noted above, a number of heteropolyoxoanion structures are known, including the Keggin $[XM_{12}O_{40}]^{n-}$, Silverton $[XM_{12}O_{42}]^{m-}$, Anderson $[H_xXM_6O_{24}]^{p-}$ and Dawson-type $[X_2M_{18}O_{62}]^{q-}$ anions [43-47], as well as lacunary, *e.g.* $[XW_{11}O_{39}]^{r-}$, and sandwich-type anions, *e.g.* $[TM_4(XW_9O_{34})_2]^{s-}$ (TM = transition metal, X = P(V), Zn(II), Co(II)), the latter being built from fragments of other heteropoly anions. In the above anions the identity of X may vary widely, including both Main Group and Transition Metal elements. All of these atoms form the primary structure [48]. Several other elements can be used as a part of heteropolyanion structure such as in $H_4[W_{12}Fe_2O_{38}H_2]$ and $H_4[W_{12}Fe_3O_{37}H]$ [49-51]. The most common primary structure is the Keggin-type structure, because of its easy synthesis, thermal stability and because it has favourable acid and redox properties [52].

Figure 12 illustrates the structure of a typical Keggin anion. The $[PMo_{12}O_{40}]^{3-}$ ion contains a central phosphorus atom, which is formally P(V), bonded to four oxygen atoms to form a tetrahedron. This tetrahedron is in turn connected to twelve molybdenum-oxygen octahedra ('*i.e.* MoO_6') arranged in four groups of three edge-sharing Mo_3O_{13} units. The overall symmetry is tetrahedral, T_d. The Mo-O distances increase in the order Mo=O(terminal; a double bond) < Mo-O(bridging; within the Mo_3O_{13} subunits) < Mo-O(bridging; between the Mo_3O_{13} subunits) < Mo-O(central; part of the PO_4 tetrahedron).

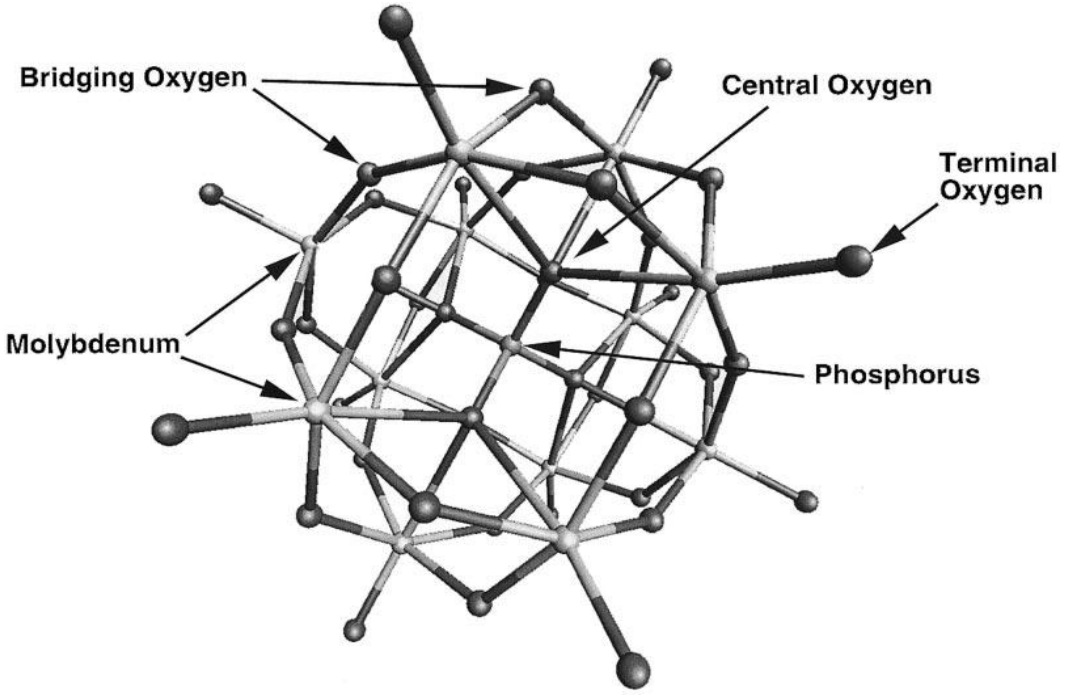

Figure 12. The Keggin structure of $[PMo_{12}O_{40}]^{3-}$ [53].

1.3.1.3.2 Secondary structure

This type of structure refers to the three-dimensional arrangement of the heteropolyanions, the counter cations such as Cs^{+}, Cu^{2+} or Ag^{+}, and other molecules such as the water of crystallisation. The last may vary widely even for one compound. In order to understand the catalytic processes of a heteropolyoxoanion, it is important to distinguish between their primary and secondary structures [54].

1.3.1.3.3 Tertiary structure

At this level, the secondary structure aggregates into solid particles. It has been found that the nature of the counter-cation influences the properties of the tertiary structure, which involve considerations such as the pore diameter (*i.e.* microporosity), the particle size and the surface area [55]. Furthermore, heteropolyoxoanions that have cations with a small ionic radii to charge ratio such as H^{+}, Na^{+} or Fe^{2+} show similar properties to the parent acids [55]. These

compounds are generally soluble in water and in organic solvents and have low surface areas. In comparison, heteropolyoxoanions that have large counter-cations, such as Cs^+, Rb^+, K^+, or NH_4^+ exhibit high surface areas and thermal stability. However, they are insoluble because of the low solvation energies for the large cations, and also exhibit low absorption of polar molecules into the solid bulk [49]. A representation showing the three levels of primary, secondary and tertiary structures is shown in Figure 13.

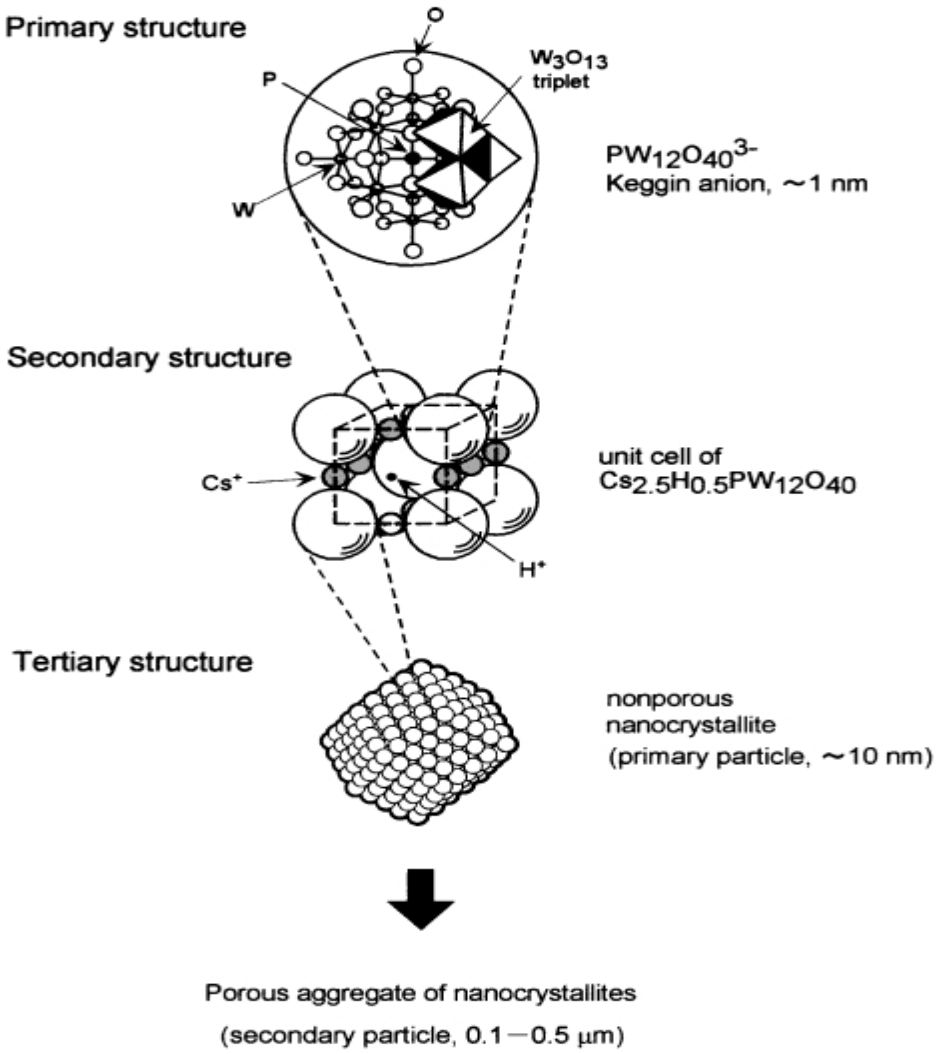

Figure 13. The primary, secondary and tertiary structures of heteropolyoxometalate compounds [55].

1.3.1.4 Pore structures

Pore structures of compounds are divided into three levels. These are microporous compounds, which have pore diameters less than 20 Å, mesoporous compounds, which have pors diameters between 20 and 500 Å, and macroporous compounds, which have diameters greater than 500 Å [56-58]. In general, for the Keggin-type phosphopolyoxomolybdate and phosphopolyoxotungstate anions, only fully substituted salts with Cs^+, Rb^+, K^+, NH_4^+, Tl^+ and some Ag^+ counter-cations exhibit microporosity [56].

1.3.1.5 Surface and bulk catalysis

Gas-solid (and liquid-solid) heterogeneous catalysis occurs on the solid surface of the catalyst. In normal surface catalysis, substrate reactions occur on both outer surfaces and on pore walls following adsorption onto the catalyst surface and activation of the substrate. In the case of the heteropolyoxometalate compounds (*e.g.* phophopolyoxomolybdate), the reactions occur not only on these surfaces, but may also involve the bulk of the catalyst [45, 55, 59-65]. Furthermore, the reactions that include the bulk of the catalyst can occur in two ways. These are designated as Bulk-type (I) catalysis (also known as pseudo-liquid phase catalysis), which refers to the migration of the substrate deep into the catalyst bulk [66], and Bulk-type (II) catalysis, which involves loss of hydrogen from the substrate and subsequent movement of the resulting H^+ and e^- throughout the catalyst bulk. Figure 14 shows representations of the three types of catalysis reactions: (a) normal surface-type catalysis on the left, (b) Bulk type (I) catalysis in the middle and (j) Bulk type (II) catalysis on the right.

In the case of surface catalysis, catalytic activity is proportional to the surface area of the catalyst. For Bulk Type (I) and Bulk Type (II) catalysis, however, catalytic activity is not dependent on the surface area, but rather on the mass of catalyst used, as in both the entire bulk of the catalyst is important to the mechanism.

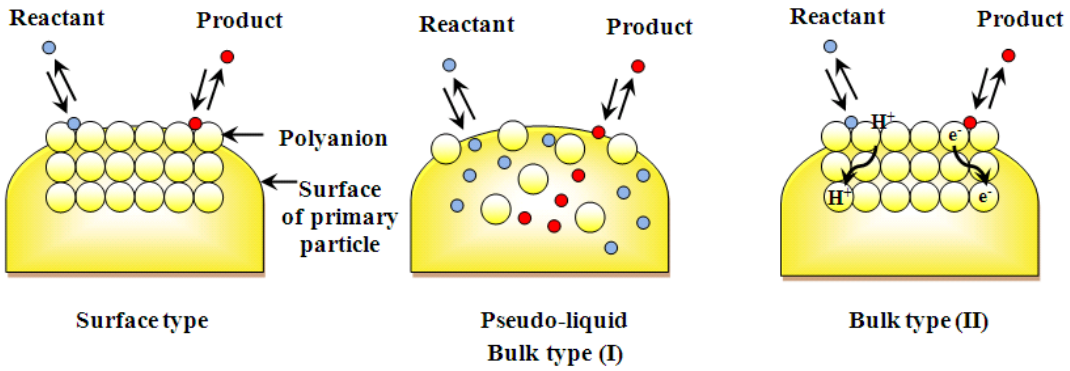

Figure 14. The three types of catalysis: surface type catalysis, Bulk type (I) catalysis and Bulk type (II) catalysis .(Diagram adapted from reference [55]).

1.3.1.6 The oxidation of isobutane; the effects of transition metals on catalytic activity of $[PMo_{12}O_{40}]^{3-}$ catatysts

There have been several studies of the oxidation of isobutane in the literature. Initially, Mizuno *et al.* [66-70] studied the catalytic efficiency of compounds of the type $Cs_{3-x}H_x[PMo_{12}O_{40}]$, and found that the greatest yield of methacrylic acid occurred for $x \approx 0.5$, *i.e.* for $Cs_{2.5}H_{0.5}[PMo_{12}O_{40}]$. The rate of reaction per area decreased progressively with increasing x. It was suggested that isobutane oxidation was a surface-type reaction, and that the catalytic activity was controlled by the oxidising ability of the catalyst surface. Substitution of transition metal ions for H^+ to give the series $Cs_{2.5}(M^{n+})_{0.08}(H)_{0.5-0.08n}[PMo_{12}O_{40}]$, where M^{n+} was a transition metal ion including Ni^{2+}, Fe^{3+}, Mn^{2+}, Cu^{2+}, Co^{2+}, Hg^{2+}, Pd^{2+} and Pt^{2+}, showed that the selectivity of methacrylic acid and methacrolein increased for Ni^{2+}, Fe^{3+}, Mn^{2+}, but that the yields of the above products decreased for the other transition metal ions. The highest activity occurred for Ni^{2+}, and the preferred Ni^{2+} content was 0.08. Also, they concluded that the oxidation of isobutane was a surface-type reaction and that the catalytic activity was

controlled by the oxidising ability of the catalyst surface [66]. A latter study reported enhanced catalytic activity by V^{5+} substitution into the Keggin anion [71].

In a series of papers, Cavani, Trifirò and co-workers reported on the oxidation of isobutane over mixed K^+/NH_4^+ salts of the $[PMo_{12}O_{40}]^{3-}$ ion including the effects of the addition of Fe^{3+}, which increased the catalytic activity but reduced the selectivities to the desired products. The iron was present as a partly hydrolysed species, $Fe(OH)_2^+$ [72-74]. This group also studied the effects of Sb^{3+} on the catalytic behaviour of a $(NH_4)_3[PMo_{12}O_{40}]$-based catalyst. The catalyst showed good activity, but poor selectivity to the desired products [75].

Langpape, Millet and co-workers [37, 76-78] studied the structures of the $Cs_{3-x}H_x[PMo_{12}O_{40}]$ salts (x = 0, 0.5, 1, 1.5, 2) and also the catalytic activities of these compounds with partial substitution of Cu^{2+} and Fe^{3+} for Cs^+, to give the series of compounds of the type $Cs_2(M^{n+})_x(H)_{1-xy}[PMo_{12}O_{40}]$ (M = Cu^{2+} and Fe^{3+}, with $0 \leq x \leq 0.43$) in the oxidation of isobutane. They found that copper had a positive effect on catalytic activity, although a negative affect on the selectivity to methacrylic acid. Iron, however, had no effect on the catalytic activity, but gave an enhanced selectivity to methacrylic acid. Interestingly, this trend was reversed at higher temperatures.

Paul *et al.* [79] applied the Mars-van Krevelen model [80] to a comprehensive study of the oxidation of isobutane over $(Cs^+/NH_4^+)_4[PMo_{11}VO_{40}]$. The rate-limiting step was found to be reaction of the isobutane on the oxidized catalyst surface. The total selectivity for methacrylic acid and methacrolein was found to depend on the extent of conversion of the isobutane, but not on the isobutane-oxygen ratio or on the temperature at which the catalysis was carried out. The effective activation energy for reduction (Mars-van Krevelen model) was 90 kJ/mol and for the reoxidation step (Mars-van Krevelan model) was 86 kJ/mol.

Jalowiecki-Duhamel *et al.* [81] studied the selective oxidation of isobutane to methacrylic acid and methacrolein over a catalyst of formulation $Cs_{1.6}H_{2.4}P_{1.7}Mo_{11}V_{1.1}O_{40}$, which was derived from $H_4[PMo_{11}VO_{40}]$. It was shown that, in a reduced state, this catalyst had anion vacancies able to store reactive hydrogen species (designated H*), which could diffuse through the solid. As loss of hydrogen from isobutane is regarded as a first step in the oxidation process, they proposed that the mechanism involves dehydrogenation with an initial heterolytic abstraction of H^- from isobutane.

Another study involved the selective oxidation of isobutane over a polyoxometalate catalyst of the type $Mo_{12}V_{0.5}P_{1.5}As_{0.4}Cu_{0.3}Cs_{1.4}O_x$, which had a Keggin-type structure based on X-ray diffraction and IR spectroscopic studies. The catalytic activity increased with increasing temperature and the partial pressure of the isobutane, but was limited by the thermal stability of the catalyst [82].

More recently, Kendell and Brown and co-workers [38, 83, 84] have studied the oxidation of isobutane using a novel low-pressure steady-state technique. Catalysts studied have included $H_3[PMo_{12}O_{40}]$, the series $Cu_{3-x}H_{2x}[PMo_{12}O_{40}]_2$ (where x = 0, 0.5, 1 and 2), the Al^{3+}, La^{3+} and Ce^{3+} salts, and the Group 1 and 2 salts of the type $(A)_{3-x}H_x[PMo_{12}O_{40}]$ (where A is a Group 1 cation and x = 0, 0.5, 1 and 2) and $(A)_{3-x}H_{2x}[PMo_{12}O_{40}]_2$ (where A is a Group 2 cation and x = 0, 1 and 2). The products observed were methacrolein, 3-methyl-2-oxetanone, acetic acid, CO_2 and water. The 3-methyl-2-oxetanone appears to be a precursor to methacrylic acid, which is observed under the low-pressure conditions operating in the instrument. The products form by two distinct reaction processes, Category 1 and Category 2. The former is associated with products forming on the catalyst surface, and which exhibit exponential temperature-dependent profiles, while the latter results from isobutane penetrating deep into the catalyst bulk, generating the products which then desorb in a series of bell-shaped profiles. Apparent activation energies were measured in all of the studies, and

vary considerably, with those of Category 1 generally showing a smaller range of values than those of Category 2.

1.3.2 Combustion catalysis

Major contributors to air pollution are the so-called volatile organic compounds (VOCs), which include aromatic solvents, hydrocarbons, oxygenated compounds and chlorocarbons. These emissions come from various human activities, mainly from mobile sources (*i.e.* transport vehicles), solvents from industrial processes, and unburned fuel from power production. They cause undesirable environmental conditions including ozone depletion and even global warming. These compounds accumulate in the atmosphere and act as catalysts for ozone decomposition because of their persistence and high volatility. For example, methane, which is the lightest volatile organic compound, is effective as a green house gas at about 20 times that of CO_2. Unfortunately, methane has lifetime of about 10 years in the atmosphere [85, 86].

This topic has thus attracted the attention of much research in the processes of the abatement of VOCs. These include absorption, flame combustion, conversion, condensation, or catalytic combustion into less harmful compounds. Air is used to oxidise the compounds in high temperature flame combustion, but a significant amount of nitrogen oxides can be formed in this process. Catalytic combustion is more effective than flame combustion and can be carried out at low temperatures by employing metal or metal oxide catalysts. Catalytic combustion is preferred because of its relatively low temperature and high selectivity. Moreover, catalytic combustion is one of the most promising technologies for the destruction of VOCs as a result of savings in energy [87, 88]. Conversion using this type of catalysis depends on the contact time or flow rate, gas composition, amount of catalyst that is used and finally the loading of the active component, and any changes in these may alter the relative

activity of the catalyst. Moreover, this reaction is a very exothermic, and it is very hard to keep the catalytic conditions isothermal. The catalysts active for VOC decomposition are inorganic in nature and include both metals and metal oxides [89].

1.3.2.1 Metal catalysts

In the last decade or so, several researchers have focused on studying catalysts based on metals, including the noble metals. These include platinum, palladium and nickel, and these are the most active catalysts for complete oxidation reactions such as hydrocarbon detection in enclosed environments and VOC removal from work-places such as in polymer processing and coating operations. Aryafar and Zaera [90] studied the oxidation of different alkanes (methane, ethane, propane, *n*-butane and isobutane) with oxygen over platinum, palladium and nickel. This study found that the oxidation reaction on palladium metal starts at about 1060 K for methane and at about 700 K for the other hydrocarbons; the reaction over platinum starts around 900 K for methane and 500-570 K for the other alkanes. Finally, for the reaction over nickel it was found that all compounds reacted slightly above 800 K. From this data, it is obvious that the combustion of methane is harder than other hydrocarbons with greater molecular masses. Furthermore, the study found that the reaction rates and activation energies decrease with an increase in the chain length of the hydrocarbons. Figure 15 shows the Arrhenius plots for the oxidation reactions of the four different alkanes over the three metals, and the activation energy data is given in Table 1.

Although metals are very active, they have several disadvantages. These include their high volatility, ease of poisoning, and poor economics (*i.e.* cost) and availability (particularly the noble metals). More recently, therefore, metal oxide catalysts have been receiving much wider attention than metals [35].

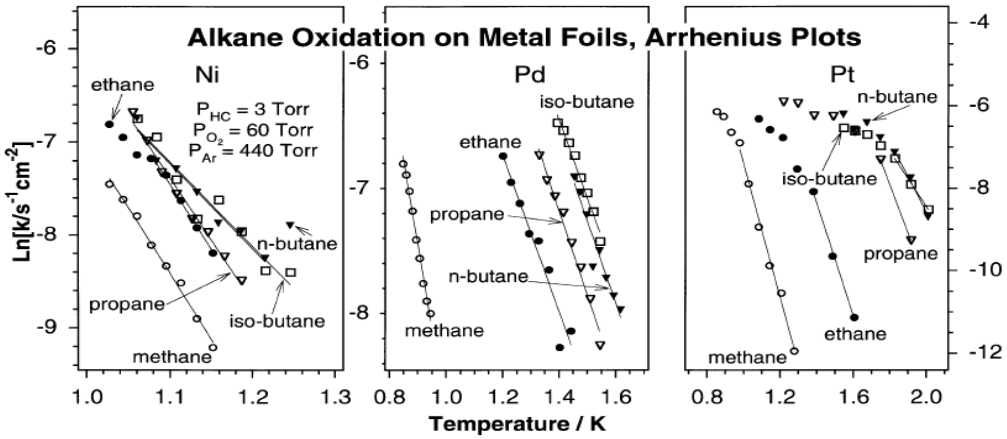

Figure 15. Arrhenius plots for the reaction between different kind of alkanes and oxygen over the metals Ni, Pd and Pt [90].

Table 1. Activation energies for different chain length hydrocarbons over Ni, Pd and Pt [90].

	Nickel		Palladium		Platinum	
	T range (K)	E_a (kcal mol^{-1})	T range (K)	E_a (kcal mol^{-1})	T range (K)	E_a (kcal mol^{-1})
methane	868–973	28.1	1058–1178	26.7	782–1173	32.1
ethane	868–973	27.8	693–833	12.4	573–973	27.3
propane	843–948	26.5	648–753	13.4	523–873	23.3
n-butane	803–943	18.2	618–688	13.0	498–673	17.0
isobutane	803–943	18.0	648–718	12.5	498–673	13.4

1.3.2.2 Metal oxide catalysts

Metal oxides have several advantages over metals. It has been reported that metal oxides are more resistant to deactivation by poisoning [26]. Moreover, they are suitable for applications in highly specific situations because they have an unlimited potential for modification. Metal oxides for VOC removal may be used as supported or unsupported oxides. The oxidation of VOCs employs several oxides of the transition metals such as those of vanadium, chromium, manganese, iron, cobalt, nickel and copper.

There are two types of metal oxides: (a) reducible metal oxides, such as TiO_2 and the oxides of the 3d metals of Groups 8 to 10 (*e.g.* Fe_2O_3, Co_3O_4, and NiO), and (b) non-reducible oxides, such as those like SiO_2 and Al_2O_3. The oxidation over metal oxides is catalysed by lattice oxygen. During the oxidation processes, the metal oxide may be reduced by hydrocarbons and reoxidised by oxygen in the input stream. This is called the Mars-van Krevelen mechanism [80].

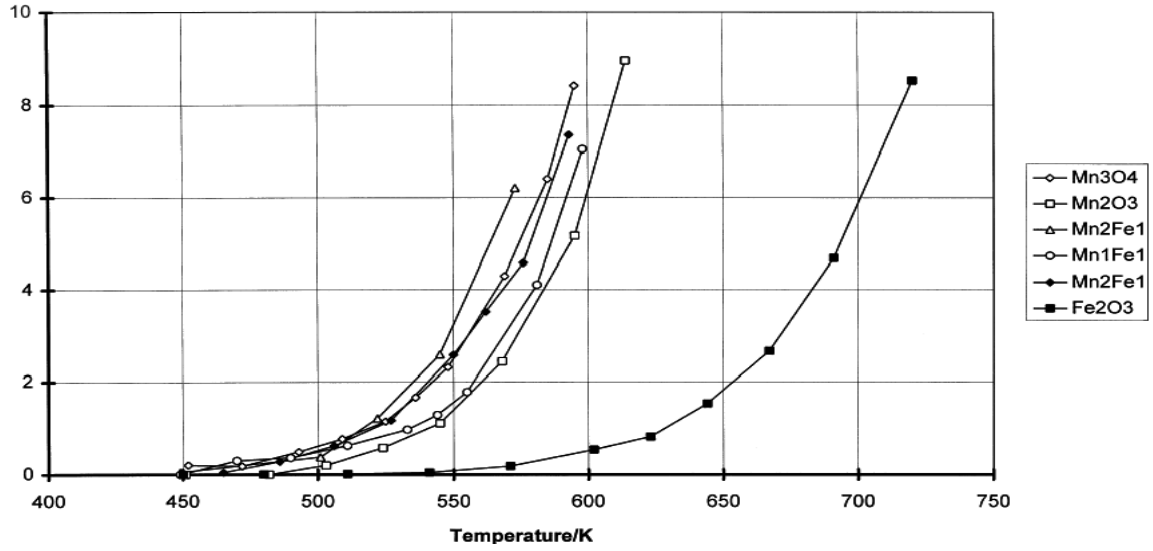

Figure 16. The conversion of propane oxidation over manganese and iron oxides (including mixed Mn/Fe oxides) [91].

Baldi *et al.* [91] studied the oxidation for propane and propene over managanese and iron oxides, including Mn/Fe oxides. Figure 16 shows the propane conversion over manganese and iron oxides. They reported that the activity of α-Mn_2O_3 for propane and propene oxidation was high compared to α-Fe_2O_3. Also, they found that Mn_3O_4 was more active than α-Mn_2O_3. The same group reported the activity of Mn_3O_4 for oxidation of C_3 hydrocarbons and oxygenates [92]. They found that propane was completely converted to CO_2 at temperatures above 400^{o}C. Cordi *et al.* [93] studied the combustion of oxygenated

VOCs over CuO catalysts. They observed that lattice oxygen is active for deep oxidation in a CuO catalyst. Lattice oxygen is formed in the presence of gas phase oxygen during the oxidation process. Marion *et al.* [94] investigated the activity of CuO dispersed on Al_2O_3 for methane combustion. They observed that the activity of supported CuO is higher than the activity of unsupported CuO. Also, they reported that low loading of the catalyst on the Al_2O_3 support resulted in well-dispersed ionic CuO compared with high loading of CuO on the Al_2O_3 support which led to poorly dispersed catalysts with a more covalent character. Thus a catalyst with more ionic character is more active in methane combustion. Arnone *et al.* [95] studied the complete oxidation of methane over a series of metal oxides. They found that the activity of Fe_2O_3 for methane combustion was low, while the oxides of Cr, Co and Mn showed high activity for the combustion reaction.

1.3.3 Gold nanoparticles and catalysis

1.3.3.1 Introduction

The catalytic activity of metal oxides is greatly increased by the addition of gold nanoparticles. When gold nanoparticles are dispersed on the support surface, they enhance the reducibility of the metal surface oxygen, and it becomes catalytically active for many reactions such as the epoxidation of propylene, the synthesis of hydrogen peroxide [96] and vinyl chloride, the selective oxidation of alcohols, the carbon-carbon coupling reaction, CO oxidation, and the combustion of hydrocarbons [97]. In general, the gold can be more active and stable when supported on reducible oxides such as TiO_2, CeO_2, Fe_2O_3, Co_3O_4 and Mn_2O_3 than when supported on non-reducible oxides such as SiO_2 and Al_2O_3 [25].

1.3.3.2 Preparative methods for gold/metal oxides

There are several ways to prepare a catalyst of gold nanoparticles supported on a metal oxide [11]. The processes are illustrated schematically in Figure 17. There are three main ways of preparation. The first method is called co-precipitation (CP) and it is the simplest process. It was one of the first to be used. Gold nanoparticles can be supported on Fe_2O_3, Co_3O_4, NiO and ZnO, but not on TiO_2, Cr_2O_3, MnO_x and CdO [98]. The disadvantage of this method is that the synthesis will yield some Na^+ and Cl^- ions as a co-product, and these may act as a catalyst poison. The second method is called deposition precipitation (DP) and it is used for producing commercial, gold-supported catalysts, and it can be applied to most support materials. The supported gold nanoparticles have smaller size particles than in the co-precipitation method, but it is recommended that the supports should have a surface area of at least 50 $m^2\ g^{-1}$. Also, this method has an advantage compared with co-precipitation as the entire active components remain on the surface of the support and are not buried within it, as occurs in the co-precipitation method. The third method is impregnation (IMP), and it generates much larger gold particles (*i.e.* larger than 30 nm), because of several factors:

- While bulk gold has a relatively low melting point (1336 K), nanosized gold with a diameter of 2 nm is even lower at 573 K, because of quantum-size effects. Thus, as small particles, gold tends to coagulate much more readily during catalyst calcination at temperatures above 573 K [98].
- The interaction between $HAuCl_4$ and an oxide support is weak, and any remaining chloride on the surface of the support following calcination may cause the gold particles to coagulate [15, 17].

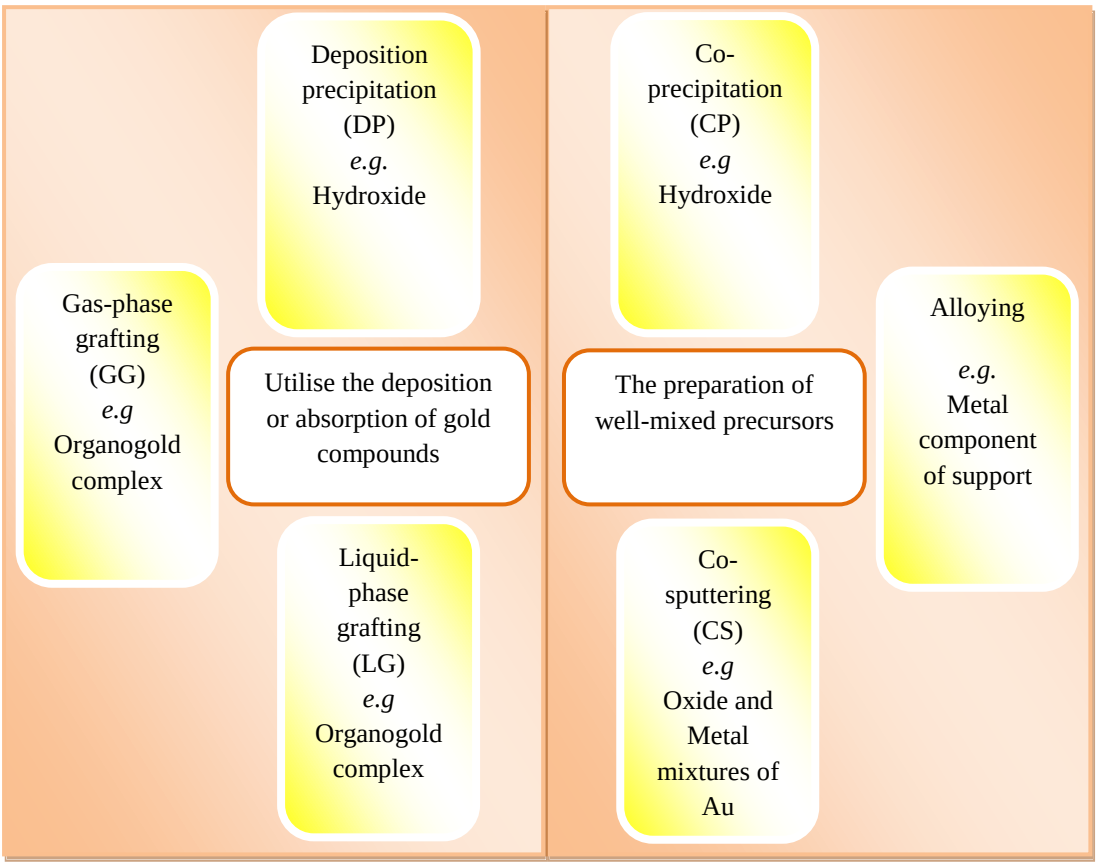

Figure 17. Methods for the preparation of gold nanoparticles supported on metal oxides.

1.3.3.3 The catalytic activity of supported gold for CO oxidation

The CO oxidation to CO_2 at low temperatures is a very important reaction for air purification systems and breathing apparatus. At present, industry used a Hopcalite catalyst ($CuMn_2O_3$), which is a mixture of copper and manganese, but deactivation of this catalyst occurs quite rapidly, and it cannot be used over the long term.

As indicated above, supported gold particles show a surprisingly high catalytic activity for CO oxidation at a temperature as low as 200 K [9, 99]. Moreover, gold nanoparticles have many edges, corners, and meta-stable surfaces. When deposited on supports, the catalytic activity of gold increases and oxidation of CO to CO_2 occurs as low as 197 K [6, 9].

In 1987, Haruta [6] was the first to show the effect of gold on CO oxidation at low temperatures. Haruta and co-workers investigated CO oxidation at temperatures below $0^{o}C$ over gold supported on MnO_2, α-Fe_2O_3, Co_3O_4, NiO, and CuO that had been prepared by the co-precipitation method. The highest activities among these metal oxides were for Au/α-Fe_2O_3, Au/Co_3O_4, and Au/NiO. The amount of gold in the last three catalysts was found to be 5 atom % in α-Fe_2O_3 and Co_3O_4, but it was about 10 atom % in NiO. Figure 18 presents the conversion of CO over the three catalysts at various temperatures.

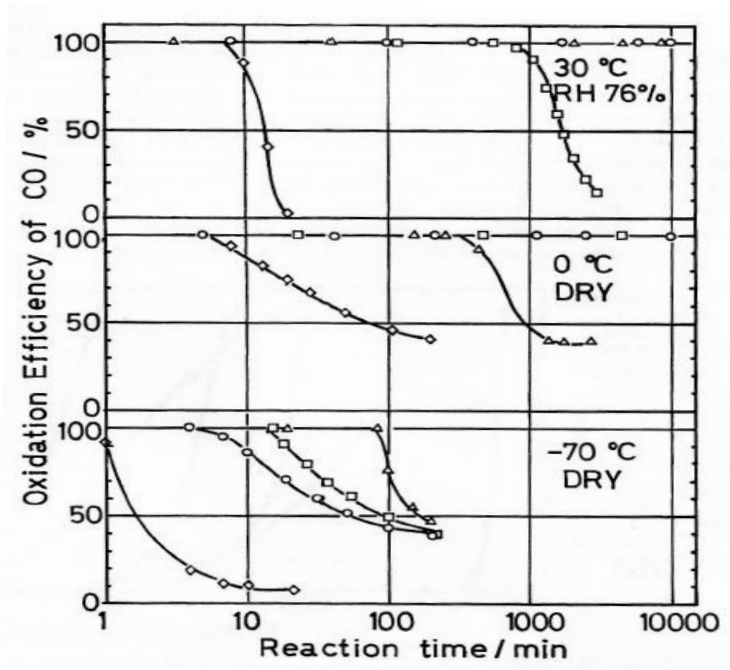

Figure 18. The CO oxidation as a function of time. (Catalyst 0.20 g, CO 1 vol % air, 66 mL/min). Au/α-Fe_2O_3 (5 atom % Au) (○), Au/Co_3O_4 (5 atom % Au) (Δ), Au/NiO (10 atom % Au) (□), and Hopcalite catalyst (◊) [6].

The data shows that these catalysts are able to oxidise the CO completely even at temperatures as low as $-70^{o}C$. Comparing these catalysts with gold powder prepared from a gold colloid and the host metal oxides under the same conditions, the catalysts exhibit a remarkably enhanced activity, as shown in Figure 19.

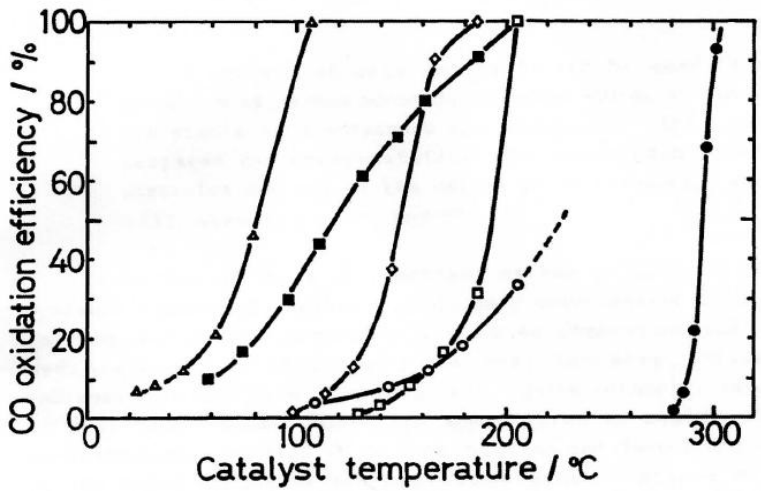

Figure 19. CO oxidation over 0.20 g of catalyst, CO 1 vol %, air 66 mL/min. Co_3O_4 (300°C) (Δ), NiO (200°C) (◊), α-Fe_2O_3 (300°C) (□), Au/α-Fe_2O_3 by impregnation (200°C) (5 atom % Au) (■), Au/γ-Al_2O_3 by impregnation (200°C) (5 atom % Au) (○), and Au powder prepared from a gold colloid (●) [6].

These compounds in their single states need much higher temperatures to complete the CO oxidation. For example, Co_3O_4 requires a temperature of about 100°C to oxidise CO, while Au powder needs about 300°C. The work by Haruta has led to a greater understanding of gold as a catalyst and an increase in the interest in the field.

Also, Haruta [100] has investigated the effect of the preparative methods on the catalytic activity of gold catalysis for CO oxidation over Pt/TiO_2 and Au/TiO_2 catalysts. Figure 20 shows that gold catalytic activity depended strongly on the method of synthesis, *i.e.* deposition-precipitation (DP), impregnation (IMP) and photodeposition (FD). The Au/TiO_2 activity decreased in the order DP >> IMP ~ FD. It should be noted that Pt/TiO_2, which is less sensitive to the preparation methods, has a high catalytic activity.

Following on from Haruta, a number of other studies have focussed on the surprising catalytic activity of gold, especially the reasons that make gold act in this manner.

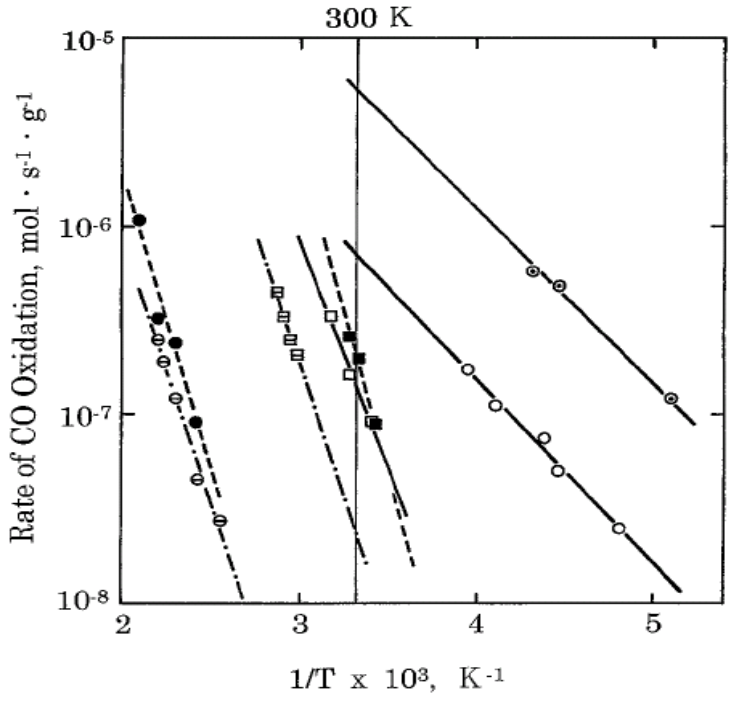

Figure 20. Logarithmic reaction rate of CO oxidation over Au/TiO_2 and Pt/TiO_2 catalysts: 1.0 wt % Pt/TiO_2 (DP)(□), 1 wt % Pt/TiO_2 (IMP) (■), 0.9 wt % Pt/TiO_2 (FD)(◙), 1.8 wt % Au/TiO_2 (DP)(Θ), 0.7 wt % Au/TiO_2 (DP) (○), 1.0 wt % Au/TiO_2 (IMP) (●), and 1.0 wt % Au/TiO_2 (FD) (Θ) [100].

According to the literature, the catalytic performance of gold depends on many factors that all contribute to its catalytic activity. Valden *et al.* [101, 102] have reported that the high activity of gold for CO oxidation is related to a quantum size effect. Haruta and coworkers [103, 104] have reported that the support type and the interface play a significant role in the catalytic activity. However, the reasons for the catalytic activity of well-dispersed gold particles on a support are still under discussion.

Gold particles have shown excellent catalytic activity when the particles are smaller than about 10 nm, even at room temperature. It has been suggested that this is attributable to a metastable inter-atomic bonding of gold atoms [27]. In the 1980s, Haruta [105] showed that finely dispersed gold nanoparticles on metal oxide supports are chemically very active catalysts for the oxidation of CO at very low temperature [20, 106]. The high catalytic

activity of gold supported on metal oxides has been explained by the capacity of gold to increase the mobility of metal oxide lattice oxygen through a Mars-van Krevelen mechanism [87, 107]. This is illustrated by the oxidation of CO on a Au-TiO_2 surface. In this mechanism (Figure 21), the CO species cover the TiO_2 surface and its perimeter interfaces around gold particles at temperatures below 200 K. The reaction between CO and O_2 occurs only on the step, edge and corner sites of the gold surface with an activation energy about 0 kJ/mol. CO oxidation proceeds at the perimeter interfaces that are covered with CO species. This also depends on the temperature [11]. Moreover, catalytic activity can be detected at any temperature if the particles of the gold are small enough.

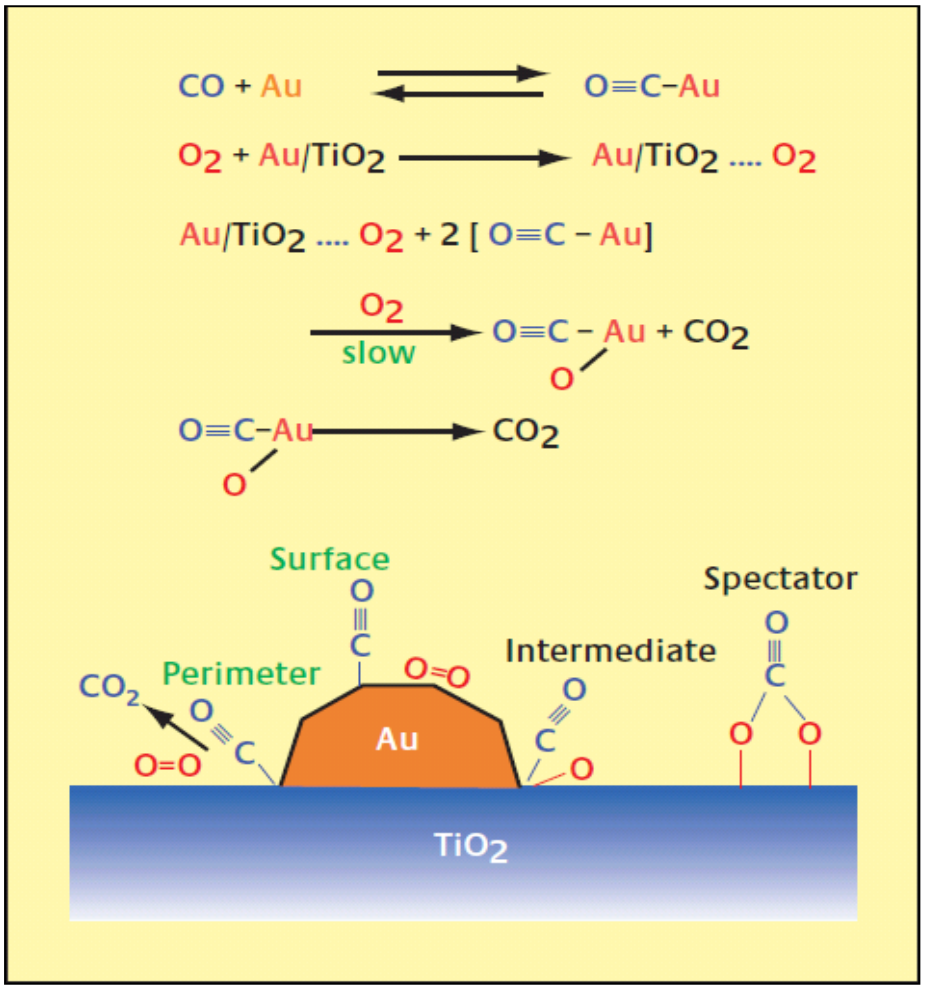

Figure 21. The proposed mechanism of CO oxidation on a Au-TiO_2 surface [7].

Figure 22 shows an IR spectroscopic study of Au/TiO_2 catalysts which were calcined in air at different temperature and used for CO oxidation, that was adsorbed at 90 K (the mean diameter of the gold particles is 2.5 nm).

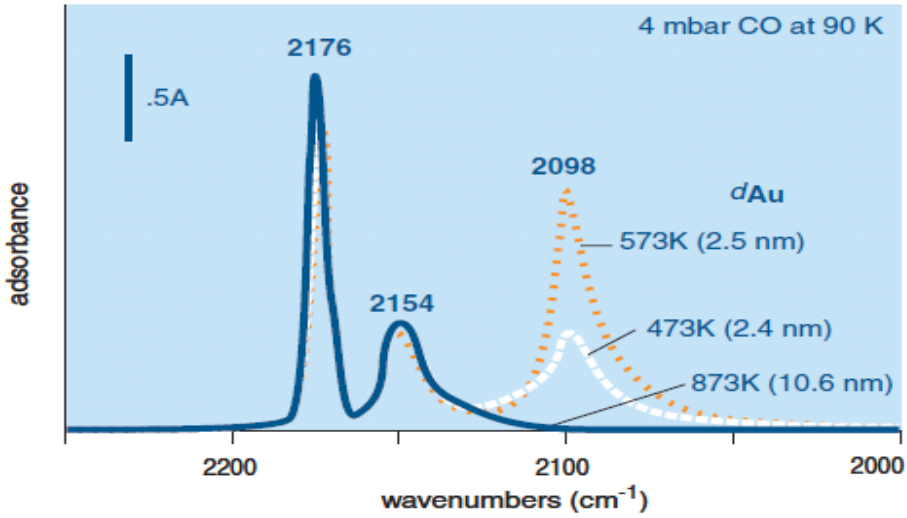

Figure 22. FT-IR of CO adsorption over Au/TiO_2 calcined at 473, 573, and 873 K [11].

The most active sample (i.e. that calcined at 573 K) has the highest intensity peak of CO adsorbed on the metallic gold sites at 2098 cm^{-1}. This corresponds to CO absorption of an Au-C≡O species (note that free gaseous CO appears at 2176 cm^{-1}, and that CO frequencies at lower wavelengths indicate coordinated CO). Note that the intensity of the CO peak is markedly reduced when the diameter of the gold particles become larger than 10 nm (the sample calcined at 873 K). This indicates that CO may be adsorbed only on steps, edges, and corners of the surface and not on a smooth surface [11].

Haruta and coworkers [11, 91] studied the reaction rates of CO oxidation over unsupported gold powder and Au/TiO_2 catalysts. Figure 23 shows the plot for the rate of CO oxidation per exposed gold surface area (equivalent to turnover frequency, TOF), over Au/TiO_2 and over unsupported gold powder. Over Au/TiO_2, the rates measured by lowering the temperature from 353 K were about one order of magnitude larger than by raising the

temperature from 203 K. This difference in behavior was related to the accumulation of carbonate species on the support surface at low temperatures, resulting in the loss of perimeter interfaces necessary for activating O_2. Thus, the rate over the Au/TiO_2 catalyst that was deactivated during studies at lower temperatures is assumed to be close to the reaction rate of CO with O_2 over the gold surface without the contribution from O_2 activation at the perimeter interfaces. Moreover, the normalised rate increases with a decrease in the diameter of the gold particles (by a factor of 2/3).

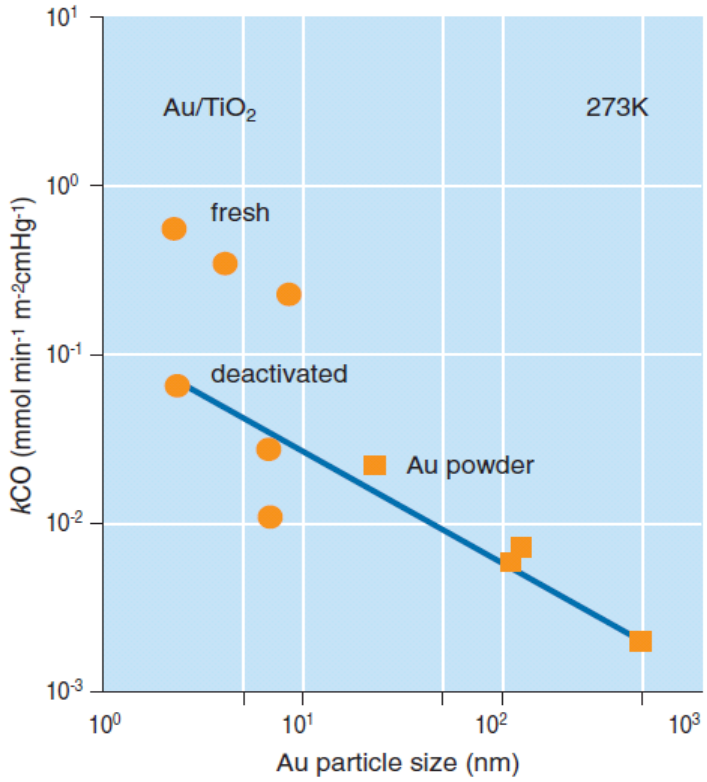

Figure 23. The reaction rate of CO oxidation over Au/TiO_2 and unsupported Au powder [11].

This behaviour may be explained if the active sites are edge, corner or step sites, which increase in number as the size of the gold particles decrease. The observed order of magnitude difference in the rate between deactivated Au/TiO_2 and fresh Au/TiO_2 (obtained by high temperature measurements), is related to the contribution of the TiO_2 support.

Also, it is known that it is not just the particle size of gold that has an effect on the activity of the catalysts, but that the choice of the support also influences catalytic activity. This is illustrated in Figure 24 [106]. In this study different oxide supports were used, and different catalytic activities were observed. Notably, the least active species was a fine gold powder of approximately 2-4 nm. The most important property for the catalysts is the active surface that increases when the size of the catalyst particles is decreased [108]. Moreover, the oxides of 3rd row transition metals, especially Group 8-10, as well as the hydroxides of the alkaline earth metals, led to high catalytic activity for CO oxidation even at temperatures as low as 203 K [109, 110]. Thus when gold nanoparticles were supported on TiO_2, Fe_2O_3 and Co_3O_4, with a particle size in the range of 2-10 nm in diameter, high catalytic activity was obtained, while when supported on $Be(OH)_2$ and $Mg(OH)_2$ the particles were smaller than 1.5 nm, and also exhibited a high catalytic activity [111].

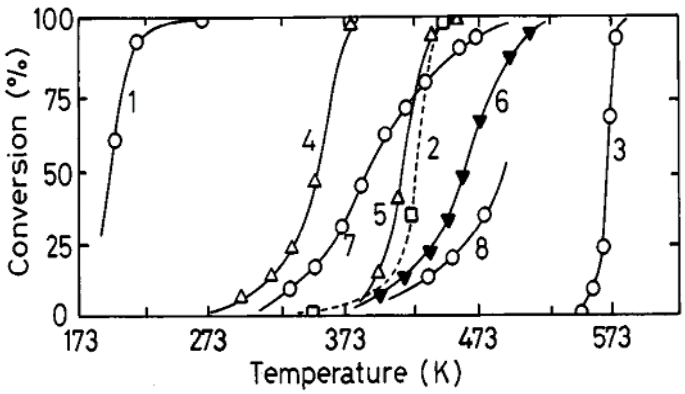

Figure 24. CO conversion over different catalysts. 1) Au/α-Fe_2O_3 (co-precipitation, 400°C), 2) 0.5 wt % Pd/γ-Al_2O_3 (impregnation, 300°C), 3) fine gold powder, 4) Co_3O_4 (carbonate, 400°C), 5) NiO (hydrate, 200°C), 6) α-Fe_2O_3 (hydrate, 400°C), 7) 5 wt % Au/α-Fe_2O_3 (impregnation, 200°C), and 8) 5 wt % Au/γ-Al_2O_3 (impregnation, 200°C) [20].

The loading of gold on the surface of the support is another factor that has a major effect on catalytic activity [15]. For example, Haruta reported that gold particles prepared by

the DP method attached to the oxide surface very strongly, while particles prepared by the IMP method attached to the surface of the support very weakly. During oxidation reactions, the particle that loaded weakly on the support surface using the IMP method required a higher temperature to complete the reaction. On the other hand, gold particles loaded using the DP method needed a much lower temperature to give complete oxidation. This study also indicated that the contact structure of the gold nanoparticles on the surface of the support, as depicted in Figure 25, contributes on the catalytic activity [106]. Obviously the gold-support interaction plays a key role in catalytic activity.

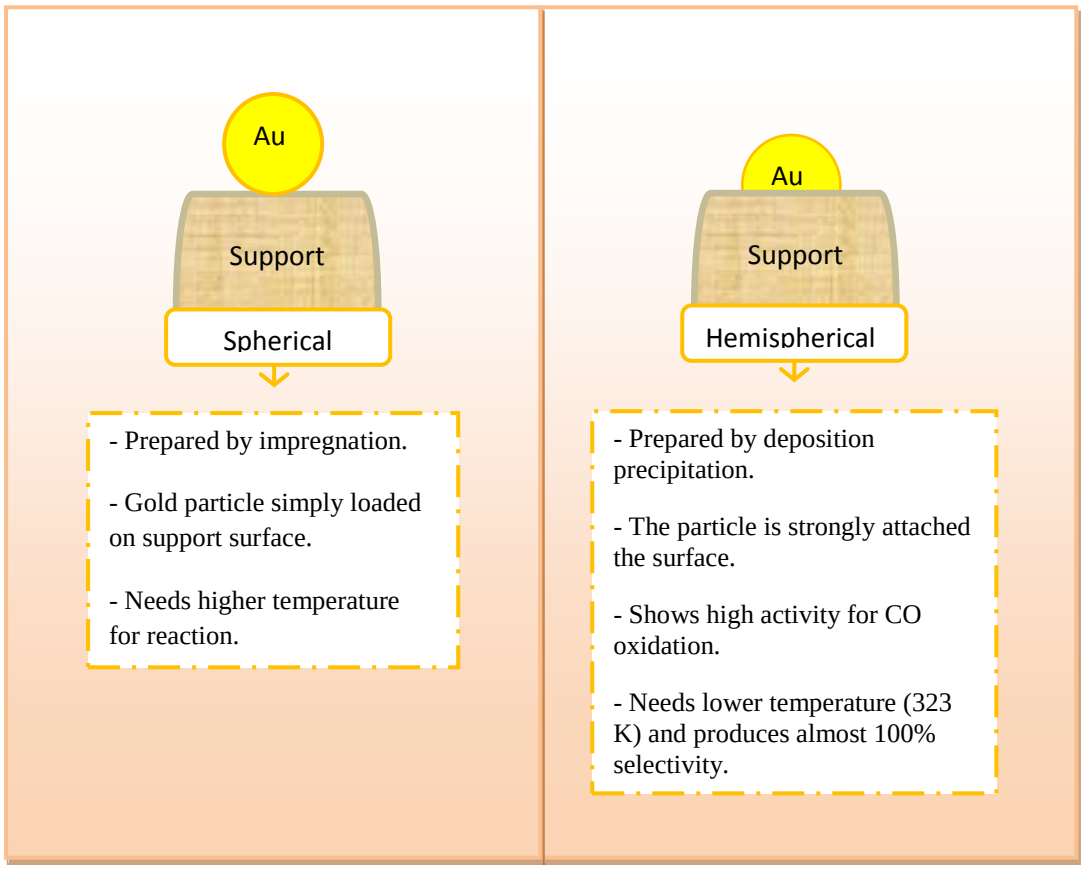

Figure 25. Different contact structures of gold supported on metal oxides for CO oxidation.

Other researchers have assumed that the pretreatment of the supported gold is the most important factor in order to produce catalysts with a high activity. Vannice and co-

workers [112] have shown that a specific sequence of pretreatments (H_2 reduction at 773 K, calcinations in 20% O_2 at 673 K, and H_2 reduction at 473 K) enhance the catalytic activity for CO oxidation over Au/TiO_2. Tusbota *et al.* [113] have investigated the effect of calcination on the catalytic activity of Au/TiO_2 for CO oxidation. They indicate that gold and TiO_2 alone are not active for CO oxidation, but when gold is deposited on TiO_2, the combination shows enhanced catalytic activity for CO oxidation. The catalytic activity of supported gold markedly changes depending on the preparation methods. Two types of catalysts were synthesised. The Au/TiO_2 catalysts were prepared by mechanical mixing (MM) and deposition precipitation. Figure 26 presents the Arrhenius plots for CO oxidation over Au/TiO_2 (MM) and Au/TiO_2 (DP). For the Au/TiO_2 (MM) catalyst, calcination at temperatures below 473 K led to poor catalytic activity, while at 325 K the activity gradually improved with time, reaching a steady state within 5 hours. It was also observed that catalytic activity increased with an increasing calcination temperature from 473 to 873 K. For Au/TiO_2 (DP), catalytic activity reduced with increasing calcination temperature to 873 K.

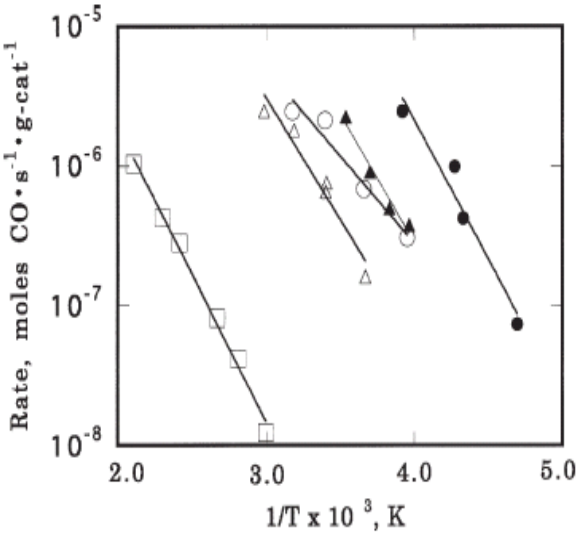

Figure 26. Arrhenius plots for CO oxidation over Au/TiO_2 (MM) (Au 3.00 wt %) calcined at 473 K(□), 673 K(Δ) and 873 K (○), and Au/TiO_2 (DP) (Au 3.3 wt %) calcined at 673 K(●), and 873 K(▲) [113].

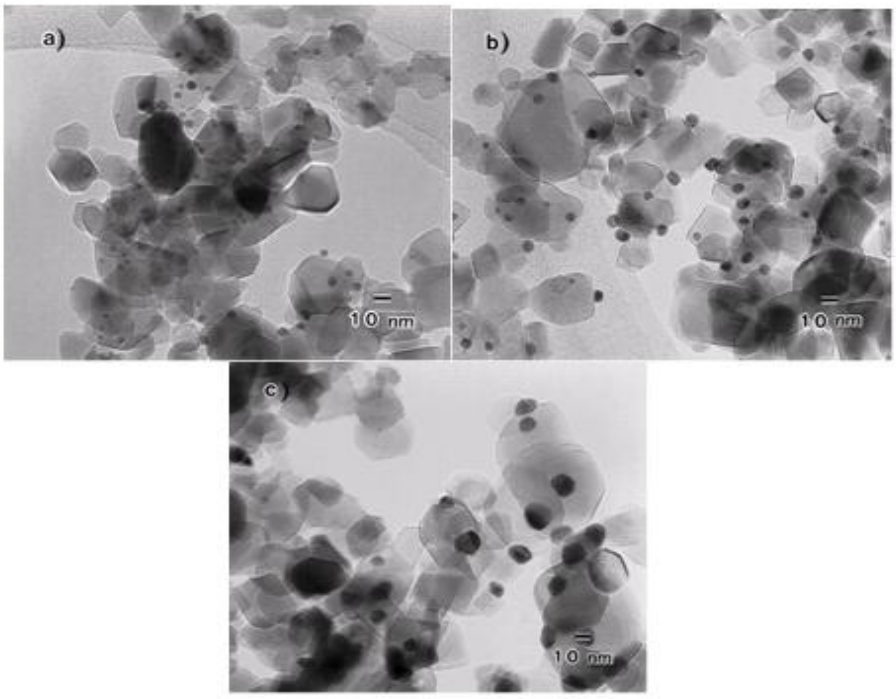

Figure 27. TEM images of Au/TiO_2 (MM) (Au 3.0 wt %) calcined at (a) 473 K, (b) 673 K, and (c) 873 K [113].

Figure 27 shows TEM images for the Au/TiO_2 (MM) sample calcined in air at 473, 673 and 873 K. At 473 K, the gold particles still retained the size and spherical shape of the original colloidal particles, but when calcined at 873 K, the particles became larger and their shape changed from round to an irregular facing. Although increasing the calcination temperature cause growth of the gold particles, it lowered the temperature for 50% conversion of CO to room temperature, as shown in Table 2.

Table 2. Kinetic data for CO oxidation over Au/TiO_2 (MM) and Au/TiO_2 (DP) [113].

Catalyst[a]	Au diameter (nm)	$T_{1/2}$ (K)	Rate (273 K) ($mol\,s^{-1}\,g^{-1}$)	TOF (273 K) (s^{-1})	E_a (kJ/mol)
Mix473	5.1 ± 1.3	479	5.9×10^{-10}	1.6×10^{-6}	18
Mix673	7.5 ± 2.2	303	2.1×10^{-7}	8.7×10^{-3}	15
Mix873	12 ± 2.5	278	7.3×10^{-7}	4.6×10^{-2}	10
DP673	3.6 ± 0.7	236	1.0×10^{-5}	1.9×10^{-1}	17
DP873	6.7 ± 1.4	263	1.3×10^{-6}	4.6×10^{-2}	16

The apparent activation energies of both catalysts, Au/TiO_2 (MM) and Au/TiO_2 (DP), are in the range of 10-18 kJ/mol.

1.3.3.4 The catalytic activity of supported gold for complete oxidation of hydrocarbons

Recently, gold-based catalysts have received much attention for the combustion reaction, and this reaction has been used for the oxidation of various saturated and unsaturated hydrocarbons. When gold is supported on metal oxides such as Fe_2O_3, Al_2O_3, and CeO_2, it has been shown to have a high catalytic activity for the decomposition of VOCs [18].

Catalytic oxidation is an important process for the removal of hydrocarbons from the atmosphere that appear as undesirable contaminants or waste products. Combustion can be used to limit the emission of such vapors and reduce pollution. Therefore, supported metal catalysts may be used to convert dilute waste gas streams to harmless by-products at low temperatures.

Scir *et al.* [114] tested the relative catalytic activities of the Group 11 (*i.e.* 1B) metals gold, silver and copper supported on Fe_2O_3 for the oxidation of methanol. The results of this study, as shown in Figure 38, indicated that gold was the most active catalyst, and that the catalytic activity order was $Au/Fe_2O_3 >> Ag/Fe_2O_3 > Cu/Fe_2O_3 > Fe_2O_3$. The oxidation of methanol over Au/Fe_2O_3 began around 60^oC and reached total oxidation at about 160^oC, while the oxidation over pure Fe_2O_3 (the support) started around 200^oC, with total oxidation complete at about 300^oC. The supported gold catalyst obviously shows a much higher activity compared with other metals.

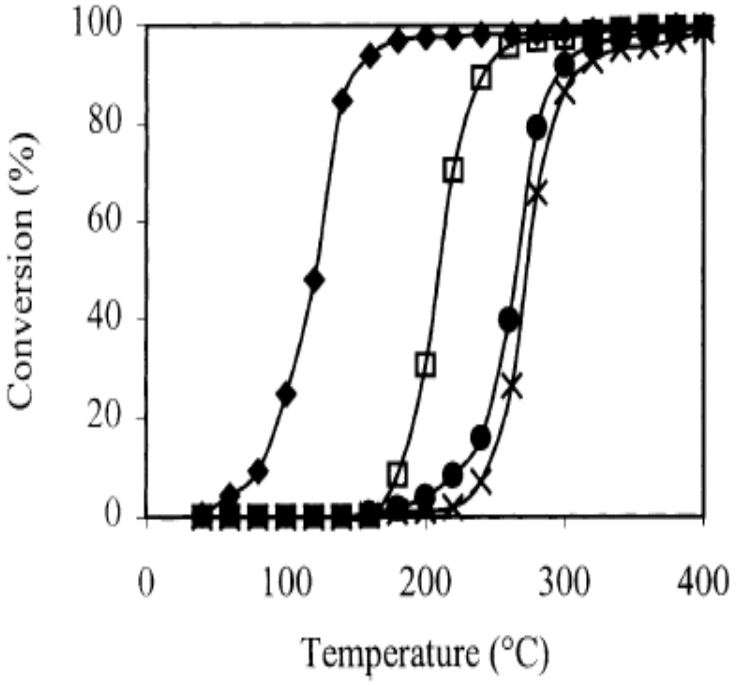

Figure 28. Conversion of methanol over Au/Fe_2O_3 (◆), Ag/Fe_2O_3 (□), Cu/Fe_2O_3 (•), and pure Fe_2O_3(×) [114].

According to the literature [97, 115], catalytic activity is affected by the method of preparation and the pretreatment conditions. Jinwinei and Weibin [116] have investigated the preparatiive effect on the catalytic activity of Au/CeO_2 for the oxidation of toluene. In this study, Au/CeO_2 catalysts were synthesised by using deposition precipitation (DP), co-precipitation (CP) and the metallic colloid deposition (MCD) method. Figure 29 shows the conversion of toluene over the three catalysts. The data indicate that the method of preparation had a remarkable effect on activity. The conversion of toluene at 300^{o}C over a Au/CeO_2 catalyst prepared by the DP method is about 85%, which is much higher than the other two catalysts prepared by the MCD (78%) and CP (69%) methods. Also, the catalytic activity of Au/CeO_2 (DP) increased with increasing reaction temperature. Table 3 summarises some relevant physical properties of these catalysts. The data indicate that the catalytic activity of the Au/CeO_2 (CP) catalyst is much lower than the other catalysts, although the gold loading and BET surface areas of Au/CeO_2 (CP) are higher.

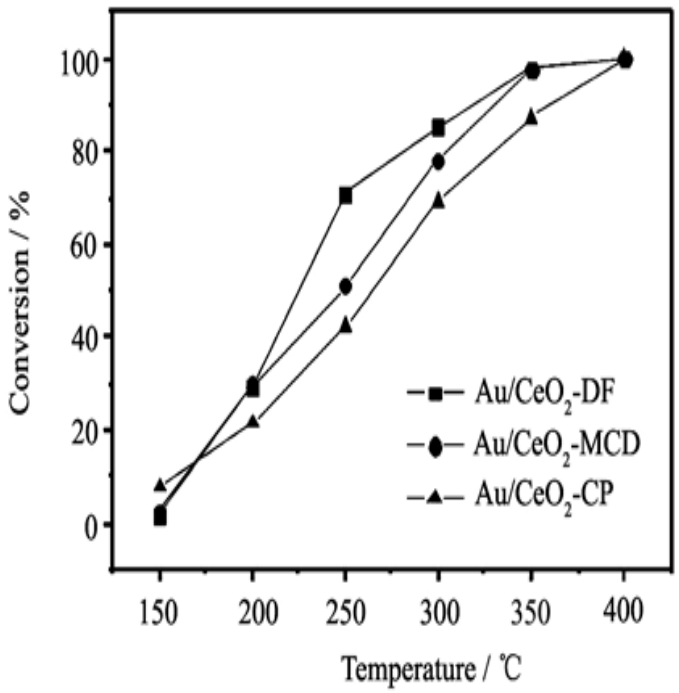

Figure 29. The % conversion of toluene over Au/CeO_2 catalysts prepared by different methods [116].

Table 3. BET surface areas, microstructure and the gold content of Au/CeO_2 catalysts prepared by different methods [116].

Samples	Crystal size/nm		S_{BET}/	Au content/
	CeO_2	Au	(m^2/g)	wt. %
Au/CeO_2-DP	13.7	n.d	50	0.89
Au/CeO_2-MCD	13.3	n.d	46	0.90
Au/CeO_2-CP	9.0	12	96	0.91

The XRD patterns of the three catalysts are given in Figure 30. The gold peaks cannot be observed in the patterns of the Au/CeO_2 (DP) and Au/CeO_2 (MCD) catalysts, while a

small broad peak at about 44.6° appears for Au/CeO_2 (CP). From the Scherrer equation, the estimated size of the gold particles on Au/CeO_2 (CP) was 12 nm.

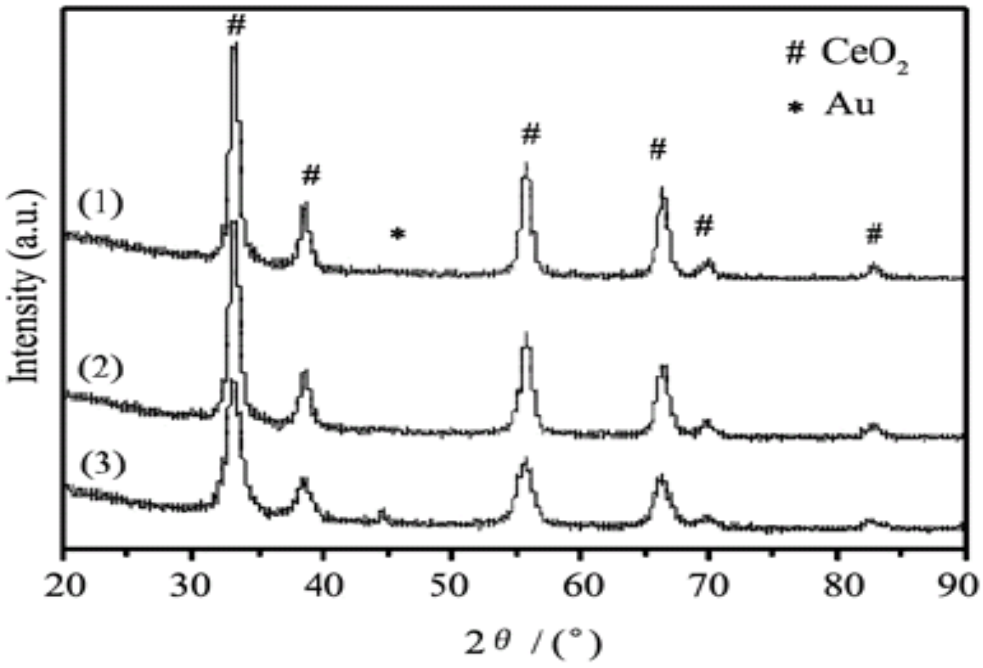

Figure 30. The XRD patterns of Au/CeO_2 prepared by different methods: (1) Au/CeO_2 (DP), (2) Au/CeO_2 (MCD), and (3) Au/CeO_2 (CP) [116].

Minic *et al.* [97] have studied the influence of calcination of Au/Fe_2O_3 at different temperatures (200, 300 and 450°C) for the oxidation reactions of methanol, 2-propanol and ethanol. The data for 2-propanol is shown in Figure 31. The % conversion of 2-propanol over Au/Fe_2O_3 that was calcined at 200°C shows total formation of CO_2 beginning at about 120°C. The sample calcined at 300°C shows thearenset of CO_2 formation at about 180°C, while the sample calcined at 450°C shows that the onset of oxidation shifted to an even higher temperature, 210°C. The same behavior occurred for methanol and ethanol. Thus the catalytic activity towards oxidation to CO_2 decreased progressively with an increase in the calcination temperature.

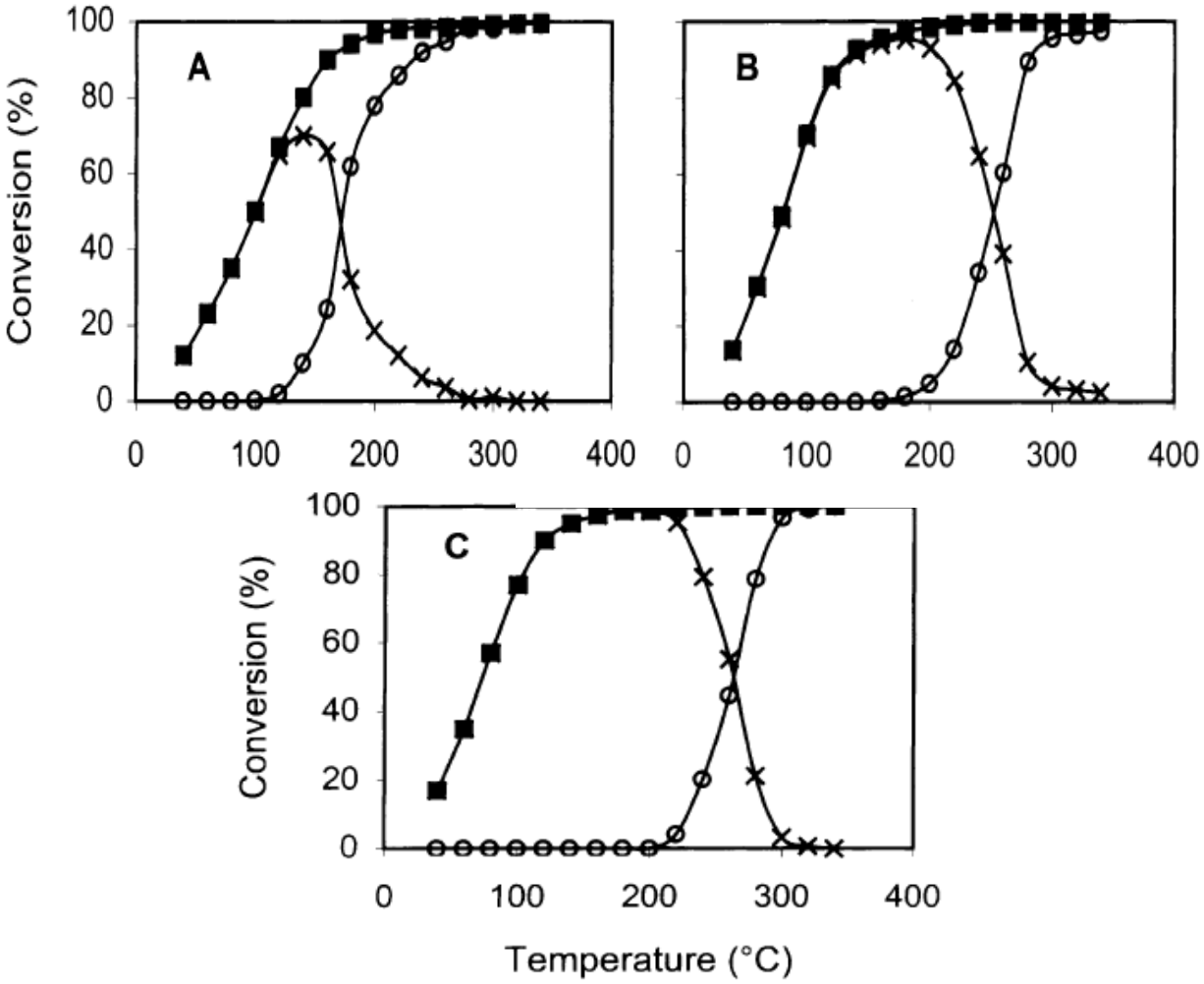

Figure 31. The % conversions of 2-propanol (■) over Au/Fe_2O_3 calcined at (A) 200°C, (B) 300°C, (C) 450°C to yield CO (o) and acetone (×) [97].

In this study, XPS analysis was also carried out. For gold, in the region of the Au 4f transitions, a single gold species (*i.e.* a single oxidation state) shows two peaks related to the Au $4f_{7/2}$ and the Au $4f_{5/2}$ transitions. The study of Minic *et al.* focussed on the Au $4f_{7/2}$ peak. The sample calcined at 200°C showed a broad peak that suggested the presence of different gold species (oxidation states), with overlap of peaks at 83.8 eV which corresponds to Au^0, 86.3 eV to Au^{3+}, and 84.7 eV, which indicates Au^+. For the samples calcined at temperatures higher than 200°C, the XPS showed a sharper peak for the Au $4f_{7/2}$ transition and shifted to a

lower binding energy. This suggested the presence of gold in just the metallic state. Several studies have observed that the presence of different gold species may modify and enhance the catalytic properties of the support [37].

Ahn and Lee [117] have synthesised several sizes of gold particle on different metal oxides including Al_2O_3 and Co_3O_4, and studied their catalytic activities for the oxidation of ethylene. They observed that the particles size of gold also depended on the method of preparation. TEM was used to determine the size of the particles. The particle size of gold in Au/Al_2O_3 that was prepared by IMP indicated large particles in the range of 30 to 100 nm, while for Au/Al_2O_3 prepared by CP the particles were in the range of 3 to 8 nm, and for Au/Al_2O_3 prepared by DP the particles were smaller than those prepared by the CP method. These catalysts were used to oxide the ethylene completely and produced only CO_2 and H_2O. The catalytic activities of the Au/Al_2O_3 catalysts for oxidation of ethylene are shown in Figure 32. The amount catalyst used was 0.3 g, containing 1 wt % of gold. It appears that the Au/Al_2O_3 catalyst prepared by DP was the most active of the catalysts, and ethylene was completely oxidised at 300^{o}C. As a result, the particle sizes of gold actually control the catalytic activity. Identical results were found for the Au/Co_3O_4 catalysts.

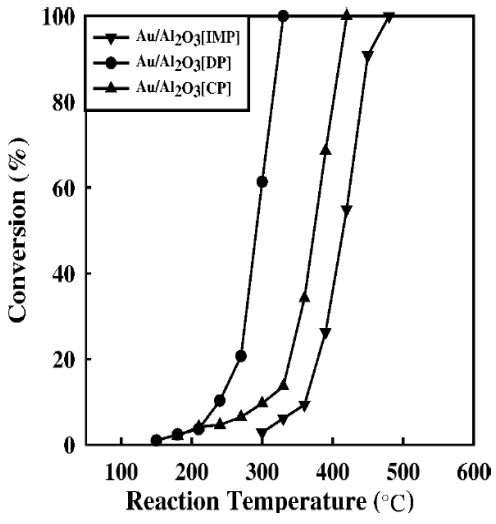

Figure 32. The catalytic activity of Au/Al_2O_3 catalyst prepared by different methods [117].

One further study [118] has reported on the influence of the gold loading (0.02, 0.5, 1 and 4%) on CeO_2 for the oxidation of propene. Figure 33 illustrates the conversion of propene, and it appears that as the gold loading increases the curves shift towards lower temperatures. Thus the catalytic activity increased with an increase in the loading of gold.

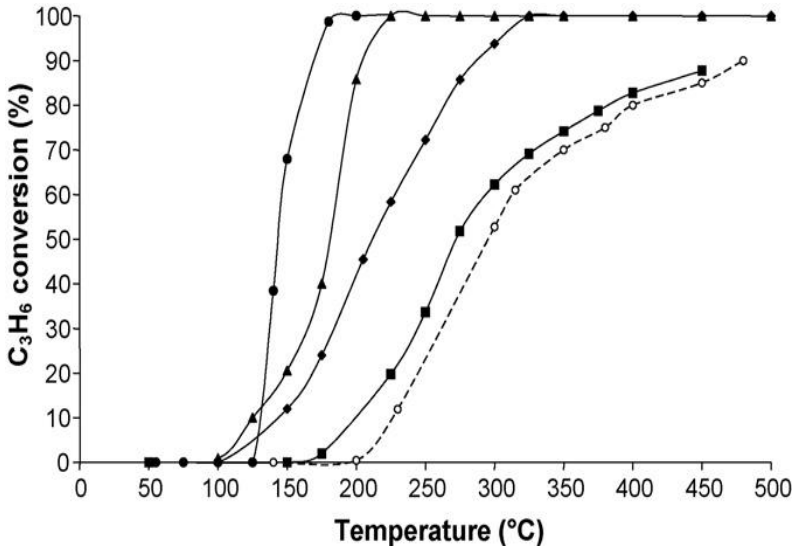

Figure 33. The conversion of propene over Au/CeO_2, activated under O_2/He at 500°C: CeO_2(○), 0.02% Au/CeO_2(■), 0.5% Au/CeO_2(♦), 1% Au/CeO_2(▲), and 4% Au/CeO_2(●) [118].

Waters *et al.* [119] studied the oxidation of methane over gold supported on MnO_X, Fe_2O_3, Co_3O_4, NiO, and CeO_X. Figure 34 shows the oxidation of methane over the four gold-supported catalysts, and also a Co_3O_4 support. The activities of the catalysts were as follows: Au/Co_3O_4 > Au/NiO > Au/MnO_X > Au/Fe_2O_3. All of the catalysts were prepared to give 5 wt % of gold supported on the transition metal oxides. The Au/Co_3O_4 catalyst was the most active between 200 and 250°C, while the CeO_X catalyst was inactive at the temperatures tested. Also, the pure Co_3O_4 catalyst was active at a temperature about 50°C above that of

Au/Co_3O_4, showing that the effect of the added gold nanoparticles was to increase the catalytic activity.

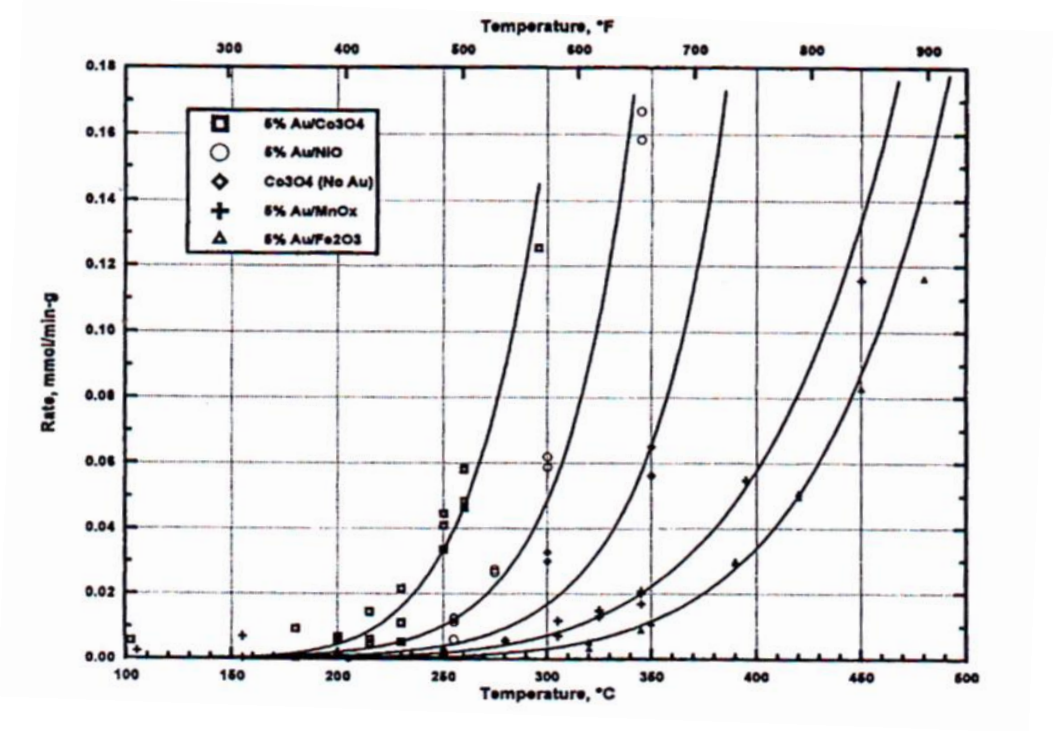

Figure 34. Methane oxidation over gold supported on MnO_X, Fe_2O_3, Co_3O_4, and NiO, (each catalysts contain 5 wt % gold) [119].

Recently, it has been reported that gold loaded on Al_2O_3 and TiO_2-based supports show high catalytic activity for the oxidation of VOCs, and these systems have become widely studied for the total oxidation of VOCs [120, 121]. For these types of catalysts, the presence of gold enhances the oxidation rate, and the final products are always CO_2 and H_2O.

Liu, S.Y. and Yang [122] have studied the effect of gold-based catalysts supported on four different metal oxides (CeO_2, Fe_2O_3, TiO_2 and Al_2O_3) for the complete oxidation of 2-propanol. In this study, was found that the catalytic activity for 2-propanol conversion over these four catalysts had the following order: $Au(1.6\%)/CeO_2$ > CeO_2 > $Au(1.7\%)/Fe_2O_3$ > $Au(1.6\%)/Al_2O_3$ > $Au(1.4\%)/TiO_2$. The % conversion and % selectivities for these catalyst

systems are shown in Figure 35 (note that the gold-free CeO_2 is not shown here). Interestingly, CeO_2 performed better than other catalysts (Fe_2O_3, Al_2O_3 and TiO_2), even with their gold loadings, although not as well as the Au(1.6%)/CeO_2 catalyst.

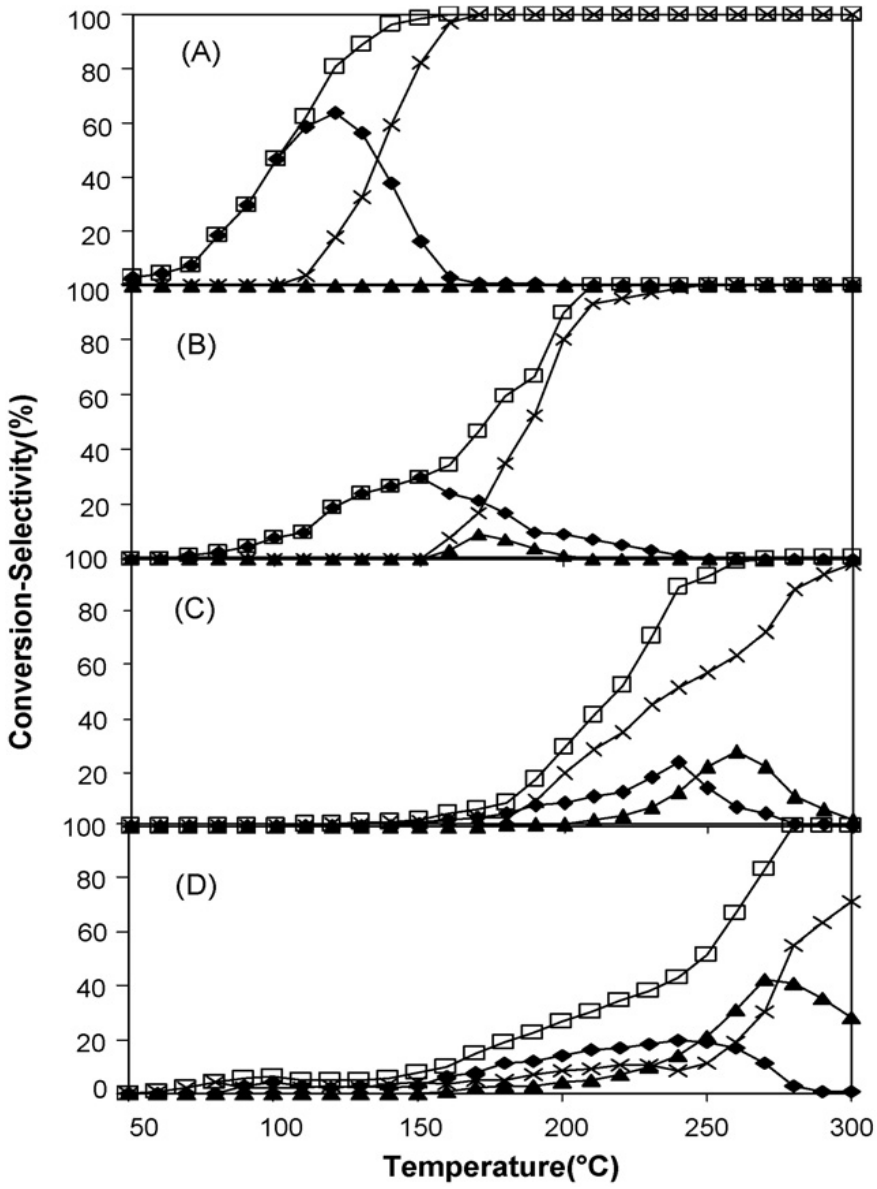

Figure 35. The % conversions (□) and % selectivities to the products (acetone (♦), propene (▲), CO_2+H_2O (x)) of 2-propanol over: (A) 1.6% Au/CeO_2, (B) 1.7% Au/Fe_2O_3, (C) 1.6% Au/Al_2O_3, and (D) 1.4% Au/TiO_2 [122].

A study of the gold loading was also carried out for CeO_2. This is shown in Figure 36. The activity of the Au/CeO_2 catalyst decreased in the order of 1.6 wt % > 2.1 wt % > 0.3 wt % > 0 wt %.During the oxidation process, the usual products were CO_2 and H_2O as the temperature increased, while acetone and propene were detected as intermediate compounds when the 2-propanol was not completely converted. To explain the activity of Au/CeO_2 it was suggested that there was a strong interaction between CeO_2 and the gold nanoparticles and that gold has the capacity to weaken the Ce-O bonds that are adjacent to gold atoms.

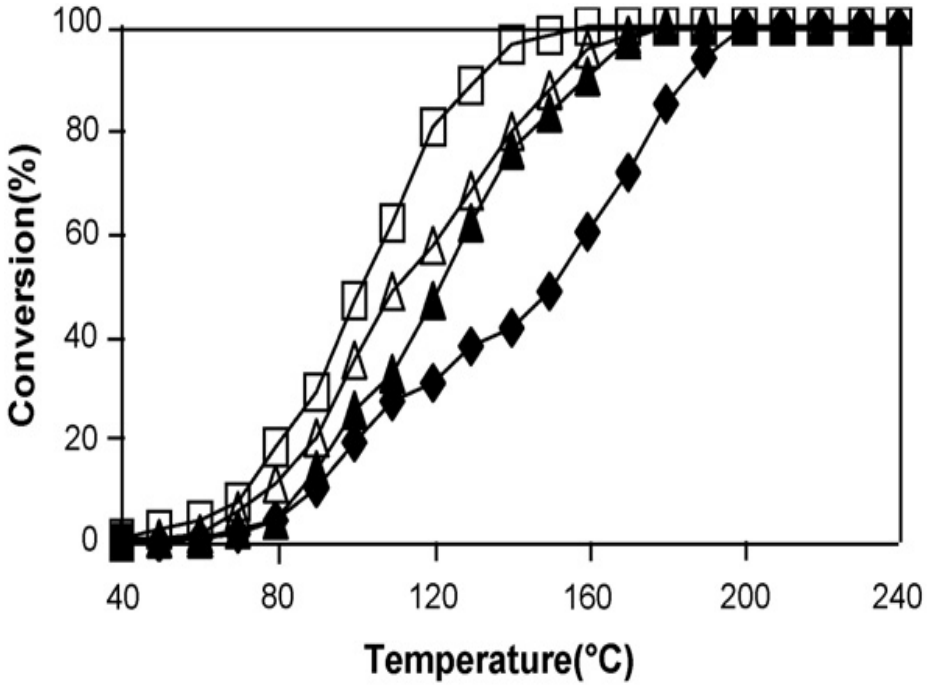

Figure 36. Percentage conversion of 2-propanol over Au/CeO_2 catlaysts using various gold loading values: (♦) 0 wt %, (▲) 0.3 wt %, (□) 1.6 wt % and (Δ) 2.1 wt % [122].

Furthermore, in the same study the authors proposed a tentative reaction route for the 2-propanol oxidation, which is shown in Figure 37. The reaction pathway for the oxidation of 2-propanol seems to begin with formation of a 2-propoxide surface species (step 1).

Subsequently, 2-propoxide proceeds to decompose by two parallel reactions: (a) dehydrogenation to propene (step 2) and (b) dehydrogenation to acetone (step 3).

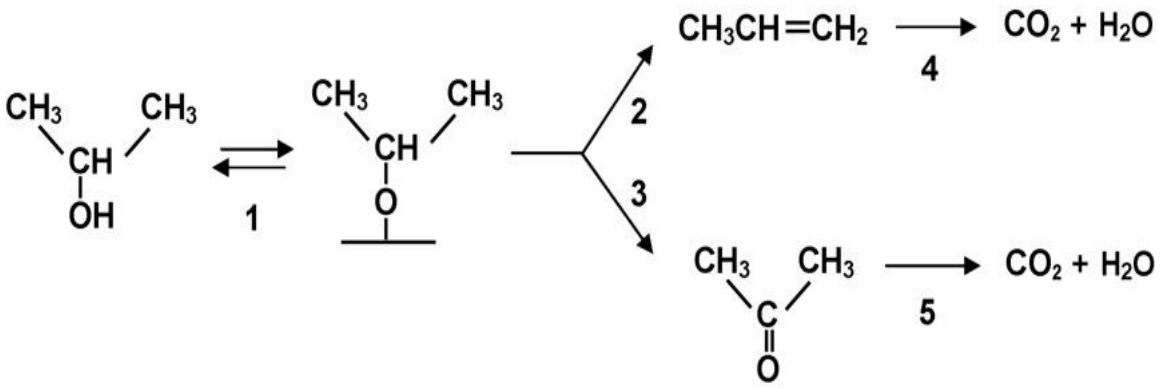

Figure 37. The proposed mechanism for the complete oxidation of 2-propanol [122].

1.4 Scope of the present study

This study involves a new approach for the preparation of nano-sized gold particles supported on Keggin-type polyoxometalates and metal oxides. As indicated above, supported gold nanoparticles have been shown to exhibit unique properties in different reactions at low temperatures. In this project, thiolate-stabilised gold nanoparticles will be investigated as a source of gold nanoparticles for two sorts of reactions, the partial (*i.e.* selective) oxidation of isobutane and the complete oxidation (*i.e.* combustion) of isobutane. For this purpose *n*-hexanethiolate-stabilised gold nanoparticles will be synthesised and characterised. Their ready synthesis, purification and prior characterisation has been reported in the literature [123]. This approach allows the isolation of thiolate-stabilised nanoparticles as a solid, which can be reconstituted in solution at a later date, and used to deliver gold nanoparticles in a known quantity to the heterogeneous catalyst. The thiolate ligand, bound to the surface of the gold nanoparticles, may be conveniently removed by slow thermolysis. The thiolate-

stabilised gold nanoparticles can be conveniently stored as a solid powder. This increases their ability to be used as a source of gold for heterogeneous catalysis.

The objectives of this study involve:

i) To explore the use of *n*-hexanethiolate-capped nanoparticles as a source of gold nanoparticles in heterogeneous catalysis. The *n*-hexanethiolate-stabilised gold nanoparticles will be characterised initially to establish the particle size. The *n*-hexanethiolate ligands may then be easily removed by simple thermolysis after impregnation of the solid catalysts with the soluble *n*-hexanethiolate-stabilised gold nanoparticles. Such an approach has not been reported previously.

ii) To characterise the structures and properties of phosphopolyoxomolybdates and metal oxides (Mn_3O_4, Co_3O_4 and Fe_3O_4) with and without supported gold nanoparticles using different instrumental techniques such as XRD, TG/DTA, FT-IR, XPS, SEM and TEM.

iii) To test the catalytic activity performance of gold nanoparticles supported on the phosphopolyoxometalates of composition $Cs_{3-x}H_x[PMo_{12}O_{40}]$ (x = 0, 0.5, 1 and 2), $Cu_{3-x}H_{2x}[PMo_{12}O_{40}]_2$ (x = 0, 1 and 2), $Ag_{3-x}H_x[PMo_{12}O_{40}]$ (x = 0, 1 and 2), and the parent acid $H_3[PMo_{12}O_{40}]$, in the partial (or selective) oxidation of isobutane. This reaction has been chosen because of its potential importance for the production of the important precursor materials methacrolein and methacrylic acid, which are used for the production of poly(methyl methacrylate), and ultimately Perspex or Plexiglass. The activity of gold nanoparticles added to heteropolyoxometalate catalysts, such as indicated above, that may be used in oxidative dehydrogenation or oxidation reactions has not been explored previously.

iv) To test the catalytic activity performance of gold nanoparticles supported on metal oxides (Mn_3O_4, Co_3O_4 and Fe_3O_4) in the complete oxidation (or combustion) of isobutane. This is a volatile organic compound (VOC), but has received little study in recent times.

Note that the catalysis studies require that the activities of the catalysts in the reactions be examined in the absence of gold nanoparticles prior to any investigation of the effects of the gold nanoparticles. This will establish a base for comparison. Some further considerations are discussed below.

1.4.1 Partial oxidation of isobutane using phosphopolyoxomolybdates

The normal mechanism of partial oxidation using polyoxomolybdates involves removal of an initial H atom from the organic substrate, which subsequently disproportionates into H^+ and e^-, which then spread throughout the entire catalyst structure. This is the Bulk type (II) catalysis mechanism, as discussed above. This is followed by removal of a second H atom, which behaves analogously. It is not certain, but it is believed that the first step in the process is the removal of H^+ from the adsorbed organic molecule, followed by electron transfer to the polyoxomolybdate catalyst, which acts as an electron reservoir. Importantly, reducible transition metal ions have been proposed as the means by which the electrons are then transferred throughout the entire bulk of the catalyst (*i.e.* from anion to anion). It is possible that gold nanoparticles may enhance this process, although this will depend on the interaction of the nanoparticles with the $[PMo_{12}O_{40}]^{3-}$ ions, and the transition metal counter-cations themselves. For this reason a selection of easily reducible counter-cations have been selected, for comparison with the $Cs_{3-x}H_x[PMo_{12}O_{40}]$ (where x = 0, 0.5 and 1) series, which contain the non-reducible Cs^+ counter-cation. The compounds with reducible counter-cations (Cu^{2+} and Ag^+) are $Cu_{3-2x}H_{2x}[PMo_{12}O_{40}]_2$ (where x = 0, 1 and 2)

and Ag^{+}, $Ag_{3-x}H_x[PMo_{12}O_{40}]$ (where x = 0, 1 and 2), both members of Group 11, along with gold. The choice of Cu^{2+} and Ag^{+} is made based on their similarity to gold, ease of reduction to the metals, and synthetic availability.

There is evidence that during oxidation reactions using gold nanoparticles, higher oxidation states of gold play a role, including Au(I) and possibly Au(III). Both are strong oxidants. Thus there could be species present under catalysis conditions with the range from neutral to tri-positive cations, allowing a multitude of potential oxidation-reduction reactions to occur, which may influence the organic oxidation process.

1.4.2 Complete oxidation of isobutane using metal oxides

It has been found that highly dispersed of gold nanoparticles on metal oxides can provide remarkable activity at low temperatures for the complete oxidation (or catalytic combustion) of VOCs. The metal oxides that will be used in this project are Mn_3O_4, Co_3O_4 and Fe_3O_4, in form of powders and nano-powders. These oxides were chosen so as to form a complete series, and all have the spinel (or inverse spinel) structure, AB_2X_4, where A and B are cations and X is anion (O^{2-} in the present case). The structures are treated in more depth in Chapter 4. Moreover, they are mixed oxidation state oxides, which contain both M^{2+} and M^{3+} ions, which may offer advantages in the oxidation process.

1.5 References

[1] G.C. Bond, Gold Bull., 5 (1972) 11.

[2] J. Schwank, Gold Bull., 18 (1985) 1.

[3] G.C. Bond, D.T. Thompson, Catal. Rev., 41 (1999) 319-388.

[4] G.C. Bond, D.T. Thompson, Gold Bull., 33 (2000) 41-50.

[5] G. Hutchings, J. Catal., 96 (1985) 292-295.

[6] M. Haruta, T. Kobayashi, H. Sano, N. Yamada, Chem. Lett., (1987) 405-408.

[7] M. Haruta, Gold Bull., 37 (2004) 27-36.

[8] M. Haruta, Chem. Rec., 3 (2003) 75-87.

[9] M. Haruta, N. Yamada, T. Kobayashi, S. Iijima, J. Catal., 115 (1989) 301-309.

[10] M. Haruta, M. Daté, Appl. Catal. A: General, 222 (2001) 427-437.

[11] M. Haruta, Cattech, 6 (2002) 102-115.

[12] M. Haruta, J. Nano. Res., 5 (2003) 3-4.

[13] M.C. Daniel, D. Astruc, Chem. Rev., 104 (2004) 293-346.

[14] S. Eustis, M. El-Sayed, Chem. Soc. Rev., 35 (2006) 209-217.

[15] V. Sharma, K. Park, M. Srinivasarao, Mater. Sci. Eng.: R: Reports, 65 (2009) 1-38.

[16] G. Hutchings, M. Brust, H. Schmidbaur, Chem. Soc. Rev., 37 (2008) 1759-1765.

[17] F. Jian, H. Xiao, Z. Zhao, P. Sun, P. Zhao, Inorg. Chem. Commun., 7 (2004) 1100-1102.

[18] R. Zsigmondy, E. Spear, J. Norton, The Chemistry of Colloids: Kolloidchemie, John Wiley & Sons, Inc., 1917.

[19] T. Svedberg, The Formation of Colloids, D. Van Nostrand, 1921.

[20] T. Svedberg, A. Tiselius, Colloid Chemistry, Book Department, The Chemical Catalog Company, Inc., 1928.

[21] J. Turkevich, P. Stevenson, J. Hillier, Gold Bull., 18 (1985) 86.

[22] G. Frens, Nature, 241 (1973) 20-22.

[23] R. Jin, Y.W. Cao, C.A. Mirkin, K. Kelly, G.C. Schatz, J. Zheng, Sci., 294 (2001) 1901.

[24] M. Pileni, Langmuir, 13 (1997) 3266-3276.

[25] C. Yee, R. Jordan, A. Ulman, H. White, A. King, M. Rafailovich, J. Sokolov, Langmuir, 15 (1999) 3486-3491.

[26] M. Brust, M. Walker, D. Bethell, D. Schiffrin, R. Whyman, J. Chem. Soc., Chem. Commun., 1994 (1994) 801-802.

[27] A. Frenkel, S. Nemzer, I. Pister, L. Soussan, T. Harris, Y. Sun, M. Rafailovich, J. Chem. Phys., 123 (2005) 184701.
[28] R. Sperling, Surface Modification and Functionalization of Colloidal Nanoparticles, in Universitätsbibliothek Marburg, 2008.
[29] Q. Huo, J. Worden, J. Nano. Res., 9 (2007) 1013-1025.
[30] J. Zhou, J. Ralston, R. Sedev, D. Beattie, J. Colloid. Interfac. Sci., 331 (2009) 251-262.
[31] M. Corbierre, R. Lennox, Chem. Mater, 17 (2005) 5691-5696.
[32] M. Hostetler, J. Wingate, C. Zhong, J. Harris, R. Vachet, M. Clark, J. Londono, S. Green, J. Stokes, G. Wignall, Langmuir, 14 (1998) 17-30.
[33] D. Leff, P. Ohara, J. Heath, W. Gelbart, J. Phys. Chem. B, 99 (1995) 7036-7041.
[34] D. Leff, L. Brandt, J. Heath, Langmuir, 12 (1996) 4723-4730.
[35] V. Choudhary, V. Patil, P. Jana, B. Uphade, Appl. Catal. A: General, 350 (2008) 186-190.
[36] N. Mizuno, M. Misono, Chem. Rev, 98 (1998) 199-218.
[37] M. Langpape, J. Millet, Appl. Catal. A: General, 200 (2000) 89-101.
[38] S. Kendell, A.-S. Alston, N. Ballam, T. Brown, R. Burns, Catal. Lett., 141 (2011) 374-390.
[39] F. Cavani, E. Etienne, R. Mezzogori, A. Pigamo, F. Trifirò, Catal. Lett., 75 (2001) 99-105.
[40] H. Krieger, L. Kirch, Process for the production of unsaturated acids, in Google Patents, 1981.
[41] F. Cavani, R. Mezzogori, A. Pigamo, F. Trifirò, E. Etienne, Catal. Today, 71 (2001) 97-110.
[42] T. Haeberle, G. Emig, Chem. Eng. Tech., 11 (1988) 392-402.
[43] P. Porta, G. Minelli, I. Pettiti, L.I. Botto, H.J. Thomas, J. Mater. Chem., (1997) 311.
[44] F. Cavani, C. Comuzzi, G. Dolcetti, E. Etienne, R.G. Finke, G. Selleri, F. Trifiro, A. Trovarelli, J. Catal., (1996) 317.
[45] M. Misono, Catal. Rev. Sci. Eng. , (1987) 269.
[46] G.A. Tsigdinos, G. Moh, Aspects of molybdenum and related chemistry, Springer-Verlag, Berlin, 1978.
[47] M. Misono, in: 10th International Congress on Catalysis (Ed.: L. Guczi), Elsevier Sience Publishers B. V., Budapest, Hungary, 1992.
[48] G.B. McGarvey, J.B. Moffat, Catal. Lett., (1992) 173.
[49] T. Okuhara, N. Mizuno, M. Misono, Adv. Catal., 41 (1996) 113-252.

[50] F. Chauveau, P. Dopplelt, J. Lefebvre, J. Chem. Res., (1978) 1727.
[51] F. Chauveau, P. Dopplelt, J. Lefebvre, J. Chem. Res., (1981) 1937.
[52] M.T. Pope, Y. Jeannin, M. Fournier, Heteropoly and Isopoly Oxometalates, Springer-Verlag Berlin, 1983.
[53] B.B. Bardin, R.J. Davis, Appl. Catal. A: General, 185 (1999) 283-292.
[54] M. Furuta, K. Sakata, M. Misono, Y. Yoneda, Chem. Lett., (1979) 31.
[55] M. Misono, J. Chem. Soc.,Chem. Commun., (2001) 1141-1152.
[56] J.B. Moffat, Metal-Oxygen Clusters: the surface and catalytic properties of heteropoly oxometalates, New York: Kluwer Academic/Plenum Publishers, 2001.
[57] K.S.W. Sing, D.H. Everett, R.A.W. Haul, L. Moscou, R.A. Pierotti, J. Rouquerol, T. Siemieniewska, Pure Appl. Chem., (1985) 603.
[58] B.D. Zdravkov, J.J. Cermak, M. Sefara, J. Janku, Central European J. Chem., (2007) 385.
[59] M. Misono, Mater. Chem. Phys., (1987) 103.
[60] M. Misono, Catal. Lett., (1992) 63.
[61] M. Misono, N. Mizuno, H. Mori, K.Y. Lee, J. Jiao, in Structure-Activity and Selectivity Relationships in Heterogeneous Catalysis (Eds.: R. K. Grasselli, A. W. Sleight), Elsevier Science Publishers B.V., Amsterdam, 1991.
[62] N. Mizuno, T. Watanabe, H. Mori, M. Misono, J. Catal., (1990) 157.
[63] T. Komaya, M. Misono, Chem. Lett., (1983) 1177.
[64] T. Okuhara, A. Kasai, N. Hayakawa, M. Misono, Y. Yoneda, Chem. Lett., (1981).
[65] T. Okuhara, A. Kasai, N. Hayakawa, Y. Yoneda, M. Misono, J. Catal., (1983) 121.
[66] N. Mizuno, M. Tateishi, M. Iwamoto, J. Catal., 163 (1996) 87-94.
[67] N. Mizuno, M. tateishi, M. iwamoto, J. Chem. Soc., Chem. Commun., (1994) 1411.
[68] J.S. Min, N. Mizuno, Catal. Today, 66 (2001) 47-52.
[69] J.S. Min, N. Mizuno, Catal. Today, 71 (2001) 89-96.
[70] N. Mizuno, M. Misono, Current Opinion in Solid State and Materials Science, 2 (1997) 84-89.
[71] N. Mizuno, M. Tateishi, M. Iwamoto, Appl. Catal. A: General, 118 (1994) L1-L4.
[72] F. Cavani, E. Etienne, M. Favaro, A. Galli, F. Trifiro, G. Hecquet, Catal. Lett., 32 (1995) 215-226.
[73] F. Cavani, E. Etienne, E. Finocchio, A. Galli, G. Selleri, F. Trifirò, J. Molec. Catal. A: Chemical, 114 (1996) 343-359.

[74] E. Etienne, F. Cavani, R. Mezzogori, F. Trifirò, G. Calestani, L. Gengembre, M. Guelton, Appl. Catal. A: General, 256 (2003) 275-290.
[75] F. Cavani, R. Mezzogori, A. Pigamo, F. Trifirò, Topics Catal, 23 (2003) 119-124.
[76] M. Langpape, J.M.M. Millet, U.S. Ozkan, M. Boudeulle, J. Catal., 181 (1999) 80-90.
[77] M. Langpape, J.M.M. Millet, U. Oskan, M. Boudeulle, J. Catal., 182 (1999) 148.
[78] S.A. Borshch, H. Duclusaud, J.M.M. Millet, Appl. Catal. A: General, 200 (2000) 103-108.
[79] S. Paul, V. Le Courtois, D. Vanhove, Industrial & Engineering Ehemistry Research, 36 (1997) 3391-3399.
[80] P. Mars, D.W. Van Krevelen, Chem. Eng. Sci., 3 (1954) 41-59.
[81] L. Jalowiecki-Duhamel, A. Monnier, Y. Barbaux, G. Hecquet, Catal. Today, 32 (1996) 237-241.
[82] G.P. Schindler, C. Knapp, T. Ui, K. Nagai, Topics Catal., 22 (2003) 117-121.
[83] S.M. Kendell, T.C. Brown, R.C. Burns, Catal. Today, 131 (2008) 526-532.
[84] S. Kendell, T. Brown, Catal. Lett., 141 (2011) 1767-1785.
[85] S. Minico., S. Scire., C. Crisafulli., R. Maggiore., S. Galvagno., Appl. Catal. B, Environmental, 28 (2000) 245-251.
[86] M. Centeno, M. Paulis, M. Montes, J. Odriozola, Appl. Catal. A: General, 234 (2002) 65-78.
[87] L. Chen, J. Hu, R. Richards, J. Am. Chem. Soc., 131 (2008) 914-915.
[88] D. Dissanayake, Applications of Metal Oxides for Volatile Organic Compound Combustion, in: Metal Oxides, CRC Press, 2005, pp. 543-568.
[89] M. Casaletto, A. Longo, A. Martorana, A. Prestianni, A. Venezia, Surf. Interfac. Anal., 38 (2006) 215-218.
[90] M. Aryafar, F. Zaera, Catalysis Letters, 48 (1997) 173-183.
[91] M. Baldi, V.S. Escribano, J.M.G. Amores, F. Milella, Appl. Catal. B: Environmental, 17 (1998) L175-L182.
[92] M. Baldi, E. Finocchio, F. Milella, G. Busca, Appl. Catal. B, Environmental, 16 (1998) 43-51.
[93] E.M. Cordi, P.J. O'Neill, J.L. Falconer, Appl. Catal B: Environmental, 14 (1997) 23-36.
[94] M.C. Marion, E. Garbowski, M. Primet, J. Chem. Soc., Faraday Trans., 86 (1990) 3027-3032.
[95] S. Arnone, G. Bagnasco, Stud. Surf. Sci. Catal., 119 (1998) 65-70.

[96] P. Landon, P. Collier, A. Papworth, C. Kiely, G. Hutchings, J. Chem. Soc., Chem. Commun., 2002 (2002) 2058-2059.
[97] J. Fierro-Gonzalez, J. Guzman, B. Gates, Topics Catal., 44 (2007) 103-114.
[98] S.A.C. Carabineiro, D.T. Thompson, Nanocatal., (2007) 377-489.
[99] M. Haruta, S. Tsubota, T. Kobayashi, H. Kageyama, M. Genet, B. Delmon, J. Catal, 144 (1993) 175.
[100] G.R. Bamwenda, S. Tsubota, T. Nakamura, M. Haruta, Catal. Lett., 44 (1997) 83-87.
[101] M. Valden, S. Pak, X. Lai, D. Goodman, Catal. Lett., 56 (1998) 7-10.
[102] M. Valden, X. Lai, D.W. Goodman, Sci., 281 (1998) 1647.
[103] M. Haruta, Catal. Surveys from Japan, 1 (1997) 61-73.
[104] M. Haruta, Catal. Today, 36 (1997) 153-166.
[105] C. Yang, C. He, J. Am. Chem. Soc, 127 (2005) 6966-6967.
[106] J. Fierro Gonzalez, B. Gates, ChemInform, 39 (2008).
[107] F. Porta, L. Prati, M. Rossi, S. Coluccia, G. Martra, Catal. Today, 61 (2000) 165-172.
[108] A.S.K. Hashmi, G.J. Hutchings, Angew. Chem. Internat. Ed., 45 (2006) 7896-7936.
[109] M. Haruta, K. Saika, T. Kobayashi, S. Tsubota, Y. Nakahara, Chem. Express, 3 (1988) 159-162.
[110] S. Tsubota, M. Haruta, T. Kobayashi, A. Ueda, Y. Nakahara, Stud. Surf. Sci. Catal., 63 (1991) 695-704.
[111] W. Vogel, D. Cunningham, K. Tanaka, M. Haruta, Catal. Lett., 40 (1996) 175-181.
[112] S. Lin, M. Bollinger, M. Vannice, Catal. Lett., 17 (1993) 245-262.
[113] S. Tsubota, T. Nakamura, K. Tanaka, M. Haruta, Catal. Lett., 56 (1998) 131-135.
[114] S. Scir , S. Minic , C. Crisafulli, S. Galvagno, Catal. Commun., 2 (2001) 229-232.
[115] K. Zhu, D. Wang, J. Liu, Nano Res., 2 (2009) 1-29.
[116] L. Jinwinei, L. Weibin, J. Rare Earths, 28 (2010) 547-551.
[117] H.G. Ahn, D.J. Lee, Res. Chem. Interm., 28 (2002) 451-459.
[118] L. Delannoy, K. Fajerwerg, P. Lakshmanan, C. Potvin, C. Methivier, C. Louis, Applied Catalysis B: Environmental, 94 (2010) 117-124.
[119] R. Waters, J. Weimer, J. Smith, Catal. Lett., 30 (1994) 181-188.
[120] O. Larsson, H. Berggren, A. Andersson, O. Augustsson, Catal. Today., 35 (1997) 137.
[121] E.M. Cordi, J.L. Falconer, Appl. Catal., A, 151 (1997) 179.
[122] S.Y. Liu, S.M. Yang, Appl. Catal. A: General, 334 (2008) 92-99.
[123] A. Ernst, L. Sun, K. Wiaderek, A. Kolary, S. Zoladek, P. Kulesza, J. Cox, Electroanalysis, 19 (2007) 2103-2109.

CHAPTER 2

Experimental – Catalysis Studies and Instrumentation

2.1 Design of the Apparatus for Heterogeneous Catalytic Reactions

2.1.1 A Brief Overview

Solid catalysts are employed in many heterogeneous industrial catalysis processes, as well as in the laboratory. Several types of reactors are used for heterogeneous catalytic reactions. These may be divided broadly into two classes, batch reactors and continuous flow reactors. In the former, measured quantities of reactants are placed in a closed system with the catalyst at a fixed temperature to yield the desired product(s). However, in continuous flow reactors, the reactants are continuously introduced to the catalyst bed in an open system (*i.e.* at atmospheric pressure), and the product(s) continuously removed. Continuous reactors are more economical from an industrial standpoint, because the products can be continually produced in large quantities on a commercial scale. Batch reactors are often used for the manufacture of small quantities of materials, such as pharmaceuticals or speciality chemicals, or even to test a new catalyst.

Different types of catalytic reactors may be employed, depending on the form of the catalyst and the process requirements. These include fixed bed, moving bed, fluidised bed and entrained bed reactors, as well as slurry reactors and three-phase packed column reactors. All of these are used in different fields such as in the petroleum and petrochemical industries.

The choice of reactor depends on the relative requirements for mass transfer, degree of *(i.e.* percentage) conversion of the substrate, and heat transfer [1].

2.1.2 Reactors for Catalytic Gas Phase Processes

The fixed bed flow reactor is the most common reactor type that is used for catalytic gas phase processes in a laboratory setting. The reactor consists of a vessel that may be arranged vertically or horizontally, with the catalyst held between non-reactive (*e.g*. quartz or glass wool) end supports. The catalyst is generally in the form of relatively small particles, which are randomly orientated. The input gas stream flows through the interstices between the particles, accessing the pore structure of the catalyst. Ideally, solid catalysts usually have high surface areas and porosities. Moreover, they may be supported or unsupported. The advantage of this reactor type is that it is relatively simple to construct. On the other hand, it does have the disadvantage in that it only allows relatively poor heat transfer to the reactor walls [2, 3].

In the present study, both the partial (*i.e.* selective) and complete oxidation of isobutane was carried out using a conventional flow, fixed bed reactor at atmospheric pressure [4-7]. Such systems are commonly used for catalysis studies of heteropolyoxometalate and metal oxide catalysts, including oxidation and oxidative dehydrogenation reactions. The design of the experimental system used in the present studies is shown in Figure 1.

The catalysis system consists of three parts: (1) the feed control system, (2) the reaction section and, (3) the analysis section. The main part of the reactor was built from Swagelok high-pressure, flexible metal hoses (FM series) and 1/4″ o.d. stainless steel tubing.

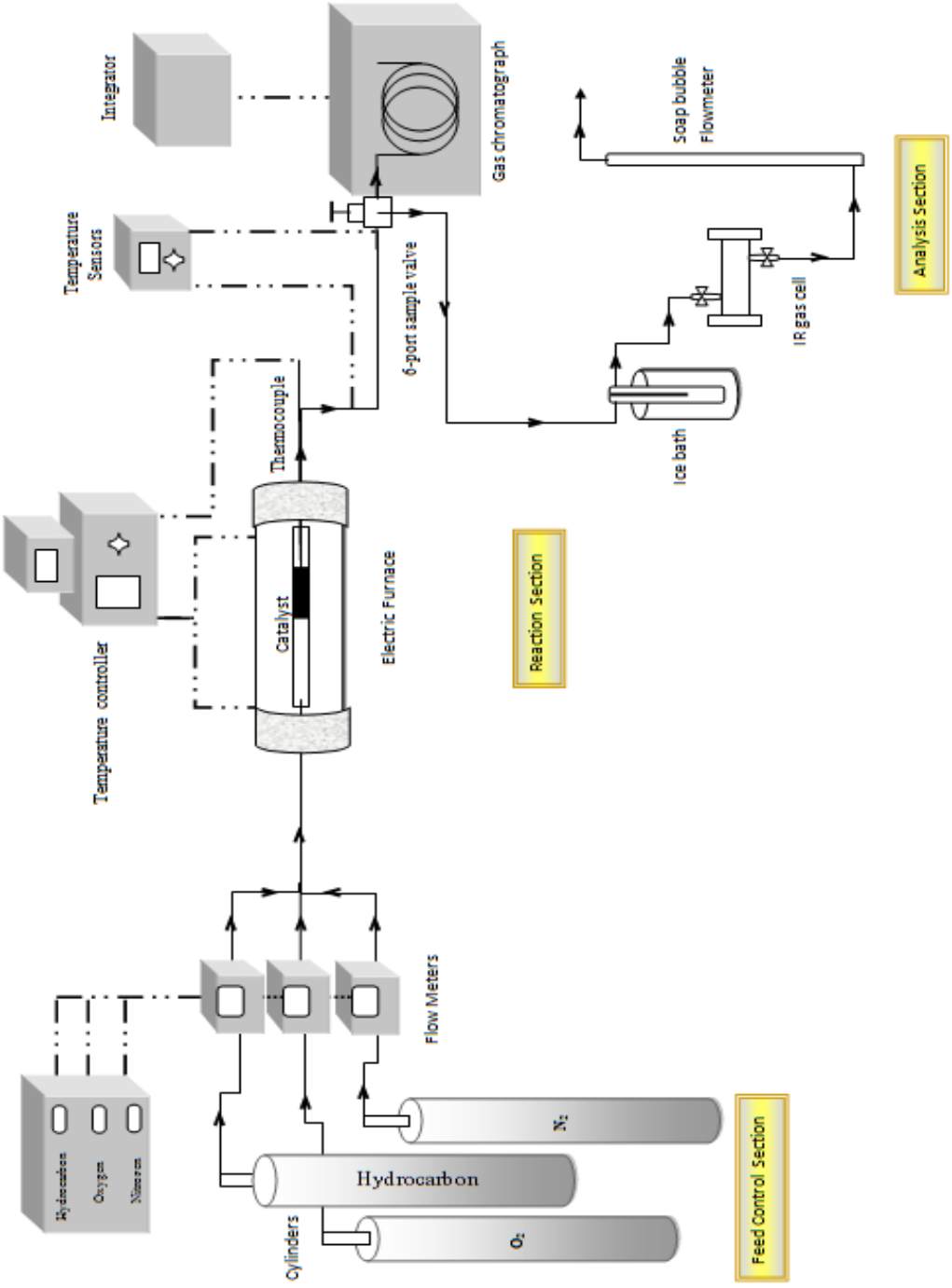

Figure 1. Schematic diagram of the experimental set up for partial and complete oxidation of isobutane.

The gas flows from the isobutane, air and nitrogen cylinders first passed through Swagelok all-welded inline filters (2 μm porosity) (FW series) prior to the flexible hoses.

The tubing from all filters to the mass flow controllers were high-pressure, flexible metal hoses with 1/4″ stainless steel tubing used thereafter to prevent constrictions in the flow once the individual gas flows had been set. The 1/4″ stainless steel tubing was joined with stainless steel Swagelok unions and "T" pieces using stainless steel ferrules, while teflon ferrules were employed to join the quartz or glass reactor section to the metal tubing sections. The mass flow controllers were Sierra Instruments, Inc., Smart-Trak Series 100 controllers (N_2: C100L-DD-2-OV1-SV1-PV2-V1-S0-C0; O_2: C100L-DD-2-OV1-SV1-PV2-S0-C0-LF; isobutane: C100L-DD-2-OV1-SK1-PV2-V1-S0-C0-GS).

The reactor system consisted of a 300 mm long quartz or Pyrex glass tube with an external diameter of 10 mm and an internal diameter of 8 mm. It was heated with a home-built cylindrical electrical furnace, ~20 cm long with an internal diameter of ~4.5 cm and operated using a BTC-9090 furnace controller (Ceramic Engineering, Marrickville, Australia). The quartz or glass reactor tube, which contained the catalyst and quartz wool (Grace Davison, Product # 3111973) located before and after the sample to hold it in the chosen place, was placed concentrically within the tube furnace, while the ends of the furnace were filled with Kaowool (Thermal Ceramics) plugs to ensure that the temperature within the catalyst bed remained constant once it had been set. The catalyst bed in the quartz or Pyrex tube was located lengthwise in the centre of the cylindrical furnace and varied in length from ~10 to ~25 mm, depending on the type of experiment performed. The reactor tube was made from Pyrex glass for the partial oxidation catalysis runs (which were carried out at 340^{o}C), but was made from quartz for the complete combustion experiments because of the higher temperatures required.

The thermocouple (1/16″ o.d., D & N Engineering Supplies, Lambton, Australia) was mounted within the catalyst reactor tube using a Swagelok adaptor system, with the tip located immediately after the rear quartz wool support of the catalyst and directly in the gas stream. The furnace controller was linked directly to the thermocouple. This allowed accurate control of the temperature within the catalyst bed once the temperature had been set (to an accuracy of < 1^{o}C).

The analysis system consisted of a gas chromatograph (plus integrator) and a demountable IR gas cell (8.75 cm path length, 4.5 cm internal diameter), which was fitted with NaCl plates. The outflow from the reaction system passed through 1/4″ tubing, which was heated using a Thermolyne fibrox heavy-duty electric heating tape connected to a Thermolyne Type 45500 power controller unit. The temperature in the line was always kept at a temperature greater than the highest boiling point product (methacrylic acid, 163^{o}C, for the partial oxidation of isobutane, and water, 100^{o}C, for the complete combustion of isobutane). The outflow from the reactor system was sampled using a manually-controlled Valco Instruments Co., Inc., 6-port external volume sample injector Type 46 UWE with a 0.5 mL zero dead volume sample loop, which was attached to the gas chromatograph, and which was maintained at 200^{o}C using the electric heating tape for the partial oxidation of isobutane, but only 165^{o}C for the complete oxidation of isobutane. The gas flow then passed through a liquid phase collector at ice temperature and then through the demountable gas IR cell, and finally though a soap bubble flow meter. The gas chromatograph used to analyse the unreacted isobutane and the partial oxidation products methacrolein (MAL), methacrylic acid (MAA), acetic acid (ACA) and isobutyric acid (IBA) for the selective oxidation of isobutane was a Shimadzu GC-17A fitted with a packed bed column (an Alltech 6′ × 1/8″ stainless steel column with a 10% FFAP stationary phase on acid-washed Chromasorb W 80/10 as the solid

support), while for the complete combustion of isobutane a Restek Rt-Alumina BOND/KCl, 30 m long and 0.53 mm i.d., capillary column was employed. In neither study was the water produced in the reactions quantitatively determined. The gas chromatograph was connected a Shimadzu C-R8A Chromatopac integrator.

The liquid phase collector was built from a Quickfit Pyrex glass bubbler (MF 28/2) with the exit of the central delivery tube placed less than 5 mm from the bottom of the enclosing Quickfit "test tube". This tube was replaceable and was used to collect the liquid phase of the catalyst reaction for later disposal, and was cooled in a bath of ice during a catalysis run. The outlet of the liquid phase collector then passed through the demountable IR gas cell, and from there to a soap bubble flow meter for flow rate verification.

The gases used in the catalysis system were nitrogen (BOC Gases, Ultra High Purity), oxygen (BOC Gases, High Purity) and isobutane (BOC Gases, Instrument Grade). The standard feed composition for the partial oxidation of isobutane was 25.0 volume % isobutane, 12.5 volume % oxygen, and 62.5 volume % nitrogen, with a total flow rate of 20 mL/min, while the standard feed composition for complete oxidation of isobutane consisted of 2 volume % isobutane, 20 volume % oxygen and 78 volume % nitrogen, with a total flow rate of 50 mL/min. Experiments were also performed with varying isobutane:oxygen ratios and different flow rates, and these will be indicated in the appropriate sections.

2.2 Separation and Quantitative Analysis of the Catalysis Products

2.2.1 The Partial Oxidation of Isobutane

For the partial oxidation of isobutane over polyoxometalate catalysts (with and without added gold nanoparticles) the products of reaction were methacrolein (MAL), methacrylic acid (MAA), acetic acid (ACA), isobutyric acid (IBA), carbon monoxide (CO),

carbon dioxide (CO_2) and water. The unreacted isobutane and the products MAL, MAA, ACA and IBA were analysed by direct injection into the gas chromatograph using a 6-port external sample valve fitted with a 0.5 mL sampling loop, as indicated above. The CO and CO_2 were measured using IR spectroscopy.

2.2.2 Separation of Isobutane and Oxidation Products by Gas Chromatography (GC)

2.2.2.1 Carrier and Other Gases

For the Shimadzu 17A gas chromatograph, nitrogen (BOC, High Purity, 99.99%) was used as the carrier gas, while compressed air (BOC or Coregas, Instrument Grade) and compressed hydrogen (BOC, High Purity, or Coregas 4.0) served to provide a flame for the flame ionisation detector.

2.2.2.2 Temperatures of the Injection Port, Column and Detector

For the partial oxidation catalysis of isobutane, the temperature in the injection port must be hot enough to avoid any loss of sample components during injection. Also, it must be low enough to prevent decomposition of the sample components. As the electric heating tape was used to keep the sampling valve and loop at 205^{o}C in this study, the injection temperature was also chosen to be close to this temperature. Thus the temperature was set to 190^{o}C, which was higher than that of any of products to be analysed, and also avoided any decomposition of the products. The boiling points of the products are shown in Table 1.

Table 1. The boiling points of the organic products of the partial oxidation of isobutane.

Compound	MAL	MAA	ACA	IBA
Boiling point (^{o}C)	69	163	117.9	154.7

The temperature of the column must be high enough to analyse the products in a reasonable length of time, while low enough to obtain a desired separation of the components in the sample. In the present study unreacted isobutane (b. pt. = -11.7^{o}C) also had to be determined, so that a two-stage approach to analysis was employed. This consisted of a 2 minute isothermal section at 40^{o}C, which allowed analysis of the unreacted isobutane and methacrolein, followed by a 10^{o}C/minute temperature ramp to 190^{o}C for acetic, isobutyric and methacrylic acids. A complete analysis run took 17 minutes.

The detector temperature depends on the type of the detector employed, which in the present study was a flame ionisation detector. The connections from the column exit to the detector must be hot enough to prevent the condensation of the sample, and the detector temperature must also be high enough to avoid condensation of the water or any by-products formed in the ionization process. In this study, the temperature was chosen to be 195^{o}C, which was higher than the injection port by 5^{o}C.

2.2.3 Quantitative Analysis of Reactant and Products – Calibration Curves for Isobutane, Methacrolein, Methacrylic Acid, Acetic Acid and Isobutyric Acid

2.2.3.1 Calibration Curve for Isobutane

A calibration curve for isobutane was constructed at room temperature with different isobutane volume contributions, and at a total flow rate of 20 mL/min. Volume contributions

of 0.5, 1.0, 1.5, 2.0, 2.5, 3.0, 3.5, 4.0, 4.5 and 5.0 mL/min in a total volume of 20 mL/min were used to construct the calibration curve. The maximum errors in flow according to the supplied calibrations were 0.70% for isobutane, 0.39% for N_2 and 0.87% for O_2. The volumes were converted to the number of moles of isobutane in the gas stream, assuming ideal gas behaviour. The calibration curve is shown in Figure 2. Thus isobutane at the beginning of a catalysis run (see later), or residual isobutane that is present in the gas stream at any time could be evaluated and related to a known amount of isobutane at room temperature.

2.2.3.2 Preparation of standard samples and calibration curves for methacrolein, methacrylic acid, acetic acid and isobutyric acid

For the calibration curves of the products of the partial oxidation of isobutane, samples of methacrolein (MAL), methacrylic acid (MAA), acetic acid (ACA) and isobutyric acid (IBA) were pipetted into weighed 5 mL volumetric flasks using an Eppendorf Multipipette© plus fitted with a 1 mL Combitip plus, and the flasks reweighed to obtain the accurate mass of the sample. The solutions were made up to volume with acetonitrile. More details are shown in Table 2, and the resulting linear calibrations are shown in Figure 3.

Table 2. Added volumes for the calibration samples of methacrolein, methacrylic acid, acetic acid and isobutyric acid (µL).

Product	**Flask 1** (µL)	**Flask 2** (µL)	**Flask 3** (µL)	**Flask 4** (µL)
MAL	20	40	60	80
MAA	10	20	30	40
ACA	20	15	10	5
IBA	20	15	10	5

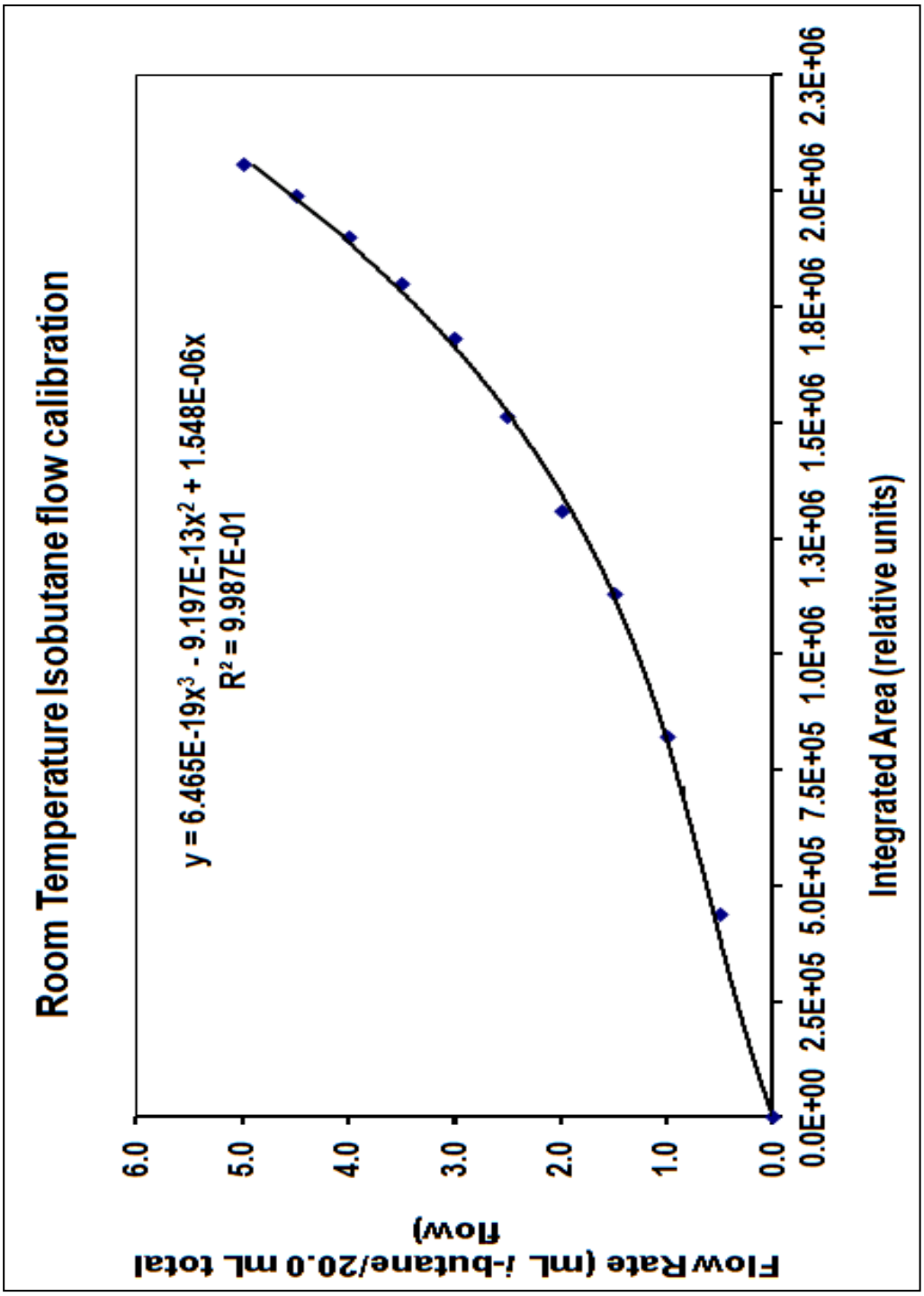

Figure 2. Calibration curve for the partial oxidation of isobutane.

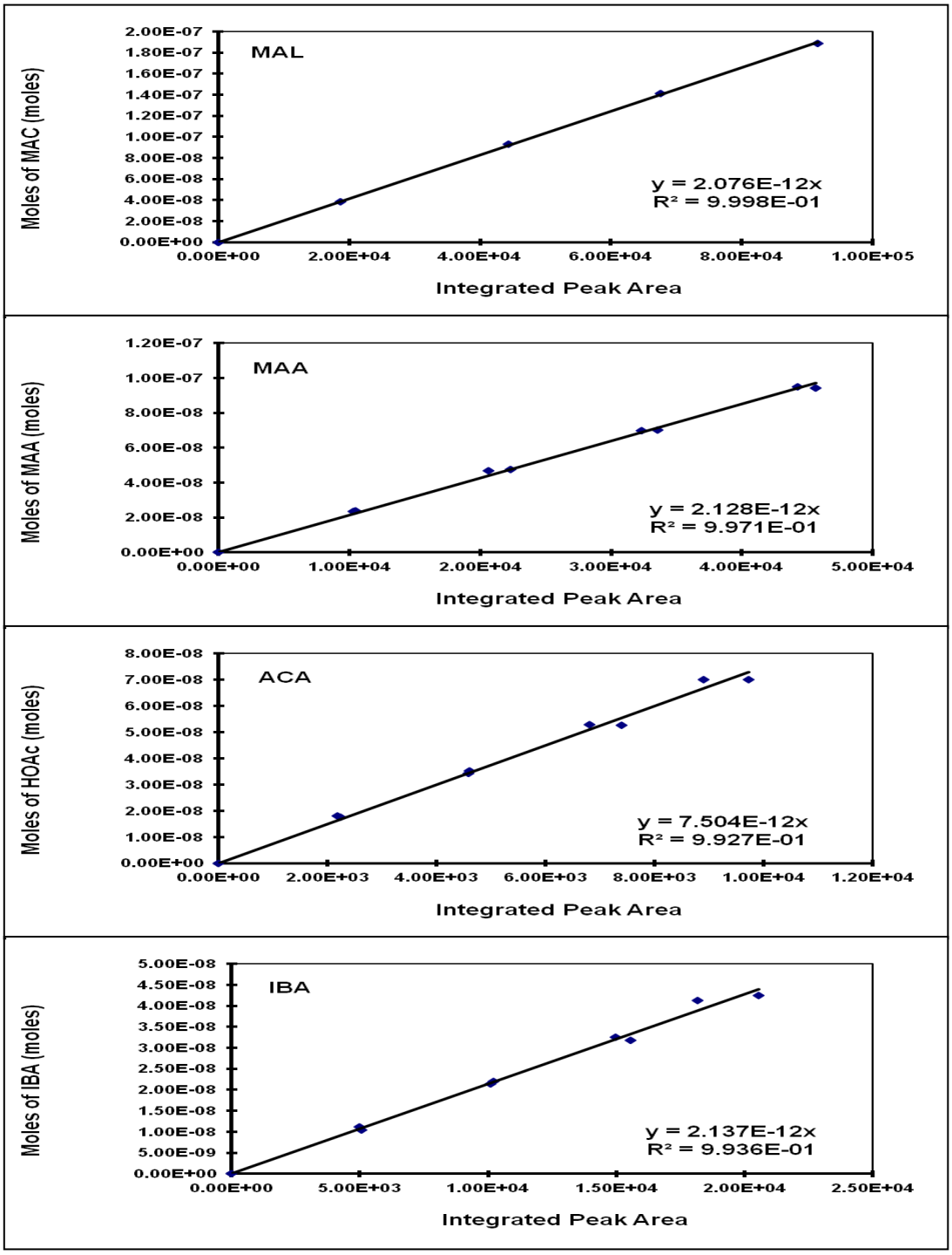

Figure 3. The calibration curves for methacrolein (MAL), methacrylic acid (MAA), acetic acid (ACA) and isobutyric acid (IBA).

2.2.4 The Quantitative Analysis of CO and CO_2 by Infrared Spectroscopy

2.2.4.1 A Brief Theory

Infrared (IR) spectroscopy may be applied both for the quantitative and qualitative analysis of gases. In this study, IR spectroscopy was used for the quantitative analysis of both CO and CO_2.

The Beer-Lambert law, equation (1) describes the relationship between the absorption of radiation by the sample and the concentration of the desired component, as well as to the path length of the sample [8]. The following equation describes the Beer-Lambert law:

$$A = \log_{10} (I_o/I) = \varepsilon cd \quad (1)$$

In this equation A = the absorbance of the sample, I_o = the radiant power impinging on the sample (the incident radiation), I = the radiant power transmitted by the sample (the transmitted radiation), ε = the constant of proportionality, referred to as molar absorptivity, c = the concentration and d = the path length of the sample. The resulting absorbance is dimensionless, as is transmittance (T), which is expressed as:

$$T = I/I_o \quad (2)$$

The Beer-Lambert law tell us that the plot of absorbance (A) against concentration (c) should give a line with a gradient of εd and should pass through the origin. However, the plot of absorbance against concentration is usually linear only over a short concentration range. The reason for this failure is attributable to the non-ideal behaviour of the sample, which is related to molecular interactions between the solute and solvent molecules (solution or gas phases). In the gas phase, especially at 1 atmosphere, there can be significant interactions

between the gas phase molecules, specifically the residual isobutane, nitrogen, and the CO and CO_2, as well as pressure broadening [8].

A calibration curve is therefore the best approach in order to obtain accurate analyses. This approach generates a calibration curve which will correct for or cancel out any errors. The procedure of gas analysis is similar to the analysis of a liquid. The only difference between these two analyses is that the x-axis of the calibration curve, which represents the concentration in liquid analysis, in gas analysis represents the partial pressure which is related to concentration, and can always be converted to concentrations if necessary.

2.2.4.2 Infrared Analysis

A Shimadzu FTIR-8400 spectrophotometer with sample compartment purging system was used to determine CO and CO_2, which were both produced during the partial oxidation of isobutane. Wavelengths of 2171 and 2341 cm^{-1} were used to construct the calibration curves for CO and CO_2, respectively, with the base (or zero) values taken at 2000 and 2400 cm^{-1}, respectively. A resolution of 8.0 cm^{-1} and 64 scans were used in the construction of the calibration curves and in the analysis of the gas phase products of isobutane oxidation.

2.2.4.3 Calibration Curves for CO and CO_2

Calibration curves at room temperature for CO and CO_2 were constructed with different gas volume contributions, by injection of known volumes of either CO or CO_2 into the nitrogen-purged gas cell using 5 and 10 mL SGE gas-tight syringes. Volume contributions for CO of 0.5, 1.0, 1.5, 2.0, 2.5, 3.0, 3.5, 4.0, 4.5 and 5.0 mL, and for CO_2 of 1.0, 2.0, 3.0, 4.0, 4.5 and 5.0 mL in a total gas volume of 142 mL (with the remainder nitrogen) were used to construct each calibration curve. Prior to each addition of CO or CO_2 the cell was flushed with nitrogen (BOC, High Purity) for at least 10 minutes to remove

residual CO or CO_2. The volumes were converted to the number of moles of isobutane in the gas stream, assuming ideal gas behaviour. IR spectra were recorded using a purged sample chamber, such that the residual peak from CO_2 was always a minimum. This took about 10-15 minutes depending on the flow of gas through the sample compartment. The calibration curves for CO and CO_2 are shown in Figures 4 and 5, respectively. Note that the curves are not linear, indicating that there were significant interactions between CO and CO_2 with nitrogen, and likely that some pressure broadening occurred at the total pressure of 1 atmosphere inside the gas cell. The experimental points were fitted to a higher order polynomial in each case (a quadratic for CO and a cubic for CO_2). These gave better than a 0.9996 agreement with the experimental points.

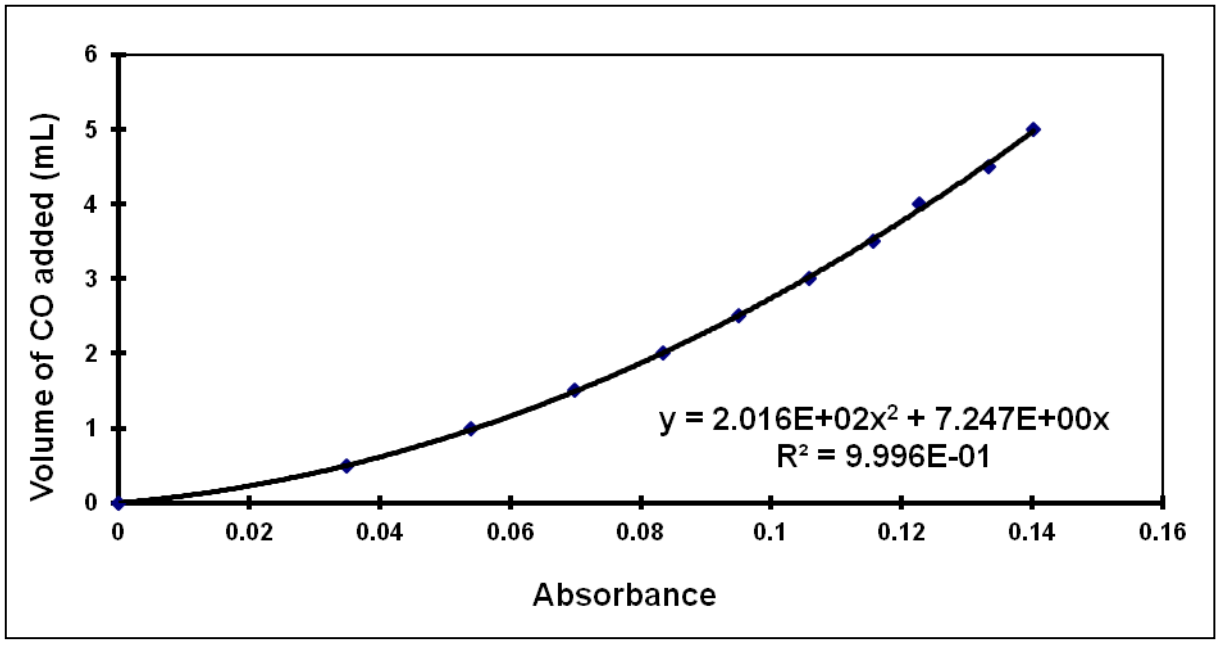

Figure 4. Calibration curve for CO. (A wavelength of 2171 cm^{-1} was used to construct the calibration curve, with the zero value taken at 2000 cm^{-1}.)

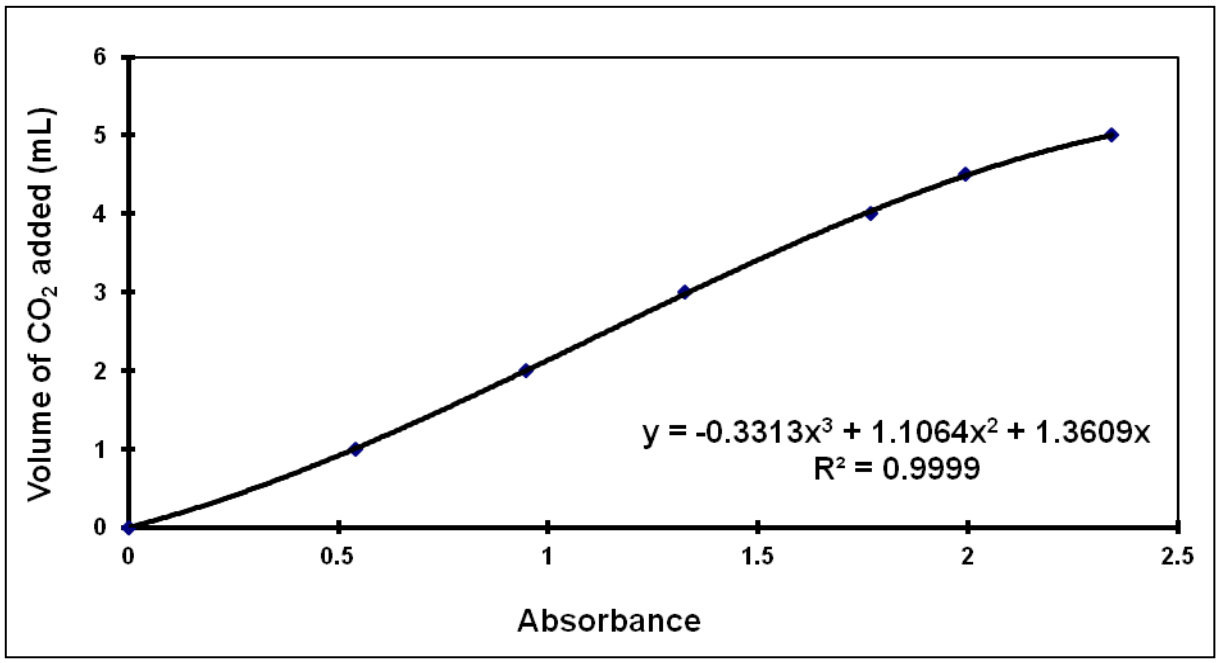

Figure 5. Calibration curve for CO_2. (A wavelength of 2341 cm^{-1} was used to construct the calibration curve, with the zero value taken at 2400 cm^{-1}.)

2.2.5 A Typical Catalysis Run

The catalytic tests were carried out in a fixed-bed reactor, as indicated above. As in previous studies [4, 9], the phosphopolyoxomolybdate catalysts were not supported, but were pure samples. This avoided any possible reactions of isobutane with a catalyst support.

Each catalyst was dried in air at 105^{o}C for 1 hour and compressed at a pressure of 1.7 ton/cm^2 using an IR press, then broken up and passed through a series of sieves (40 to 80 mesh). After that, 1.70 g of catalyst (see below for the preparation of catalysis samples with added gold nanoparticles) was loaded in a 10 mm o.d. glass tube reactor and connected to the system. Each catalysis run required two days as follows:

A. *Day 1 (calcinations)*:

i. The flow meters for N_2 and O_2 were set to the required flow rates (N_2 = 17.5 mL/min; O_2 = 2.5 mL/min).

ii. The tube furnace was set to the calcination temperature of 350^{o}C (10^{o}C higher than the actual catalysis temperature).

iii. The calcination was continued for 1 hour at 340^{o}C, and then the power to the electric furnace was turned off.

iv. The flows of N_2 and O_2 were adjusted to N_2 = 1.5 and O_2 = 1.0 mL/min, and left overnight.

B. *Day 2 (catalysis run)*:

i. The power to the heating tape was switched on and the temperature adjusted to 200^{o}C.

ii. After the heating tape reached temperature equilibrium, the flows of N_2, O_2, and isobutane were adjusted to their required rates (N_2 = 12.5, O_2 = 2.5 and IBU = 5.0 mL/min).

iii. The GC was turned on, and four inital measurements of isobutane were performed to obtain the initial isobutane calibration delivered to the GC by the sampling valve and 0.5 mL sample loop.

iv. The tube furnace was turned on and the temperature at the catalysis sample was set to 340^{o}C.

v. On reaching the desired value, a GC run was performed each hour for the next four hours, or until product generation reached stable GC integrated intensity values.

vi. During this time the IR gas cell was connected to the catalysis line. The cell was continuously purged with the outlet gases from the reaction, after passing through the sampling valve and liquid phase collector. After the catalysis reaction had reached equilibrium with continuous purging of the IR cell, the cell was quickly

sealed and removed from the catalysis line and placed in the sample chamber of the IR spectrophotometer. After 10 to 15 minutes of purging with dry nitrogen, the CO and CO_2 spectra were recorded several times (2 or 3) to obtained average values for the absorbances of CO and CO_2. Before analysis of the gas phase for CO and CO_2, a background was recorded after 15 minutes of purging of the sample compartment with dry nitrogen, to remove the interfering water and atmospheric CO_2.

vii. At the end of the catalysis run, the system was closed down, and the following day the spent catalyst sample was recovered and stored for future analysis (*e.g.* XPS study).

2.2.5.1 The preparation of gold nanoparticle/phosphopolyoxomolybdate catalysts

The additions of gold nanoparticles to $[PMo_{12}O_{40}]^{-3}$ salts were accomplished as following:

i. The equivalent of a 5 mass % solution of *n*-hexanethiolate-stabilised gold nanoparticles (mass of stabilised gold nanoparticles) was prepared in *n*-hexane.
ii. This solution was added to 1.7 g of the $[PMo_{12}O_{40}]^{3-}$ salt in a porcelain crucible and thoroughly mixed using a glass rod (in some case excess *n*-hexane was added to ensure thorough mixing of the gold nanoparticle solution with the solid catalyst).
iii. The mixture was allowed to dry in a fume hood.
iv. The catalyst sample with added *n*-hexanethiol-stabilised gold nanoparticles was heated slowly to 150^{o}C, then to 220^{o}C, at which temperature the thiolate ligand on the surface of the gold nanoparticles was thermally decomposed (see Chapter 3),

and finally to 300^{o}C, where it was left for 1 hour to remove any thiolate decomposition products from the catalyst.

The percentage conversion of isobutane was calculated as follows:

% conversion = 100 × (1 - [moles of unreacted isobutane / moles of isobutane introduced])

The number of moles of each product was calculated by using the previously established calibration curves. The percentage selectivity of each product component was calculated as follows:

% selectivity = 100 × [moles of component / total number of moles]

The carbon balance was calculated according to the equation (where n = number of moles):

Carbon balance (%) =

$$100 \times \{[(n_{MAL}) + (n_{MAA}) + (n_{IBA}) + (0.5 \times n_{ACA}) + (0.25 \times n_{CO}) + (0.25 \times n_{CO2})] / [n_{IBU}]\}$$

These were always better than 90% in the partial oxidation of isobutane studies.

Estimated errors for residual isobutane flow rates are no greater than 0.70%, based on the calibration curves provided by the manufacturer (over the total range of flow rates accessible by the isobutane flow meter, the calibration errors range from 0.02 to 0.70%, with and average of 0.38%). This gives an error in the residual % isobutane of <0.5%. For MAL, MAA, ACA and IBA the gas chromatographic calibration curves were obtained using 3 injections and the peak areas averaged. All calibrations had linear correlation coefficient R^2 values of >0.992 (page 73). The estimated errors in the % selectivity values are a maximum of 1% for MAL, 3% for MAA, 1% for IBA and 3% for ACA. For CO and CO_2, the combined

errors (sample and background) in absobance were 0.23% and 0.36%, but these are less than the stated accuracy of the gas-tight syringes, ±1%. Thus the combined errors in the % selectivities are 1.23 % for CO and 1.36% for CO_2.

The contact time was determined as the weight of catalyst/total flow rate (W/F) through the catalyst (g s mL^{-1}). In this study, the masses of the catalyst varied from ~1.75 to ~1.85 g (including taking into account the addition of gold nanoparticles, which combined with the total flow rate of 20 mL/min gave contact times between ~2.7 to ~4.1 s.

2.2.6 The Complete Combustion (Oxidation) of Isobutane

The products in the complete oxidation of isobutane over the metal oxides Mn_3O_4, Co_3O_4, and Fe_3O_4 (with or without the addition of gold nanoparticles) were CO, CO_2, and H_2O. The unreacted isobutane was analysed by gas chromatography, while CO and CO_2 were identified by gas-phase IR spectroscopy when the conversion of isobutane reached ~20-25%.

In the complete oxidation of isobutane, as the only products were CO, CO_2 and H_2O, the output of the reactor did not have to be kept at the high temperature required to maintain the products in the gas phase as in the partial oxidation studies, so for the complete oxidation of isobutane the sampling valve and loop were set at 165^{o}C using the electrical heating tape and controller.

As indicated above, for the complete combustion of isobutane a capillary column was used in the gas chromatograph. This was employed so as to separate any product hydrocarbons that might form from the isobutane substrate. The column temperature was set at 75^{o}C, which was chosen based on the retention time of isobutane and possible side products (*e.g.* isobutene, propane, propene) while the temperature of the injection port and detector were both 200^{o}C. This gave a catalysis run of 5 minutes. The column was

conditioned after a group of four successive catalysis runs, to eliminate the build-up of water inside the column, and hence loss of sensitivity and variation in retention time of the isobutane.

2.2.6.1 Calibration Curve for Isobutane

As the temperature in the reactor in a catalysis run involving the complete combustion of isobutane was continuously ramped from room temperature to the maximum temperature required to achieve 100% oxidation of the isobutane (this was ~200-470^{o}C, depending on the catalyst), the temperature of the gas flow exiting the reactor also continuously changed. This coupled with the relatively high flow rate of 50 mL/min resulted in an increasing temperature at the sampling valve and loop, despite the electric heating tape being set to 165^{o}C. Consequently, the effective volume of isobutane in the sampling valve decreased as the temperature was ramped, irrespective of whether catalytic combustion was occurring in the reactor or not. A calibration curve to account for this temperature effect was therefore constructed, which involved measuring the isobutane actually in the 0.5 mL sampling loop that was sent to the inlet of the gas chromatograph when no catalysis occurred. To accomplish this, the reactor was charged with just SiC (the catalyst diluent used in the combustion studies, see below), which has no catalytic oxidation effect, and the isobutane measured as the temperature of the reactor was ramped from 25 to 500^{o}C, the latter being higher than that required to obtain 100% oxidation of isobutane. The isobutane calibration curve for 50 mL/min is shown in Figure 6. Not unexpectedly, the major corrections in the calibration curve occur at the beginning and end of a catalysis run, 25 to ~150^{o}C and >~400^{o}C, respectively, when the temperature in the reactor is very different from the temperature of the sampling valve.

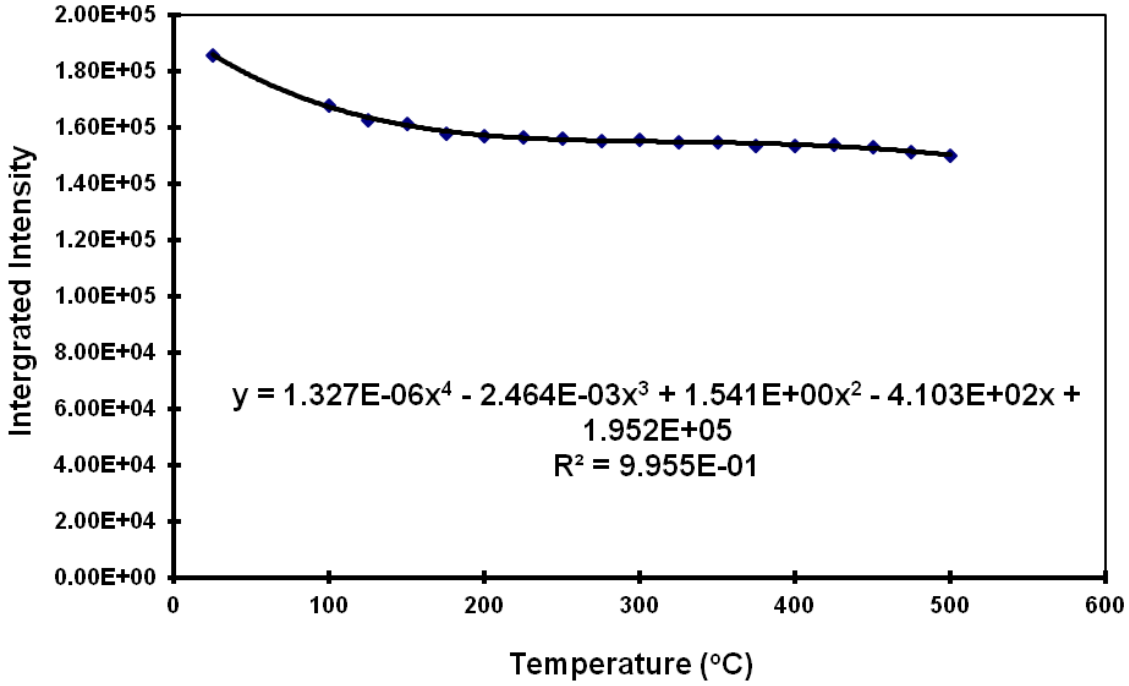

Figure 6. Calibration curve for the complete oxidation of isobutane.

2.2.7 A Typical Catalysis Run

The catalytic measurements were carried out in fixed-bed reactor. Each catalyst was dried in air at 105°C for 1 hour and 0.10 g of catalyst was diluted with 0.50 g of SiC (note that some studies were performed with different amounts of SiC). As the combustion of isobutane produced large amounts of heat, the dilution by SiC was found necessary in order to achieve satisfactory temperature control of the catalyst bed (see Chapter 4). The catalyst was loaded in a 10 mm o.d. quartz tube and connected to the analysis system. No calcination prior to the catalysis run was performed in these studies. A catalysis run was carried out as follows:

A. The heating tape power was turned on and the temperature was set at 165°C .
B. After the temperature reached 165°C, the mass flow controllers for N_2, O_2, and IBU were switched on and adjusted to the required flow rates (N_2 = 39 mL/min, O_2 = 10

mL/min and IBU = 1 mL/min). Note that some studies were carried out with different total flow rates or compositions and these were set as required.

C. The GC was switched on and performed three initial measurements for isobutane were performed at room temperature (RT).

D. The tube furnace was turned on and the temperature was set sequentially to the desired values. The temperature was raised each 10^{o}C in the range of 100 to 500^{o}C.

E. After reaching the desired temperature, a GC analysis was performed after 5 minutes temperature equilibration. Generally, three separate analyses were performed to ensure temperature equilibration had been achieved.

F. At the end of catalysis run, the system was closed down, and the next day the spent catalyst was collected and stored for future analysis (*e.g.* XPS study).

2.3 Characterisation of Catalysts and Instrumentation

2.3.1 Catalyst Characterisation

In this study, several techniques were used to characterise the phosphopolyoxomolybdate and metal oxide catalysts, including those with supported gold nanoparticles, prior to and following the catalysis studies. These techniques included infrared spectroscopy, UV-visible spectroscopy, thermogravimetric and differential thermal analysis, X-ray powder diffraction, X-ray photoelectron spectroscopy, surface area and porosity measurements, transmission electron microscopy and scanning electron microscopy. Use of these techniques allows the results of the catalysis studies, including the effects of added gold nanoparticles, to be related to measurable physical properties of the catalyst samples, and aids in the interpretation of the observed trends in the catalysis results

2.3.2 Characterisation Methods

UV-visible spectroscopy, TEM and TG/DTA were used to characterise the *n*-hexanethiolate-stabilised gold nanoparticles. This enabled the size of the particles to be determined before they were loaded onto the catalysts.

2.3.2.2 UV-visible spectroscopy (UV-vis)

UV-visible spectroscopy was used to obtain a measure of the size of the *n*-hexanethiolate-stabilised gold nanoparticles as they were initially prepared. This was achieved by comparing the size of the surface plasmon band at ~520 nm with spectra previously reported [10]. Spectra were recorded on a Shimadzu UV-1700 PharmaSpec spectrophotometer.

2.3.2.1 Transmission Electron Microscopy (TEM)

The sizes of the *n*-hexanethiolate-stabilised gold nanoparticles were also characterised by transmission electron microscopy on a Jeol 1200-EXII transmission electron microscopy operating at 120 kV. Samples were prepared by dissolving the *n*-hexanethiolate-stabilised gold nanoparticles in *n*-hexane. Drops of solution were placed on carbon-coated copper grids and allowed to dry in the air.

2.3.2.2 Thermogravimetric/Differential Thermal Analysis (TG/DTA)

Thermogravimetric and differential thermal analyses were performed on the *n*-hexanethiol-stabilised gold nanoparticles to establish the organic content, and hence the % mass of gold in the stabilised gold nanoparticles, as well to establish the thermal decomposition temperature of the stabilised gold nanoparticles. Studies were carried out on a Perkin-Elmer Diamond TG/DTA thermal analysis system. Samples were contained in a

standard platinum pan, with a reference Al_2O_3 sample contained in a platinum pan for the DTA studies. Thermal runs on each sample were recorded under flowing nitrogen (30 mL/min) from 30 to 600^oC using a thermal ramp rate of 20^oC/min for the *n*-hexanethiolate-stabilised gold nanoparticles, and at 10^oC/min for all other samples.

2.3.2.3 X-ray Photoelectron Spectroscopy (XPS)

X-ray photoelectron spectroscopy measurements were performed to investigate the surface oxidation states of the catalyst and gold nanoparticle-catalyst samples, both before and following catalysis studies. Spectra were recorded using either:

(a) Specs PHIOBOS 100 Anayser using Al-K_α radiation (1486.6 eV) operating at 12.5 kV and 12 mA, or

(b) Physical Electronics Industries, Inc., PHI550 instrument, using Mg-K_α radiation (1253.6 eV), operating at 12.5 kV and 20 mA.

The linearity of the energy scale was established using the Au $4f_{7/2}$, Ag $3d_{5/2}$ and Cu $2p_{3/2}$ lines at 84.0, 368.2 and 932.6 eV, respectively. Samples were mounted on carbon tape and spectra were referenced to the carbon 1s line of adventitious carbon (248.8 eV), and ultimately to the Au $4f_{7/2}$ line at 83.8 eV. All spectra were recorded at pressures from 1.4×10^{-8} to 0.9×10^{-7} torr. The XPS spectra were analysed using CASA-XPS software (version 2.3.16) [11].

2.3.2.4 X-ray Powder Diffraction (XRD)

X-ray powder diffraction (XRD) patterns were recorded to obtain information about the structure and composition of the catalyst materials and to calculate the crystallite size of the gold nanoparticles following removal of the thiolate ligands on the surface of the

nanoparticles. XRD patterns were recorded at room temperature with a Philips X'pert Pro MPD instrument. Routine spectra were recorded from 5 to 90^{o} with a step size of 0.008^{o}, taking 1 hour, while the high resolution X-ray diffraction patterns were recorded from 30 to 50^{o} with a step size of 0.002^{o}, and taking 8 hours per scan. Samples for high temperature XRD study were mounted on an Anton-Parr HTK16 hot-stage in the Philips X'pert Pro MPD instrument. The XRD patterns were recorded from 5-90^{o}, with a step size of 0.008^{o}.

2.3.2.5 Infrared Spectroscopy (IR)

Infrared spectra were recorded on a Shimadzu FT-8400 spectrophotometer for the CO-CO_2 analysis from a catalysis run. IR spectra on the *n*-hexanethiolate-stabilised gold nanoparticles and the phosphopolyoxomolybdate catalysts were obtained using a Perkin Elmer FT-IR Spectrum BX System.

2.3.2.6 Scanning Electron Microscopy (SEM)

Scanning electron microscopy was recorded on a Philips XL30 SEM operating at 15-30 kV. Samples were mounted on double-sided carbon tabs, and were sputtered with ~20 nm of gold before transfer to the SEM instrument.

2.3.2.6 Surface Area Analysis

BET surface areas were determined using nitrogen adsorption on a Micromeritics ASAP 2020 accelerated surface area and porosimetry instrument. Samples were degassed at either 100^{o}C prior to analysis.

2.4 References

[1] D. Thoenes, Chemical Reactor Development, 1994.

[2] P. Andrigo, R. Bagatin, G. Pagani, Catal. Today, 52 (1999) 197-221.

[3] G. Eigenberger, Fixed-bed reactors, Ullmann's Encyclopedia of Industrial Chemistry, Vol. B4, VCH Publishers, Weinheim (Germany), 1992.

[4] J. Hu, R. Burns, J. Catal., 195 (2000) 360-375.

[5] S. Scir, S. Minic, C. Crisafulli, C. Satriano, A. Pistone, Appl. Catal. B: Environmental, 40 (2003) 43-49.

[6] B.E. Solsona, T. Garcia, C. Jones, S.H. Taylor, A.F. Carley, G.J. Hutchings, Appl. Catal. A: General, 312 (2006) 67-76.

[7] S. Minico, S. Scire, C. Crisafulli, R. Maggiore, S. Galvagno, Appl. Catal. B, Environmental, 28 (2000) 245-251.

[8] B. Stuart, in Infrared Spectroscopy, 2004.

[9] M. Langpape, J.M.M. Millet, U.S. Ozkan, M. Boudeulle, J. Catal., 181 (1999) 80-90.

[10] M. Hostetler, J. Wingate, C. Zhong, J. Harris, R. Vachet, M. Clark, J. Londono, S. Green, J. Stokes, G. Wignall, Langmuir, 14 (1998) 17-30.

[11] Casa-XPS; Processing Software for XPS, AES, SIMS. Version 2.3.16, http://www.casaxps.com/berlin/.

CHAPTER 3

Synthesis, Characterisation and Catalysis using Gold Nanoparticles deposited on Keggin-type $[PMo_{12}O_{40}]^{3-}$ Salts for the Partial Oxidation of Isobutane

3.1 Introduction

Keggin-type polyoxometalate acids and salts, generally based around the $[PMo_{12}O_{40}]^{3-}$ anion, are known to be effective in heterogeneous catalysis for the gas-phase partial (*i.e.* selective) oxidation of organic substrates. Examples include the oxidation of methacrolein to methacylic acid [1], the oxidative dehydrogenation of isobutyric acid to methacrylic acid [2, 3] and isobutyraldehyde to methacrolein [4] and, more recently, the oxidation/oxidative dehydrogenation of isobutane to methacrolein and methacrylic acid [5-9]. The oxidative dehydrogenation (ODH) of lower alkanes has received much attention in recent years, particularly isobutane. This is because the oxidation/oxidative dehydrogenation of isobutane leads to the formation of methacrolein and methacrylic acid, and ultimately to poly(methyl methacrylate). Esterification of methacrylic acid with methanol yields methyl methacrylate, and its subsequent polymerisation gives poly(methyl methacrylate), commonly known as Perspex or Plexiglass. Thus a process based on the oxidation/oxidative dehydrogenation of isobutane could replace the environmentally unfriendly acetone-cyanohydrin process which requires use of highly poisonous HCN and the formation of by-products that are difficult to store and dispose (see Chapter 1).

As noted above, the study of heteropolyoxometalate catalysis primarily involves compounds containing the Keggin-based anion $[PMo_{12}O_{40}]^{3-}$. Most of the studies on $[PMo_{12}O_{40}]^{3-}$ have used the parent acid and salts containing monovalent, divalent and trivalent cations [4, 8, 10]. Furthermore, several studies have investigated the structure, pore size, and activity of some of polyoxometalate salts including Cs^{+}, Al^{3+}, La^{3+}, and Ce^{3+} [4, 9-11].

In this chapter, the results of a study of the oxidation/oxidative dehydrogenation of isobutane are described using the free acid and selected salts of the $[PMo_{12}O_{40}]^{3-}$ anion, as well as the effects of gold nanoparticles on this process. The effects of gold nanoparticles on the selective oxidation of hydrocarbons over polyoxometalate catalysts have never been studied previously. The Keggin-type polyoxomolybdates include the parent acid $H_3[PMo_{12}O_{40}]$ and compounds containing Cs^{+}, Ag^{+} and Cu^{2+} counter-cations. The range of compounds includes $Cs_{3-x}H_x[PMo_{12}O_{40}]$ (where x = 0, 0.5, 1 and 2), $Ag_{3-x}H_x[PMo_{12}O_{40}]$ (where x = 0, 1 and 2), and $Cu_{3-x}H_{2x}[PMo_{12}O_{40}]_2$ (where x = 0, 1 and 2). A two-phase method is used to synthesise the gold nanoparticles stabilised with *n*-hexanethiolate as the ligand to create particles with a diameter of ~2.5 nm. The *n*-hexanethiolate-stabilised gold nanoparticles are characterised by a number of techniques including UV-visible spectroscopy, transition electron microscopy and thermogravimetric/differential thermal analysis. The *n*-hexanethiolate-stabilised gold nanoparticles are then used to create a 5 mass % loading on the phosphopolyoxomolybdate compounds and the stabilising thiolate ligands are removed by thermolysis. The resulting gold nanoparticles show some aggregation, and have an average diameter of 6.0 nm based on X-ray powder diffraction studies. The phosphopolyoxomolybdate species are characterised by several techniques including X-ray powder diffraction, IR spectroscopy and X-ray photoelectron spectroscopy, with the latter also used to characterise the gold nanoparticle-polyoxometalate catalysts following catalysis.

3.2 Experimental

3.2.1 Chemicals

Chloroauric acid ($HAuCl_4.3H_2O$, 51%, Aldrich), tetraoctylammonium bromide ($C_{32}H_{68}NBr$, 98%, Sigma-Aldrich), sodium borohydride ($NaBH_4$, Merck), toluene ($C_6H_5CH_3$, Merck), methanol (CH_3OH, Lab-scan), *n*-hexane ($CH_3(CH_2)_4CH_3$, Merck), *n*-hexanethiol ($CH_3(CH_2)_5SH$, 95%, Sigma-Aldrich), hydrated 12-molybdophosphoric acid ($H_3[PMo_{12}O_{40}]$, ACS Reagent, Sigma-Aldrich), cesium carbonate (Cs_2CO_3, 99.9%, Sigma-Aldrich), and silver nitrate ($AgNO_3$, 99%, Sigma-Aldrich) were all used as received.

3.2.2 Synthesis of Keggin-type polyoxomolybdate salts as catalysts

In this study, salts of Keggin-type $[PMo_{12}O_{40}]^{3-}$ anion were prepared using different synthetic approaches with methods using carbonate, sulfate, and nitrate precursor source materials. The 'carbonate method' was used to prepare the series of $(Cs^+)_xH_{3-x}[PMo_{12}O_{40}]$ compounds, while the 'sulfate and nitrate methods' were used to prepare the $(Cu^{2+})_xH_y[PMo_{12}O_{40}]_2$ and $(Ag^+)_xH_{3-x}[PMo_{12}O_{40}]$ series of compounds, respectively. Each method is described in more detail below.

3.2.2.1 Synthesis of Cs^+ salts of the $[PMo_{12}O_{40}]^{3-}$ anion

$Cs_3[PMo_{12}O_{40}]$: In a typical preparation, 12.99 g (5.46 mmol) of hydrated 12-molybdophosphoric acid, $H_3[PMo_{12}O_{40}].\sim30H_2O$ (water content determined accurately by TGA) was dissolved in 10 mL of deionized water, followed by the slow addition of 2.67 g (8.19 mmol) of Cs_2CO_3 dissolved in 5 mL of deionized water, with continuous stirring and gentle heating. A bright yellow slurry resulted. The temperature of the slurry was increased to 50-60^oC to evaporate the majority of the water. Solid $Cs_3[PMo_{12}O_{40}]$ was obtained by placing the slurry in 50 mL beaker, inside a vacuum desiccator containing dried silica gel, and

applying a vacuum. Over a period of hours to days, a bright yellow powder was obtained. The powder was dried in an oven at 105^{o}C for 1 hour and then calcined at 300^{o}C for a further hour. The preparation is given by equation (1):

$$3Cs_2CO_3 + 2H_3[PMo_{12}O_{40}] \rightarrow 2Cs_3[PMo_{12}O_{40}] + 3CO_2 + 3H_2O \quad (1)$$

$Cs_{2.5}H_{0.5}[PMo_{12}O_{40}]$, $Cs_2H[PMo_{12}O_{40}]$ and $CsH_2[PMo_{12}O_{40}]$: The three compounds containing mixed Cs^+/H^+ cations $Cs_{2.5}H_{0.5}[PMo_{12}O_{40}]$, $Cs_2H[PMo_{12}O_{40}]$ and $CsH_2[PMo_{12}O_{40}]$ were prepared by similar reactions, using the molar amounts given in Table 1.

Table 1. Masses of reagents (g) used in the preparation of $Cs_3[PMo_{12}O_{40}]$, $Cs_{2.5}H_{0.5}[PMo_{12}O_{40}]$, $Cs_2H[PMo_{12}O_{40}]$, $CsH_2[PMo_{12}O_{40}]$, $Ag_3[PMo_{12}O_{40}]$, $Ag_2H[PMo_{12}O_{40}]$, $AgH_2[PMo_{12}O_{40}]$, $Cu_3[PMo_{12}O_{40}]_2$, $Cu_2H_2[PMo_{12}O_{40}]_2$ and $CuH_4[PMo_{12}O_{40}]_2$.

Compound	$H_3PMo_{12}O_{40}$ (g)	Cs_2CO_3 (g)	$AgNO_3$ (g)	$BaCl_2$ (g)	$CuSO_4.5H_2O$ (g)
$Cs_3[PMo_{12}O_{40}]$	12.9892	2.6670	-	-	-
$Cs_{2.5}H_{0.5}[PMo_{12}O_{40}]$	12.8903	2.2025	-	-	-
$Cs_2H[PMo_{12}O_{40}]$	12.8858	1.7700	-	-	-
$CsH_2[PMo_{12}O_{40}]$	5.0075	0.3632	-	-	-
$Ag_3[PMo_{12}O_{40}]$	7.5090	-	1.7083	-	-
$Ag_2H[PMo_{12}O_{40}]$	7.5168	-	1.1389	-	-
$AgH_3[PMo_{12}O_{40}]$	7.5069	-	0.5690	-	-
$Cu_3[PMo_{12}O_{40}]_2$	12.8740	-	-	1.7037	2.1557
$Cu_2H_2[PMo_{12}O_{40}]_2$	12.7432	-	-	1.1247	1.4221
$CuH_4[PMo_{12}O_{40}]_2$	12.5447	-	-	0.5537	0.7006

3.2.2.2 Synthesis of Ag^{+} salts of the $[PMo_{12}O_{40}]^{3-}$ anion

$Ag_3[PMo_{12}O_{40}]$: A sample of $H_3[PMo_{12}O_{40}].\sim 23H_2O$ (7.51 g, 3.35 mmol) (exact water content determined by TGA) was dissolved in 10 mL of deionized water. In another beaker, the required mass of $AgNO_3$ (1.71 g, 10.05 mmol) was dissolved in 5 mL of deionized water and slowly added to the acid solution. The mixture was evaporated to dryness at 50^oC. It should be noted that the evaporation process was performed inside a fumehood, to vent the product HNO_3, which is volatile at 86^oC. The solid yellow $Ag_3[PMo_{12}O_{40}]$ was dried at 105^oC for 1 hour and finally at 300^oC for another hour. The preparation is given by equation (2):

$$3AgNO_3 + H_3[PMo_{12}O_{40}] \rightarrow Ag_3[PMo_{12}O_{40}] + 3HNO_3 \quad (2)$$

$Ag_2H[PMo_{12}O_{40}]$ and $AgH_2[PMo_{12}O_{40}]$: The compounds $Ag_2H[PMo_{12}O_{40}]$ and $AgH_2[PMo_{12}O_{40}]$ were prepared using the same synthetic approach as described above, with the molar amounts shown in Table 1.

3.2.2.3 Synthesis of Cu^{2+} salts of $[PMo_{12}O_{40}]^{3-}$ anion

$Cu_3[PMo_{12}O_{40}]_2$: In a typical preparation, 12.87 g (5.76 mmol) of $H_3[PMo_{12}O_{40}].\sim 23H_2O$ (exact water content determined by TGA) was dissolved in 10 mL of deionized water to form a clear, bright yellow solution. Hydrated copper sulfate, $CuSO_4.5H_2O$ (2.16 g. 8.63 mmol) was added to the solution, which was stirred until the solid dissolved. Solid $BaCO_3$ (1.70 g, 8.63 mmol) was then slowly added with continuous stirring and gentle heating (~30-40^oC), and the solution was heated to 50-60^oC to complete CO_2 generation. On cooling, the mixture was stirred for 1-2 hours and the solid $BaSO_4$ filtered off using a 0.45-µm filter paper. The solid was washed with a small amount of water (~5 mL), which was combined with the original filtrate. A yellow solid material was obtained upon evaporation of the solution in a vacuum desiccator containing silica gel. The yellow product

was dried in an oven at 105^{o}C for 1 hour, and allowed to equilibrate in the atmosphere overnight. This allowed the compound to rehydrate. The preparation is described by equation (3):

$$3CuSO_4 + 3BaCO_3 + 2H_3[PMo_{12}O_{40}] \rightarrow Cu_3[PMo_{12}O_{40}]_2 + 3BaSO_4 + 3CO_2 + 3H_2O \quad (3)$$

$Cu_2H_2[PMo_{12}O_{40}]_2$ and $CuH_4[PMo_{12}O_{40}]_2$: The compounds $Cu_2H_2[PMo_{12}O_{40}]_2$ and $CuH_4[PMo_{12}O_{40}]_2$ were prepared using similar reactions to that described above, with the molar amounts shown in Table 1.

3.2.3 Preparation of gold nanoparticles and their deposition on catalyst support surfaces

The two-phase method was used to prepare the gold nanoparticles. In this method, thiolate is used as a ligand to stabilise the gold nanoparticles from aggregation, yielding particles of diameter ~2.5 nm. Moreover, gold nanoparticles are known to be soluble in organic solvents such as hexane, toluene, *etc.*. Because of the ability of thiolate-stabilised gold nanoparticles to dissolve in these organic solvents, they may be easily used in heterogeneous catalysis to introduce gold nanoparticles onto the catalyst surface and into the pore structure of the catalyst. The synthesis of gold nanoparticles and the preparation of the catalysts of $[PMo_{12}O_{40}]^{3+}$ salts with gold nanoparticles is described below.

3.2.3.1 Synthesis of gold nanoparticles

Gold nanoparticles were prepared by following the Brust-Schiffrin method [12]. Briefly, hydrated $HAuCl_4.3H_2O$ (0.5 g, 1.27 mmol) dissolved in 32 mL of H_2O was added to a solution containing 1.92 g (3.51 mmol) of tetraoctylammonium bromide dissolved in 105

mL of toluene. The mixture was stirred for ~5 minutes, and then the organic phase (which was orange-brown in colour) was isolated using a separatory funnel. *n*-Hexanethiol (1.1 mL, 7.806 mmol) was added to the organic phase, and a colour change from orange-brown to colourless was noted within 5 minutes. The solution was stirred for a further 60 minutes at room temperature. Next, an aqueous solution of $NaBH_4$ was prepared by dissolving 0.5 g (13.21 mmol) of $NaBH_4$ in 32 mL H_2O and added drop by drop to the stirred organic solution. The solution was then stirred for at least 4 hours and generally overnight. The next day, the organic phase was separated from the aqueous phase and the organic solvent removed by using a rotary evaporator, at a low temperature of 45-50^oC, to prevent any partial decomposition of the product. The resulting solid was washed with methanol to remove excess *n*-hexanethiol. The solid was dissolved in *n*-hexane and precipitated with methanol. The solution was decanted off. Finally, the solid was washed with methanol several times and dried in a desiccator over silica gel overnight. The thiolate-stabilised gold nanoparticles were stored in a desiccator.

3.2.3.2 Synthesis of catalyst samples of Cs^+, Ag^+ and Cu^{2+} salts of the Keggin-type $[PMo_{12}O_{40}]^{3-}$ anion containing supported gold nanoparticles

Samples of the catalysts containing gold nanoparticles were prepared using a two-step process. Firstly, the thiolate-stabilised gold nanoparticles were added to the $[PMo_{12}O_{40}]^{3-}$ salts and, secondly, the thiolate shell on the nanoparticles was removed by thermolysis, leaving just the gold nanoparticles.

The first step was accomplished by adding a solution containing the equivalent of 5 mass % of gold nanoparticles in *n*-hexane (0.12 g of thiolate-stabilised gold nanoparticles in about 3 mL of *n*-hexane) to 2.0 g of the selected $[PMo_{12}O_{40}]^{3-}$ salt and thoroughly mixing them by gently stirring with a glass rod until the almost black solution permeated completely

the insoluble catalyst. Each pre-catalyst was then allowed to dry in a fumehood to remove the *n*-hexane. The samples were then heated slowly to 150^{o}C, and then slowly past 220^{o}C so as to thermolyse the thiolate-stabilised gold nanoparticles. The temperature range of 150-220^{o}C was established by TG/DTA of the *n*-hexanethiolate-stabilised gold nanoparticles, which indicated the thermal decomposition temperature (see below). This removed the thiolate ligand and left gold nanoparticles with no stabilizing ligand. This thermolysis must be carried out slowly to avoid aggregation of the resulting gold nanoparticles. The 5 mass % dilution of the gold nanoparticles helps in this regard. The resulting catalysts were calcined at 300^{o}C for 1 hour and characterised to make sure that gold was well dispersed on the surface and in the pore structure of the catalysts using XRD and XPS. The catalysts, both with and without the addition of gold nanoparticles, were used for the partial oxidation of isobutane.

3.3 Characterization of thiolate-stabilised gold nanoparticles, the polyoxomolybdate catalysts, and the catalysts loaded with gold nanoparticles

The prepared thiolate-stabilised gold nanoparticles and the polyoxomolybdate salts and acid salts were characterised using several techniques. These included powder X-ray diffraction (XRD), X-ray photoelectron spectroscopy (XPS), transmission electron microscopy (TEM), scanning electron microscopy (SEM), thermogravimetric analysis and differential thermal analysis (TG/DTA), ultraviolet-visible (*i.e.* electronic) spectroscopy (UV-vis) and infrared spectroscopy (IR).

3.3.1 Preparation and characterization of gold nanoparticles

There are several techniques that are used to characterise and measure the physical properties of these particles including UV-vis spectroscopy, TEM, XPS, and TG/DTA. The

first two techniques provide a measure of the size of the particles, while XPS provides information on the oxidation states of the contributing elements, and the last provides a measure of the composition of the thiolate-stabilised gold nanoparticles, that is the percentage of gold in the nanoparticles, which is important for the preparation of the polyoxomolybdate catalysts with added gold nanoparticles.

3.3.1.1 Synthesis of gold nanoparticles

The Brust-Schiffrin method or 'two-phase' transfer method [13, 14] was used for the preparation of the thiolate-stabilised gold nanoparticles in this study. This synthesis depends on using a thiol to generate thiolate as a ligand to bind strongly with bare gold atoms on the surface of the gold nanoparticles and make them stable to further aggregation. The synthesis begins by transferring an aqueous solution of $HAuCl_4$ to an organic phase (toluene) by using tetraoctylammonium bromide (TOAB), which works as a phase-transfer agent and stabilizer. The aqueous phase is removed. *n*-Hexanethiol, the source if the thiolate ligand (formally *n*-hexanethiolate) is added to the organic solution to replace the TOAB interaction ($AuCl_4^-$.TOAB) with *n*-hexanethiol $(\text{-AuSR-})_n$ and left to stir for at least an hour. This also reduces the Au(III) to Au(I), as evidenced by the change in colour. Following this step, a reducing agent ($NaBH_4$) in aqueous solution is added to the organic solution and left to stir overnight. This effectively reduces the Au(I) to mainly Au(0) (except for the stabilising outer layer of thiolate-stabilsed Au(I) on the nanoparticles [15-17]. The next step involves isolation of the organic phase from the aqueous phase and removal of the solvent (toluene) using a rotary evaporator. Finally, the *n*-hexanethiolate-stabilised gold nanoparticles (NPS) are washed from the remaining (excess) thiol by using excess methanol, and left to dry overnight [16, 18, 19]. The gold NPS may be redissolved in toluene and re-precipitated using methanol several

times to ensure removal of excess *n*-hexanthiol. The synthesis can be described by the following equations [17]:

$$AuCl_4^- (aq) + TOAB (org) \rightarrow AuCl_4^-.TOAB (org) \quad (4)$$

$$AuCl_4^-.TOAB (org) + C_6H_{13}SH (org) \rightarrow (-AuSR-)_n (polymer) (org) \quad (5)$$

$$(-AuSR-)_n (org) + NaBH_4 (aq) \rightarrow Au_x(SR)_y (org) \quad (6)$$

3.3.1.2 UV-visible spectroscopy

A UV-visible spectrum may be used to determine the approximate size of the gold nanoparticles that are prepared. A typical spectrum of the hexanethiol-capped gold nanoparticles prepared in this study is presented in Figure 1, and shows a very weak plasmon band in the visible range from 500-520 nm. This indicates that this synthetic approach has created particles that are less than 5 nm in size. As indicated by Hostetler *et al.*, [20] the size of the particles affects the intensity of the plasmon band, which decreases in intensity gradually with a decrease in the particle size [20, 21]. Careful comparison of the intensity of the plasmon band with the series of spectra provided by Hostetler *et al.* (as reproduced in Chapter 1, Figure 5) shows that the gold nanoparticles are about 2.5 nm in diameter.

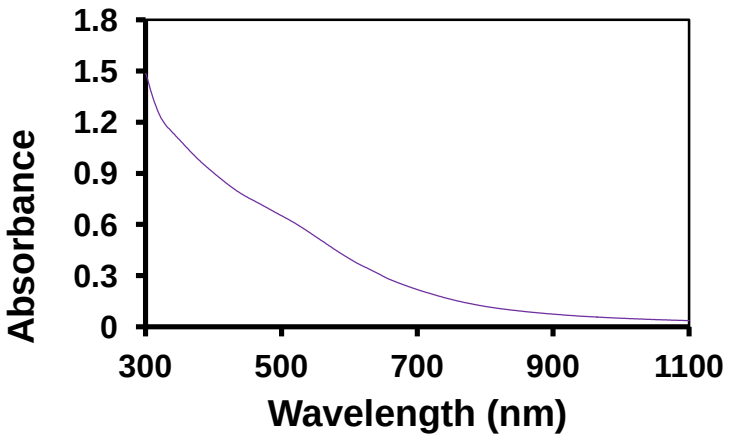

Figure 1. A typical UV-visible spectrum of *n*-hexanethiol-capped gold nanoparticles.

Thus the visible spectra show the sizes of the *n*-hexanethiolate-stabilised gold nanoparticles that are added to the catalyst [22].

3.3.1.3 Transmission electron microscopy

TEM images showed the individual *n*-hexanethiolate-stabilised gold nanoparticles and may also be used to determine the sizes and shapes of the particles. For the TEM sample, a dilute solution was prepared of a small amount of *n*-hexanethiolate-stabilised gold nanoparticles dissolved in a suitable organic solvent (typically *n*-hexane), and dropped onto a thin carbon film and left until the solvent evaporated. The resulting images as shown in Figure 2 indicate spherical shapes and different sizes of particles ranging from about 2 to 5 nm in the top diagram, and about 2 to less than 10 nm in the bottom diagram. It is apparent that in the latter, some aggregation has occurred as the gold nanoparticle solution has dried. This is evidenced by the ring of concentrated particles, where all of the larger particles can be found.

3.3.1.4 Thermogravimetric/differential thermal analysis study

A typical TG/DTA study is shown in Figure 3. It was performed by raising the temperature gradually, thereby allowing the mass ratio of Au:thiolate to be determined. This is important as the amount of gold ultimately added to the catalyst must be known (with the thiolate ligands being removed by thermolysis prior to use of the catalyst). Using a sample of mass 2-4 mg, TG/DTA was performed from 30 to 320^{o}C at a heating rate of 20^{o}C/min using a platinum pan. The second pan contained an approximately equal mass of α-Al_2O_3, which serves as the DTA reference, and has no phase transformations over the temperature range examined. All studies were recorded under an N_2 atmosphere. The thiol started to decompose at 217^{o}C, and gave 81.6% of gold in the *n*-hexanethiolate-stabilised gold nanoparticles. The

decomposition process was exothermic, as shown by the sharp peak at 217^{o}C in the DTA trace. The mass loss varied only from 80 to 84 % for different preparations of *n*-hexanethiol-stabilised gold nanoparticles. No further decomposition occurred up to 600^{o}C. The material remaining after therrmolysis was essentially pure gold, as indicated by its colour.

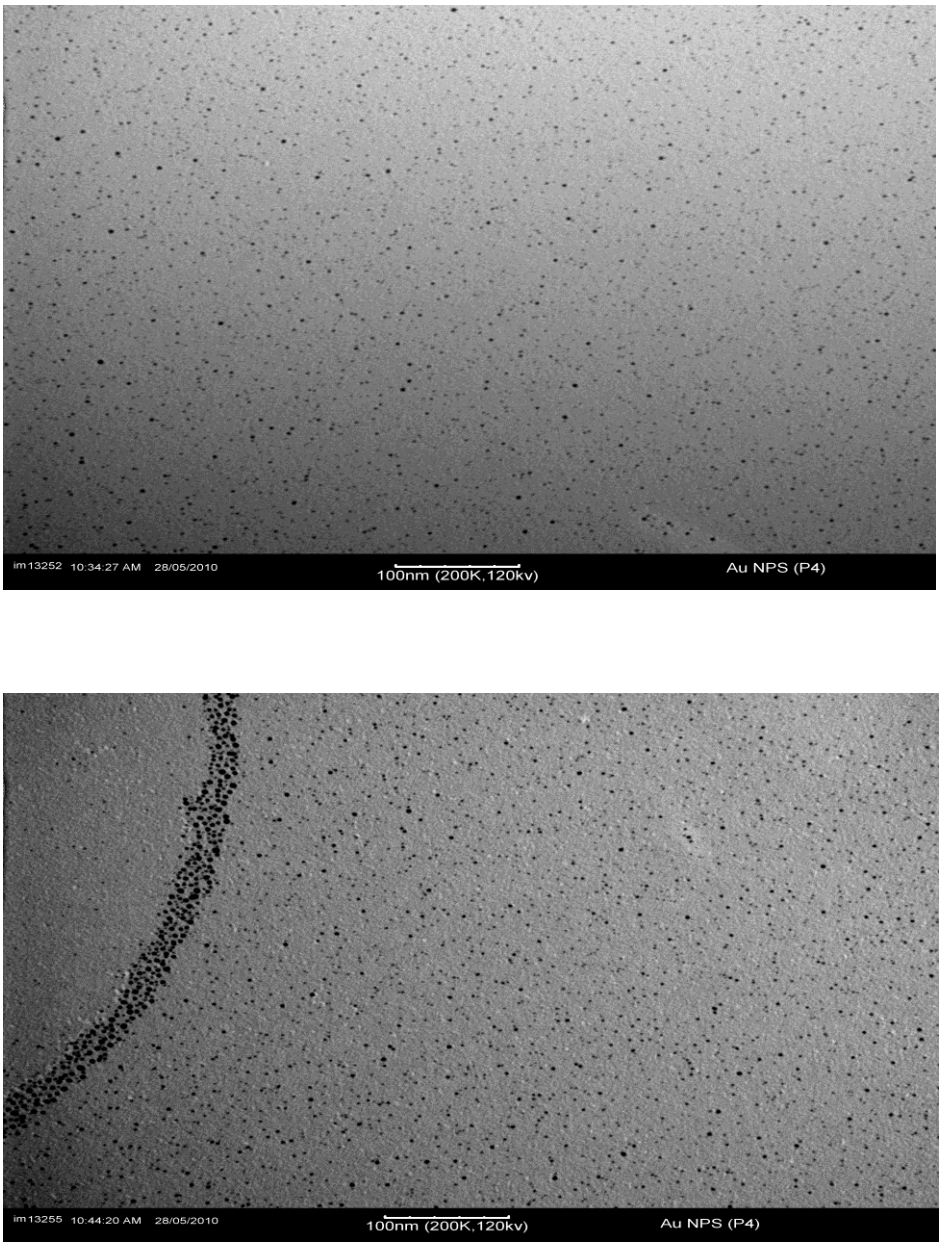

Figure 2. TEM images of *n*-hexanethiolate-stabilised gold nanoparticles.

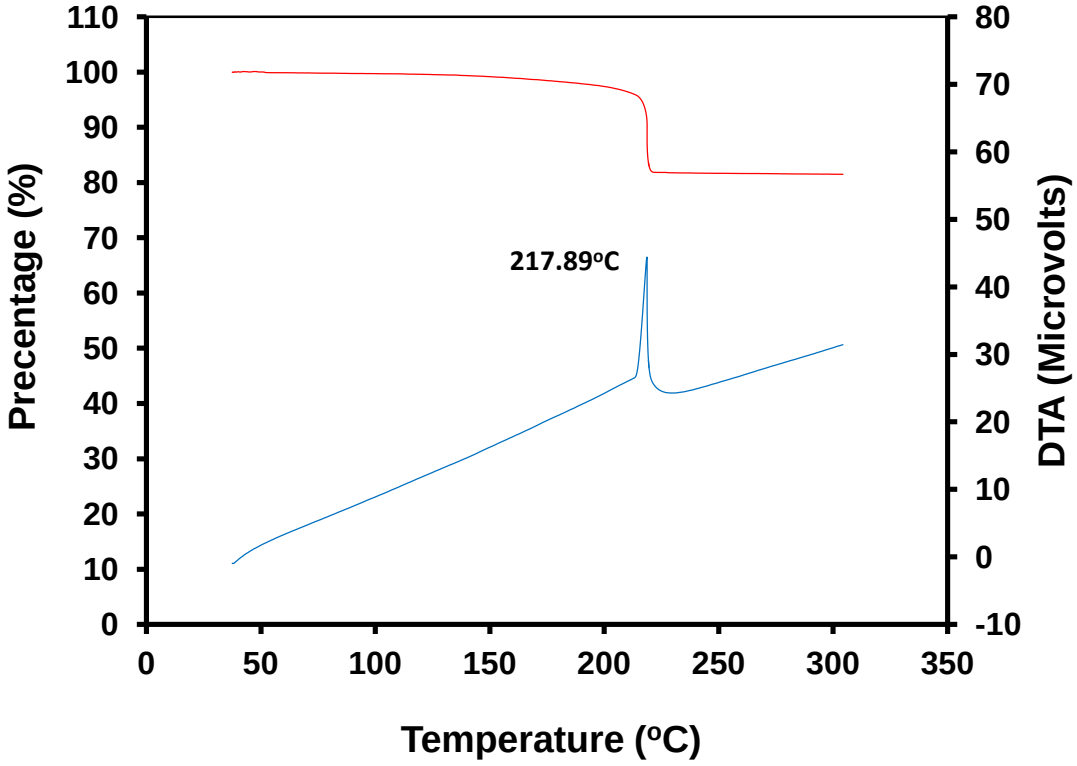

Figure 3. TG/DTA (exothermic: up) curves of *n*-hexanethiol-capped gold nanoparticles.

3.3.1.5 XPS analysis

XPS is a surface analysis technique that measures the presence and electronic valence state of each element on the surface of a solid material. XPS was carried out to determine the valence states of gold nanoparticles stabilised (and covered) by *n*-hexanethiolate ligands. A survey scan is shown in Figure 4. Higher resolution spectra of gold, S and C are presented in Figure 5. These spectra show the binding energies of Au $4f_{7/2}$ at 83.5 eV and Au $4f_{5/2}$ at 87.1 eV. The other spectra are for S which exhibited two peaks, the $2p_{3/2}$ at 161.9 eV and a $2p_{1/2}$ shoulder at 163.7 eV, although the latter is comparable to the noise in the spectrum so that the binding energy may not be accurate. The last spectrum is for C at 284.7 eV, which corresponds to C_{1S} of the alkyl CH_2 and CH_3 groups in the *n*-hexane chain. This peak, equivalent to 'adventitious' carbon found in an XPS spectrum is usually used as the reference

[16, 20, 23, 24]. Notably, Au(I) on the surface associated with the thiolate ligands was not observed. This is consistent with the data on *n*-butane and *n*-pentanethiolate-stabilised gold nanoparticles, which has been reported by Bourg *et al.* [25], and that for dodecanethiolate-stabilised gold nanoparticles, reported by Brust *et al*. [13] The data for the Au $4f_{7/2}$ peak in these species are given in Table 2. As noted by Bourg *et al.* and Brust *et al.*, no evidence for a Au $4f_{7/2}$ peak corresponding to Au(I) is observed, which is found for Au(I) in gold(I) *n*-alkylthiolate compounds at about 84.2-84.9 eV [26]. This has been discussed in depth by Bourg *et al.*, who showed that the surface Au(I)-S bond has strong covalent character and consequently strong electron donation from the sulphur donor atom to the surface Au(I). If Au^{+} and/or Au^{3+} are present in a system, such as following a catalysis study, the Au binding energies for the $4f_{7/2}$ and $4f_{5/2}$ lines will be broadened to higher binding energies, or separate peaks will be observed. This will be discussed below.

Table 2. XPS data on *n*-alkanethiolate-stabilised gold nanoparticles and selected *n*-alkanethiolate-Au(I) compounds.

Compound	Au $4f_{7/2}$ Binding Energy (eV)	Reference
n-hexanethiol Au NPS [a]	83.5	This work
n-butanethiol Au NPS	83.8	[25]
n-pentanethiol Au NPS	83.8	[25]
dodecanethiol Au NPS	83.3	[13]
n-C4S/Au(I) compound	84.4	[25]
n-C5S/Au(I) compound	84.2	[25]
n-C8S/Au(I) compound	84.9	[13]

[a] NPS = nanoparticles.

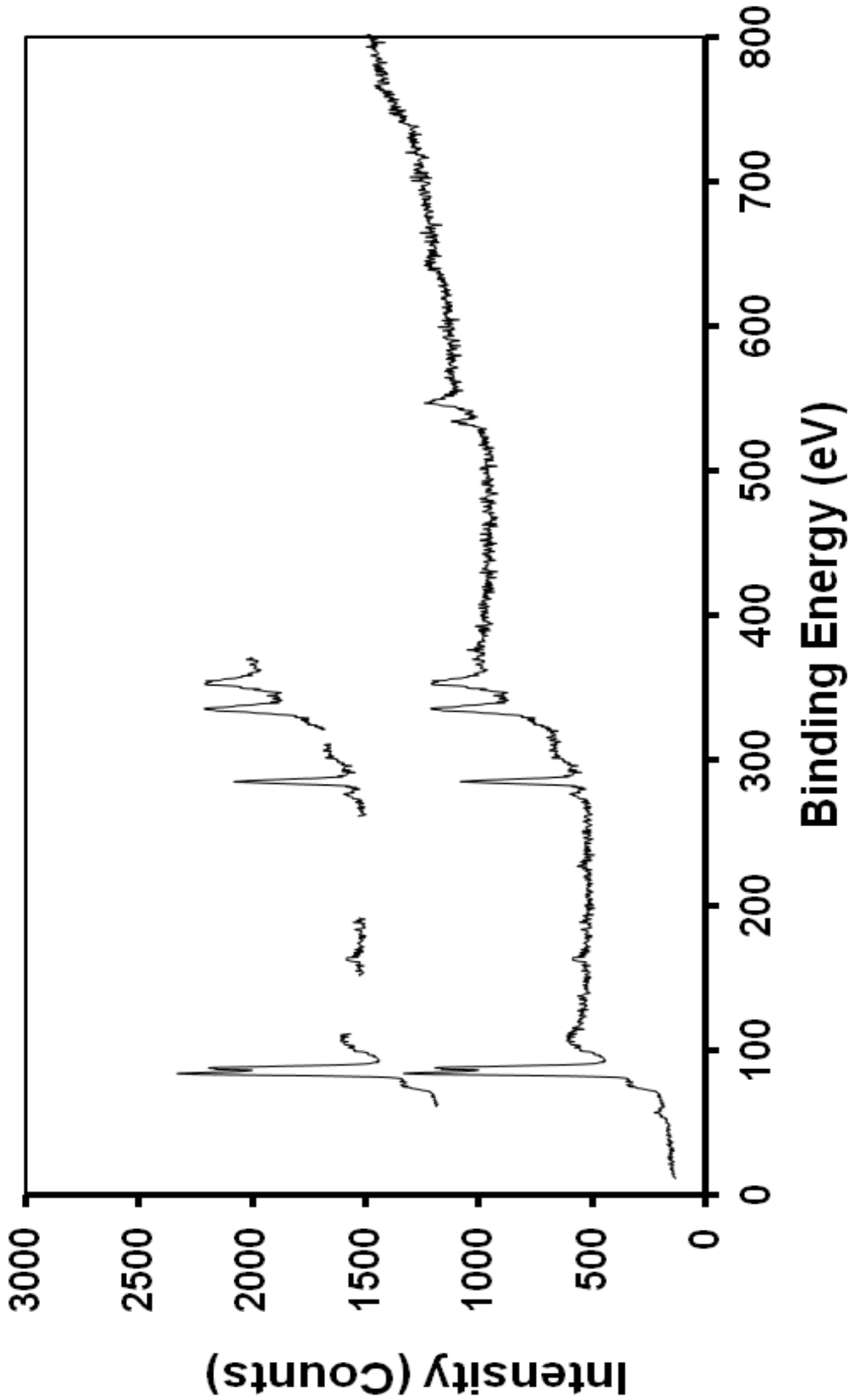

Figure 4. The XPS spectrum (survey scan) of *n*-hexanthiolate-stabilised gold nanoparticles.

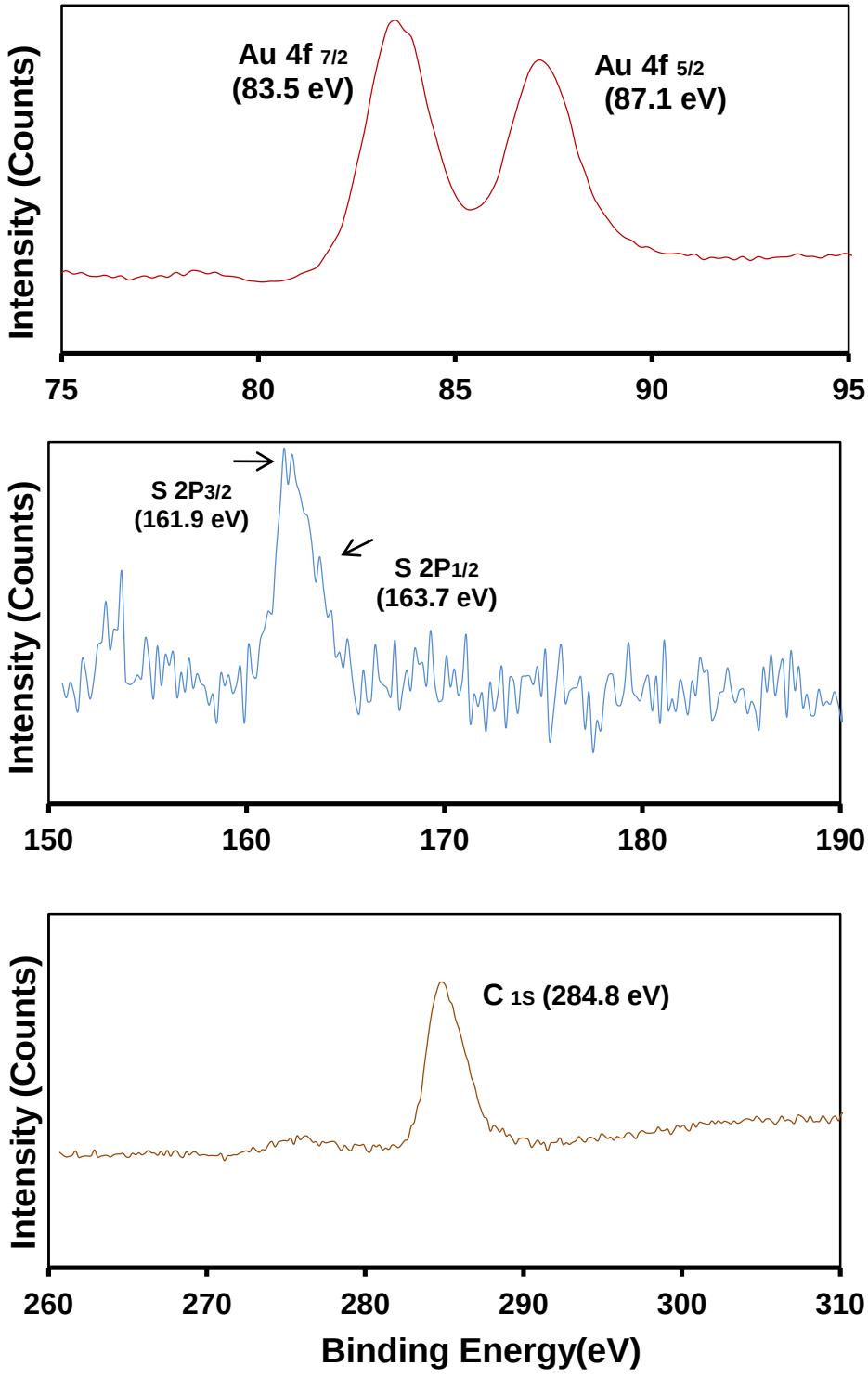

Figure 5. XPS of Au, S and C of *n*-hexanethiolate-stabilised gold nanoparticles.

3.3.1.6 IR spectroscopy

The infrared spectrum of *n*-hexanethiolate stabilised gold nanoparticles is shown in Figure 6. The sample was prepared by dissolving *n*-hexanethiolate-stabilised gold nanoparticles into *n*-hexane and depositing a drop of the solution onto a NaCl plate. The spectrum was run after evaporation of the *n*-hexane solution. The IR spectrum is identical to that reported by Ernst *et al.* [19], and agrees with the data of Hostetler *et al.*, who reported and assigned the IR spectra (KBr discs) of *n*-alkanethiolate-stabilised gold nanoparticles for C3 to C8, C10, C12, C16, C20 and C24 alkanethiolates [27].

3.3.2 Characterisation of the Keggin-type $[PMo_{12}O_{40}]^{3-}$ catalysts with and without gold nanoparticles

3.3.2.1 Infrared (IR) Spectroscopy

The infrared spectral data of the compounds $Cs_{3-x}H_x[PMo_{12}O_{40}]$ (where x = 0, 0.5, 1 and 2), $Ag_{3-x}H_x[PMo_{12}O_{40}]$ (where x = 0, 1 and 2), $Cu_{3-x}H_{2x}[PMo_{12}O_{40}]_2$ (where x = 0, 1 and 2) and $H_3[PMo_{12}O_{40}]$ are given in Table 3. Representative spectra of $Cs_3[PMo_{12}O_{40}]$, $Cu_3[PMo_{12}O_{40}]_2$, $Ag_3[PMo_{12}O_{40}]$ and $H_3[PMo_{12}O_{40}]$, from 1400-400 cm^{-1}, are shown in Figure 7. The samples were prepared by mixing the $[PMo_{12}O_{40}]^{3-}$ salts with dried KBr and then ground via a mortar and pestle into a fine powder, followed by pressing into discs.

The four bands in the $[PMo_{12}O_{40}]^{3-}$ infrared spectra have been assigned as $\nu_{as}(P\text{-}O_a)$, $\nu_{as}(Mo{=}O_d)$, $\nu_{as}(M\text{-}O_b\text{-}M)$ and $\nu_{as}(M\text{-}O_c\text{-}M)$, respectively, where O_a is an internal oxygen atom of the central PO_4 group, O_b and O_c bridging oxygen atoms that are located between, *i.e.* linking, and within the $Mo_{13}O_{13}$ subunits of the $[PMo_{12}O_{40}]^{3-}$ ion and O_d is a terminal oxygen atom of the anion.

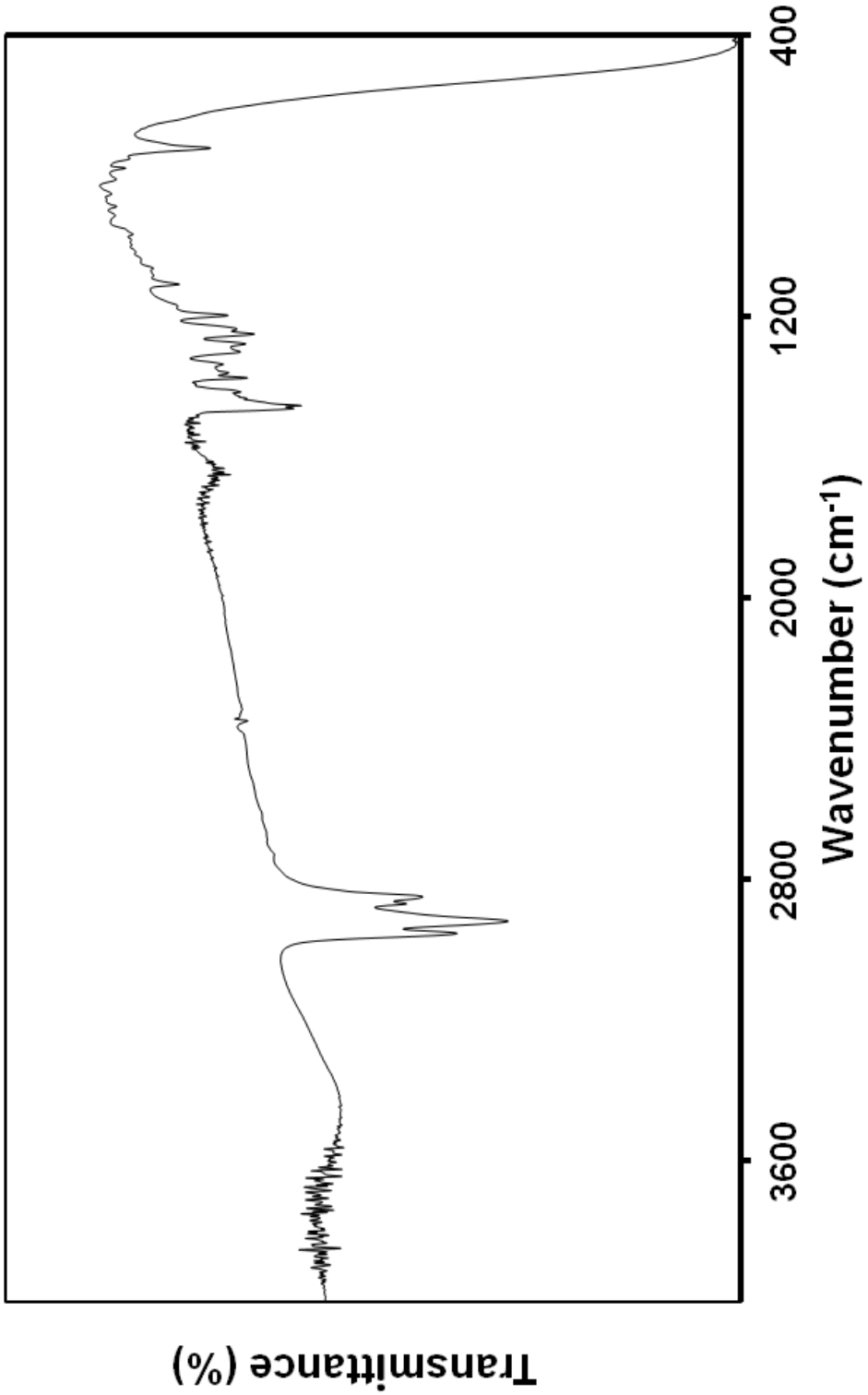

Figure 6. FT-IR of *n*-hexanethiolate-capped gold nanoparticles (sample layered on NaCl plate).

Table 3. The infrared spectral data (cm^{-1}) of the $Cs_{3-x}H_x[PMo_{12}O_{40}]$ (where x = 0, 0.5, 1 and 2), $Ag_{3-x}H_x[PMo_{12}O_{40}]$ (where x = 0, 1 and 2) and $Cu_{3-x}H_{2x}[PMo_{12}O_{40}]_2$ (where x = 0, 1 and 2) salts, and the parent acid $H_3[PMo_{12}O_{40}]$

Compound	ν_{as}(P-O_a) [a]	ν_{as}(Mo=O_d) [a,b]	ν_{as}(M-O_b-M) [a]	ν_{as}(M-O_c-M) [a,c]
$H_3[PMo_{12}O_{40}].\sim 29H_2O$	1064	972sh, 962	870	786br
$Cs_3[PMo_{12}O_{40}]$	1064	973sh, 962	872	785br
$Cs_{2.5}H_{0.5}[PMo_{12}O_{40}]$	1063	972sh, 961	873	786br
$Cs_2H[PMo_{12}O_{40}]$	1063	973sh, 961	869	788br
$CsH_2[PMo_{12}O_{40}]$	1062	976sh, 962	870	788br
$Cu_3[PMo_{12}O_{40}]_2.xH_2O$	1063	975sh, 960	871	788br
$Cu_2H_2[PMo_{12}O_{40}]_2.xH_2O$	1062	976sh, 961	871	784br
$CuH_4[PMo_{12}O_{40}]_2.xH_2O$	1063	974sh, 960	871	784br
$Ag_3[PMo_{12}O_{40}]$	1062	974sh, 960	871	788br
$Ag_2H[PMo_{12}O_{40}]$	1064	976sh, 961	872	785br
$AgH_2[PMo_{12}O_{40}]$	1064	972sh, 962	872	784br

[a] as = asymmetric, [b] sh = shoulder, [c] br = broad

The infrared spectra for all $[PMo_{12}O_{40}]^{3-}$ salts were almost identical in both the ν(P-O) and ν(Mo-O) stretching regions. The assignments have been discussed by Rocchiccioli-Deltcheff *et al.* [28, 29], and Silvani and Burns [30].

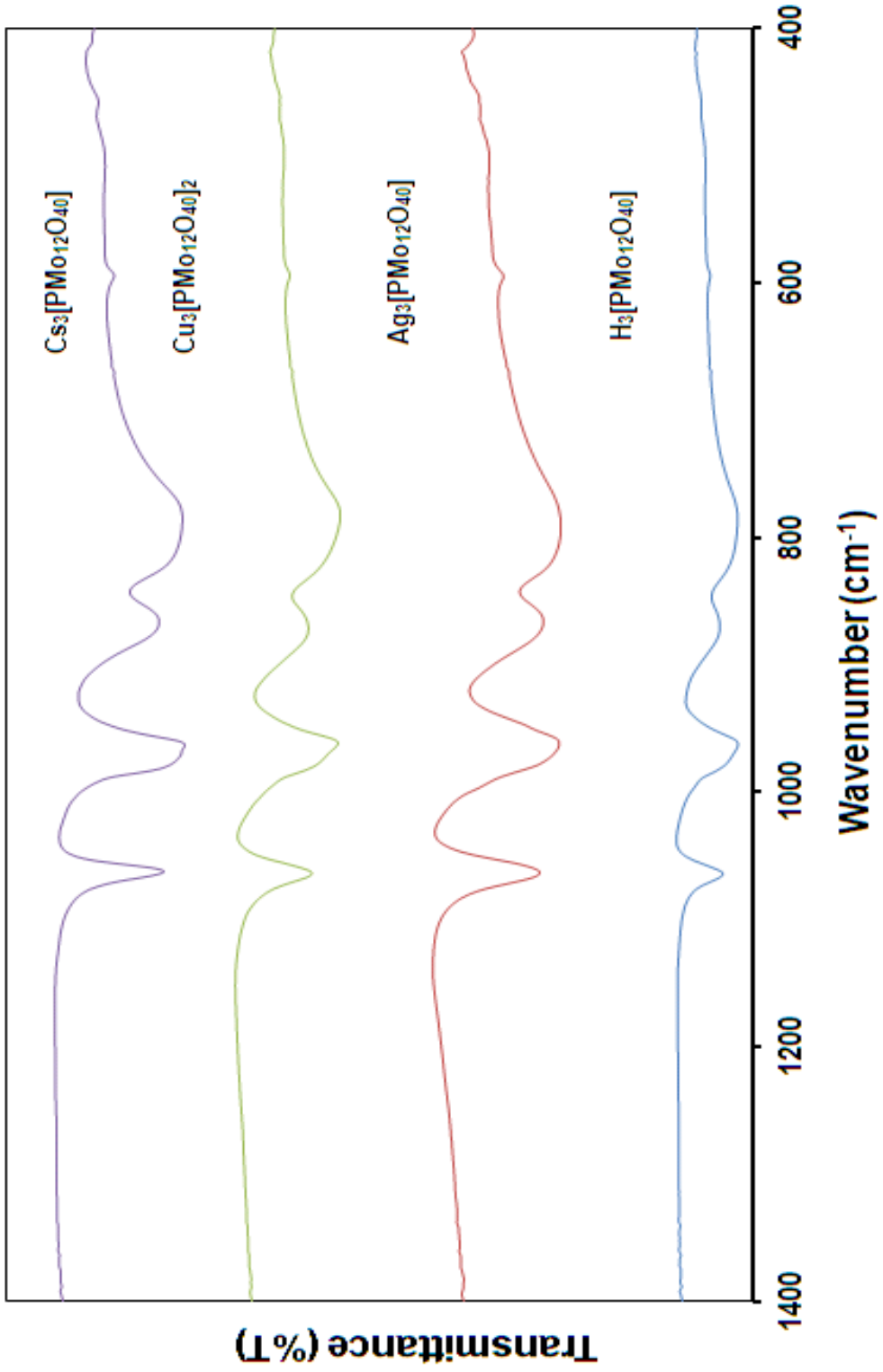

Figure 7. The FT-IR of $H_3[PMo_{12}O_{40}]$, $Ag_3[PMo_{12}O_{40}]$, $Cu_3[PMo_{12}O_{40}]$, and $Cs_3[PMo_{12}O_{40}]$.

More extensive assignments have been given recently by Bridgeman, on the basis of B3LYP density functional calculations using a LANL2DZ basis set [31], although these are in general agreement with the original assignments.

3.3.2.2 SEM investigation

In order to obtain information on the size of the gold nanoparticles loaded onto a phosphopolyoxomolybdate catalyst, a study was undertaken of $Cs_3[PMo_{12}O_{40}]$ both with and without added gold nanoparticles. For comparison, a commercial sample of spherical gold particles (Sigma-Aldrich, 99.9+ %, <10 μm) was physically mixed with a sample of $Cs_3[PMo_{12}O_{40}]$ at 5 mass %, to provide some direct comparison. The SEM image of $Cs_3[PMo_{12}O_{40}]$ is shown in Figure 8. The approximately spherical particles range from about 0.07 to 0.7 μm. Figure 9 shows the image of the commercial gold particles, which exhibits spherical particles ranging from 0.1 to 1.4 μm. Some distances (in nm) have been included in the figure, which illustrate several particle diameters. A 5 mass % loading of the commercial gold particles on $Cs_3[PMo_{12}O_{40}]$ is shown in Figure 10, and the presence of the commercial gold particles is obvious. Finally, Figure 11 illustrates an SEM image of the $Cs_3[PMo_{12}O_{40}]$ after adding gold nanoparticles, with the *n*-hexanethiolate ligands removed by thermolysis. Supported gold nanoparticles were unable to be detected on the surface of the $Cs_3[PMo_{12}O_{40}]$ particles, which indicates that the gold nanoparticles still keep their nano-size and did not aggregate even after release of the *n*-hexanethiolate ligands. Thus an upper limit of 0.04 μm for the size of the gold nanoparticles. As will be shown below, they are in fact, much smaller.

Typical SEM images of $Cu_3[PMo_{12}O_{40}]_2$ and $Ag_3[PMo_{12}O_{40}]$ are shown in Figures 12 and 13, respectively. The crystals for both $Cu_3[PMo_{12}O_{40}]_2$ and $Ag_3[PMo_{12}O_{40}]$ show irregular crystal forms, which vary in size from about 5 to greater than 25 μm for the former, and about 0.4 to 12 μm for the latter.

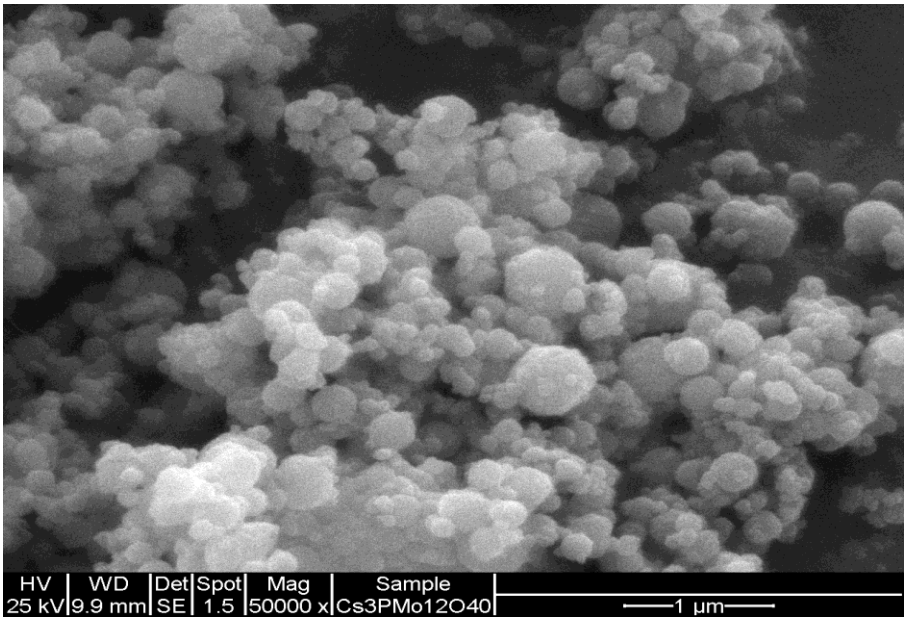

Figure 8. SEM image of $Cs_3[PMo_{12}O_{40}]$.

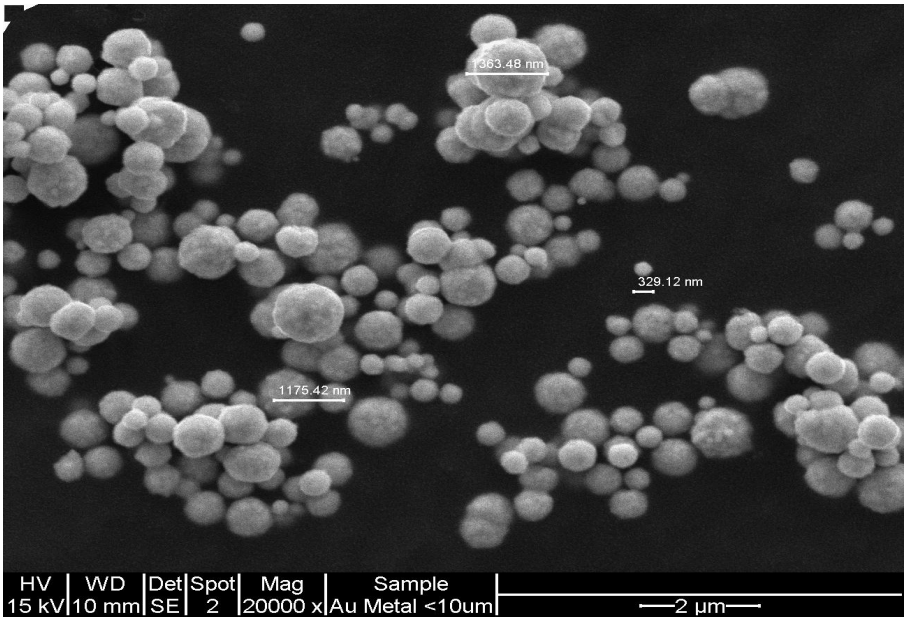

Figure 9. SEM image of gold particles (commercially obtained, <10 μm).

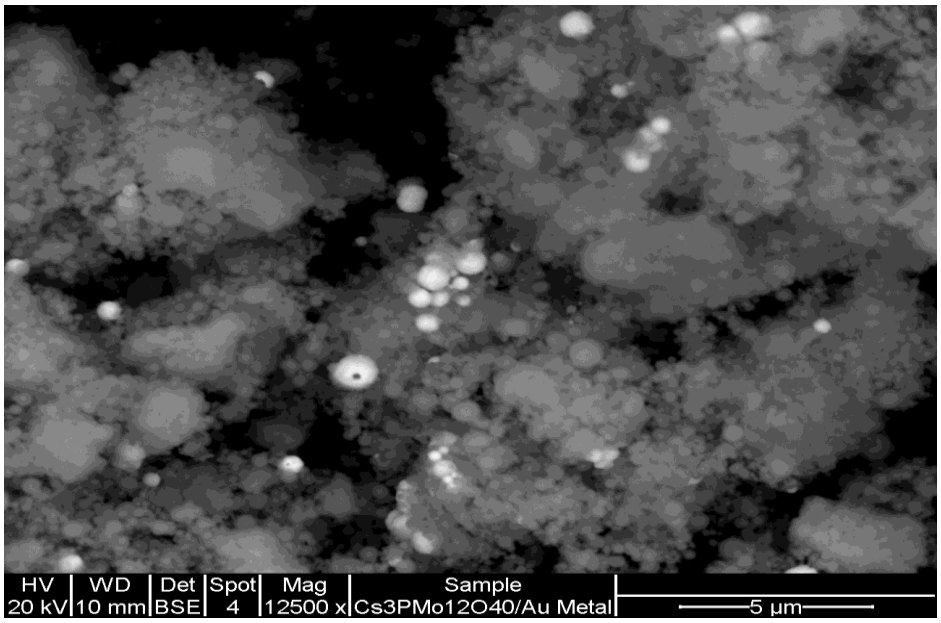

Figure 10. SEM image of gold particles (commercially obtained) supported on $Cs_3[PMo_{12}O_{40}]$

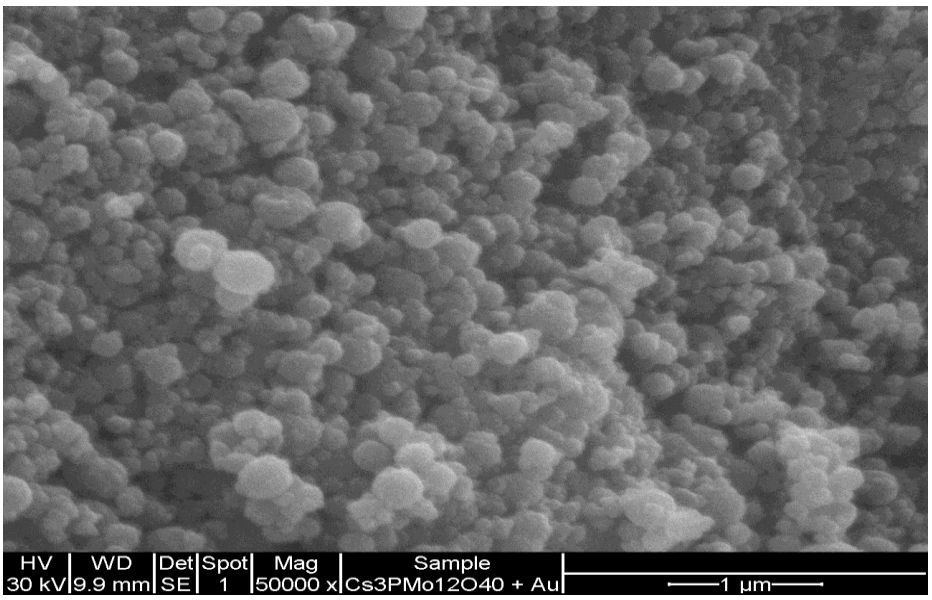

Figure 11. SEM image of gold nanoparticles dispersed on $Cs_3[PMo_{12}O_{40}]$.

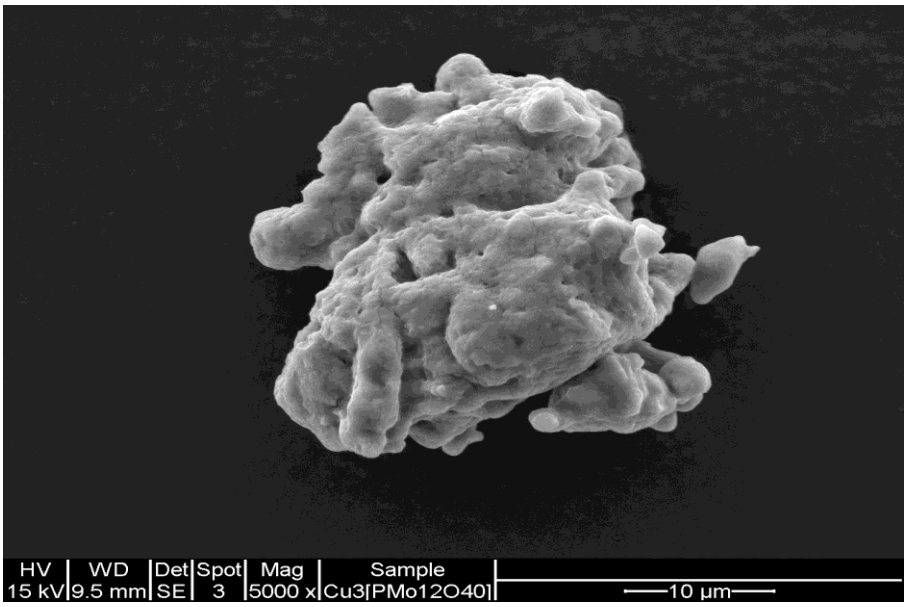

Figure 12. SEM image of $Cu_3[PMo_{12}O_{40}]_2$.

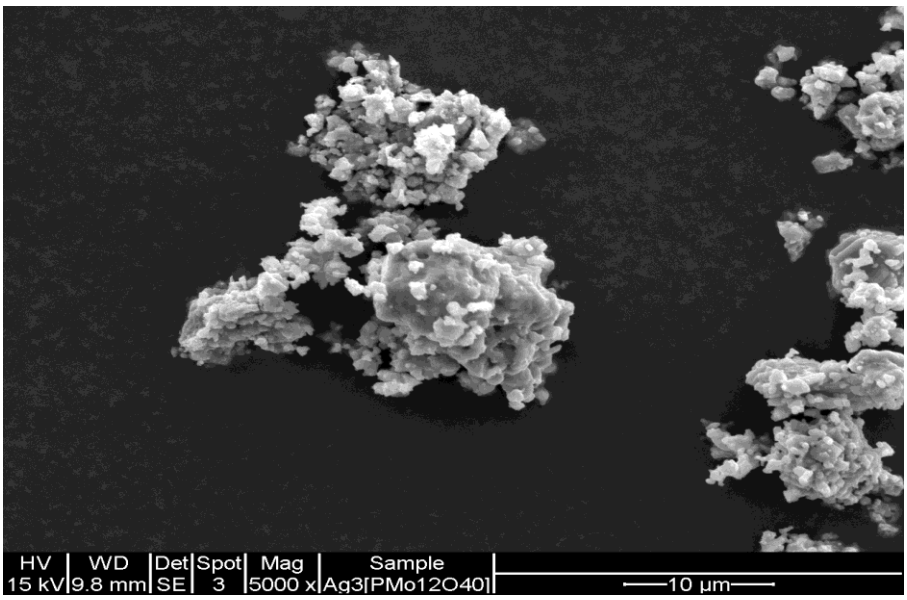

Figure 13. SEM image of $Ag_3[PMo_{12}O_{40}]$.

3.3.2.2 XRD investigations

3.3.2.2.1 XRD studies of $(Cs^+)_{3-x}H_x[PMo_{12}O_{40}]$ (where x = 0, 0.5, 1 and 2), $Cu_{3-x}H_{2x}[PMo_{12}O_{40}]_2$ (x = 0, 1 and 2) and $(Ag^+)_{3-x}H_x[PMo_{12}O_{40}]$ (x = 0, 1 and 2) salts

The X-ray powder diffraction patterns of $(Cs^+)_{3-x}H_x[PMo_{12}O_{40}]$ (where x = 0, 0.5, 1 and 2), $(Ag^+)_{3-x}H_x[PMo_{12}O_{40}]$ (where x = 0, 1 and 2) and $Cu_{3-x}H_{2x}[PMo_{12}O_{40}]_2$ (where x = 0, 1 and 2) are shown in Figures 14, 15 and 16, respectively. The $[PMo_{12}O_{40}]^{3-}$ salts of Cs^+ and Ag^+ are known to crystallise with a cubic unit cell, with a = 11.8412 and 11.9155 Å, respectively, both with space group *Pn*3*m* (224), and *Z* = 2 [32, 33]. Pure phosphomolybdic acid exists in several phases, depending upon the extent of hydration. The fully hydrated acid, $H_3[PMo_{12}O_{40}].\sim29H_2O$ is cubic, with a = 23.31 Å, space group *Fd*3*m* (227) and z = 8 [34]. Lower hydrates, such as the 23- and 13-hydrates have triclinic unit cells [35]. The substitution of a cation in the phosphomolybdic acid affects the diffraction pattern, and depends upon the cation used and the extent of replacement [9, 36].

The XRD patterns in Figure 14 show that the substitution of Cs^+ cation in the $[PMo_{12}O_{40}]^{3-}$ cause a significant structural effect compared with the pure acid. The diffraction patterns agree with those reported by Langpape *et al.* [9]. The mono-substituted of Cs^+ salt, $CsH_2[PMo_{12}O_{40}]$, is actually presented in two distinct phases; however, the more substituted Cs^+ salts, $Cs_2H[PMo_{12}O_{40}]$, $Cs_{2.5}H_{0.5}[PMo_{12}O_{40}]$ and $Cs_3[PMo_{12}O_{40}]$, display only the cubic structure phase, which is attributed to the epitaxial growth of $H_3[PMo_{12}O_{40}]$ on the $Cs_3[PMo_{12}O_{40}]$ phase.

The same phenomenon occurred when protons were partially substituted by Ag^+, as shown in Figure 15.

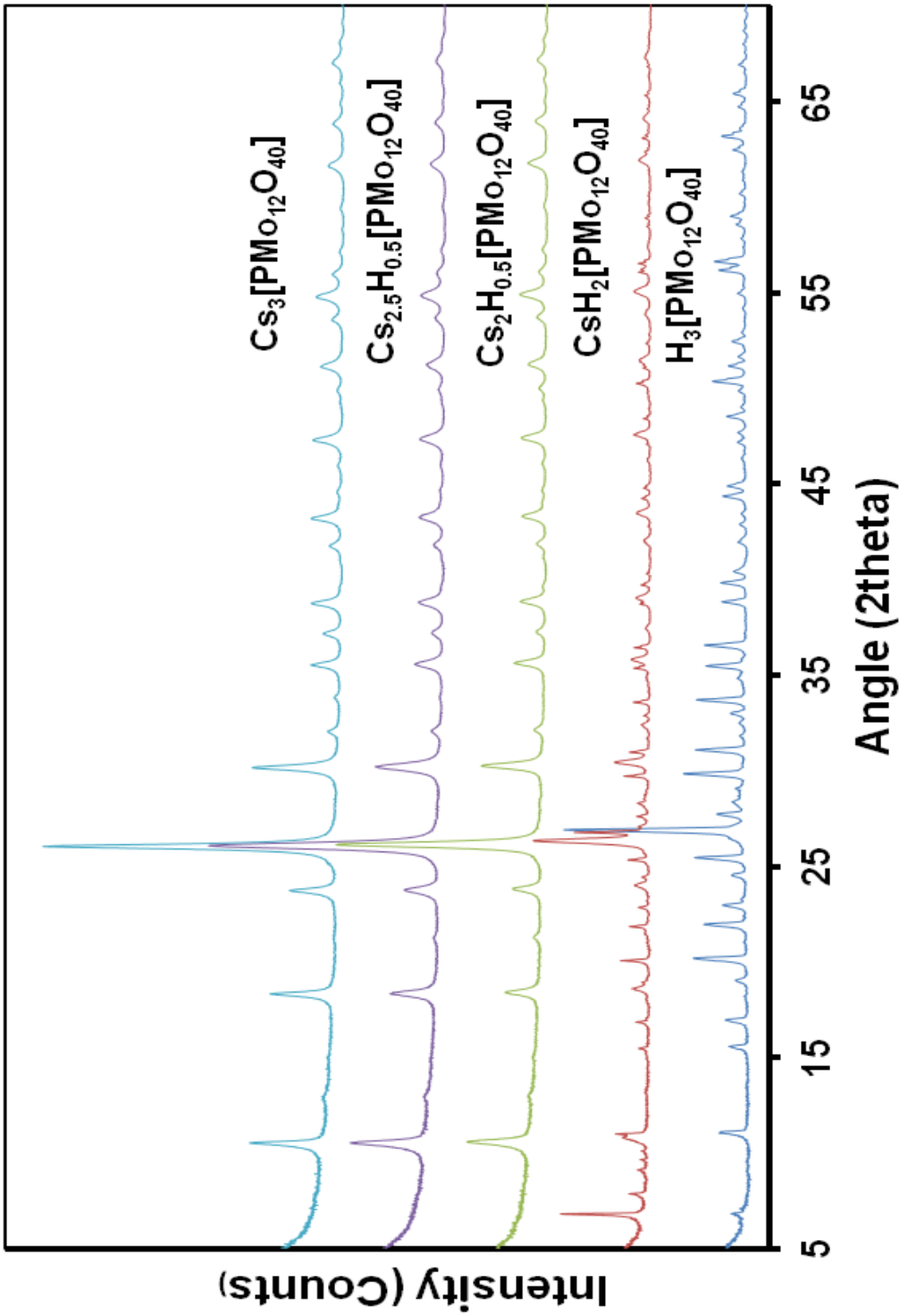

Figure 14. The XRD patterns of $H_3[PMo_{12}O_{40}].XH_2O$, $CsH_2[PMo_{12}O_{40}]$, $Cs_2H[PMo_{12}O_{40}]$, $Cs_{2.5}H_{0.5}[PMo_{12}O_{40}]$ and $Cs_3[PMo_{12}O_{40}]$.

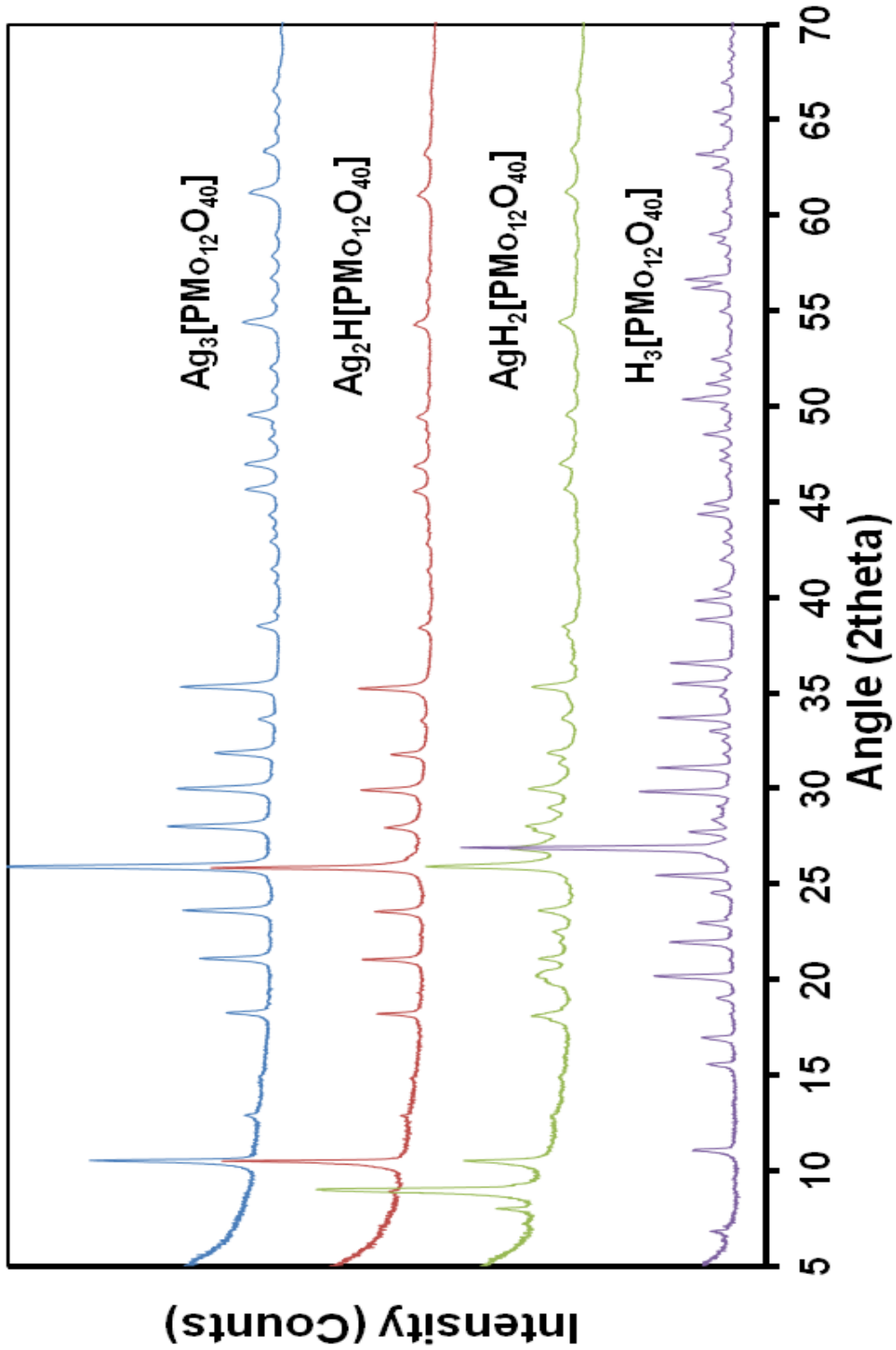

Figure 15. The XRD patterns of $H_3[PMo_{12}O_{40}]$, $AgH_2[PMo_{12}O_{40}]$, $Ag_2H[PMo_{12}O_{40}]$ and $Ag_3[PMo_{12}O_{40}]$.

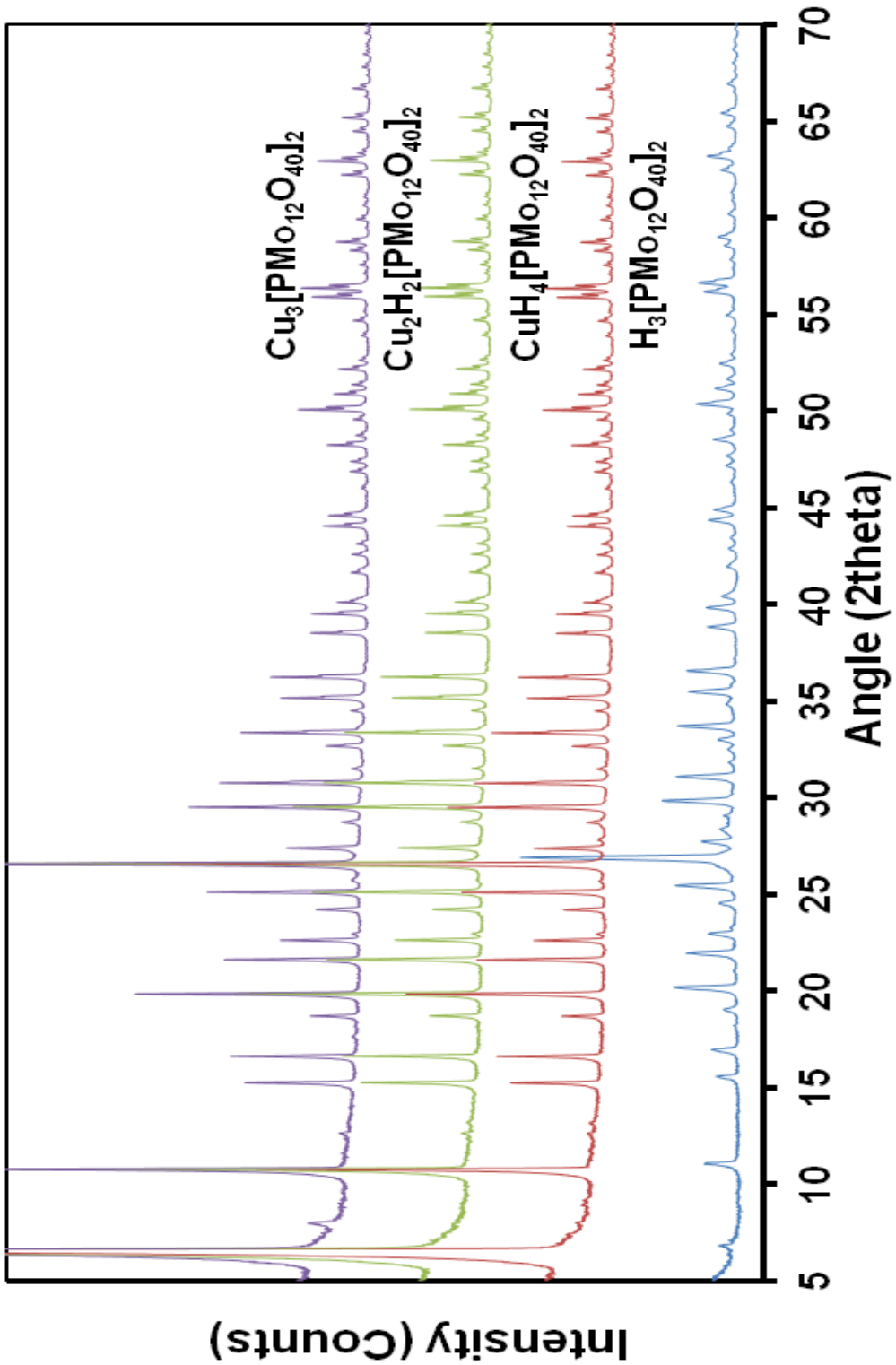

Figure 16. The XRD patterns of $H_3[PMo_{12}O_{40}]$, $CuH_4[PMo_{12}O_{40}]_2$, $Cu_2H_2[PMo_{12}O_{40}]_2$ and $Cu_3[PMo_{12}O_{40}]_2$.

The diffraction pattern of $AgH_2[PMo_{12}O_{40}]$ shows two phases, while only one phase was observable with further substitution of Ag^+, to give, $Ag_2H[PMo_{12}O_{40}]$ and $Ag_3[PMo_{12}O_{40}]$. Comparison of the diffraction patterns of $CsH_2[PMo_{12}O_{40}]$ and $AgH_2[PMo_{12}O_{40}]$ with $H_3[PMo_{12}O_{40}]$ shows some similarity for the Cs^+ containing salt, but none for the Ag^+ salt. The pattern of $H_3[PMo_{12}O_{40}]$ was obtained on acid that had been previously dehydrated and equilibrated at room temperature in air overnight. TG/DTA studies, as discussed below, showed that it contained about 9.9 H_2O per $[PMo_{12}O_{40}]^{3-}$ unit. This suggests that the $H_3[PMo_{12}O_{40}]$ in both $CsH_2[PMo_{12}O_{40}]$ and $AgH_2[PMo_{12}O_{40}]$ absorb water, and for $CsH_2[PMo_{12}O_{40}]$ the water content is ~9.9 H_2O. For $AgH_2[PMo_{12}O_{40}]$ there are no similarities, so it is suggested that the water content is different. It should be noted that the pattern of the acid, $H_3[PMo_{12}O_{40}].\sim 9.9H_2O$ is different to that reported by Langpape *et al.*, for $CsH_2[PMo_{12}O_{40}]$ dried for two weeks over silica gel, which was shown to be triclinic $H_3[PMo_{12}O_{40}].13H_2O$ [9].

The XRD patterns of $Cu_3[PMo_{12}O_{40}]_2$, $Cu_2H_2[PMo_{12}O_{40}]_2$ and $CuH_4[PMo_{12}O_{40}]_2$ are shown in Figure 16. The patterns of all the three Cu^{2+} salts are almost the same. There are two possible explanations. Firstly, all H^+ for Cu^{2+} substitution could simply result in epitaxial growth of $H_3[PMo_{12}O_{40}]$ on $Cu_3[PMo_{12}O_{40}]_2$, so that both $Cu_2H_2[PMo_{12}O_{40}]_2$ and $CuH_4[PMo_{12}O_{40}]_2$ shows epitaxy. Secondly, rather than forming any epitaxial growth, the Cu^{2+}-containing structures $Cu_2H_2[PMo_{12}O_{40}]_2$ and $CuH_4[PMo_{12}O_{40}]_2$ could have the same arrangement of $[PMo_{12}O_{40}]^{3-}$ anions in the unit cell as $Cu_3[PMo_{12}O_{40}]_2$, with H^+ replacing Cu^{2+} and, as two H^+ are required to replace every Cu^{2+}, the remaining H^+ would then likely be disordered within the structure. Of the two possibilities, the latter is most likely. This is because in the first case, when epitaxial growth occurs, such as in the $(Cs/H)_3[PMo_{12}O_{40}]$ and $(Ag/H)_3[PMo_{12}O_{40}]$ systems, the parent compounds, $Cs_3[PMo_{12}O_{40}]$ and $Ag_3[PMo_{12}O_{40}]$ are insoluble and precipitate with no water of hydration and the dehydrated $H_3[PMo_{12}O_{40}]$ has a

unit cell that can be easily distorted to give the cubic unit cell of the former compounds [37]. Hence epitaxial growth is easy to achieve. However, $Cu_3[PMo_{12}O_{40}]_2$ and $H_3[PMo_{12}O_{40}]$ are both soluble in water, and hence no insoluble foundation is available for epitaxial growth, so that $Cu_2H_2[PMo_{12}O_{40}]_2$ and $CuH_4[PMo_{12}O_{40}]_2$ are most likely to have mixed Cu^{2+} and H^+ cations, and are isostructural with $Cu_3[PMo_{12}O_{40}]_2$, likely with disordered cation locations. Examination of the pattern of $H_3[PMo_{12}O_{40}].\sim 9.9H_2O$ shows that it is similar to those of the hydrated $Cu_3[PMo_{12}O_{40}]_2$, $Cu_2H_2[PMo_{12}O_{40}]_2$ and $CuH_4[PMo_{12}O_{40}]_2$ salts. However, the diffraction pattern is shifted to higher angles (*i.e.* increasing 2θ, or a smaller d-spacing). Thus the unit cell is smaller for the hydrated acid than the three hydrated Cu^{2+}-containing compounds. It is likely therefore, that it could form a solid solution with $Cu_3[PMo_{12}O_{40}]_2$ to give the three isostructural hydrated salts $Cu_3[PMo_{12}O_{40}]_2$, $Cu_2H_2[PMo_{12}O_{40}]_2$ and $CuH_4[PMo_{12}O_{40}]_2$, which is consistent with the suggestion given above.

A study of the temperature dependence of the XRD pattern of hydrated $Cu_3[PMo_{12}O_{40}]_2$ was performed up to 340^{o}C, the temperature at which the catalysis studies were made. The XRD patterns were recorded at room temperature, 100, 200, 300 and 340^{o}C. The data are shown in Figure 17. The hydrated $Cu_3[PMo_{12}O_{40}]_2$ was layered using *n*-hexane on the heatable platinum strip of the support. The XRD pattern at room temperature shows several diffraction lines attributable to platinum metal (2θ = 39.6, 46.1 and 67.2^o, ICDD 01-087-0642) [38]. The XRD pattern of platinum is shown in Figure 17. These three lines can be observed at the higher temperatures studied and progressively shift to lower angles as the temperature increases. This is consistent with the thermal expansion of the metal. The XRD pattern at room temperature is different to that presented in Figure 16. This is likely a result of the mounting process. Although hydrated $Cu_3[PMo_{12}O_{40}]_2$ is insoluble in *n*-hexane, the water content is quite variable with temperature (see Section 3.3.2.3 below). Thus mounting the sample likely changed the water content of the hydrated $Cu_3[PMo_{12}O_{40}]_2$.

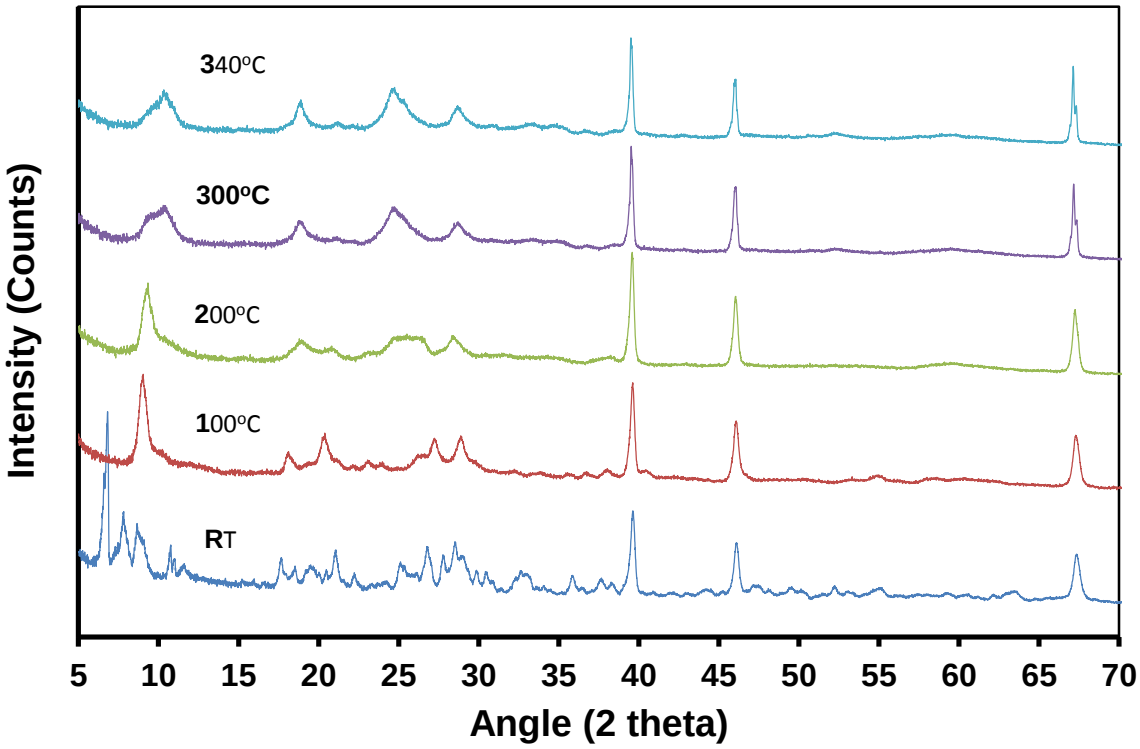

Figure 17. The XRD pattern of hydrated $Cu_3[PMo_{12}O_{40}]_2$ at 25, 100, 200, 300 and 340°C. mounted on the platinum strip.

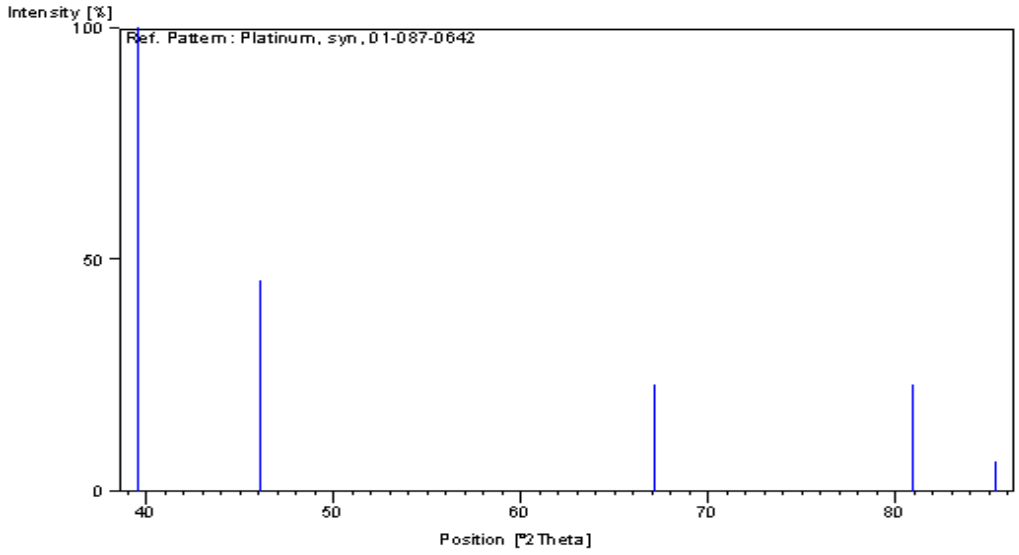

Figure 18. The standard XRD pattern of platinum metal (ICDD 01-087-0642 [38])

At higher temperatures the XRD pattern changes, which is attributable to dehydration of the compound. This will also be discussed in Section 3.3.2.3. It can be seen that by 300^{o}C the diffraction pattern no longer changes, and that at 340^{o}C, the temperature at which the catalysis investigations were performed, the compound is fully dehydrated. The diffraction lines are slightly broadened at high temperature (300-340^{o}C), indicating that the structure is not highly crystalline. It is expected that both hydrated $Cu_2H_2[PMo_{12}O_{40}]_2$ and hydrated $CuH_4[PMo_{12}O_{40}]_2$, as they are isostructural with hydrated $Cu_3[PMo_{12}O_{40}]_2$ as indicated above, would behave in a similar manner. Thus all three compounds $Cu_3[PMo_{12}O_{40}]_2$, $Cu_2H_2[PMo_{12}O_{40}]_2$ and $CuH_4[PMo_{12}O_{40}]_2$, would be completely dehydrated at 340^{o}C. It is known that $H_3[PMo_{12}O_{40}]$ is fully dehydrated above ~150^{o}C (see Section 3.3.2.3), and does not thermally decompose until 370-440^{o}C [30], so the three dehydrated Cu^{2+}-containing compounds will be thermally stable at the catalysis temperature.

3.3.2.2.2 $Cs_3[PMo_{12}O_{40}]$ and $Ag_3[PMo_{12}O_{40}]$ with added gold nanoparticles

The XRD patterns of $Cs_3[PMo_{12}O_{40}]$ and $Ag_3[PMo_{12}O_{40}]$ before and after the addition of gold nanoparticles are shown in Figures 19 and 20, respectively. *n*-Hexanethiolate-stabilised gold nanoparticles were added so as to give a 5 mass % amount of gold. The loaded catalysts were then thermolysed so as to remove the *n*-hexanethiolate ligands around the gold nanoparticles. The patterns are shown only over selected angles where the Au (111) and (200) peaks occur. From an analysis of the width of the peaks, particularly the (111) peak, which is the most intense peak in the gold XRD pattern, an estimate of the sizes of the gold nanoparticles can be obtained using the Scherrer equation.

The patterns of both compounds show weak broad peaks, which appeared after the addition of the gold nanoparticles, and are attributed to the nanoparticles of gold that are dispersed on the surface and in the pore structures of both $Cs_3[PMo_{12}O_{40}]$ and

$Ag_3[PMo_{12}O_{40}]$, after calcination at 300°C for 5 hours. These two patterns provide evidence that gold nanoparticles have been released from the thiolate ligand and are located on the surface and in the pore structures of the supports after calcination.

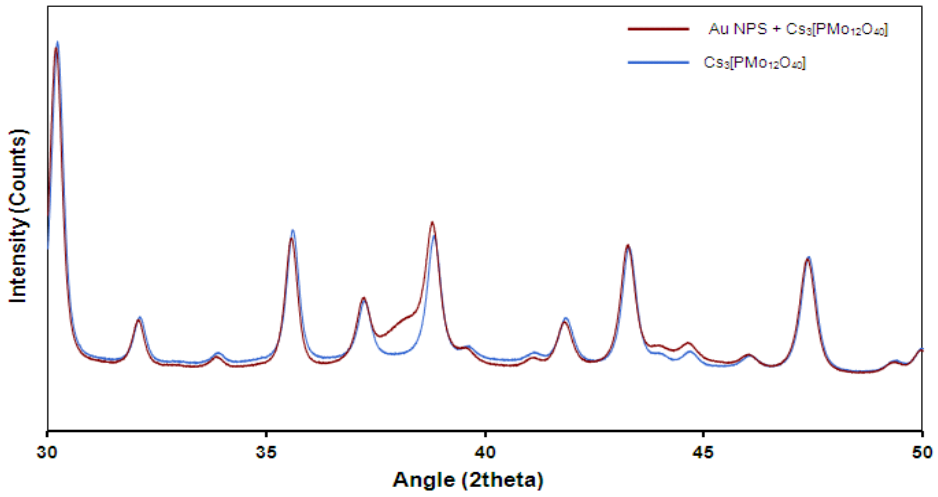

Figure 19. XRD pattern of $Cs_3[PMo_{12}O_{40}]$ before and after the addition of gold nanoparticles.

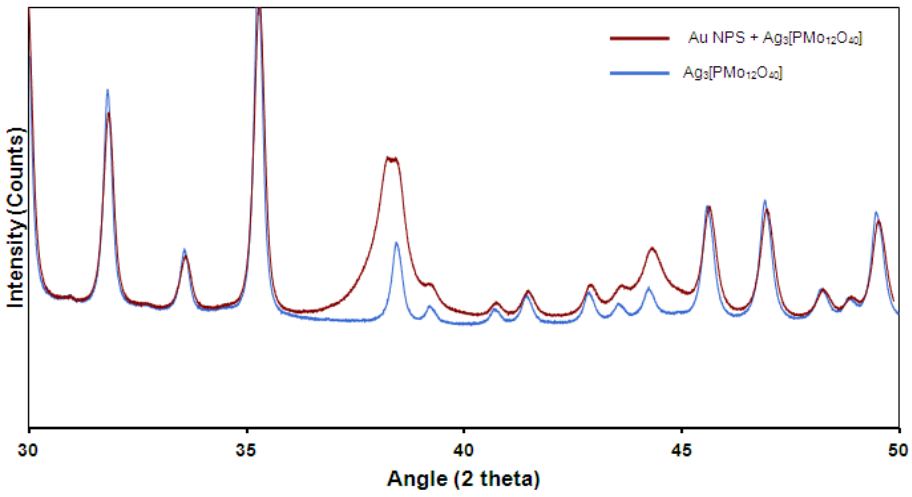

Figure 20. XRD pattern of $Ag_3[PMo_{12}O_{40}]$ before and after the addition of gold nanoparticles.

The (111) reflection is observable at about $2\theta = 38.2^o$ and the (200) reflection at about $2\theta = 44.4^o$. The (111) reflection was used to estimate the size of the gold nanoparticles. The reason that the peaks of the gold nanoparticles appear more intense in the case of

$Ag_3[PMo_{12}O_{40}]$ may be associated with the surface area and pore structure of the two compounds.

For the $Cs_3[PMo_{12}O_{40}]$ system, the XRD pattern of the gold nanoparticles is shown in Figure 21, which may be obtained following subtraction of the diffraction pattern of $Cs_3[PMo_{12}O_{40}]$ from the diffraction pattern of the $Cs_3[PMo_{12}O_{40}]$-Au nanoparticle system. The Scherrer equation allows calculation of the mean crystal diameter $(MCD)_{hkl}$, and is given by:

$$(MCD)_{hkl} = \frac{K\lambda}{\beta\cos\theta} \qquad (7)$$

In this equation K is a constant (= 0.9 × 57.3), λ is the wavelength of the X-rays (Cu $K_{\alpha 1}$ = 1.54060 Å), β is the width of the peak (hkl) at half-height corrected for instrumental broadening, and θ is the Bragg angle. Instrumental broadening was estimated from the LaB_6 reflection at $2\theta = 37.45^o$, which was obtained from a separate XRD study of LaB_6.

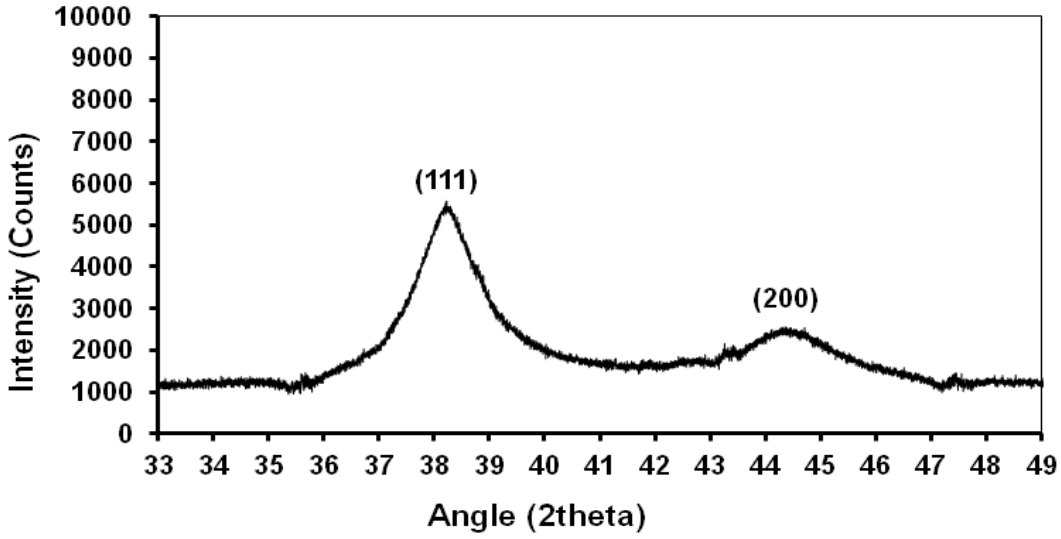

Figure 21. The XRD of gold nanoparticles following the removal of the $Cs_3[PMo_{12}O_{40}]$ diffraction pattern.

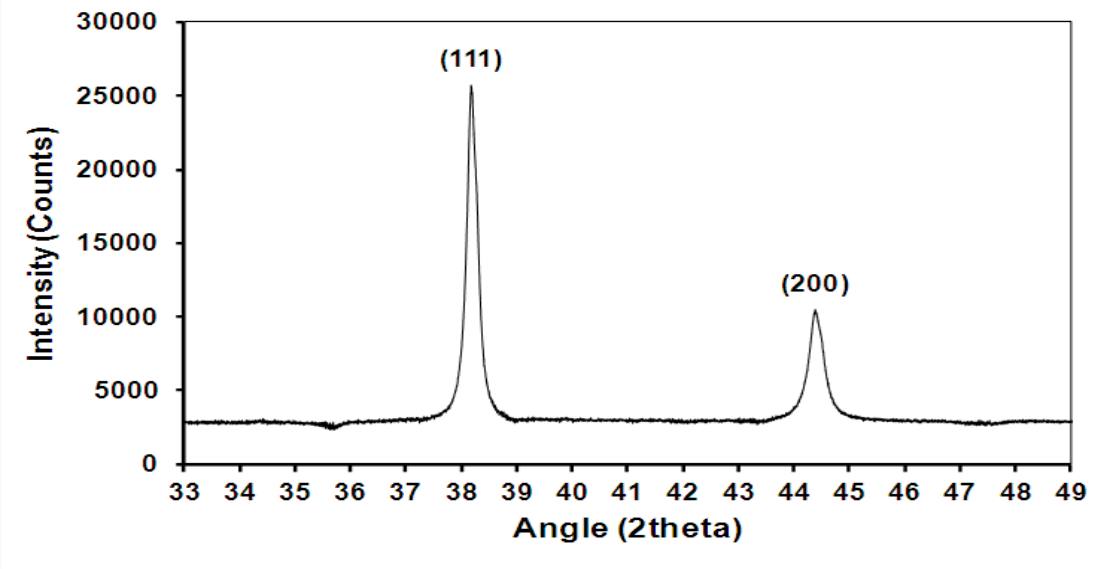

Figure 22. The XRD pattern of gold particles (commercially obtained, <10 μm) following the removal of the $Cs_3[PMo_{12}O_{40}]$ diffraction pattern.

For the Au/$Cs_3[PMo_{12}O_{40}]$ and Au/$Ag_3[PMo_{12}O_{40}]$ systems, the $(MCD)_{hkl}$, or size of the gold nanoparticles, was 6.0 nm in each case. As the original preparation produced *n*-hexanethiolate-stabilised gold nanoparticles of about 2 nm (based on the UV-visible spectrum and TEM studies), some aggregation of gold has occurred. This is not surprising as to remove the stabilising *n*-hexanethiolate ligand, the gold-doped catalyst was heated higher than ~220^{o}C, the temperature at which TG/DTA indicates thermolysis of *n*-hexanethiol-stabilised gold nanoparticles (see Section 3.3.1.4), and was actually calcined at 300^{o}C for 5 hours. This time period was selected based on the time required for the isobutane catalysis to reach a steady state (see below).

A similar study was performed with commercial gold particles (<10 μm) in diameter, which had been physically mixed with on $Cs_3[PMo_{12}O_{40}]$. This is a related study to that which was employed for the SEM studies described above (see Section 3.3.2.2). The

diffraction pattern of $Cs_3[PMo_{12}O_{40}]$ with 5 mass % of added gold particles is shown in Figure 22.

The pattern shows narrow peaks related to large particles of the commercial gold dispersed on $Cs_3[PMo_{12}O_{40}]$. Application of the Scherrer equation gives a particle size of gold of 0.48 nm for the (111) reflection, and 0.11 nm for the (200) reflection. The former best represents the average size of the gold particles, and agrees with the size of the gold particles as shown in the SEM image, Figure 8.

3.3.2.3 TG/DTA Investigation

TG/DTA studies were used to determine the water content per Keggin unit, $[PMo_{12}O_{40}]^{3-}$, in the hydrated salts $Cu_3[PMo_{12}O_{40}]_2$, $Cu_2H_2[PMo_{12}O_{40}]_2$, $CuH_4[PMo_{12}O_{40}]_2$ and, for comparison, $H_3[PMo_{12}O_{40}]$. The results are shown in Figures 23, 24, 25 and 26, respectively.

On heating to a temperature of 220-260^oC the results show that the water content of $Cu_3[PMo_{12}O_{40}]_2$, $Cu_2H_2[PMo_{12}O_{40}]_2$, and $CuH_4[PMo_{12}O_{40}]_2$ were 43.5 , 48.5, and 51.9 H_2O per two $[PMo_{12}O_{40}]^{3-}$ units respectively, or 21.75, 24.25 and 25.95 H_2O per Keggin unit, respectively. All water losses were endothermic. In comparison, the $H_3[PMo_{12}O_{40}]$ had previously been dehydrated at 200^oC for 4 hours, and allowed to rehydrate in the atmosphere for 24 hours. The water content was 9.9 H_2O per $[PMo_{12}O_{40}]^{3-}$ unit. When fully hydrated the acid, $H_3[PMo_{12}O_{40}]$, the Group 1 salts with Li^+ and Na^+ counter-cations, the Group 2 salts with Mg^{2+}, Ca^{2+}, Sr^{2+} and Ba^{2+} counter-cations, as well as the transition metal salts of Mn(II), Co(II), Ni(II), Zn(II) and Cd(II), all have ~29 H_2O per $[PMo_{12}O_{40}]^{3-}$ unit [30, 34, 39, 40].

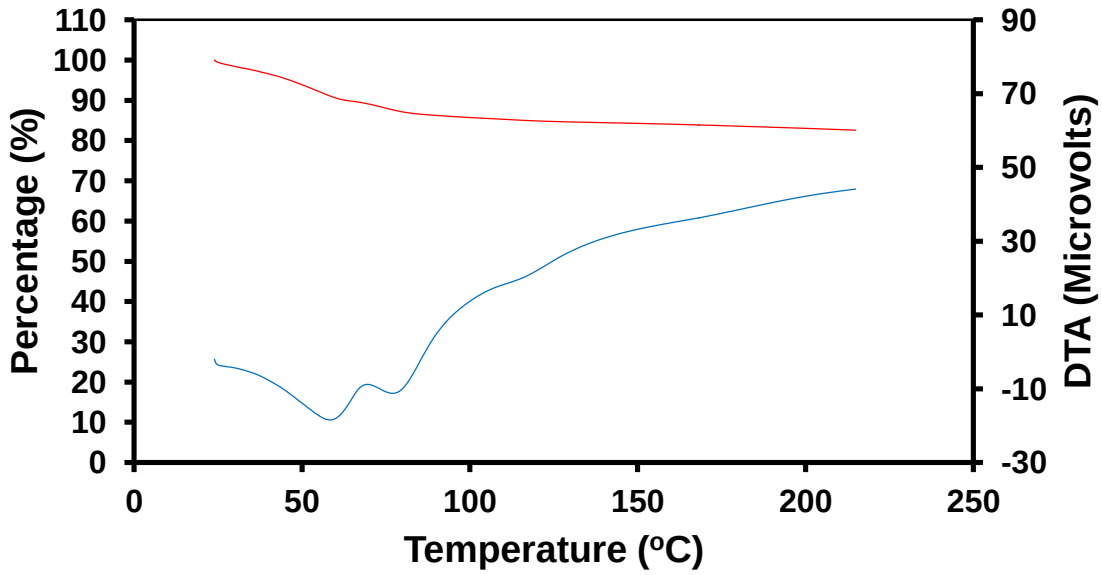

Figure 23. TG/DTA (exothermic: up) profile of $Cu_3[PMo_{12}O_{40}].(43.5)H_2O$.

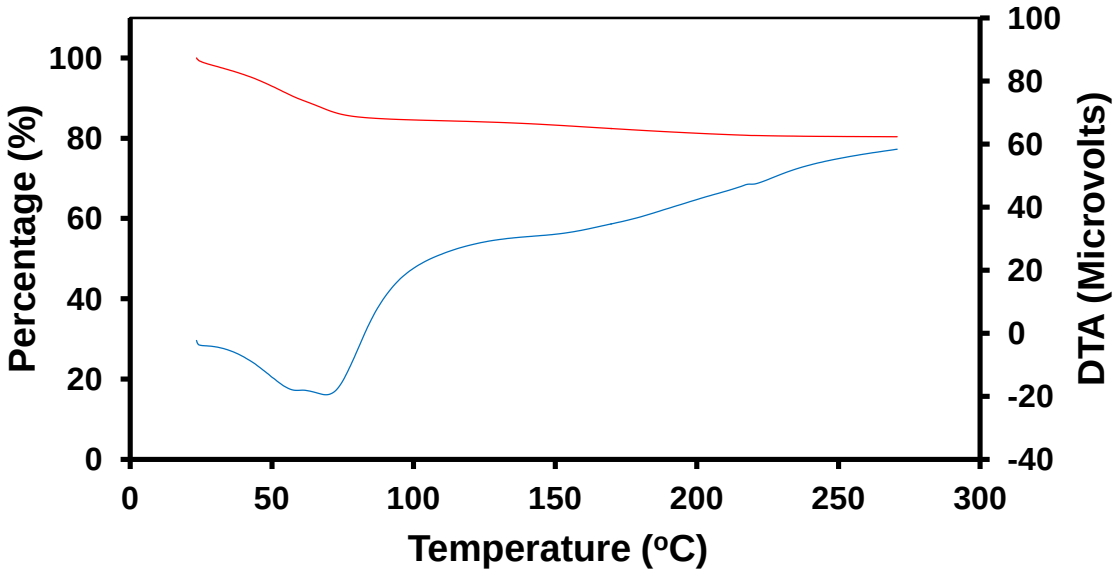

Figure 24. TG/DTA (exothermic: up) profile of $Cu_2H_2[PMo_{12}O_{40}].(48.5)H_2O$.

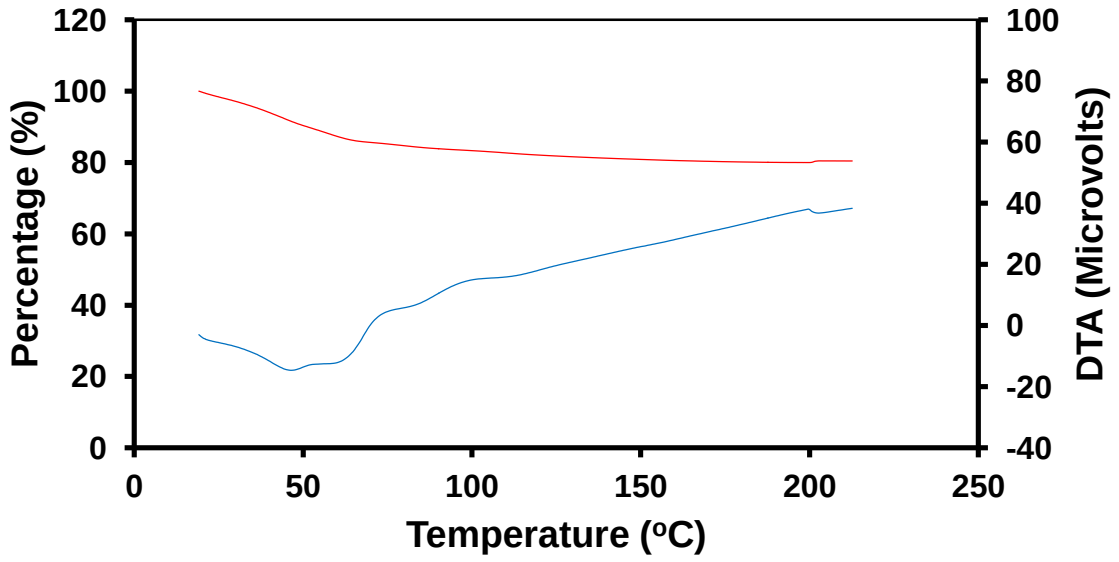

Figure 25. TG/DTA (exothermic: up) profile on $CuH_4[PMo_{12}O_{40}]_2.(51.9)H_2O$

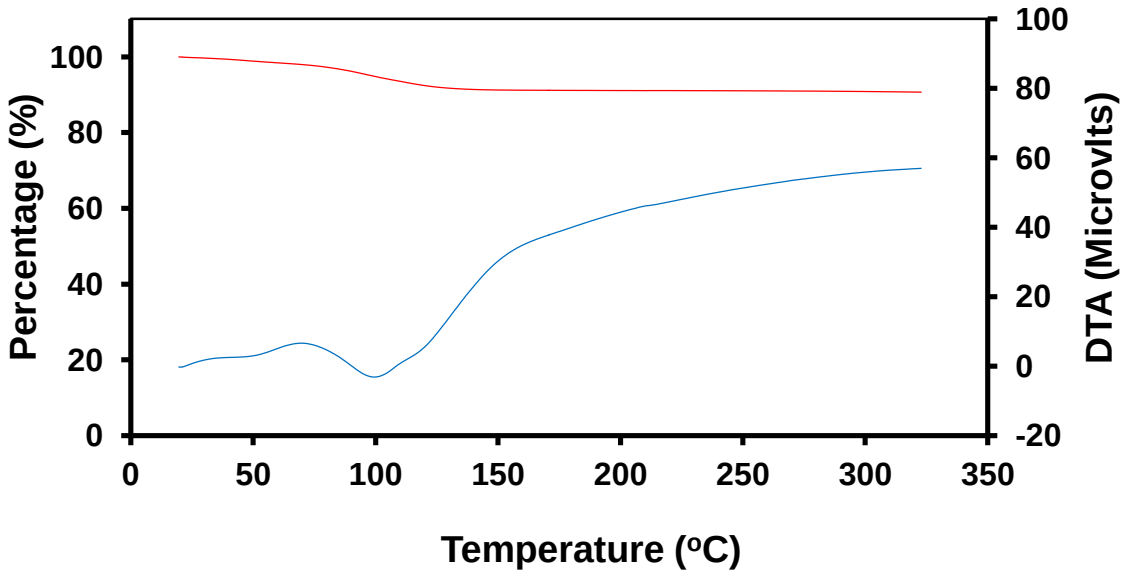

Figure 26. TG/DTA (exothermic: up) profile of $H_3[PMo_{12}O_{40}].(\sim 9.91)H_2O$.

Thus the values for the extent of hydration obtained above for the Cu(II)-containing salts (~21-26 H_2O per $[PMo_{12}O_{40}]^{3-}$ unit) are consistent with this value, as on equilibration in an air atmosphere all of the above salts lose water of hydration, reducing their water content below the value of ~29 H_2O per $[PMo_{12}O_{40}]^{3-}$ unit.

No studies were performed on the Cs^+-containing salts, as these have already been reported by Langpape *et al.* [9] These studies simply show that, except for loss of adsorbed water at <~100^oC, the acid $H_3[PMo_{12}O_{40}]$ on the surface of the $Cs_3[PMo_{12}O_{40}]$ particles, or mixed with the $Cs_3[PMo_{12}O_{40}]$ salt in the case of $CsH_2[PMo_{12}O_{40}]$, just decomposed at >350^oC. The XRD studies given above on the Ag^+-containing salts, $Ag_3[PMo_{12}O_{40}]$, $Ag_2H[PMo_{12}O_{40}]$ and $AgH_2[PMo_{12}O_{40}]$, indicate that these salts are similar to the Cs^+-containing salts, and thus the Ag^+ salts are expected to behave in a similar way, that is by simple decomposition of the $H_3[PMo_{12}O_{40}]$ component in these compounds when this is present.

It is noted that the extent of hydration of $H_3[PMo_{12}O_{40}]$ is about 9.9 H_2O per $[PMo_{12}O_{40}]^{3-}$ unit, which is just a little less than the extent of hydration in $H_3[PMo_{12}O_{40}]$.(13-14)H_2O. The structure of this compound has been reported by D'Amour and Allmann [35]. Further equilibration in moist air for longer periods of time is likely to give a species with this amount of water of hydration.

3.3.2.4 XPS investigation

Another technique that was employed to study the catalysts, both before and after they had been used in the catalysis studies was XPS analysis. Importantly, it provides evidence of the oxidation states of gold supported on the catalyst following a catalysis run.

3.3.2.4.1 XPS study of catalysis prior to use in catalysis studies

Three compounds were chosen to investigate their XPS spectra prior to catalysis studies. These were $Cs_3[PMo_{12}O_{40}]$, $Ag_3[PMo_{12}O_{40}]$ and $Cu_3[PMo_{12}O_{40}]_2$. The data are shown in Table 4, along with data on relevant reference compounds. The latter were chosen so that the anions were oxoanion species, and hence the counter cations experienced an environment similar to the oxo environment of the $[PMo_{12}O_{40}]^{3-}$ ion that the cations experience in the phosphopolyoxomolybdate salts. Also, the reference compound was chosen so that the coordination of the relevant element (in its particular oxidation state) was the same, or as close as possible, to that of the element (*e.g.* Mo(VI)) being studied.

For $Cs_3[PMo_{12}O_{40}]$, $Ag_3[PMo_{12}O_{40}]$ and $Cu_3[PMo_{12}O_{40}]_2$, the XPS data for Cs^+, Ag^+ and Cu^{2+} agree the data on the reference compounds, where available, and provide a base to compare the XPS data on the spent catalysts which will be discussed below. Likewise the data on Mo(VI) agrees well with the XPS data on $(NH_4)_6Mo_7O_{24}.4H_2O$, which contains Mo(VI) in an oxomolybdate environment and with the same octahedral coordination around the Mo(VI).

A survey XPS of $Cs_3[PMo_{12}O_{40}]$ after calcination at 300^{o}C for 5 hours is shown in Figure 27. Figure 28 shows the XPS of $(Au)_{NPS}/Cs_3[PMo_{12}O_{40}]$ after calcination under the same conditions, which produces gold nanoparticles loaded onto the $Cs_3[PMo_{12}O_{40}]$ catalyst. Table 5 lists the XPS data on the $Au_{NPS}/Cs_3[PMo_{12}O_{40}]$ catalyst, as well as the data on gold metal (foil) for comparison. It can be seen that the *n*-hexanethiolate ligand has been thermolysed, and generated gold nanoparticles in the solid. In this analysis, the carbon 1s peak for adventitious carbon was used as a reference, and set to 284.8 eV. Sulfur peaks were not detected on the surface after calcination of the $Au/Cs_3[PMo_{12}O_{40}]$ catalyst at 300^{o}C, which indicates effectively complete removal of the thiolate ligand.

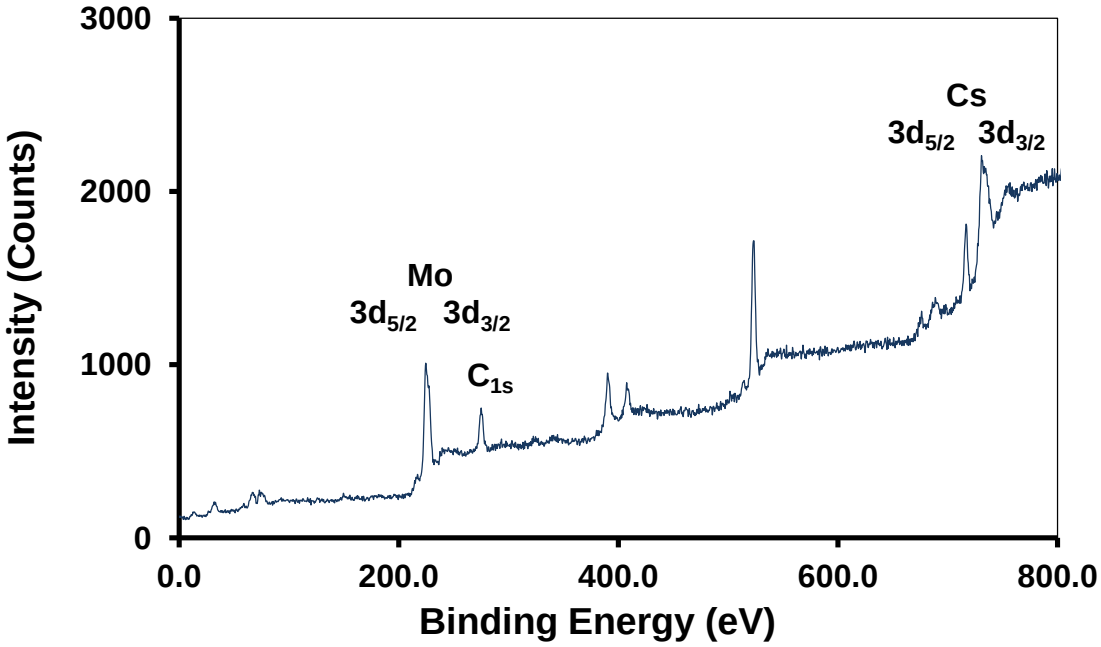

Figure 27. The XPS survey spectrum of $Cs_3[PMo_{12}O_{40}]$ calcined at 300°C for 5 hours.

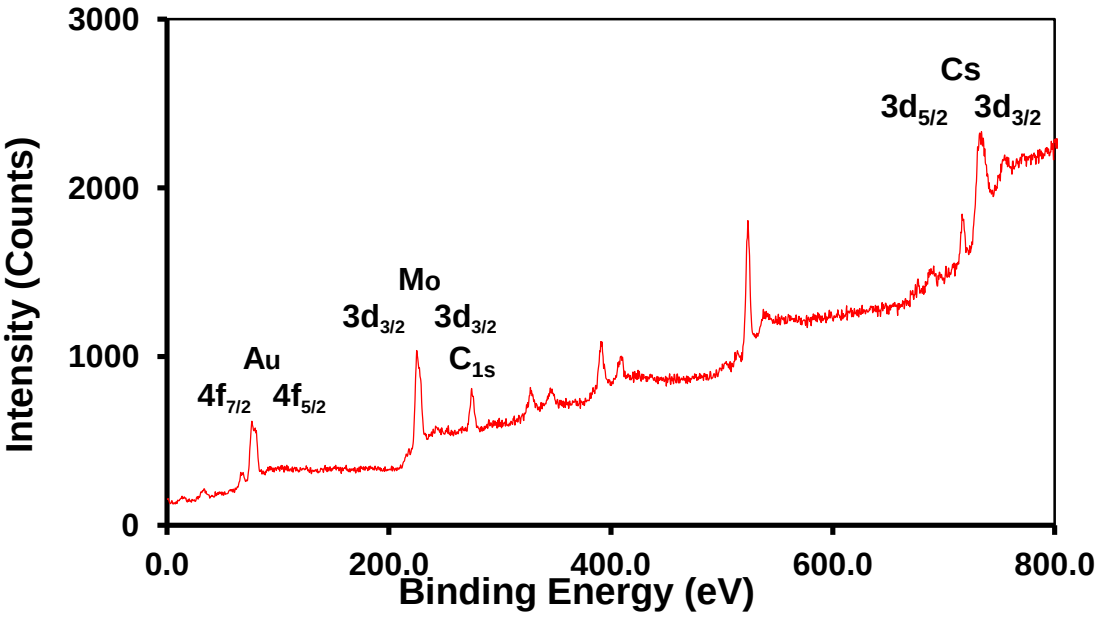

Figure 28. The XPS survey spectrum of $(Au)_{NPS}/Cs_3[PMo_{12}O_{40}]$ following calcination at 300°C for 5 hours.

Table 4. XPS data on $Cs_3[PMo_{12}O_{40}]$, $Ag_3[PMo_{12}O_{40}]$ and $Cu_3[PMo_{12}O_{40}]_2$, and on reference compounds taken from the NIST XPS data base [41].

Compound	Cs Binding Energy (eV)		Ag Binding Energy (eV)		Cu Binding Energy (eV)		Mo Binding Energy (eV)	
	$3d_{5/2}$	$3d_{3/2}$	$3d_{5/2}$	$3d_{3/2}$	$3p_{3/2}$	$3p_{1/2}$	$3d_{5/2}$	$3d_{3/2}$
$Cs_3[PMo_{12}O_{40}]$	724.1	738.1	-	-	-	-	232.9	235.9
$Ag_3[PMo_{12}O_{40}]$	-	-	368.7	374.8	-	-	232.9	236.0
$Cu_3[PMo_{12}O_{40}]_2$	-	-	-	-	934.7	954.7	233.1	236.3
$CsClO_4$	724.2	N/R [a]	-	-	-	-	-	-
$AgNO_3$	-	-	368.2	N/R	-	-	-	-
$Cu(NO_3)_2$	-	-	-	-	935.5	N/R	-	-
$CuCO_3$	-	-	-	-	935.0	N/R	-	-
$(NH_4)_6Mo_7O_{24}$	-	-	-	-	-	-	232.8	235.9

[a] N/R = Not reported

Table 5. The XPS data for Au/$Cs_3[PMo_{12}O_{40}]$, Au nanoparticles and Au metal.

Compound	Au Binding Energy (eV)		Mo Binding Energy (eV)	
	$4f_{7/2}$	$4f_{5/2}$	$3d_{5/2}$	$3d_{3/2}$
$Cs_3[PMo_{12}O_{40}]$/Au nanoparticles (before calcination)	84.3	87.8	232.8	235.3
$Cs_3[PMo_{12}O_{40}]$/Au nanoparticles (after calcination)	84.1	87.3	232.8	235.3
n-hexanethiolate-stabilised Au nanoparticles	83.5	87.1	-	-
Au metal (foil)	84.1	87.7	-	-

3.3.2.4.2 XPS studies of spent catalysts

The XPS data on a selection of the spent catalysts is given in Table 6. Relevant reference compounds taken from the NIST XPS data base are listed in Table 7 [41]. Examples of the curve fitting, using CASA-XPS (version 2.3.16) [42], to the experimental spectra are shown in Figures 29 and 30 for $Ag_3[PMo_{12}O_{40}]$. The curve-fit for the Au 4f spectrum shows two components, separated by 3.6 eV, corresponding to Au(0) and Au(I). The fitting for Mo indicated two components related to Mo(VI) and Mo(V), which are separated by 3.1 and 3.2 eV, respectively. The relative amounts of Mo(VI) and Mo(V) are comparable, which indicates that there is considerable reduction of Mo(VI) at the surface of the catalysts as expected for a phosphopolyoxomolybdate.

All compounds showed the presence of Mo(V) in addition to Mo(VI), which indicated that reduction of the phosphopolyoxomolybdate catalysts occur under the working conditions of the catalytic reactions. XPS data on phosphopolyoxomolybdates as heterogeneous catalysts has been reviewed by Okuhara *et al.* [43], and the data for Mo(VI) and Mo(V) agree with the values presented in the review. More interestingly, however, is the data for gold. All XPS spectra show some oxidation of Au(0) to Au(I), which suggests that the presence of the relatively strong oxidant Au(I) (E^o = +1.69 V [44]) may play a role in the partial oxidation of isobutane and even help determine the selectivities of the products. The XPS data for Ag^+ and Cu^{2+} indicate no evidence for other oxidation states. However, the E^o values [44] for the Ag^+/Ag (E^o = +0.80 V) and Cu^{2+}/Cu^+ (E^o = +0.16 V) or Cu^{2+}/Cu (E^o = +0.34 V) couples are lower than that of Au^+/Au, which might suggest that any reduction of Ag^+ or Cu^{2+} may not be observable in the spent catalysts as they are easily oxidised.

Table 6. XPS data on the spent catalysts, which include $(Au)_{NPS}/Cs_{3-x}H_x[PMo_{12}O_{40}]$ (x = 0, 0.5 and 1), $(Au)_{NPS}/Ag_{3-x}H_x[PMo_{12}O_{40}]$ (x = 0, 1 and 2) and $(Au)_{NPS}/Cu_{3-2x}H_{2x}[PMo_{12}O_{40}]_2$ (x = 0, 1 and 2).

Compound	**Au Binding Energy (eV)**		**Ag Binding Energy (eV)**		**Cu Binding Energy (eV)**		**Mo Binding Energy (eV)**	
	$4f_{7/2}$	**$4f_{5/2}$**	**$3d_{5/2}$**	**$3d_{3/2}$**	**$2p_{3/2}$**	**$2p_{1/2}$**	**$3d_{5/2}$**	**$3d_{3/2}$**
$H_3[PMo_{12}O_{40}]$	83.6 [a] 84.1 [b]	87.4 [a] 87.8 [b]	-	-	-	-	231.9 [c] 232.4 [d]	235.3 [c] 235.5 [d]
$Cs_3[PMo_{12}O_{40}]$	83.6 [a] 84.1 [b]	87.4 [a] 87.7 [b]	-	-	-	-	232.2 [c] 232.5 [d]	236.1 [c] 235.5 [d]
$Cs_{2.5}H_{0.5}[PMo_{12}O_{40}]$	83.4 [a] 85.1 [b]	87.2 [a] 88.9 [b]	-	-	-	-	232.0 [c] 233.3 [d]	235.1 [c] 236.7 [d]
$Cs_2H[PMo_{12}O_{40}]$	83.6 [a] 84.8 [b]	87.9 [a] 88.5 [b]	-	-	-	-	232.1 [c] 233.1 [d]	235.2 [c] 236.3 [d]
$Ag_3[PMo_{12}O_{40}]$	83.5 [a] 84.3 [b]	87.7 [a] 87.2 [b]	367.8	373.8	-	-	233.0 [c] 232.2 [d]	236.1 [c] 235.4 [d]
$Ag_2H[PMo_{12}O_{40}]$	83.8 [a] 84.5 [b]	87.8 [a] 87.4 [b]	367.8	373.8	-	-	233.7 [c] 232.3 [d]	237.0 [c] 235.4 [d]
$AgH_2[PMo_{12}O_{40}]$	83.9 [a] 85.3 [b]	87.6 [a] 88.9 [b]	367.8	373.8	-	-	232.3 [c] 233.0 [d]	235.5 [c] 236.6 [d]
$Cu_3[PMo_{12}O_{40}]_2$	83.7 [a] 85.0 [b]	87.4 [a] 89.0 [b]	-	-	934.4	954.6	233.6 [c] 232.3 [d]	237.0 [c] 235.2 [d]
$Cu_2H_2[PMo_{12}O_{40}]_2$	83.8 [a] 84.2 [b]	87.9 [a] 87.7 [b]	-	-	933.5	954.4	232.1 [c] 232.6 [d]	235.5 [c] 235.8 [d]

[a] Au(0); [b] Au(I); [c] Mo(VI); [d] Mo(V)

Table 7. The reference compounds obtained from the NIST data base [41].

Compound	Au Binding Energy (eV)		Ag Binding Energy (eV)		Cu Binding Energy (eV)		Mo Binding Energy (eV)	
	$4f_{7/2}$	$4f_{5/2}$	$3d_{5/2}$	$3d_{3/2}$	$2p_{3/2}$	$2p_{1/2}$	$3d_{5/2}$	$3d_{3/2}$
Au (foil)	84.1	87.7	-	-	-	-	-	-
$Na[Au^{I}(O_2CCH_2$-$CH(SH)CO_2]$	84.9	N/R [a]	-	-	-	-	-	-
$Au^{I}Cl$	84.60	88.30						
$(Au^{III})_2O_3$	85.9	N/R	-	-	-	-	-	-
$AgNO_3$	-	-	368.2	N/R	-	-	-	-
$Cu(NO_3)_2$	-	-	-	-	935.5	N/R	-	-
$CuCO_3$	-	-	-	-	935.0	N/R	-	-
$(NH_4)_6Mo_7O_{24}$	-	-	-	-	-	-	232.8	235.9
$[PMo_{12}O_{40}]^{4-}$ (H^+ salt) [b]							231.6	234.7

[a] Not reported; [b] Reference [45].

3.4 Catalysis studies

3.4.1 Catalysis studies in the absence of gold nanoparticles – the effects of counter-cations and H^+ on the partial (selective) oxidation of isobutane

The selective oxidation of isobutane over phosphopolyoxomolybdate catalysts produces methacrolein, methacrylic acid, acetic acid, isobutyric acid, CO, CO_2 and H_2O. The stoichiometric reactions can be written as follows, where n[O] represents a lattice oxygen:

$$C_4H_{10} \xrightarrow{3[O]} CH_2{=}C(CH_3)COH + 2H_2O$$

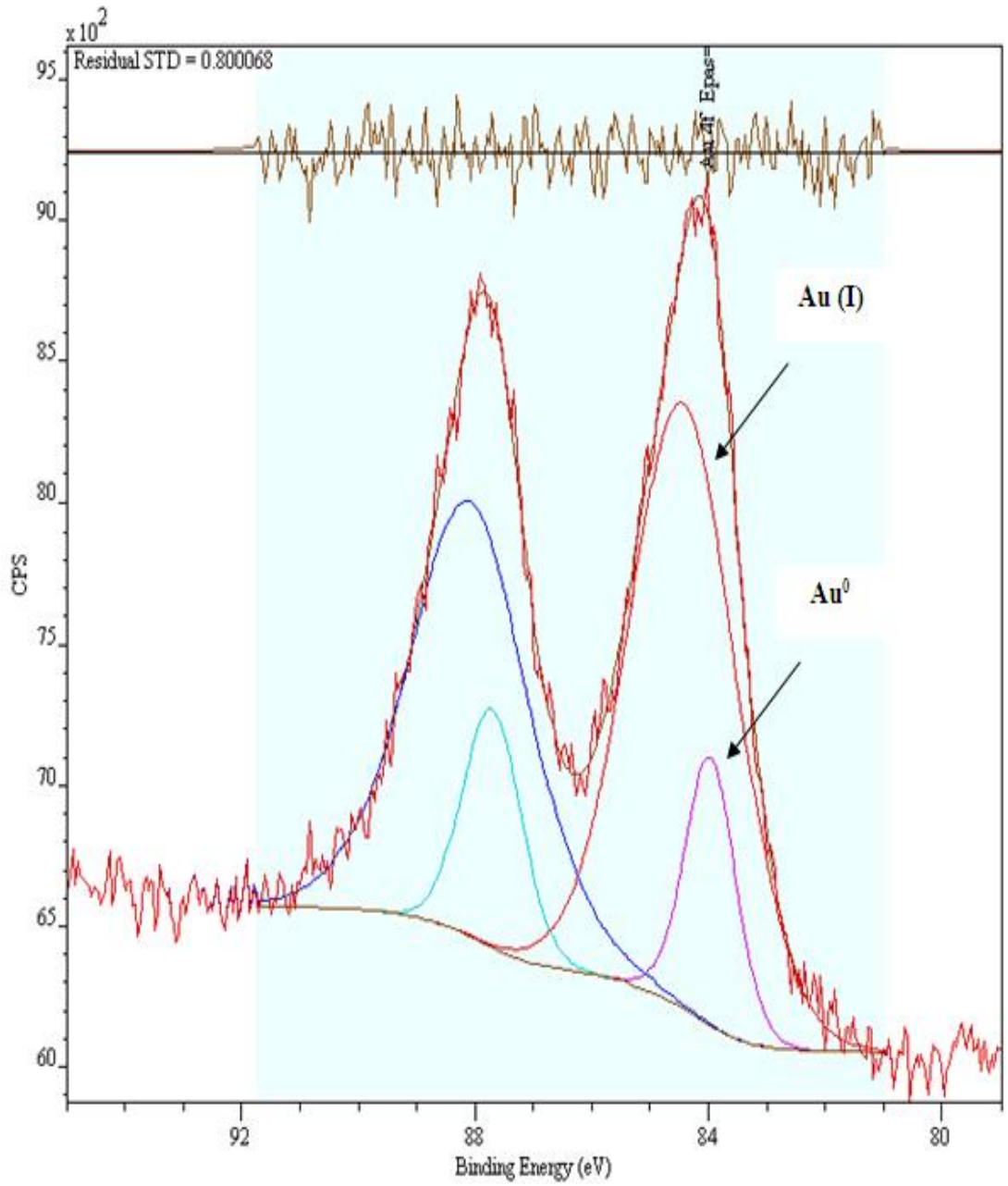

Figure 29. The curve fit analysis of the XPS spectrum for the Au $4f_{7/2}$ and $4f_{5/2}$ levels in $Ag_3[PMo_{12}O_{40}]$

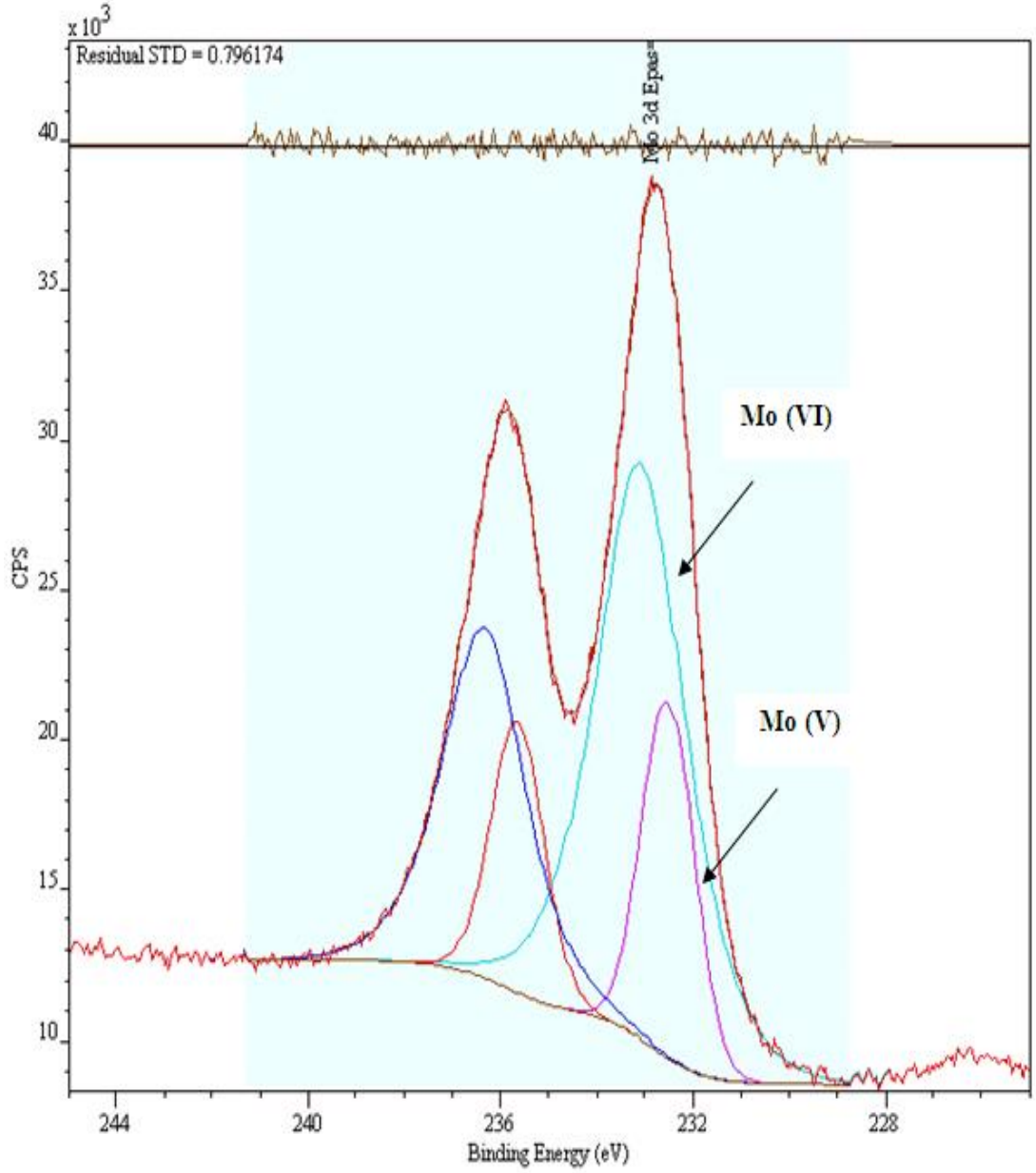

Figure 30. The curve fit analysis of the XPS spectrum for the Mo $3d_{5/2}$ and $3d_{3/2}$ levels in $Ag_3[PMo_{12}O_{40}]$

$$C_4H_{10} \xrightarrow{4[O]} CH_2=C(CH_3)COOH + 2H_2O$$

$$C_4H_{10} \xrightarrow{5[O]} 2CH_3COOH + H_2O$$

$$C_4H_{10} \xrightarrow{3[O]} (CH_3)_2CHCOOH + H_2O$$

$$C_4H_{10} \xrightarrow{9[O]} 4CO + 5H_2O$$

$$C_4H_{10} \xrightarrow{13[O]} 4CO_2 + 5H_2O$$

There are several other reactions that could occur over the phosphopolyoxomolybdate catalysts used in the present study, involving some of the products of the above reactions. Methacrolein could be oxidised to methacrylic acid, with the formation of acetic acid, CO and CO_2 as side products [1], while isobutyric acid could be oxidatively dehydrogenated to methacrylic acid, with the formation of propene, CO and CO_2 as side products [2, 3]. The first reaction requires long contact times of 2-5 s [1, 46], which are similar to the contact times used in the present work (2.7-4.1 s, Chapter 2), and this suggests that some oxidation of methacrolein could occur. However, the methacrolein has to form initially and this involves the introduction of a C=C bond and addition of an oxygen atom into the isobutane, which are likely to be sequential and thus relatively time consuming steps. In the case of the oxidative dehydrogenation of isobutyric acid, GC and IR spectroscopic analyses of the gas phase products could find no evidence of propene formation (*e.g.* a ν(C=C) band). Thus it is unlikely that these two reactions will occur to any great extent, and that they will make a major contribution to the products. Other reactions could include the full oxidation of any of the organic products to CO and CO_2, but it is assumed that these may make only a minor contribution to the overall formation of CO and CO_2 as the organic product precursors have to form first.

The partial (selective) oxidation reaction of isobutane involves both oxidation reactions (addition of oxygen to produce oxygenated products), and oxidative dehydrogenation reactions (to form unsaturated sites in some products, *i.e.* methacrolein and methacrylic acid). In general, oxidation reactions using phosphopolyoxomolybdates, such as the oxidation of methacrolein to methacrylic acid depends on the surface area of the catalyst [43, 46], while oxidative dehydrogenation reactions, such as the oxidative dehydrogenation of isobutyric acid to methacrylic acid and isobutraldehyde to methacrolein [1, 4], follow a Bulk Catalysis Type-II mechanism, where only the mass of the catalyst is important and not the surface area [43, 46]. As the partial oxidation of isobutane involves both types of reactions, the dependence on surface area could be complex.

Table 8 shows the percentage conversion and percentage selectivities to the products of the partial oxidation of isobutane using catalysts of the type $Cs_{3-x}H_x[PMo_{12}O_{40}]$ (x = 0, 0.5, 1 and 2), $Cu_{3-x}H_x[PMo_{12}O_{40}]_2$ (x = 0, 2 and 4), $Ag_{3-x}H_x[PMo_{12}O_{40}]$ (x = 0, 1 and 2) and $H_3[PMo_{12}O_{40}]$. Important in the discussion of the catalytic activities of the above series of compounds are their surface areas.

The literature data on the surface areas of available species are given in Table 9. All of the literature surface area data have been determined by the Brunauer-Emmett-Teller (BET) method, using nitrogen adsorption. Of all the compounds, only $Cs_3[PMo_{12}O_{40}]$ has a high surface area and is microporous. The salts $Cs_{2.5}H_{0.5}[PMo_{12}O_{40}]$ and $Cs_2H[PMo_{12}O_{40}]$ have lower surface areas than $Cs_3[PMo_{12}O_{40}]$, but their microporous nature has not been determined. The remaining compounds, including the parent acid, $H_3[PMo_{12}O_{40}]$, have low surface areas that vary from 0.78-2.2 $m^2\ g^{-1}$. For some mixed cation/H^+ compounds containing Cu^{2+} and Ag^+ there is no data available, but these compounds are expected to have low surface areas (<~3 $m^2\ g^{-1}$) as do the fully substituted salts.

Table 8. Percentage conversion of isobutane, percentage selectivities to the products and carbon balance (%) in the partial oxidation of isobutane at 340°C by: $Cs_{3-x}H_x[PMo_{12}O_{40}]$ (x = 0, 0.5, 1 and 2), $Cu_{3-x}H_x[PMo_{12}O_{40}]_2$ (x = 0, 2 and 4), $Ag_{3-x}H_x[PMo_{12}O_{40}]$ (x = 0, 1 and 2) and $H_3[PMo_{12}O_{40}]$.

Compound	Conv'n (%)	Selectivity (%)						Carbon balance (%)
		MAL	MAA	ACA	IBA	CO	CO_2	
$Cs_3[PMo_{12}O_{40}]$	13.8	1.6	2.5	3.0	0.7	52.1	40.0	92
$Cs_{2.5}H_{0.5}[PMo_{12}O_{40}]$	14.1	12.9	6.3	1.8	0.3	45.9	32.8	95
$Cs_2H[PMo_{12}O_{40}]$	6.5	31.3	9.2	4.1	0.5	36.8	18.1	99
$CsH_2[PMo_{12}O_{40}]$	7.6	20.9	4.7	6.6	0.4	47.7	19.8	98
$Cu_3[PMo_{12}O_{40}]_2$	2.1	20.9	0.3	2.3	0.1	51.3	25.2	103
$Cu_2H_2[PMo_{12}O_{40}]_2$	10.0	17.6	0.3	1.3	0.1	51.4	29.4	96
$CuH_4[PMo_{12}O_{40}]_2$	16.9	13.9	4.1	6.3	0.4	49.4	25.9	92
$Ag_3[PMo_{12}O_{40}]$	2.5	3.3	0.0	0.3	0.1	51.2	45.0	99
$Ag_2H[PMo_{12}O_{40}]$	14.6	15.0	2.1	3.9	0.2	50.8	28.0	93
$AgH_2[PMo_{12}O_{40}]$	16.1	14.1	4.3	6.7	0.3	48.7	25.9	92
$H_3[PMo_{12}O_{40}]$	6.1	11.4	2.4	8.2	0.2	56.1	21.8	98

Examination of the % conversions for $Cu_3[PMo_{12}O_{40}]_2$ and $Ag_3[PMo_{12}O_{40}]$ show that they are very similar (~2-2.5%), but that of $Cs_3[PMo_{12}O_{40}]$ is much higher, at 13.8%. Thus, in the absence of H^+ counter-cations, the % conversion appears to depend on the surface areas of the catalysts.

Table 9. BET surface areas and micropore diameters for $Cs_{3-x}H_x[PMo_{12}O_{40}]$ (x = 0, 0.5, 1 and 2), $Ag_{3-x}H_x[PMo_{12}O_{40}]$ (x = 0, ~0.5) and $H_3[PMo_{12}O_{40}]$.

Compound	BET surface area ($m^2\ g^{-1}$)	Micropore diameter (Å)	Reference
$Cs_3[PMo_{12}O_{40}]$	117;145.5,46.0	14.3	[4, 8, 47, 48]
$Cs_{2.5}H_{0.5}[PMo_{12}O_{40}]$	77,9.5	Not determined	[4, 8, 48]
$Cs_2H[PMo_{12}O_{40}]$	2.9,5.9	Not determined	[4, 8, 48]
$CsH_2[PMo_{12}O_{40}]$	0.8,2.1	Not determined	[4, 8, 48]
$Cu_3[PMo_{12}O_{40}]_2$	2.2	Not determined	[49]
$Ag_3[PMo_{12}O_{40}]$	1.5	Not microporous	[50]
$\sim Ag_{2.5}H_{0.5}[PMo_{12}O_{40}]$	1.3	Not microporous	[50]
$H_3[PMo_{12}O_{40}]$	1.2;0.78;2 to 3	Not microporous	[4, 10, 51]

$Cs_3[PMo_{12}O_{40}]$ has a much higher surface area than either $Cu_3[PMo_{12}O_{40}]_2$ or $Ag_3[PMo_{12}O_{40}]$. The % conversion therefore appears to be controlled by an oxidation reaction (surface area dependent) rather than an oxidative dehydrogenation reaction (surface area independent). However, the real difference in the three compounds occurs in the % selectivities, which show a much higher % selectivity to methacrolein in the case of $Cu_3[PMo_{12}O_{40}]_2$, at the expense of CO_2 formation. The % selectivity data for $Cs_3[PMo_{12}O_{40}]$ and $Ag_3[PMo_{12}O_{40}]$ are similar. Both of these compounds have almost identical cubic structures, as indicated above, while that of $Cu_3[PMo_{12}O_{40}]_2$ is different and shows evidence of some lack of crystallinity, with broad XRD peaks in the diffraction pattern at 340^oC. The % selectivity difference may therefore be related to the surface structures of the three catalysts, and the counter-cations that the adsorbed isobutane encounters or is close to on the catalyst surface during reaction. The type of counter-cation is known to have a strong effect on the catalytic oxidations and oxidative dehydrogenation reactions of

phosphopolyoxomolybdates, with reduced % conversion with increasing charge and smaller ionic radii, *i.e.* a higher ionic potential, as defined by charge/ionic radius [4]. Both Cs^+ and Ag^+ are singly charged and relatively large (crystal radii: Cs^+ = 1.81 Å; Ag^+ = 1.29 Å, both 6-coordination), while Cu^{2+} is doubly charged and significantly smaller (crystal radius: 0.87 Å, 6-coordination) [52]. While ionic potential favours Cs^+ and Ag^+, the chance of encountering a Cu^{2+} counter-cation on the catalyst surface is less probable for the Cu^{2+}-containing salts, which likely leads to the greater % conversions in these salts.

It has been suggested that reducible counter-cations are able to play a role in the Bulk Catalysis Type-II mechanism of polyoxomolybdate catalysts. Reducible counter-cations are able to help in the transfer of electrons from anion to anion as part of the above mechanism. In the present case, the Cs^+ is not reducible under the experimental conditions, but both Cu^{2+} and Ag^+ could potentially be involved in such a process. However, the standard electrode (reduction) potential E^o of the Cu^{2+}/Cu^+ couple is lower than that of Ag^+/Ag, 0.16 vs 0.80 V [44], respectively, yet it is Cs^+ and Ag^+ that show similar % selectivities. Thus cation reducibility would not appear to be a factor in the product distribution.

Addition of H^+ to the counter-cation makeup has a major effect on both the % conversion of isobutane and the % selectivities to the products. This is supported by the % conversion and % selectivities to the products of the parent acid, $H_3[PMo_{12}O_{40}]$, which is a relatively good catalyst itself. In the examples containing the Cu^{2+} and Ag^+ counter-cations, progressive addition of H^+ to $Cu_3[PMo_{12}O_{40}]_2$ or $Ag_3[PMo_{12}O_{40}]$, to give $Cu_2H_2[PMo_{12}O_{40}]_2$ and $CuH_4[PMo_{12}O_{40}]_2$ or $Ag_2H[PMo_{12}O_{40}]$ and $AgH_2[PMo_{12}O_{40}]$, respectively, results in progressively increasing % conversions in both cases. The surface areas of these compounds, where available, do not change significantly (Table 8), so that the effect must be associated with the introduction of the H^+. However, in the series $Cs_3[PMo_{12}O_{40}]$, $Cs_{2.5}H_{0.5}[PMo_{12}O_{40}]$, $Cs_2H[PMo_{12}O_{40}]$ and $CsH_2[PMo_{12}O_{40}]$, the % conversions of $Cs_3[PMo_{12}O_{40}]$ and

$Cs_{2.5}H_{0.5}[PMo_{12}O_{40}]$ are about the same, but then % conversion decreases with addition of further H^+, such that $Cs_2H[PMo_{12}O_{40}]$ and $CsH_2[PMo_{12}O_{40}]$ have about the same % conversions as does $H_3[PMo_{12}O_{40}]$. This trend parallels the progressive decrease in surface areas of the compounds and is consistent with the catalytic reaction for the Cs^+-containing catalysts being controlled by an oxidation step, as indicated above. Note, however, that the % conversions of $Cu_2H_2[PMo_{12}O_{40}]_2$, $CuH_4[PMo_{12}O_{40}]_2$, $Ag_2H[PMo_{12}O_{40}]$ and $AgH_2[PMo_{12}O_{40}]$ are all greater than that of $H_3[PMo_{12}O_{40}]$, and increase with increasing H^+ content. There are two possible reasons for this:

(i) The reduction of the counter-cations Ag^+ and Cu^{2+} are dependent on the presence of H^+, which presumably occurs on the catalyst surface, and/or

(ii) The surface structures of the catalysts are critical to the formation of products and, as the surface areas of the Cu^{2+}- and Ag^+-containing salts are slightly greater than that of $H_3[PMo_{12}O_{40}]$ there may be some slight surface area dependence among these compounds.

There is no likely mechanism by which the first explanation is possible under the oxidising conditions present in the catalysis reactions, so that the difference is likely to be the effects of differences in surface area.

Addition of H^+ in these compounds also has an effect on methacrolein and methacrylic acid formation, but depends on the counter-cation. For the Cs^+-containing salts, methacrolein and methacrylic acid formation peak at $Cs_2H[PMo_{12}O_{40}]$, generally at the expense of CO and CO_2 formation. Unfortunately, while the % selectivities to these products are quite good for this compound, the % conversion is small (only 6.5%). For the Cu^{2+}- and Ag^+-containing salts, the total % selectivity (to methacrolein and methacrylic acid) is ~17-18%, with slightly higher % selectivity to methacrylic acid in the case of the lower metal ion-

containing salts $CuH_4[PMo_{12}O_{40}]_2$ and $AgH_2[PMo_{12}O_{40}]$. These two salts also have a higher % selectivity to the fragmentation product acetic acid (6.3-6.7%), which is consistent with the higher acetic acid % selectivity for the parent acid, $H_3[PMo_{12}O_{40}]$ (8.2%).

There is little data available for comparison from literature studies. However, Mizuno *et al.* performed a similar study with the compounds $Cs_{3-x}H_x[PMo_{12}O_{40}]$, where x = 0, 0.5, 1, 2 and 3, except that the catalysis study was performed in the presence of excess O_2 [8, 48]. The data are given in Table 10. In this study the catalysis conditions were: isobutane, 17 vol %; oxygen, 33 volume %; with the balance nitrogen; temperature of catalysis = 340^oC; 1.0 g of catalyst and a flow rate of 30 mL/min. In general the conditions were similar to those used in this study, except for the presence of excess oxygen. The trend in the % conversions approximately parallels the trend found in the present work, except that $Cs_3[PMo_{12}O_{40}]$ is much less catalytically active in the study of Mizuno *et al*. Also, the % selectivities to methacrolein, methacrylic acid and acetic acid were higher in the studies of Mizuno *et al.*, which is not surprising as the isobutane:oxygen rations were reversed. Thus a higher oxygen:isobutane ratio has lead to more of the organic oxidation products, while CO and CO_2 form in greater amounts under isobutane-rich conditions. Also note that isobutyric acid was not observed as a product in the study of Mizuno *et al.*.

Finally, as noted in their low-pressure studies of the oxidation of isobutane over phosphopolyoxomolybdate catalysts containing H^+ and Cu^{2+} as counter-cations, Kendell *et al.* [53] observed that while methacrolein and acetic acid (as well as the β-lactone, 3-methyl-2-oxetanone, a precursor to methacrylic acid) formed in parallel independent reactions, acetic acid and CO_2 evolved in consecutive reactions. Note that in that study CO was not measured. In the present study there is a modest inverse relationship between the % selectivities of acetic acid and CO_2 (linear correlation coefficient, R^2 = 0.456).

Table 10. Percentage conversion of isobutane and percentage selectivities to the products in the partial oxidation of isobutane at 340°C by $Cs_{3-x}H_x[PMo_{12}O_{40}]$ (x = 0, 0.5, 1, 2 and 3).

Compound	Conv'n (%)	Selectivity (%)						Sum of yields of MAL and MAA (%)
		MAL	MAA	ACA	IBA	CO	CO_2	
$Cs_3[PMo_{12}O_{40}]$	8	10	0	6	-	32	35	0.8
$Cs_{2.5}H_{0.5}[PMo_{12}O_{40}]$	16	7	24	7	-	41	21	5.1
$Cs_2H[PMo_{12}O_{40}]$	11	10	34	7	-	29	21	4.8
$CsH_2[PMo_{12}O_{40}]$	6	17	23	10	-	32	18	2.4
$H_3[PMo_{12}O_{40}]$	7	18	4	8	-	44	26	1.5

Thus although the conditions of the two studies are very different, the present results are consistent with this observation. Moreover, it may be noted that in the low pressure studies, O_2 is not supplied as a reactant. The catalysts operate by using oxygen from the lattice. Thus they operate by a Mars-van Krevelen mechanism.

It also should be possible to correlate the apparent activation energies, E_{app}, for methacrolein formation obtained from the low pressure studies with the % conversions obtained in the present studies. However, there appears to be little correlation. In the present studies the % conversion increases with decreasing Cu^{2+} content although $H_3[PMo_{12}O_{40}]$ does not follow this trend. The data from Kendell *et al.* is given in Table 10. The order of E_{app} is $Cu_2H_2[PMo_{12}O_{40}]_2 < CuH_4[PMo_{12}O_{40}]_2 < Cu_3[PMo_{12}O_{40}]_2 < H_3[PMo_{12}O_{40}]_2$, which shows no relationship to the order for % conversion found in the present study. The order established by Kendell *et al.* is also that found for the rate constants for methacrolein formation at 340°C

[53]. However, in the present studies the % conversion includes contributions from all product species, not just methacrolein so it is not surprising that the above correlation is poor. Interestingly, however, the observed order for the % selectivities for methacrolein formation established here does parallel the order for E_{app} obtained for the same series of compounds (Table 9), except that in the present studies $Cu_3[PMo_{12}O_{40}]_2$ is much more reactive than in the low pressure studies. There is no obvious reason for this difference. Similar correlations for methacrolein formation can also be made with the compounds $Cs_{3-x}H_x[PMo_{12}O_{40}]$, where x = 0, 0.5, 1 and 2, which has been reported recently by Kendell and Brown [54]. The data are also given in Table 11. The order of E_{app} is $Cs_2H[PMo_{12}O_{40}]$ < $CsH_2[PMo_{12}O_{40}]$ < $Cs_{2.5}H_{0.5}[PMo_{12}O_{40}]$ < $Cs_3[PMo_{12}O_{40}]$. Again the observed trend in % conversion observed here does not follow the order of E_{app}. However, as in the previous studies with Cu^{2+} as the counter cation, the % selectivities to methacrolein formation for the series exactly parallels the decreasing order of % selectivity to methacrolein obtained in the present studies.

3.4.2 Catalysis studies in the presence of gold nanoparticles; their effect on the partial oxidation of isobutane

The analogous catalysis data obtained under identical conditions but with the addition of 5 mass % of gold nanoparticles are given in Table 12. For the compounds $Cs_3[PMo_{12}O_{40}]$, $Cu_3[PMo_{12}O_{40}]_2$ and $Ag_3[PMo_{12}O_{40}]$, the % conversions have changed markedly. The % conversion for $Cs_3[PMo_{12}O_{40}]$ has decreased by a factor of about 2, while the % conversions for $Cu_3[PMo_{12}O_{40}]_2$ and $Ag_3[PMo_{12}O_{40}]$ both increase, particularly for the former compound. It is apparent that the presence of the gold nanoparticles has had a significant effect. For $Cs_3[PMo_{12}O_{40}]$ it is likely that the presence of the gold nanoparticles has either blocked the pore structure of this microporous salt (Table 8), and/or has reduced the surface area available for adsorption of the isobutane.

Table 11. Apparent activation energy, E_{app}, and pre-exponential factor data for methacrolein formation from the low pressure oxidation of isobutane.

Compound	Temperature range (K)	E_{app} (kJ mol^{-1}) for MAL formation	Pre-exponential factor ($\log_{10}$ A)	Reference
$Cs_3[PMo_{12}O_{40}]$	370-434	119 ± 4	10.9 ± 0.8	[54]
$Cs_{2.5}H_{0.5}[PMo_{12}O_{40}]$	342-444	106.1 ± 1.6	9.96 ± 0.15	[54]
$Cs_2H[PMo_{12}O_{40}]$	347-417	72 ± 1	7.5 ± 0.1	[54]
$CsH_2[PMo_{12}O_{40}]$	290-372	93 ± 5	9 ± 1	[54]
$Cu_3[PMo_{12}O_{40}]_2$	342-500	75.4 ± 1.2	4.59 ± 0.10	[53]
$Cu_2H_2[PMo_{12}O_{40}]_2$	325-501	58.4 ± 0.9	3.44 ± 0.13	[53]
$CuH_4[PMo_{12}O_{40}]_2$	353-502	61.3 ± 1.9	3.62 ± 0.08	[53]
$H_3[PMo_{12}O_{40}]$	246-451	99.3 ± 1.1	6.21 ± 0.10	[53]

This would have the effect of reducing the % conversion, as is observed. This appears to be less of a problem for $Cu_3[PMo_{12}O_{40}]_2$ and $Ag_3[PMo_{12}O_{40}]$ as both already have low surface areas (Table 8). Alternatively, the XPS studies have shown that some gold had been converted to Au^+ in the spent catalysts (Table 6), thus any reduction of Cu^{2+} and Ag^+ ions to Cu^+/Cu and Ag as part of the electron transfer process between the phosphopolyoxomolybdate anions - the Bulk Catalysis Type-II mechanism - would likely undergo fast re-oxidation to their original oxidation states. This would likely accelerate the overall reaction and lead to a greater % conversions. As Cu^{2+} is more easily oxidised than Ag^+, this may contribute to the larger increase in % conversion for this compound.

Table 12. Percentage conversion of isobutane, percentage selectivities to the products and carbon balance (%) in the partial oxidation of isobutane at 340^{o}C by: $Cs_{3-x}H_x[PMo_{12}O_{40}]$ (x = 0, 0.5, 1 and 2), $Cu_{3-x}H_x[PMo_{12}O_{40}]_2$ (x = 0, 2 and 4), $Ag_{3-x}H_x[PMo_{12}O_{40}]$ (x = 0, 1 and 2) and $H_3[PMo_{12}O_{40}]$ following inclusion of 5 mass % of gold nanoparticles.

Compound (with 5 mass % gold nanoparticles)	Conv'n (%)	Selectivity (%)						Carbon balance (%)
		MAL	MAA	ACA	IBA	CO	CO_2	
$Cs_3[PMo_{12}O_{40}]$	7.0	0.0	0.3	0.0	0.0	3.1	96.6	96
$Cs_{2.5}H_{0.5}[PMo_{12}O_{40}]$	14.6	16.2	4.4	3.4	0.8	30.6	44.6	93
$Cs_2H[PMo_{12}O_{40}]$	4.3	27.3	4.9	1.3	0.6	29.6	36.3	99
$CsH_2[PMo_{12}O_{40}]$	7.4	21.7	3.5	5.7	0.4	46.0	22.8	97
$Cu_3[PMo_{12}O_{40}]_2$	7.2	16.7	0.3	2.4	0.1	50.7	29.8	97
$Cu_2H_2[PMo_{12}O_{40}]_2$	9.4	17.0	0.4	2.6	0.1	50.2	29.7	96
$CuH_4[PMo_{12}O_{40}]_2$	14.9	12.1	0.9	4.8	0.2	52.7	29.1	92
$Ag_3[PMo_{12}O_{40}]$	3.3	3.2	0.2	0.0	0.0	54.4	42.2	98
$Ag_2H[PMo_{12}O_{40}]$	11.4	14.7	1.1	5.1	0.2	50.3	28.6	95
$AgH_2[PMo_{12}O_{40}]$	13.6	9.9	3.1	5.6	0.3	52.3	28.8	94
$H_3[PMo_{12}O_{40}]$	15.7	13.6	4.4	6.0	0.4	44.8	30.8	93

Moreover, the Au^+ may play this role as well, if it cycles between Au and Au^+. At present the origin of the Au^+ species is unknown, but this could arise by oxidation from the molecular oxygen in the input stream. However, although gold nanoparticles are known to oxidise at lower temperatures than bulk gold, there is no evidence that oxidation of gold nanoparticles occurs at 340^{o}C. The species identity of gold that is oxidised to Au^+ when gold nanoparticles are supported on different oxides (SiO_2, CeO_2 and TiO_2) has been suggested to be AuO^-, which can be stabilised by suitable cations from the oxide structure [23]. In the

present case these cations are likely to be the counter-cations of the polyoxomolybdates. These can be made available by reduction in oxidation state of the Mo(VI) to Mo(V), which occurs as part of the oxidation/oxidative dehydrogenation reaction, and as shown by the present XPS studies (see Section 3.3.2.4.2).

Addition of the gold nanoparticles has also had a range of effects on the % selectivities in these three compounds. For $Cs_3[PMo_{12}O_{40}]$ the % selectivity to methacrylic acid has been significantly reduced (2.3 to 0.3%), while formation of methacrolein (as well as acetic acid and isobutyric acid) has been entirely eliminated. Also, formation of CO has been severely reduced from 52.1 to 3.1%. The beneficiary of this has been CO_2. Thus the gold nanoparticles have converted $Cs_3[PMo_{12}O_{40}]$ into a 'combustion' catalyst. Alternatively, it might be argued that $Cs_3[PMo_{12}O_{40}]$ is simply acting mainly as a support for the gold nanoparticles that function as the combustion catalyst. For $Ag_3[PMo_{12}O_{40}]$ the % selectivities have changed little on addition of the gold nanoparticles, while for $Cu_3[PMo_{12}O_{40}]_2$ the % selectivity to methacrolein has dropped, although that of methacrylic acid has remained about the same. The fully oxidised oxidation product CO_2 has become more important than CO, although the changes in the % selectivities are not great.

For the parent acid, $H_3[PMo_{12}O_{40}]$, the % conversion has increased significantly (6.1 to 15.7%) on addition of the gold nanoparticles, while the % selectivities to methacrolein and methacrylic acid have also increased. The % selectivity to the fragmentation product acetic acid has decreased, as has that to the oxidation product CO, while that of the fully oxidised product CO_2 has increased. This is consistent with the gold nanoparticles acting to help the oxidation process.

Addition of H^+ to the compositions of the counter-cations has again had an effect, both to the % conversions and % selectivities to the products. For $Cu_2H_2[PMo_{12}O_{40}]_2$,

$CuH_4[PMo_{12}O_{40}]_2$, $Ag_2H[PMo_{12}O_{40}]$ and $AgH_2[PMo_{12}O_{40}]$, the presence of the added gold nanoparticles has generally resulted in a slight decrease in % conversion in each case compared to the % conversions in the absence of gold nanoparticles. However, the same pattern of increased % conversion in those compounds with the more H^+-rich counter-cation composition, *i.e.* $CuH_4[PMo_{12}O_{40}]_2$ and $AgH_2[PMo_{12}O_{40}]$, still exhibited greater % conversions. In all four cases the reduced % conversion may be caused by blocking of the surface area to isobutane adsorption by the presence of the gold nanoparticles. Note, however, this was not observed for the parent acid, $H_3[PMo_{12}O_{40}]$. Further investigation of the surface characteristics of $H_3[PMo_{12}O_{40}]$ and its salts would therefore appear to be necessary. Notably, XPS studies showed the presence of Au^+ in addition to Au in the spent catalysts, and there was no evidence of other oxidation states of Cu and Ag other than Cu^{2+} and Ag^+. All compounds showed the presence of significant amounts of Mo(V) in addition to Mo(VI), but this is expected as reduction of Mo(VI) to Mo(V) is part of the Mars-van Krevelan reaction mechanism that must occur in these oxidation catalysts.

The presence of gold nanoparticles also had an effect on the % selectivities to the products for the catalysts. For the series $Cs_{2.5}H_{0.5}[PMo_{12}O_{40}]$, $Cs_2H[PMo_{12}O_{40}]$ and $CsH_2[PMo_{12}O_{40}]$ the % selectivities to methacrolein and methacrylic acid again reach a maximum at $Cs_2H[PMo_{12}O_{40}]$ in the presence of the gold nanoparticles. However, while $Cs_{2.5}H_{0.5}[PMo_{12}O_{40}]$ and $CsH_2[PMo_{12}O_{40}]$ had slightly greater % selectivities to methacrolein on addition of the gold nanoparticles, that for $Cs_2H[PMo_{12}O_{40}]$ was slightly reduced. In all three compounds the % selectivity to methacrylic acid was also reduced in the presence of the gold nanoparticles and, while the % selectivity to CO was also reduced, that of CO_2 increased in all cases. Again, it is apparent that the gold nanoparticles act to increase oxidation to CO_2, but the effects on the methacrolein and methacrylic acid are complex.

For $Cu_2H_2[PMo_{12}O_{40}]_2$, $CuH_4[PMo_{12}O_{40}]_2$, $Ag_2H[PMo_{12}O_{40}]$ and $AgH_2[PMo_{12}O_{40}]$ the pattern of % selectivity changes is slightly different to that found for the Cs^+-containing compounds. For all four compounds the % selectivity to methacrolein decreases on addition of the gold nanoparticles, although this is more significant for the compounds that have a higher H^+ content. The % selectivityies to methacrylic acid also decrease for all four compounds, while the % selectivities to CO and CO_2 remain almost unchanged. The effect of the presence of H^+ appears to have reduced the oxidation effect of the gold nanoparticles compared to the Cs^+-containing compounds. This is not the trend observed with $H_3[PMo_{12}O_{40}]$, and it must be assumed that the presence of the Cu^{2+} and Ag^+ counter-cations must play a role.

3.5 Conclusions

In this chapter, a new approach to supporting gold nanoparticles on an oxide or oxide-related support has been demonstrated. Gold nanoparticles were supported on the surface and within the pore structures of several series of phosphopolyoxomolybdate salts: these included the series $Au_{NPS}/(Cs^+)_{3-x}H_x[PMo_{12}O_{40}]$ (x = 0, 0.5, 1 and 2), $Au_{NPS}/(Ag^+)_{3-x}H_x[PMo_{12}O_{40}]$ (x = 0, 1 and 2), $Au_{NPS}/(Cu^{2+})_{3-2x}H_{2x}[PMo_{12}O_{40}]_2$ (x = 0, 1 and 2) and $Au_{NPS}/H_3[PMo_{12}O_{40}]$. The method uses a slow thermolysis treatment following the addition of *n*-hexanethiolate-stabilised gold nanoparticles in an *n*-hexane solution to the (insoluble) phosphopolyoxomolybdate salts. The thermolysis treatment is used to remove the thiolate ligand from the surface of the gold nanoparticles and thus convert them to pure gold nanoparticles. The prepared gold nanoparticles supported on the surfaces of phospopolyoxomolybdate salts were used as catalysts in the partial (selective) oxidation of isobutane.

n-Hexanethiolate-stabilised gold nanoparticles were prepared using the two-phase synthesis (see Chapter 1). The produced gold nanoparticles were easily separated out of solution and stored in the form of a black powder. The size and shape of the gold nanoparticles were characterised using different techniques such as TEM and UV-visible spectroscopy.

During this study, a number of phosphopolyoxomolybdate salts were synthesised and characterised including $(Cs^{+})_{3-x}H_x[PMo_{12}O_{40}]$ (x = 0, 0.5,1 and 2), $(Ag^{+})_{3-x}H_x[PMo_{12}O_{40}]$ (x = 0, 1 and 2) and $(Cu^{2+})_{3-2x}H_{2x}[PMo_{12}O_{40}]_2$ (x = 0, 1 and 2). The produced salts, in addition to the parent acid $H_3[PMo_{12}O_{40}]$, were used as supports for gold nanoparticles in order to study their effects on the catalytic activities of the above salts for the oxidation/oxidative dehydrogenation of isobutane. While the *n*-hexanethiolare-stabilised gold nanoparticles were synthesised with a size of about 2.5 nm, following addition to the phosphopolyoxomolybdate supports there was some agglomeration to yield gold nanoparticles of a diameter of 6.0 nm. The addition of gold nanoparticles had a significant effect on the % conversions and % selectivites to the products of all of the employed phosphopolyoxomolybdates salts. Studies in the absence of gold nanoparticles were performed prior to the studies of the effects of the gold nanoparticles on the oxidation process. In some cases the effects of addition of gold nanoparticles had a positive influence, and in others a detrimental effect. This depended on the presence, or not, of H^{+} in the catalyst make-up. Some effects may perhaps be related to the presence of the gold nanoparticles reducing the surface area or by blocking the pore structure of the salts. Further studies of the effect of the presence of the gold nanoparticles on the surface areas and pore structure of the catalysts would be required to answer this proposal. XPS studies showed the presence of Au^{+} in all of the spent catalysts, which suggests that this species (probably as AuO^{-}) plays a significant role in the oxidation process.

3.6 References

[1] Y. Konishi, K. Sakata, M. Misono, Y. Yoneda, J. Catal., 77 (1982) 169-179.

[2] M. Akimoto, Y. Tsuchuda, k. Sato, E. Echigoya, J. Catal., 72 (1981) 83-94.

[3] M. Akimoto, K. Shima, H. Ikeda, E. Echigoya, J. Catal., 86 (1984) 173-186.

[4] J. Hu, R. Burns, J. Catal., 195 (2000) 360-375.

[5] F. Cavani, E. Etienne, R. Mezzogori, A. Pigamo, F. Trifirò, Catal. Lett., 75 (2001) 99-105.

[6] W. Li, W. Ueda, Catal. Lett., 46 (1997) 261-265.

[7] F. Cavani, R. Mezzogori, A. Pigamo, F. Trifirò, Chem. Eng. J., 82 (2001) 33-42.

[8] N. Mizuno, M. Tateishi, M. Iwamoto, J. Catal., 163 (1996) 87-94.

[9] M. Langpape, J.M.M. Millet, U.S. Ozkan, M. Boudeulle, J. Catal., 181 (1999) 80-90.

[10] S. Kendell, A.-S. Alston, N. Ballam, T. Brown, R. Burns, Catal. Lett., 141 (2011) 374-390.

[11] N. Mizuno, M. Misono, Chem. Lett., (1987) 967-970.

[12] M. Brust, M. Walker, D. Bethell, D.J. Schiffrin, R. Whyman, J. Chem. Soc., Chem. Commun., 1994 (1994) 801-802.

[13] M. Brust, M. Walker, D. Bethell, D. Schiffrin, R. Whyman, J. Chem. Soc., Chem. Commun., 1994 (1994) 801-802.

[14] M. Brust, J. Fink, D. Bethell, D. Schiffrin, C. Kiely, J. Chem. Soc., Chem. Commun., (1995) 1655-1656.

[15] M. Corbierre, R. Lennox, Chem. Mater, 17 (2005) 5691-5696.

[16] Z. Xu, C. Shen, T. Yang, H. Zhang, H. Li, J. Li, H. Gao, Chem. Phys. Lett., 415 (2005) 342-345.

[17] J. Zhou, J. Ralston, R. Sedev, D. Beattie, J. Colloid. Interfac. Sci., 331 (2009) 251-262.

[18] D. Shalom, R. Wootton, R. Winkle, B. Cottam, R. Vilar, A. Demello, C. Wilde, Mater. Lett., 61 (2007) 1146-1150.

[19] A. Ernst, L. Sun, K. Wiaderek, A. Kolary, S. Zoladek, P. Kulesza, J. Cox, Electroanalysis, 19 (2007) 2103-2109.

[20] M. Hostetler, J. Wingate, C. Zhong, J. Harris, R. Vachet, M. Clark, J. Londono, S. Green, J. Stokes, G. Wignall, Langmuir, 14 (1998) 17-30.

[21] D. Leff, P. Ohara, J. Heath, W. Gelbart, J. Phys. Chem. B, 99 (1995) 7036-7041.

[22] C. Yee, R. Jordan, A. Ulman, H. White, A. King, M. Rafailovich, J. Sokolov, Langmuir, 15 (1999) 3486-3491.

[23] M. Casaletto, A. Longo, A. Martorana, A. Prestianni, A. Venezia, Surf. Interfac. Anal., 38 (2006) 215-218.
[24] D. Leff, L. Brandt, J. Heath, Langmuir, 12 (1996) 4723-4730.
[25] M.C. Bourg, A. Badia, R.B. Lennox, J. Phys. Chem. B., 104 (2000) 6562-6567.
[26] A. McNeillie, D.H. Brown, W.E. Smith, M. Gibson, L. Watson, J. Chem. Soc., Dalton Transactions, (1980) 767.
[27] M.J. Hostetler, J.J. Stokes, R.W. Murray, Langmuir, 12 (1996) 3604-3612.
[28] C. Rocchiccioli-Deltcheff, R. Thouvenot, R. Franck, Spectrochim Acta Part A: Molecular Spectroscopy, 32 (1976) 587-597.
[29] C. Rocchiccioli-Deltcheff, M. Fournier, R. Franck, R. Thouvenot, Inorg. Chem., 22 (1983) 207-216.
[30] E. Silviani, R.C. Burns, J. Molec. Catal. A: Chemical, 219 (2004) 327-342.
[31] A.J. Bridgeman, Chem. Phys. Lett., 287 (2003) 55-69.
[32] F. Cavani, C. Comuzzi, G. Dolcetti, R.G. Finke, A. Lucchi, F. Trifirò, A. Trovarelli, Heterogeneous Hydrocarbon Oxidation, Am. Chem. Soc., Washington, 1996.
[33] J. Arnott, Department of Chemistry, B.Sc. (Honor) (2003).
[34] R. Strandberg, Acta Chem. Scand. A, 29 (1975) 359-364.
[35] H. D'Amour, R. Allmann, Z. Krist., 143 (1976) 1.
[36] J. Black, N. Clayden, P. Gai, J. Scott, E. Serwicka, J. Goodenough, J. Catal, 106 (1987) 1-15.
[37] L. Marosi, E.E. Platero, J. Cifre, C.O. Areán, J. Mater. Chem., 10 (2000) 1949-1955.
[38] International Centre for Diffraction Data, http://www.icdd.com/.
[39] R. Allmann, Acta Chem. Scand. A, 30 (1976) 152.
[40] A. Ferrari, L. Cavalca, M. Nardelli, Gazz. Chem. Ital., 79 (1949) 61.
[41] NIST; X-ray Photoelectron Spectroscopy Database, Version 3.5; http://srdata.nist.gov/xps/.
[42] Casa-XPS; Processing Software for XPS, AES, SIMS. Version 2.3.16, http://www.casaxps.com/berlin/.
[43] T. Okuhara, N. Mizuno, M. Misono, Adv. Catal., 41 (1996) 113-252.
[44] G. Aylward, T. Findlay, SI Chemical Data, 6th ed., John Wiley and Sons Australia, Ltd, 2008.
[45] W. Turek, A. Pron, J. Haber, J. Catal., 189 (2000) 297-313.
[46] M. Misono, Catal. Rev. Sci. Eng., 29 (1987) 269-321.
[47] J. McMonagle, J. Moffat, J. Coll. and Interfac. Sci., 101 (1984) 479-488.

[48] N. Mizuno, M. Tateishi, M. Iwamoto, J. Chem. Soc., Chem. Commun., (1994) 1411-1412.
[49] K. Eguchi, I. Aso, N. Yamazoe, T. Seiyama, Chem. Lett., (1979) 1345-1346.
[50] M. Parent, J. Moffat, Langmuir, 12 (1996) 3733-3739.
[51] M. Misono, N. Mizuno, K. Katamura, A. Kasai, Y. Konishi, K. Sakata, T. Okuhara, Y. Yoneda, Bull. Chem. Soc. Japan, 55 (1982) 400-406.
[52] R. Shannon, Acta Crystallograph Section A: Crystal Physics, Diffraction, Theoretical and General Crystallography, 32 (1976) 751-767.
[53] S.M. Kendell, T.C. Brown, R.C. Burns, Catal. Today, 131 (2008) 526-532.
[54] S. Kendell, T. Brown, Catal. Lett., 141 (2011) 1767-1785.

CHAPTER 4

Synthesis, Characterisation and Catalytic Properties of Gold Nanoparticles deposited on M_3O_4 Structures (M = Mn, Co, Fe) for the Complete Oxidation of Isobutane

4.1 Introduction

In the past, the complete oxidation of hydrocarbons has been investigated with a number of practical applications in mind including hydrocarbon detection in enclosed environments [1, 2], odour control [3], volatile organic compound removal during polymer processing, coating operations, spray painting and offset printing [4, 5], domestic [6, 7] and other heating systems [8, 9], industrial boilers [10], gas turbines [11-14] and fuel cells [15].

In 1987, Haruta [16] found that when gold is deposited as nanoparticles on metal oxides, it exhibited a surprisingly high catalytic activity for CO oxidation. This finding has attracted many scientists to investigate the catalytic behaviour of gold in several applications of industrial and environmental importance. In addition, gold can be used for heterogeneous catalysis since it can be deposited on metal oxides as nanoparticles using different synthetic methods including co-precipitation and deposition-precipitation. These have been discussed in Chapter 1.

A number of research studies [16-19] have focussed on gold catalysis and have shown that supported gold exhibits a unique activity and selectivity for a number of reactions, including oxidations, hydrogenations and hydrochlorination reactions. Gold nanoparticles

have been found to exhibit a unique catalytic facility when deposited on a variety of metal oxides. Supported gold nanoparticles can be applied in low-temperature oxidations, catalytic combustion reactions, partial oxidation of hydrocarbons, oxidation of CO, hydrogenation of carbon oxides, and unsaturated hydrocarbon reduction of NO [16-20]. The present chapter deals with the deposition of gold nanoparticles on the binary spinel (mixed oxidation state) oxides of manganese, cobalt and iron and their effects on the complete oxidation (*i.e.* combustion) of isobutane, as well as a base study of the parent spinels.

Spinel is the given name of the mineral $MgAl_2O_4$. The general formula of a spinel structure is AB_2X_4, where A and B are cations which have oxidation states of (II) and (III), respectively, and X is an anion, usually oxygen, although other anions from Group 16 are possible, such as those of S, Se, Te. A spinel can be normal or have an inverse spinel structure, depending upon the arrangement of the cations. In a normal spinel structure, the A^{2+} and B^{3+} ions occupy tetrahedral and octahedral sites, respectively, while in an inverse spinel, which is an alternative arrangement, half of the B^{3+} ions occupy the tetrahedral sites while the A^{2+} ions are found in the octahedral sites along with half of the remaining B^{3+} ions. Thus the occupation factor, or degree of inversion, is defined as the fraction of B^{3+} ions occupying tetrahedral sites, giving a maximum degree of inversion of 50%. However, intermediate occupation factors are known. In many cases the choice between a spinel or inverse spinel structure depends on the balance of the crystal field stabilisation energies of the cations in the tetrahedral and octahedral oxide environments. The structure of a normal spinel is shown in Figure 1, and the compositions of the three M_3O_4 (M = Mn, Co and Fe) used as combustion catalysts in the present work are given in Table 1. The M_3O_4 compounds are mixed valence compounds and can be written as $(M^{2+})(M^{3+})_2O_4$. Thus Mn_3O_4 and Co_3O_4, used in this study for the combustion catalysis of isobutane, are examples of a spinel structure, while Fe_3O_4 has an inverse spinel structure [21, 22].

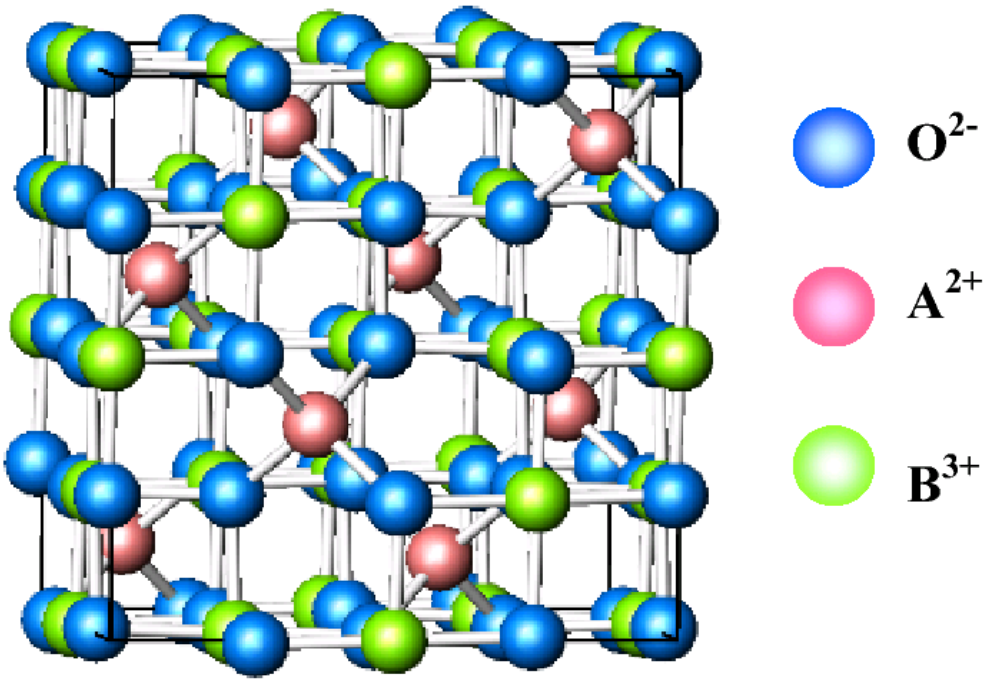

Figure 1. The normal spinel structure [23].

Table 1. The occupation of tetrahedral and octahedral sites in M_3O_4 (M = Mn, Co and Fe).

Formula	**Spinel**			**Inverse spinel**		
	$A_{tet}\,(B_2)_{oct}\,X_4$			$B_{tet}\,(A_{oct}\,B_{oct})\,X_4$		
	Tet	**Oct**	**X**	**Tet**	**Oct**	**X**
Mn_3O_4	Mn^{2+}	$(Mn^{3+})_2$	O^{2-}	-	-	-
Co_3O_4	Co^{2+}	$(Co^{3+})_2$	O^{2-}			
Fe_3O_4	-	-	-	Fe^{3+}	(Fe^{2+},Fe^{3+})	O^{2-}

While the three mixed-valence state oxides all have the same formula, they do not have the same crystallographic structures. Mn_3O_4 is tetragonal, space group $I4_1/amd$ (141), with a = 5.7621 Å, c = 9.4696 Å and Z = 4 (ICDD 00-024-0734) [24]. In contrast, both Co_3O_4 and Fe_3O_4 are isostructural, and are cubic, space group $Fd3m$ (227), a = 8.169(14) Å for Co_3O_4 (ICDD 01-080-1545) and a = 8.394 Å for Fe_3O_4 (ICDD 01-89-3854), and Z = 8 [24].

There are several known manganese oxides. These include MnO, Mn_3O_4 (hausmannite) Mn_2O_3, MnO_2 (α-MnO_2, pyrolusite) and Mn_2O_7. Manganese oxides have a wide range of applications, including high density magnetic storage media, molecular adsorption, electrochemical materials, solar energy transfer, and as catalysts [25-28], MnO_2 is also used in dry-cell batteries. Mn_3O_4 has been widely used as the main source of ferrite materials [29]. Moreover, to synthesis manganese oxides at a nanoscale level, different methods can be applied, such as chemical bath deposition, solid-state reaction, and γ-ray irradiation [29]. However, it the catalytic properties of manganese oxides that are important to the present study, particularly those of Mn_3O_4.

Iron oxides are widespread in nature and are easily synthesised in laboratory. Table 2 lists 16 types of iron oxides that consist of iron in oxidation states (II) and (III), together with O^{2-} and/or OH^-. Most of iron oxides exist in the trivalent state; three of these compounds, that is FeO, $Fe(OH)_2$ and Fe_3O_4, contain Fe^{2+}.

Table 2. The known iron oxides [30].

Oxide-hydroxides and hydroxides	Oxides
Goethite α-FeOOH	Hematite α-Fe_2O_3
Lepidocrocite γ-FeOOH	Magnetite Fe_3O_4
Akaganeite β-FeOOH	Maghemite γ-Fe_2O_3
Schwertmannite $Fe_{16}O_{16}(OH)_y(SO_4)_z.nH_2O$	B-Fe_2O_3
δ-FeOOH	ε-Fe_2O_3
Feroxyhyte δ-FeOOH	Wustite FeO
High-pressure FeOOH	-
Ferrihydrite δ-$Fe_5HO_8.4H_2O$	-
Bernalite $Fe(OH)_3$	-
$Fe(OH)_2$	-
Green Rusts $Fe_x^{III}Fe_y^{II}(OH)_{3x+2y-z}(A^-)_z$:A- = Cl^-; $^1/_2SO_4^{2-}$	-

Magnetite, Fe_3O_4, like hematite, is a most important source of iron ore. It may be used as a black pigment, and is also used as a catalyst source for the Haber-Bosch process, and a catalyst for the water-gas shift reaction [30, 31].

There are four cobalt oxides known, which include CoO, Co_3O_4, Co_2O_3 and CoO_2, Also, it has been found that 'cobalt oxide' with an oxidation state higher than (III) is unstable in the environment. Lower oxides are used in industry. Co_3O_4 can be applied in various industrial sectors such as a catalyst for the abatement of CO, as a magnetic material, in CO sensors, and in rechargeable batteries [31, 32].

In this chapter, the focus is on the catalytic total oxidation of isobutane over the metal oxides Co_3O_4, Mn_3O_4, and Fe_3O_4, either on their own, or with supported gold nanoparticles (1 and 5 wt %). These oxides were chosen as they have good stability under oxidising conditions, although Fe_3O_4 is prone to oxidation to give Fe_2O_3. Moreover, they have two different oxidation states, *i.e.* (II) and (II), which may lead to a range of different rates of oxidation of the substrate isobutane under surface heterogeneous catalytic conditions. While there have been several studies using these types of oxides for the oxidation of methane, ethane and propane, no studies have been performed on isobutane.

4.2 Experimental

In this chapter, Mn_3O_4 nanoparticles were prepared by following the synthetic procedure of Li *et al.* [33], while the other metal oxides Mn_3O_4, Co_3O_4, and Fe_3O_4 were commercially obtained in the form of powders and nano-powders.

4.2.1 Chemicals

n-Hexane ($CH_3(CH_2)_4CH_3$, Merck, 98%), ethanol (C_2H_5OH, Ajax Finechem Pty Ltd, >99.5%), manganese(II) acetate tetrahydrate ($Mn(CH_3COO)_2.4H_2O$, Sigma-Aldrich, 99%),

manganese(II,III) oxide (Mn_3O_4, 325 mesh, Sigma-Aldrich, 97%), iron(II,III) oxide (Fe_3O_4, 5 μm, Sigma-Aldrich, 98%), nano-powder iron(II,III) oxide (20-30 nm, Sigma-Aldrich, ≥98%), cobalt(II,III) oxide (Co_3O_4, ≤10 μm, Sigma-Aldrich), nano-powder cobalt(II,III) oxide (<50 nm, Sigma-Aldrich, 99.8%), iron(III) oxide (Fe_2O_3, Sigma-Aldrich, 99.98%), silicon carbide (Sigma-Aldrich, 200-450 mesh), silica gel (Riedel-deHaën, 0.063-0.2 mm). All materials were used as received.

4.2.2 Synthesis of Mn_3O_4 nanoparticles

In this study, manganese(II,III) oxide nanoparticles, Mn_3O_4, were prepared according to the method of Xi *et al.* [33]. In a typical preparation, 1.2 g (2.06 mmol) of $Mn(CH_3COO)_2.4H_2O$ was dissolving in anhydrous ethanol (60 mL, 1.02×10^{-3} mmol) with stirring until the $Mn(CH_3COO)_2.4H_2O$ dissolved. The solution was placed into a 100 mL glass-lined stainless steel autoclave (Parr Instrument Company, Moline, Illinois, USA, Model 452HC, 300 mL capacity), and thermal treatment was carried out at 90^{o}C for 24 hours. The following day the autoclave was cooled to room temperature, the product was isolated by centrifugation, washed with de-ionized water and acetone, and then dried at 30^{o}C for 12 hours. The product was a red-brown powder.

4.2.3 Deposition of gold nanoparticles on the metal oxides Mn_3O_4, Co_3O_4, and Fe_3O_4 (powders and nano-powders)

Two different percentages of gold nanoparticles (5 and 1 mass %) were used in this study, as shown in Table 3. The 5 mass % loading of gold nanoparticle-capped catalysts were prepared as follows. In a typical preparation, a solution containing 5 mass % (0.0066 g) of *n*-hexanethiolate-stabilised gold nanoparticles in 3 mL of *n*-hexane was added to 0.10 g of metal oxide in a porcelain crucible and stirred with a glass rod until the black solution

absorbed onto the surface of the oxide. In most cases extra *n*-hexane was required before the liquid turned colourless. This generally took about 30 minutes. The mixture was allowed to dry in the fumehood. The samples were heated initially to 150^{o}C, then slowly to 220^{o}C, and finally at 300^{o}C for 1 hour. This treatment released the thiolate ligand and left the gold nanoparticles loaded on the surface of the oxide particles. The same procedure was followed with the 1 mass % loading of gold nanoparticles on Mn_3O_4 nano-powder, with the same amount (0.10 g) of Mn_3O_4 catalyst.

Table 3. Masses (g) of catalysts used to prepare Au_{NPS}/Mn_3O_4 powder, Au_{NPS}/Mn_3O_4 nano-powder, Au_{NPS}/Co_3O_4 powder, Au_{NPS}/Co_3O_4 nano-powder, Au_{NPS}/Fe_3O_4 powder and Au_{NPS}/Fe_3O_4 nano-powder.

Compound	**Loading of catalyst (g)**	**Loading of Au nanoparticles (g)**	
		1 mass %	**5 mass %**
Mn_3O_4 powder	0.10291	-	0.00655
Mn_3O_4 nano-powder	0.10341	0.00133	0.00651
Co_3O_4 powder	0.10482	-	0.00663
Co_3O_4 nano-powder	0.10297	-	0.00652
Fe_3O_4 powder	0.10920	-	0.00650
Fe_3O_4 nano-powder	0.10368	-	0.00659

4.3 Characterisation

Several techniques have been applied to characterise and measure the physical properties of the metal oxides Mn_3O_4, Co_3O_4 and Fe_3O_4, including TEM, SEM, XRD and XPS. These were used to analyse the structures, the sizes of the catalyst particles and their surface areas. This also included the addition of gold nanoparticles to the metal oxides.

4.3.1 TEM analysis - Mn_3O_4 nanoparticles

TEM was used to characterise the size and shape of Mn_3O_4 nanoparticles. A TEM image is shown in Figure 2. The sample was prepared by supporting a small amount of the synthesised Mn_3O_4 nanoparticles in *n*-hexane which were then loaded onto a thin carbon film and left until evaporation of the solvent. The image presents block-shaped crystals and a size range from ~6 to 20 nm, with a larger crystal of ~40 nm observable in the top right-hand corner. Li *et al.* [33] have reported that the average diameter of the Mn_3O_4 nanoparticles depends on the growth temperature, and that the lower the growth temperature, the smaller the diameter of Mn_3O_4 nanoparticles. In this study, the nanoparticles were obtained at 90^{o}C, which is the lowest temperature used in the investigation of Li *et al.*. In that study Mn_3O_4 nanoparticles of about 10 nm were obtained, which are comparable to the present results.

Figure 2. TEM image of Mn_3O_4 nanoparticles.

4.3.2 SEM analysis – Mn_3O_4, Co_3O_4, Fe_3O_4 powders; Co_3O_4 and Fe_3O_4 nano-powders

Scanning electron microscopy (SEM) was employed to investigate the physical form and the sizes of Mn_3O_4 powder, Co_3O_4 powder, Fe_3O_4 powder, Co_3O_4 nano-powder and Fe_3O_4 nano-powder. Silicon carbide, which was used as a diluent, was also studied. The SEM images are shown in Figures 3, 4, 5, 6, 7 and 8, respectively. The crystals in the Mn_3O_4 and Co_3O_4 powders have very similar shapes. In general, the crystals appeared to be large and irregular-shaped. The sizes of the Mn_3O_4 particles varied from about 1 to 25 μm, while for Co_3O_4 the sizes varied from about 1 to 12 μm. Some smooth crystal faces can be easily seen for Co_3O_4. The Fe_3O_4 powder appeared to consist of agglomerates of smaller crystals, as shown in Figure 5. A typical structure is shown in the figure, and is about 60 μm in size. The range varied from about 1 to 60 μm.

The crystals of Co_3O_4 nano-powder, Figure 6, exhibited smaller particles than Co_3O_4 powder, and appeared to be fairly constant in size, about 0.4-0.6 μm, which massed together to give larger agglomerates of up to 11-12 μm. Comparing the Co_3O_4 crystals in the powder form and as a nano-powder, the former are larger and appear better formed than the crystals of the latter. The Fe_3O_4 nano-powder, shown in Figure 7, exhibit irregular crystal shapes with sizes of about 0.3 to10 μm.

Silicon carbide (SiC) was used in the combustion catalysis study as a diluent. Preliminary studies showed that the temperature ramp could not be controlled if the pure oxides were used. Two diluents were studied and SiC was chosen for this purpose. This is discussed in more detail below. Figures 8 and 9 show SEM images of SiC. There are large irregular particles of varying sizes. The particles vary from 5 to 100 μm but were mostly

found in the range of 50-100 μm. The particle sizes of the SiC that was supplied commercially reportedly ranged from 200-450 mesh, which gives a particle size range of 74 to 33 μm.

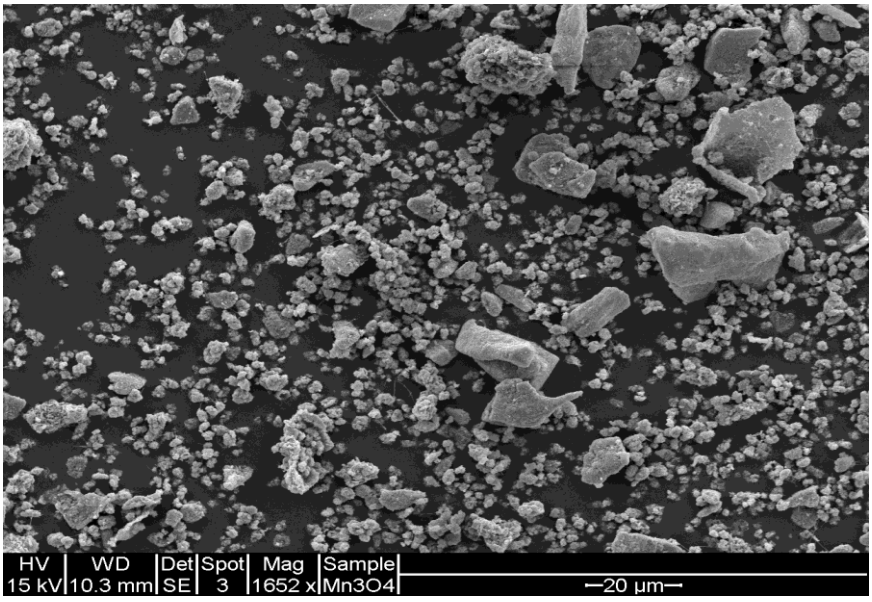

Figure 3. SEM image of Mn_3O_4 powder.

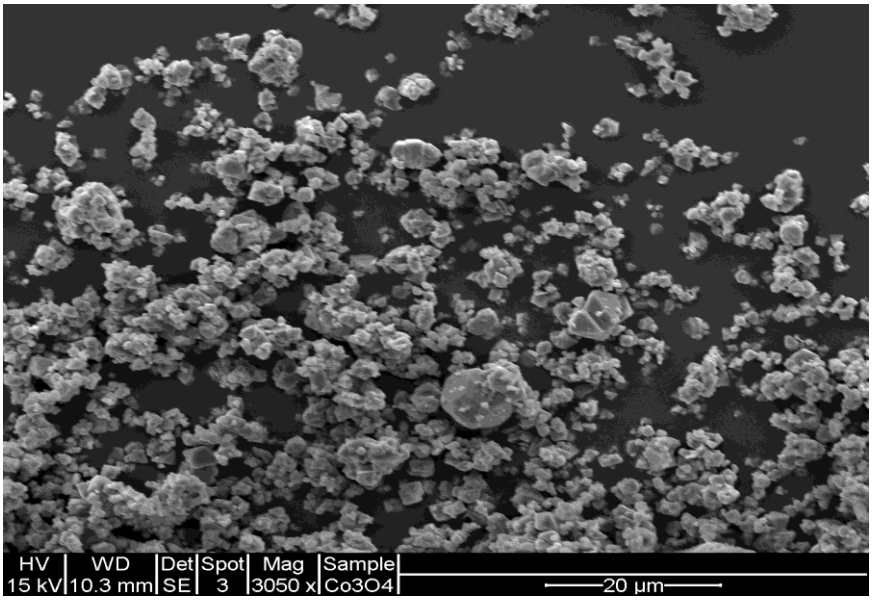

Figure 4. SEM image of Co_3O_4 powder.

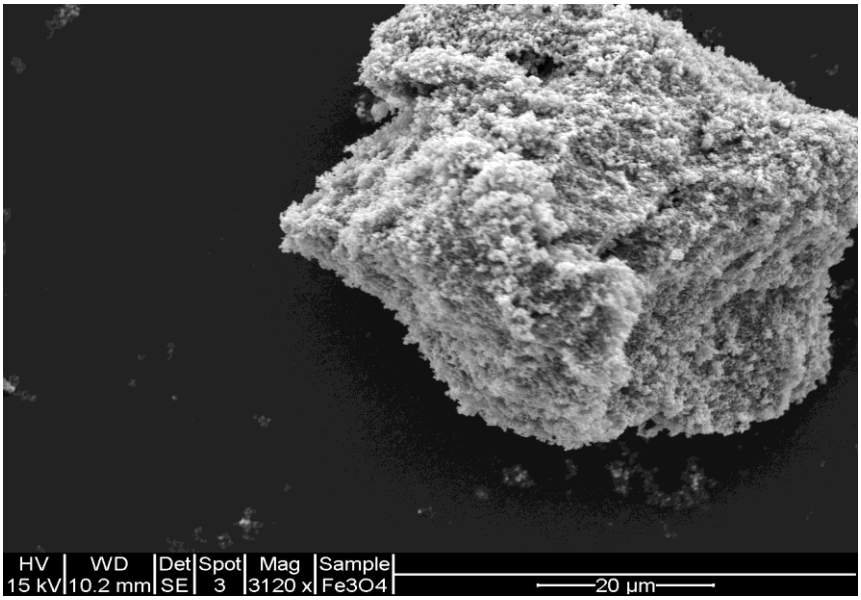

Figure 5. SEM image of Fe_3O_4 powder.

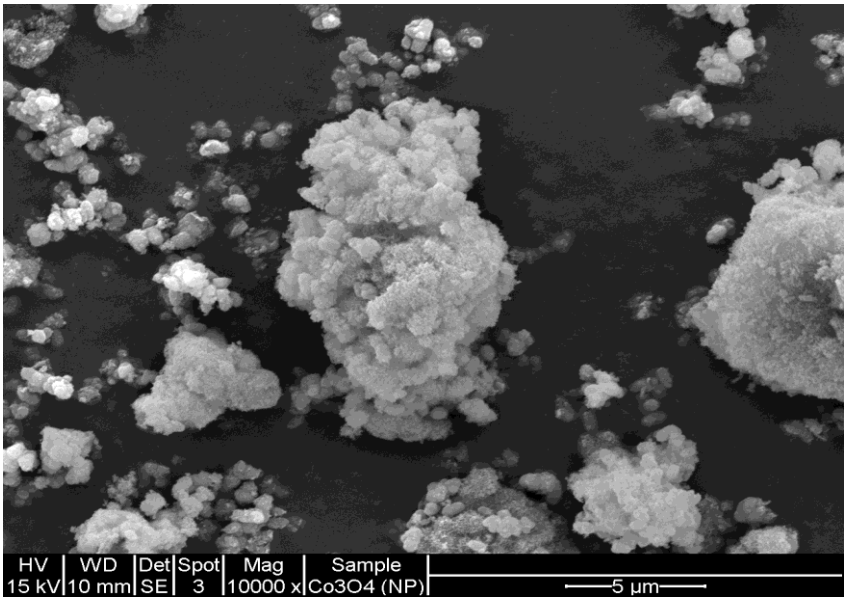

Figure 6. SEM image of Co_3O_4 nano-powder particles.

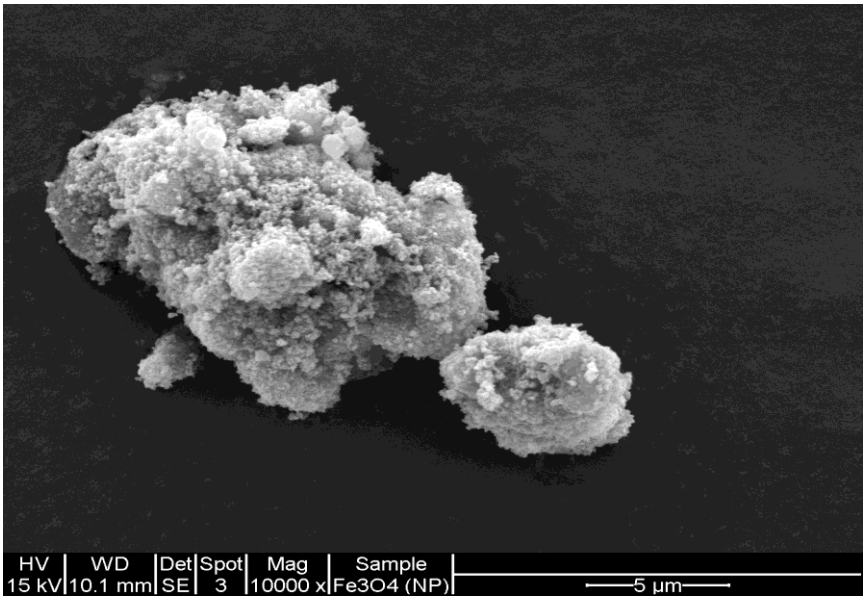

Figure 7. SEM image of Fe_3O_4 nano-powder particles.

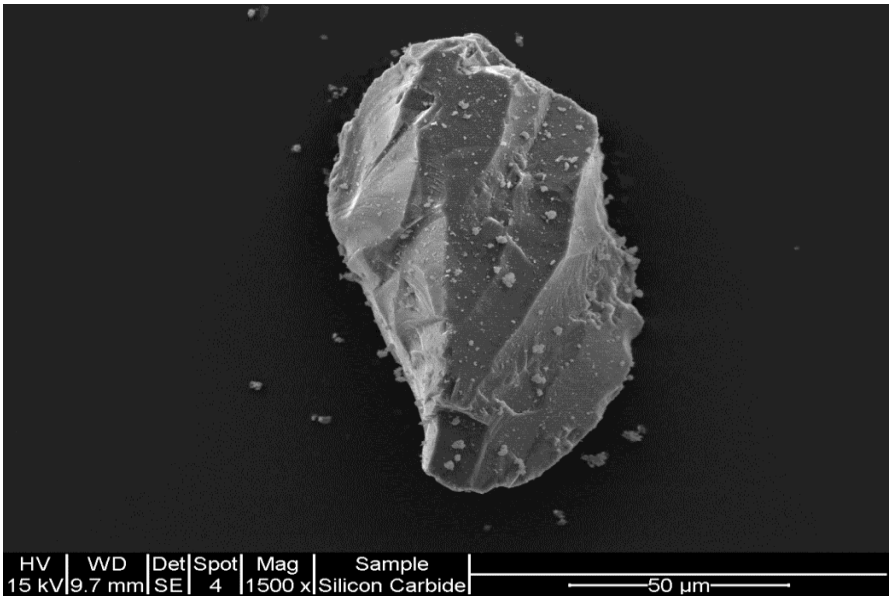

Figure 8. SEM image of silicon carbide (SiC).

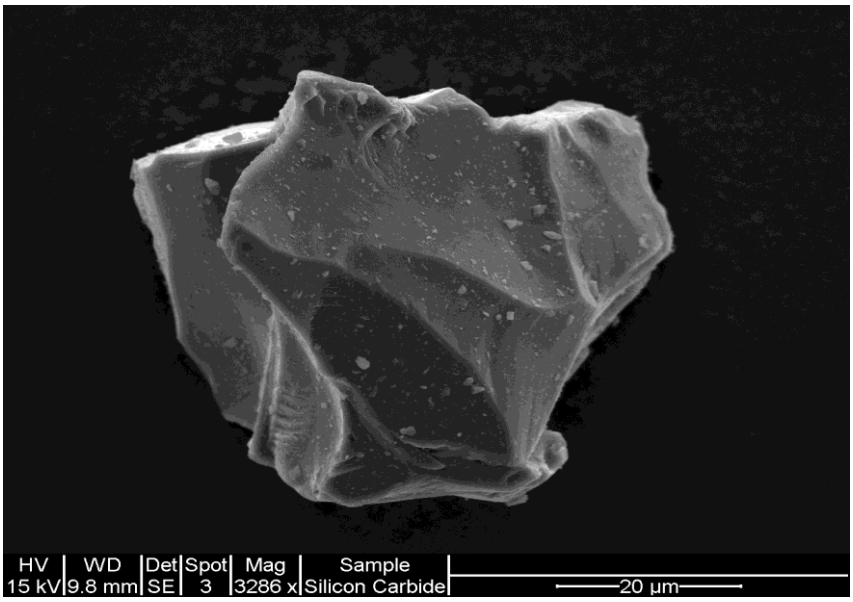

Figure 9. SEM image of silicon carbide (SiC).

4.3.3 TG/DTA investigation

4.3.3.1 Supports for catalysis studies

Preliminary investigations of the combustion of isobutane indicated that the temperature of the catalyst bed was impossible to control if the metal oxides were used on their own. This was a result of the extremely exothermic nature of the combustion reaction. As a result it was decided to use a diluent to enable dispersal of the heat and give control of the catalytic reactions. In this study, two types of support, silica gel (SG) and silicon carbide (SiC), were investigated using TG/DTA studies, which would allow a choice of a suitable diluent. Figure 10 presents the TG/DTA profile of silica gel. The TGA study shows that the support loses mass continuously even up to 1000^{o}C, while the DTA profile shows no strong exothermic or endothermic peaks, except for a weak exothermic peak, corresponding to a small mass loss at ~300^{o}C. It is likely that the continuous mass loss involves the release of water. Thus silica gel was found to be a poor choice and it would have had a detrimental

effect on the catalysis results from particle size variations and movement of the particles in the catalyst bed as a result of the loss of water as the temperature was increased. In contrast, SiC was found to show no loss of mass from room temperature up to about 900^{o}C, as shown in Figure 11, indicating that the support was stable over the temperature range. Also, there was no exothermic or endothermic process over this temperature range indicating that no phase change occurred that could potentially interfere with the catalysis results.

4.3.3.2 TG/DTA studies of Mn_3O_4, Co_3O_4 and Fe_3O_4

TG/DTA was used to study the effects of temperature on Mn_3O_4, Co_3O_4 and Fe_3O_4 as both powders and nano-powders. Two different atmospheric conditions, N_2 and air, were used in this investigation.

The TGA data obtained under a nitrogen atmosphere (not shown) on Mn_3O_4 (powder and nano-powder), Co_3O_4 (powder and nano-powder) and Fe_3O_4 (nano-powder) showed only very slight decreases in their masses up to 600^{o}C, probably from adsorbed water loss, while the DTA results show no sign of any major exothermic or endothermic peaks. This indicates that there are no phase transitions over this temperature range for these compounds. However, the result for Fe_3O_4 was different to the others. The TGA data shows a small increase in the mass starting at ~230^{o}C that is likely associated with the oxidation of Fe_3O_4 to Fe_2O_3. The DTA profile showed a small exothermic peak at 350^{o}C and that also could be related to the structural change from Fe_3O_4 to Fe_2O_3. It would appear that there may have been a slight amount of oxygen present in the TG/DTA study of Fe_3O_4 powder that was not present in the Fe_3O_4 nano-powder. The mass increase did not correspond to complete oxidation of Fe_3O_4 to Fe_2O_3.

A similar study was performed under air, that is, in the presence of oxygen, which is more relevant to the conditions used in the catalysis studies (which consisted of 2 vol % isobutene and 20 vol % of oxygen).

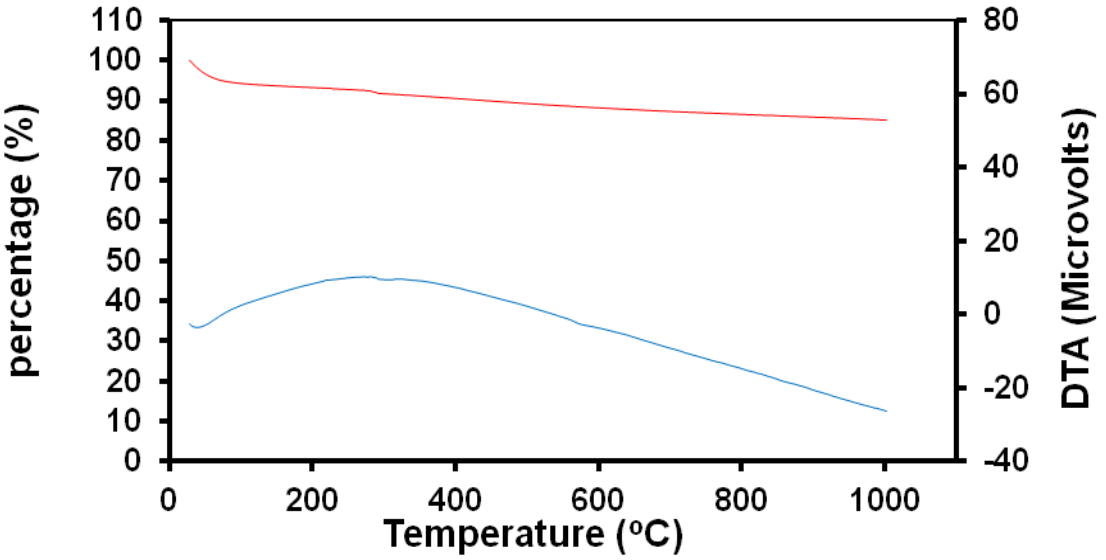

Figure 10. The TGA/DTA profile of silica gel (SG); temperature range from room temperature to ~1000^{o}C (heating rate 20^{o}C/min).

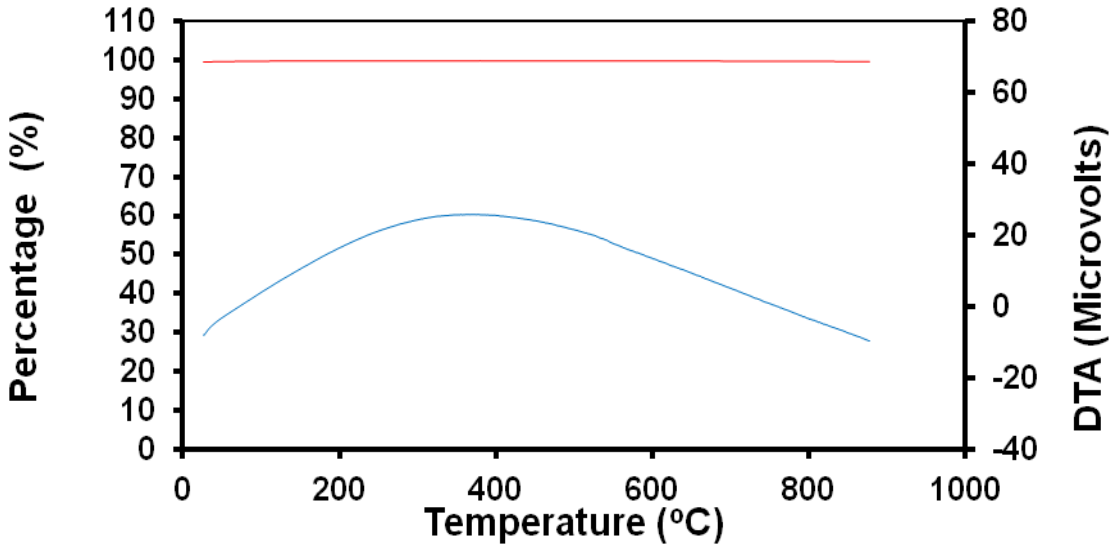

Figure 11. The TGA/DTA profile of silicon carbide (SiC); temperature range from room temperature to ~900^{o}C (heating rate 20^{o}C/min).

The TGA/DTA profiles of Mn_3O_4 powder and nano-powder under an air atmosphere are presented in Figures 12 and 13, respectively. The TGA profile of Mn_3O_4 powder showed no change in mass up to 500^oC, which is above the maximum temperature required for the combustion studies. The TGA result for Mn_3O_4 nanoparticles was slightly different from the Mn_3O_4 powder. Figure 13 shows that Mn_3O_4 nanoparticles lost mass beginning at ~140^oC, which is associated with an exothermic peak at 180^oC. This is likely loss of strongly adsorbed species, such as ethanol (used in the preparation), water or acetone (both used for washing the product) or acetic acid (a product of reaction). After that temperature, no further change in mass was observed up to 500^oC, as was observed for the Mn_3O_4 powder.

The TG/DTA investigation on Co_3O_4 powder and nano-powder in an air atmosphere are shown in Figures 14 and 15, respectively. The TGA study of Co_3O_4 powder shows no mass loss as the temperature increased from room temperature to 500^oC. Moreover, no exothermic or endothermic peaks were detected. The same result was observed for the Co_3O_4 nano-powder.

The TG/DTA profiles for Fe_3O_4 powder and nano-powder in an air environment are displayed in Figures 16 and 17, respectively. The Fe_3O_4 powder increased in mass from ~200 to 400^oC. The DTA presents a weak exothermic peak centered at ~240^oC, which is linked to the increase in mass. This increase in mass corresponded to the transformation of Fe_3O_4 to Fe_2O_3. For Fe_3O_4 nano-powder, the mass began increasing as low as ~50^oC, presumably because of the high surface area and hence greater exposure to oxygen. The DTA profile shows an exothermic trend above ~50^oC, and stronger features from 200-300^oC and at ~600^oC, all corresponding to the oxidation of Fe_3O_4 to Fe_2O_3.

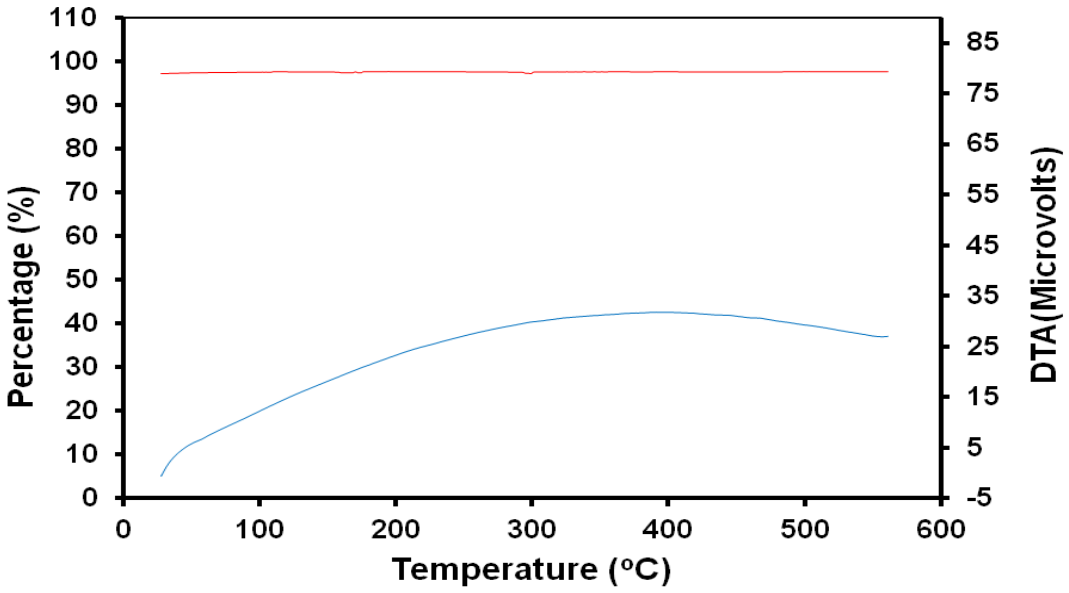

Figure 12. The TGA/DTA profile of Mn_3O_4 powder; temperature range from room temperature to ~560°C (heating rate 20°C/min).

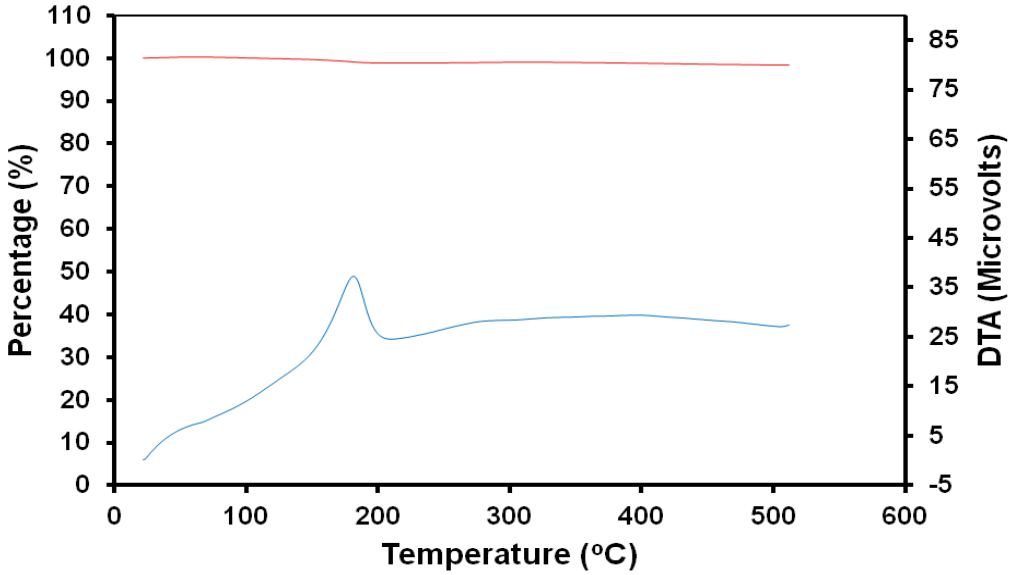

Figure 13. The TGA/DTA profile of Mn_3O_4 nano-powder; temperature range from room temperature to ~510°C (heating rate 20°C/min).

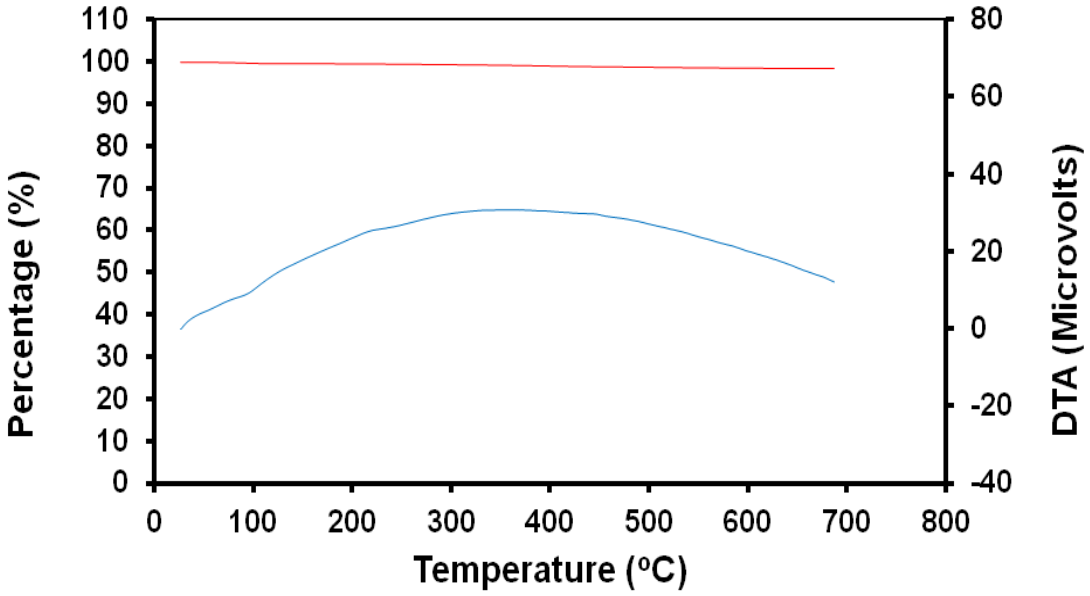

Figure 14. The TGA/DTA profile of Co_3O_4 powder; temperature range from room temperature to ~700°C (heating rate 20°C/min).

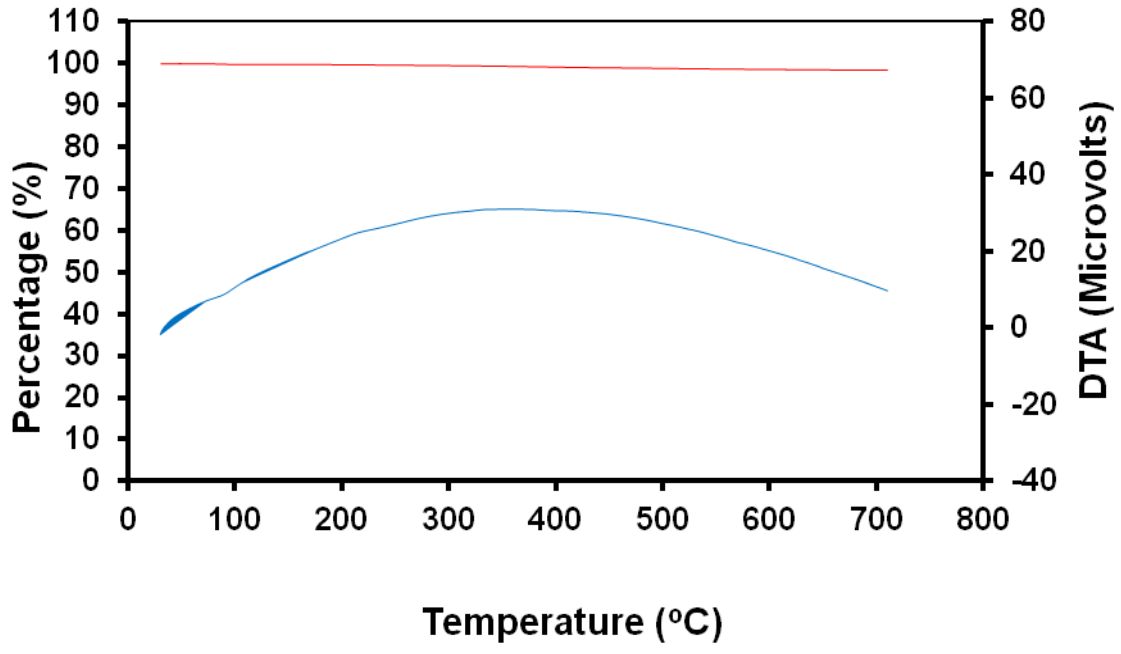

Figure 15. The TGA/DTA profile of Co_3O_4 nano-powder; temperature range from room temperature to ~700°C (heating rate 20°C/min).

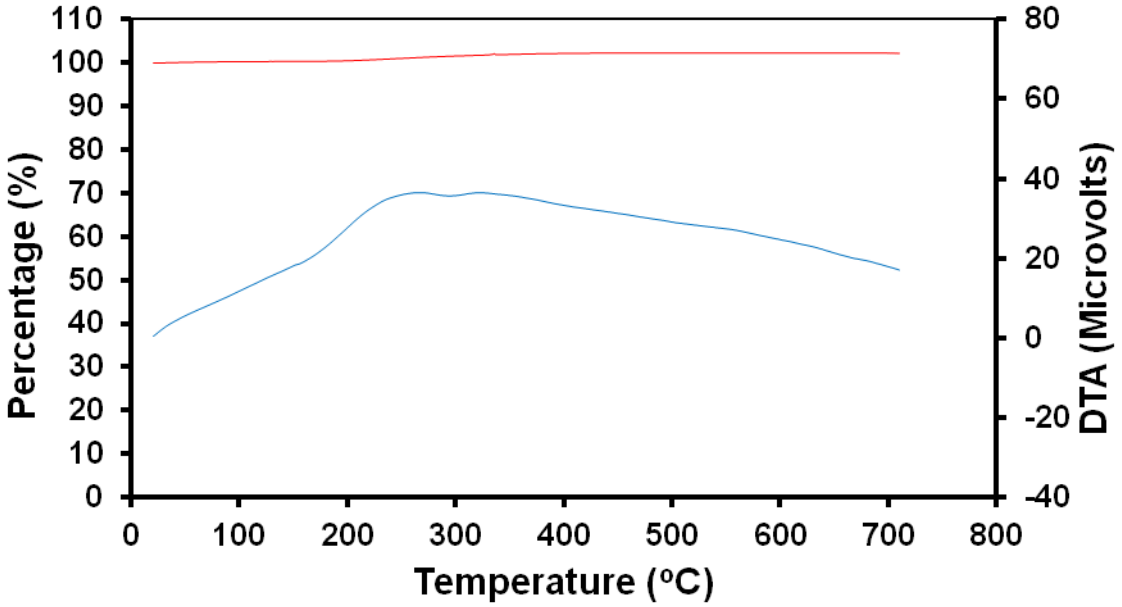

Figure 16. The TGA/DTA profile of Fe_3O_4 powder; temperature range from room temperature to ~700°C (heating rate 20°C/min).

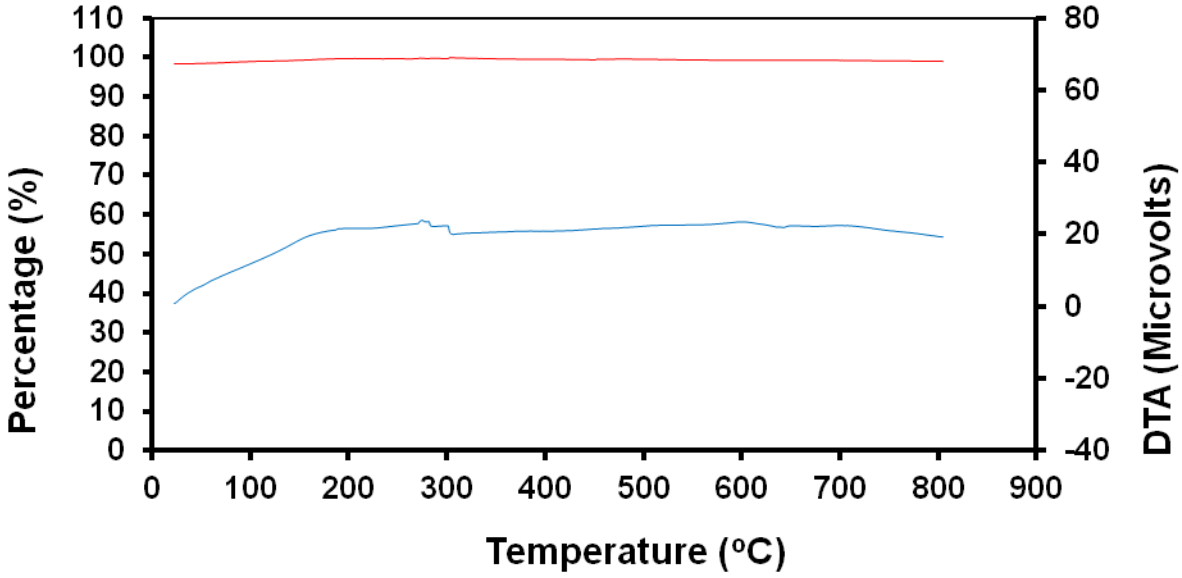

Figure 17. The TGA/DTA profile of Fe_3O_4 nano-powder; temperature range from room temperature to ~700°C (heating rate 20°C/min).

4.3.4 XRD investigation

4.3.4.1 XRD studies of Mn_3O_4, Co_3O_4 and Fe_3O_4 in powders and nano-powders

The X-ray diffraction patterns of Mn_3O_4, Co_3O_4 and Fe_3O_4 as both powders and as nano-powders are presented in Figures 18, 19 and 20, respectively. The diffraction pattern of the commercial Mn_3O_4 powder, as shown in Figure 18, exhibits narrow peaks, however, the synthesized Mn_3O_4 nano-powder pattern shows broader peaks compared with the former, which is consistent with the presence of very small crystals. The XRD pattern of the synthesized Mn_3O_4 nano-powder is consistent with the XRD data on Mn_3O_4 (ICDD 00-24-0734) [24]. An estimate of the particle size based on the Scherrer equation, using the intense (211) line is ~17 nm. This value is in agreement with the data reported by Li *et al.* [33], which is ~10 nm when prepared at 90^{o}C. The size of the particles is consistent with the TEM study, which gave a particle size range of ~6-20 nm.

The XRD patterns of Co_3O_4 and Fe_3O_4, as shown in Figures 19 and 20, present narrow peaks in each case, and much broader and less intense peaks in the nano-powders. Estimates from the Scherrer equation give values of the crystal size of ~28 and ~31 nm for Co_3O_4 and Fe_3O_4 nano-powders respectively. The width of the diffraction lines for Mn_3O_4, Co_3O_4 and Fe_3O_4 powders are much sharper, indicating larger crystal sizes.

Magnetite, Fe_3O_4, is known to oxidize to Fe_2O_3 at high temperatures. In order to establish the temperature of conversion, which may impact on the catalysis studies to be discussed below, a temperature-dependence study of Fe_3O_4 oxidation was carried out. The temperature dependence of the XRD pattern of Fe_3O_4 on the hot-stage platinum strip, is displayed in Figure 21, and was measured at room temperature (25^{o}C), 100, 200, 250, 300, 350, 400, 450 and 500^{o}C in an air atmosphere.

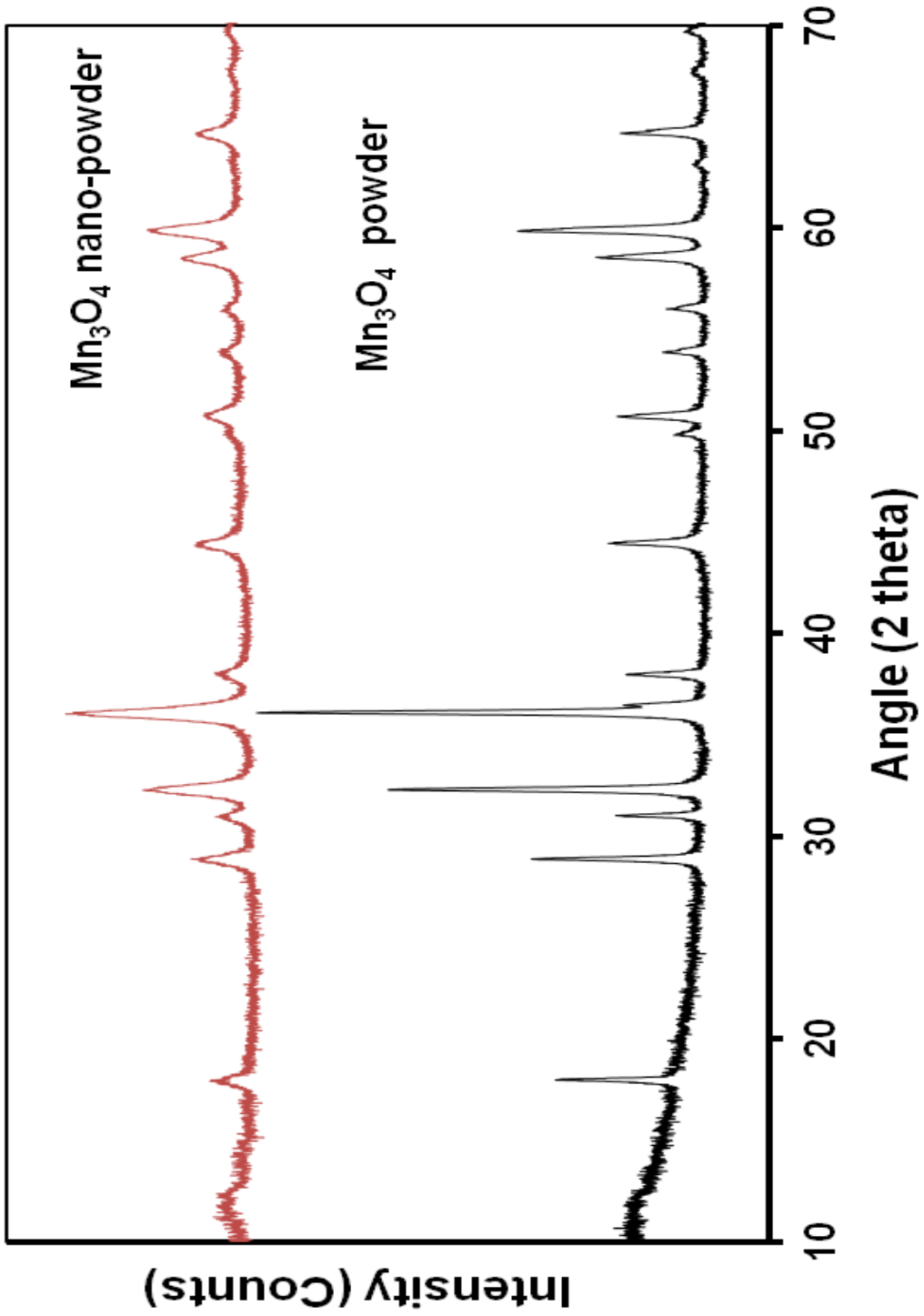

Figure 18. The XRD patterns of Mn_3O_4 powder and nano-powder.

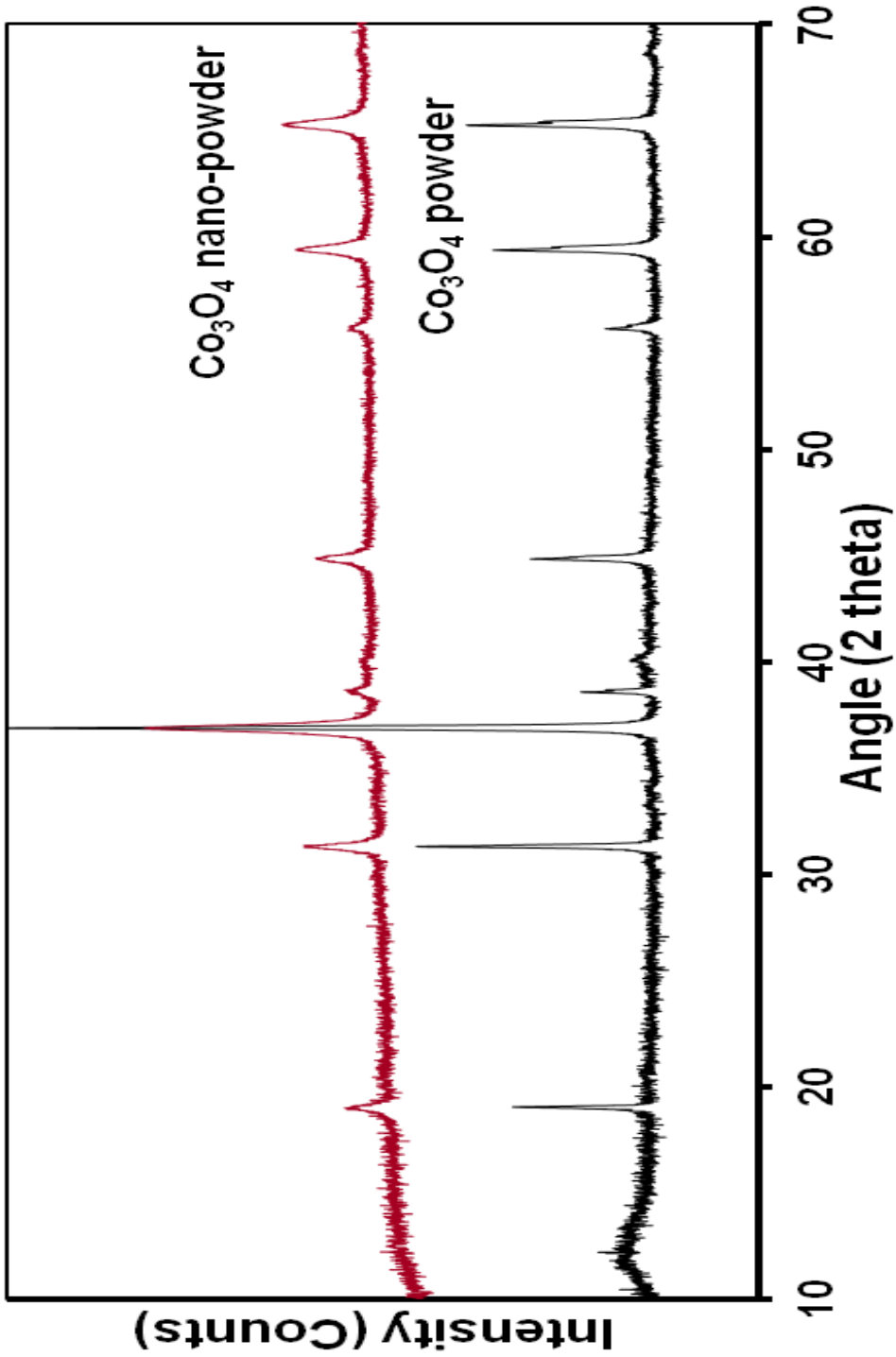

Figure 19. The XRD patterns of Co_3O_4 powder and nano-powder.

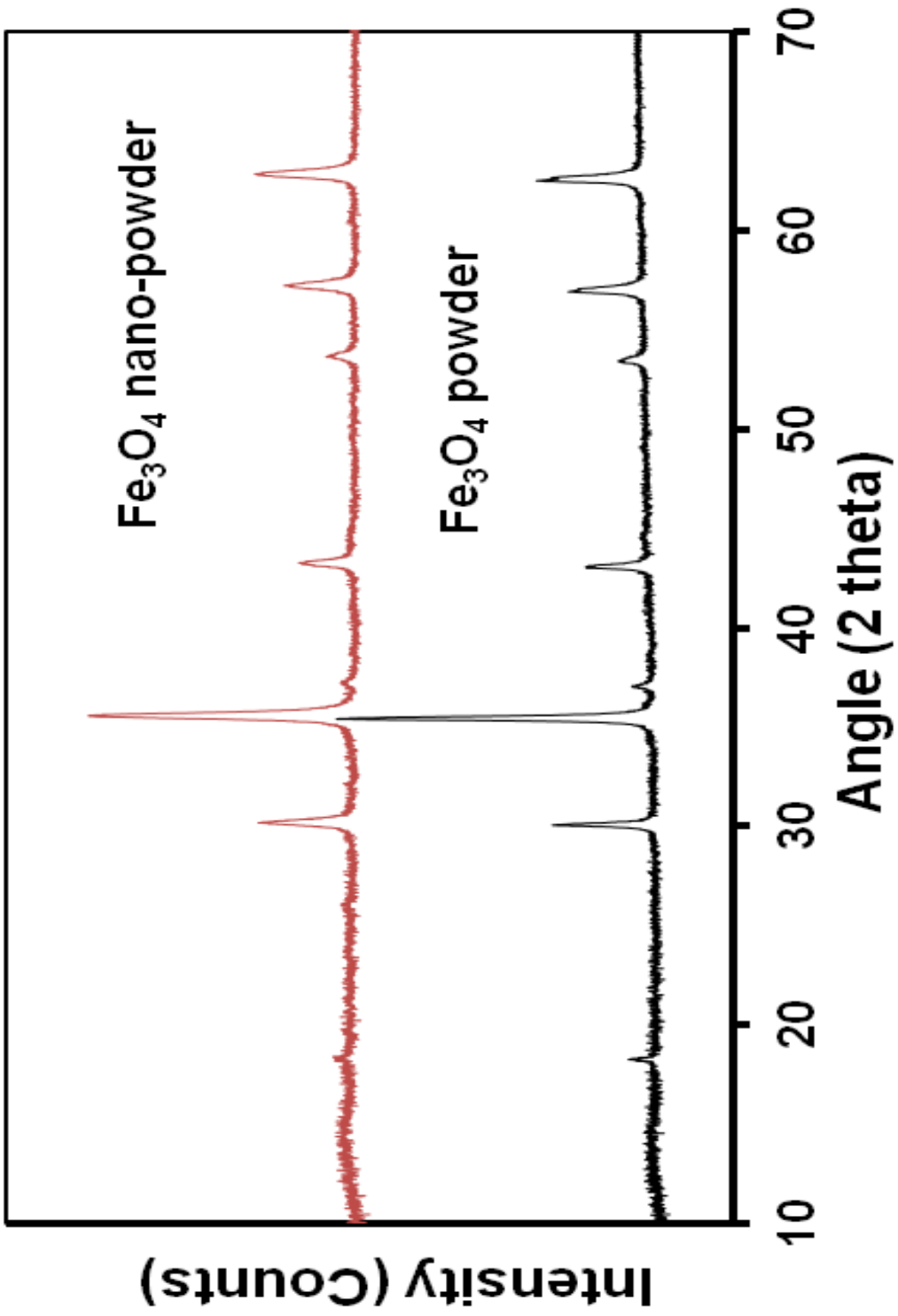

Figure 20. The XRD patterns of Fe_3O_4 powder and nano-powder.

The Fe_3O_4 was mounted on the hot-stage using *n*-hexane. The pattern also reveals two bands corresponding to platinum metal (2θ = 39.6 and 46.1^o), which indicates incomplete coverage, but act as markers. The results show that the pattern at 25^{o}C is different to the pattern at 500^{o}C, which relates to the conversion of Fe_3O_4 to α-Fe_2O_3. It appears that the Fe_3O_4 is stable up to about 250^{o}C, but begins to oxidize above this temperature. The presence of hematite, α-Fe_2O_3 (rhombohedral, hexagonal setting, space group *R*3c (161), a = 5.04 Å, c = 13.75 Å, *Z* = 6, ICDD 01-089-2810) [24] can just be detected at 300^{o}C and above by, for example, strong diffraction peaks that appear at 2θ = 24.1, 33.1, 40.8, 49.4, 62.4 and 63.9^o.

4.3.4.2 XRD studies of Mn_3O_4, Co_3O_4 and Fe_3O_4 in powders and nano-powders with added gold nanoparticles

The XRD patterns of Mn_3O_4 powder, Mn_3O_4 nano-powder, Co_3O_4 powder, Co_3O_4 nano-powder, Fe_3O_4 powder and Fe_3O_4 nano-powder before and after the addition of gold nanoparticles are displayed in Figures 22, 23, 24, 25, 26 and 27, respectively. The 5 mass % of *n*-hexanethiolate-stabilised gold nanoparticles were added to the catalysts as *n*-hexane solutions and the catalysts were thermolysed to remove the thiolate ligands from the gold nanoparticles.

The XRD patterns of all six catalysts show two low intensity peaks for gold metal at 2θ = 38.2^o and 44.4^o, which correspond to the (111) and (200) reflections, respectively. Both gold peaks overlap with diffraction peaks from the Mn_3O_4, but are more observable in Co_3O_4 and Fe_3O_4. This is because of the different types and sizes of the unit cells in these compounds (see above). The gold (111) reflection is the most intense peak, and was used to calculate the sizes of the gold particles using the Scherrer equation for Co_3O_4 and Fe_3O_4 powders and Fe_3O_4 nanopowder. For the other compositions, peak overlap was regarded as too severe to provide meaningful results. However, it is apparent that the gold nanoparticles have aggregated in the all of the M_3O_4 (M = Mn, Co and Fe) powders and nano-powders.

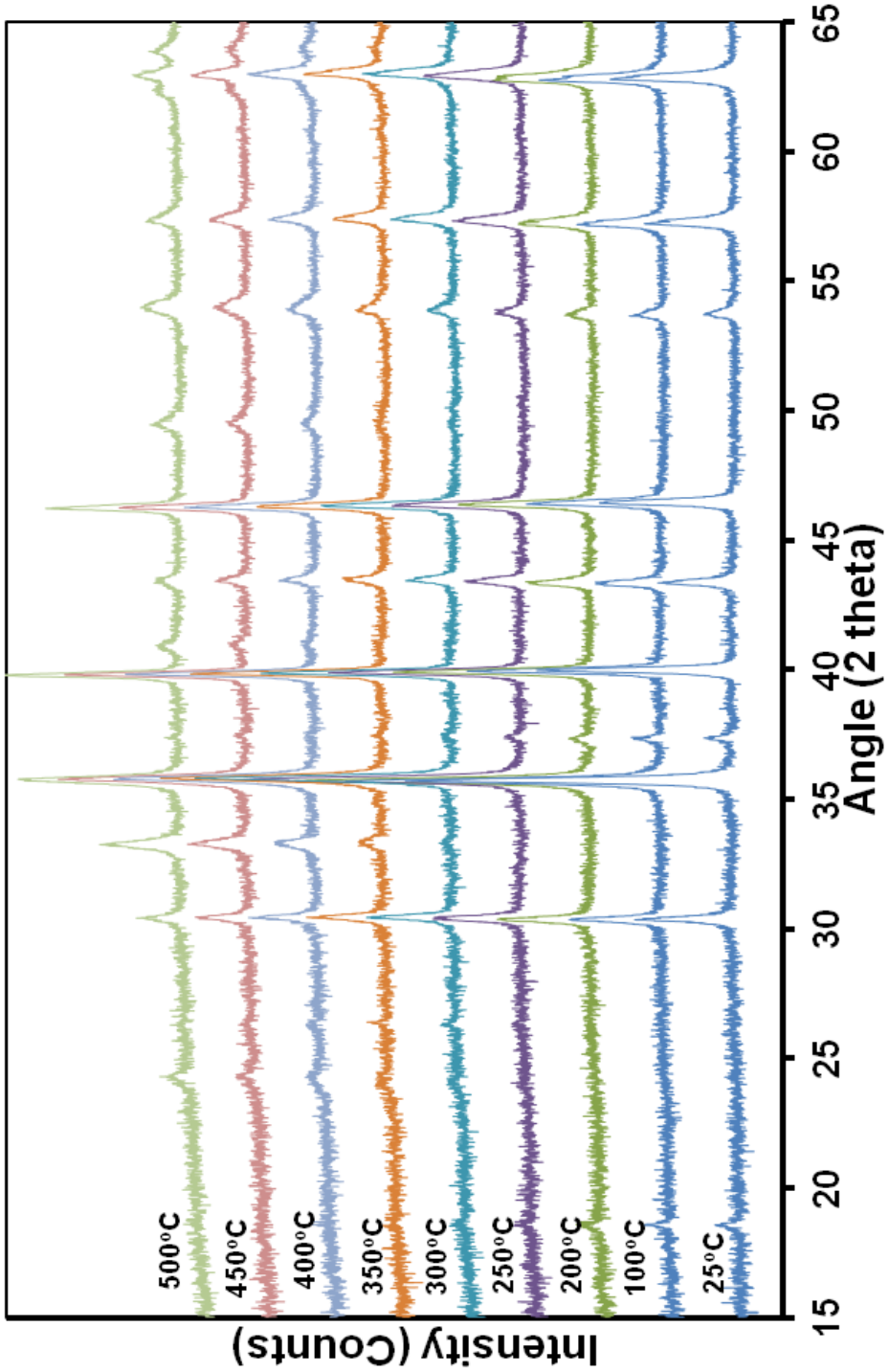

Figure 21. The XRD patterns of Fe_3O_4 at room temperature (~25), 100, 200, 250, 300, 350, 400, 450 and 500^{o}C mounted on a hot-stage platinum strip. (Platinum lines can be observed at 2θ = 39.6 and 46.1^{o}).

The cubic unit cells for Co_3O_4 and Fe_3O_4 were sufficiently different to allow easy estimation of the line widths for the gold particles in these compounds. Table 4 reports the average size of the gold nanoparticles in these three catalyst preparations, which have been calculated using the Scherrer equation. It can be seen that the measured crystallite sizes are much larger than those found in the phosphopolyoxomolybdate study in Chapter 3 (these were 6.0 nm). The gold has aggregated into larger particle sizes for these compounds. This may be related to the adsoption properties of the surfaces of the M_3O_4 (M = Mn, Co and Fe) solids, although another interpretation may be invoked, as discussed below. Using the (111) reflection the sizes of the particles range from 48-71 nm. The values obtained by using the (200) reflection generally agree with the data from the (111) reflection, except for the gold nanoparticles on the Fe_3O_4 nano-powder.

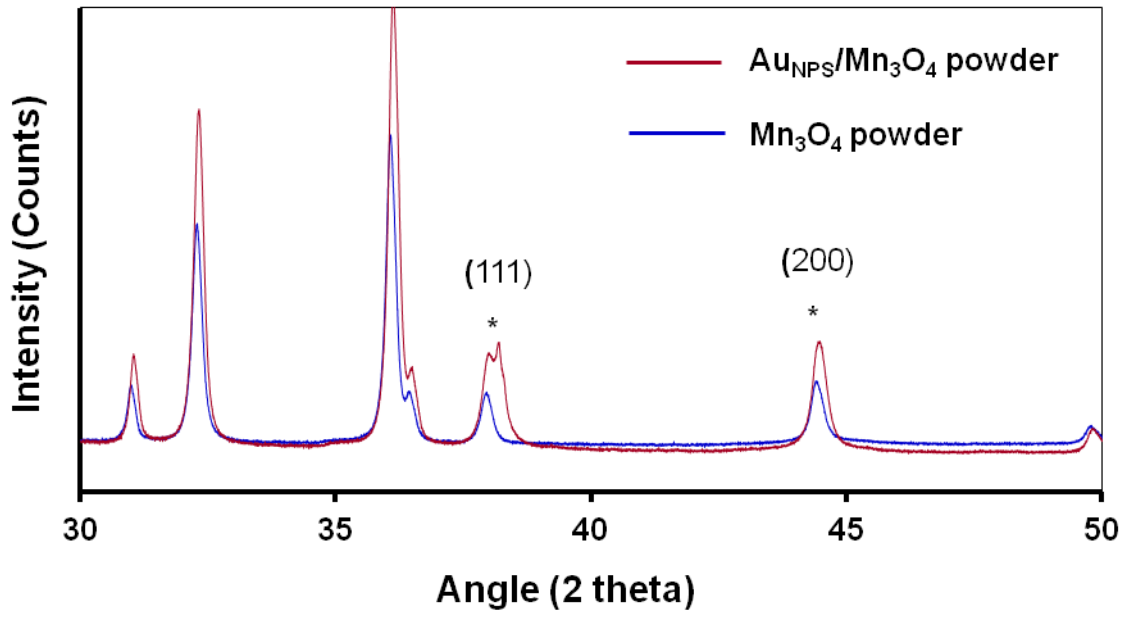

Figure 22. The XRD patterns of Au_{NPS}/Mn_3O_4 and Mn_3O_4 powders.

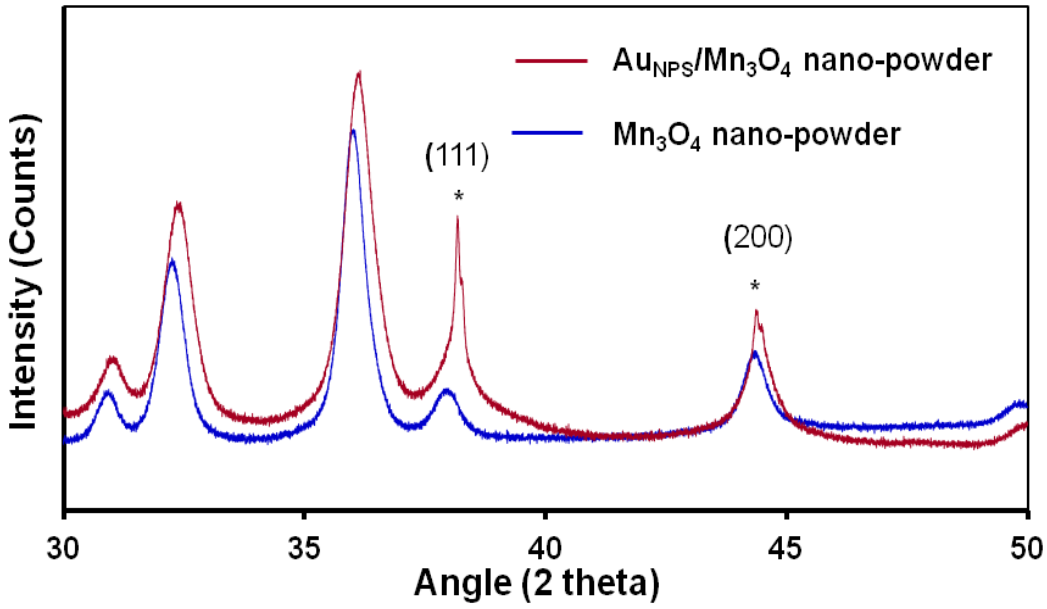

Figure 23. The XRD patterns of Au_{NPS}/Mn_3O_4 and Mn_3O_4 nano-powders.

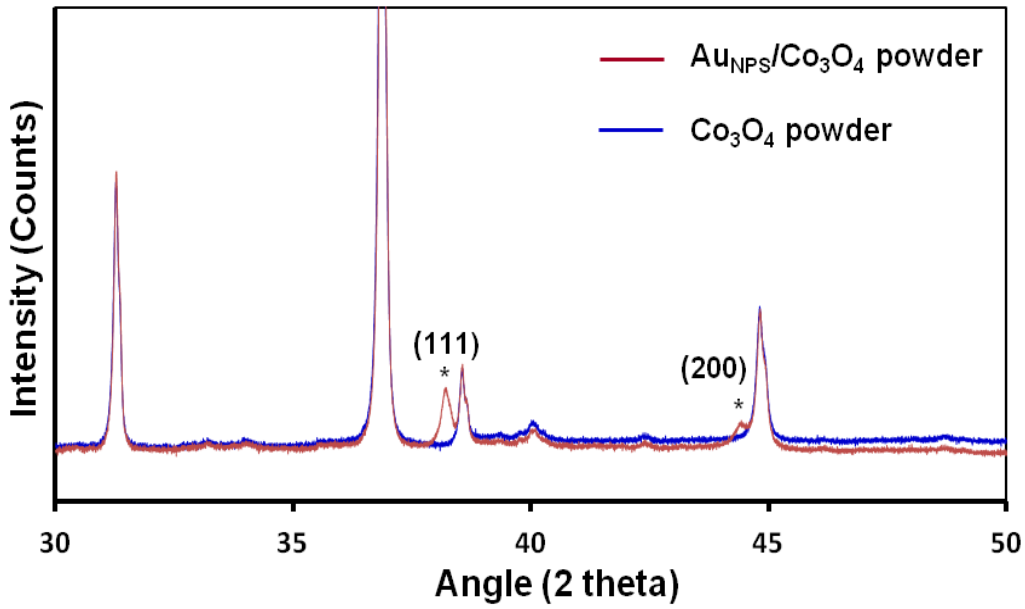

Figure 24. The XRD patterns of Au_{NPS}/Co_3O_4 and Co_3O_4 powders.

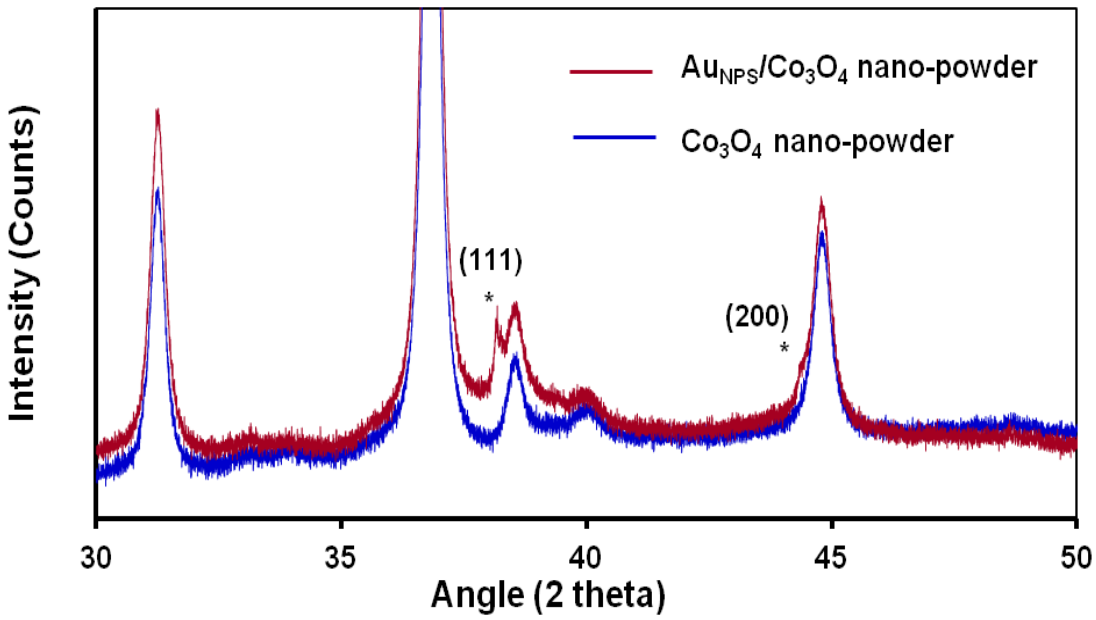

Figure 25. The XRD patterns of Au_{NPS}/Co_3O_4 and Co_3O_4 nano-powders.

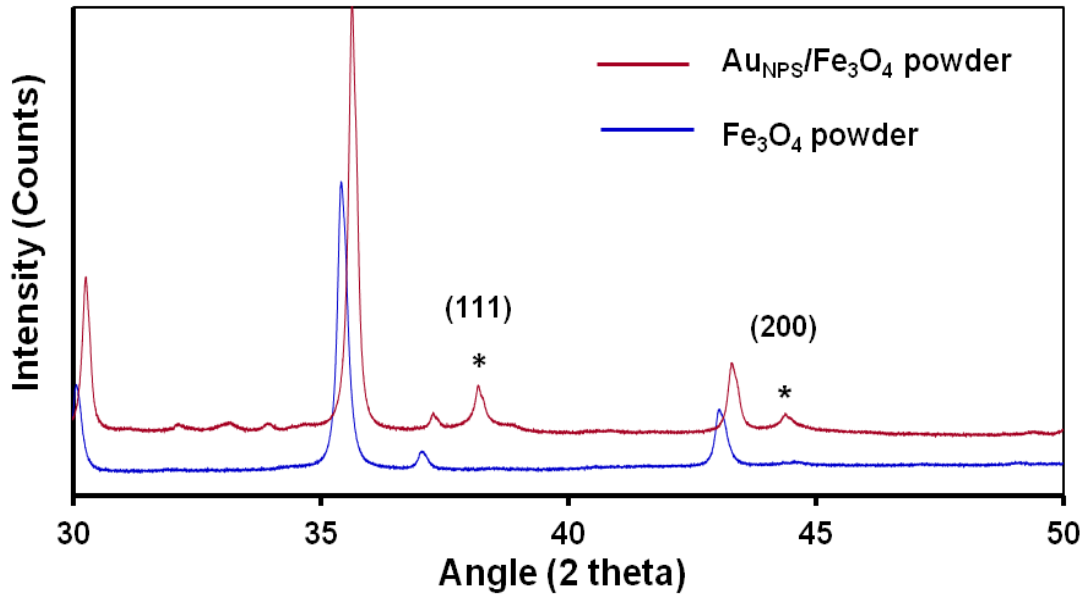

Figure 26. The XRD patterns of Au_{NPS}/Fe_3O_4 and Fe_3O_4 powders.

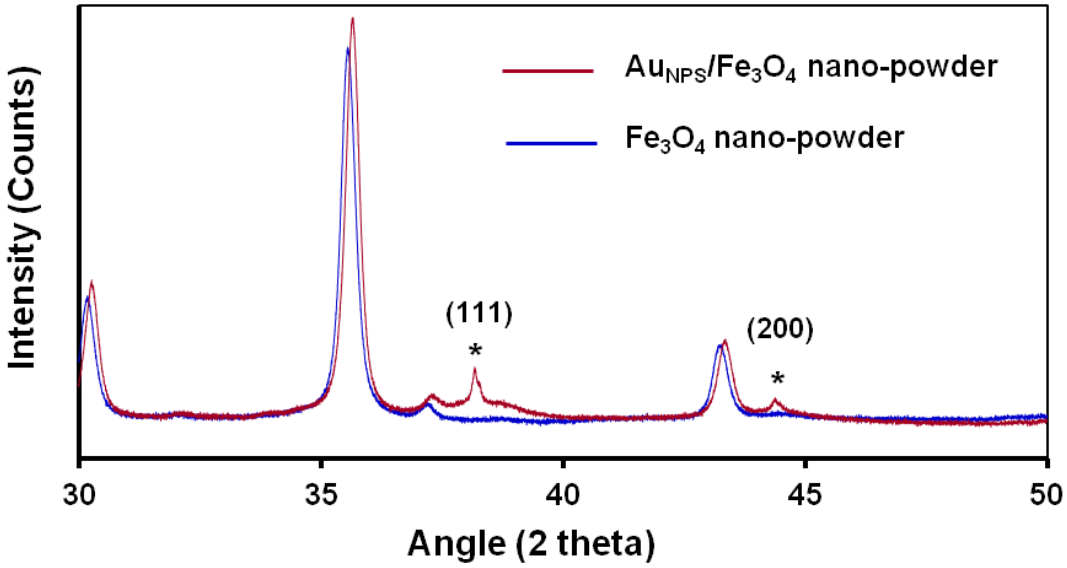

Figure 27. The XRD patterns of Au_{NPS}/Fe_3O_4 and Fe_3O_4 nano-powders.

However, the estimate for the (200) reflection is not regarded as accurate as it was found that the background was difficult to estimate, and the peak was not particularly intense.

Table 4. The gold particle sizes in Au_{NPS}/Co_3O_4 powder, Au_{NPS}/Fe_3O_4 powder and Au_{NPS}/Fe_3O_4 nano-powder.

Catalyst	**Crystallite size (nm)**	
	Miller index (111)	**Miller index (200)**
Au_{NPS}/Co_3O_4 powder	48	49
Au_{NPS}/Fe_3O_4 powder	59	60
Au_{NPS}/Fe_3O_4 nano-powder	71	54 (weak intensity, background difficult to estimate)

In the case of the Fe_3O_4, the aggregation of the gold nanoparticles may be associated with the oxidation of the compound to hematite, α-Fe_2O_3. This process involves a complete

change in structure, most likely leading to severe disruption of the surface of the Fe_3O_4 particles as oxidation occurs. This process will, in turn, involve considerable movement of the gold nanoparticles loaded onto the oxide surface, likely leading to aggregation, and hence to the observed larger gold particle sizes. Both Mn_3O_4 and Co_3O_4 show no such structural transformations over the temperature range from room temperature to 300^oC (the temperature of calcination of the gold nanoparticle catalysts following loss of the *n*-hexanethiolate stabilizing ligands), based on the TG/DTA studies (see Section 4.3.3.2). However, the larger gold particle size found for the Co_3O_4 nanoparticles suggests some similar process is operational, perhaps involving slight oxidation of Co(II) to Co(III) in the surface structure in the vicinity of the gold nanoparticles This may lead to a similar gold nanoparticle aggregation. The decomposition of the *n*-hexanethiolate stabilized gold nanoparticles is very highly exothermic, and if hot spots occur at the oxide surface at the gold nanoparticles, some surface oxidation may occur promoted by the presence of the gold nanoparticles (no oxidation normally occurs up to 500^oC, according to the TG/DTA study, Section 4.3.3.2), leading to surface disruption and to aggregation of the gold nanoparticles.

4.3.5 XPS analysis

XPS was used to examine the catalysts, both before and after a catalysis run. The XPS data on Mn_3O_4 and Co_3O_4 powders and nano-powders, and on the Au_{NPS}/Mn_3O_4 and Au_{NPS}/Co_3O_4 powders and nano-powders are presented in Table 5. A list of data on Mn_3O_4 and Co_3O_4 and other reference compounds is given in Table 6. These have been obtained from the NIST database [34]. The binding energy data on Mn_3O_4 and Co_3O_4 as both powders and nano-powders agree with the literature data. In all cases, only single peaks corresponding to the $2p_{3/2}$ and $2p_{1/2}$ peaks can be observed. Although both Mn_3O_4 and Co_3O_4 consist of mixtures of the oxidation states (II) and (III), no separate peaks for the individual oxidation states can be resolved. For example, Oku and Hirokawa have reported the XPS data on

various manganese oxides and oxy-hydroxides including Mn(II)O, α-Mn_2(III)O_3, γ-Mn_2(III)O_3, β-Mn(IV)O_2, γ-Mn(III)OOH and Mn_3(II,III)O_4 [35]. The study showed that the two oxidation states of Mn_3O_4 were undetectable by XPS investigation.

Table 5. The XPS data on Mn_3O_4 and Co_3O_4 powders and nano-powders, and on the Au_{NPS}/Mn_3O_4 and Au_{NPS}/Co_3O_4 powders and nano-powders following catalysis.

Compound	**Au Binding Energy (eV)**		**Mn Binding Energy (eV)**		**Co Binding Energy (eV)**	
	$4f_{7/2}$	**$4f_{5/2}$**	**$2p_{3/2}$**	**$2p_{1/2}$**	**$2p_{3/2}$**	**$2p_{1/2}$**
Metal oxides:						
Mn_3O_4 powder	-	-	641.9	653.2	-	-
Mn_3O_4 nano-powder	-	-	641.9	653.3	-	-
Co_3O_4 powder	-	-	-	-	780.4	796.0
Co_3O_4 nano-powder	-	-	-	-	780.2	795.5
Spent catalysts:						
Au_{NPS}[a]/Mn_3O_4 powder	- [b]	- [b]	641.9	653.3	-	-
Au_{NPS}/Mn_3O_4 nano-powder	84.2 85.5	87.9 89.5	642.7	654.4	-	-
Au_{NPS}/Co_3O_4 powder	- [b]	- [b]	-	-	781.7	797.2
Au_{NPS}/Co_3O_4 nano-powder	84.5 85.8	88.0 89.0	-	-	780.7	796.1

[a] NPS = Nanoparticles. [b] See text for discussion of this data.

The binding energy data on the spent catalysts, including that on gold, are also given in Table 6. For Mn_3O_4 and Co_3O_4 the $2p_{3/2}$ and $2p_{1/2}$ peaks are generally consistent with the data on the original compounds, suggesting that no significant conversions to other oxides have occurred, and that is there has been no apparent oxidation of Mn_3O_4 and Co_3O_4.

However, it should be pointed out that the binding energy ranges of the Mn and Co $2p_{3/2}$ and $2p_{1/2}$ peaks for possible oxidation products, *i.e.* Mn_2O_3 and Co_2O_3, are very similar to those of the mixed oxidation state products, with overlapping ranges, so that local surface oxidation of Mn(II) and Co(II) in both Mn_3O_4 and Co_3O_4 cannot be ruled out. The gold data for the normal powdered samples could not be successfully obtained. The signal-to-noise for the gold peaks was insufficient to allow curve fitting of the data, although it was evident that both Au(0) and oxidised gold were present.

Table 6. Reference compounds taken from NIST data base [34].

Compound	**Au Binding Energy (eV)**		**Mn Binding Energy (eV)**		**Co Binding Energy (eV)**	
	$4f_{7/2}$	**$4f_{5/2}$**	**$2p_{3/2}$**	**$2p_{1/2}$**	**$2p_{3/2}$**	**$2p_{1/2}$**
Mn_3O_4	-	-	641.10-641.90	653.10-653.20	-	-
$(Mn^{II})O$	-	-	640.40-642.50	653.40	-	-
$(Mn^{III})_2O_3$	-	-	641.20-642.80	653.40-653.70	-	-
$(Mn^{III})OOH$	-	-	641.50-641.70	-	-	-
Co_3O_4	-	-	-	-	779.3-780.7	794.6-797.6
$(Co^{III})_2O_3$	-	-	-	-	779.9-781.3	797.1
Au (foil)	84.1	87.7	-	-	-	-
$Na[Au^{I}(O_2CCH_2CH(SH)CO_2]$	84.9	-	-	-	-	-
$Au^{I}Cl$	84.60	88.30	-	-	-	-
$(Au^{III})_2O_3$	85.9	-	-	-	-	-

The poor signal-to-noise for these spent catalysts is likely due to the extensive dilution of the metal oxides with the diluent SiC, combined with the low loading of gold in the samples (5 mass %). However, the gold signal for the nano-powdered samples did allow the gold peaks to be resolved, resulting in the identification of both Au(0) and Au(I). It may be that the relative sizes of the powders relative to those of the nanoparticles, both in relation to that of the SiC, plays some role in the intensity of the gold XPS signal. The Au(I) species is again likely to be AuO^- [36], as has been discussed in Chapter 3 (Section 3.4.2).

4.3.6 Surface area investigation

The surface areas of several of the compounds used in the complete oxidation of isobutane were measured using the BET method with nitrogen adsorption. The surface areas and pore information are listed in Table 7. It can be seen that the surface areas of the powders ranged from 2.5 to 10 m^2 g^{-1}, while the nano-powders had surface areas that were considerably greater, and ranged from 41 to 76 m^2 g^{-1}. The Mn_3O_4 nano-powder exhibited ~10% of its surface area for pore diameters below 20 Å, while all exhibited mesoporosity.

Table 7. The BET surface areas and pore information for Mn_3O_4, Co_3O_4, Fe_3O_4 and Fe_2O_3 in powders and nano-powders.

Compound	**BET surface area (m^2 g^{-1}) (error = ± 1 m^2 g^{-1})**	**Porosity**
Mn_3O_4 powder	7	mesoporous,
Mn_3O_4 nano-powder	76	microporous, mesoporous
Co_3O_4 powder	2	mesoporous
Co_3O_4 nano-powder	41	mesoporous
Fe_3O_4 powder	7	mesoporous
Fe_2O_3	10	mesoporous

4.4 Catalysis Studies

4.4.1 The combustion of isobutane over the M_3O_4 oxides (where M = Mn, Co and Fe) - catalysis studies with and without added gold nanoparticles

In preliminary studies of the combustion of isobutane using Mn_3O_4, it was observed that the reaction was extremely exothermic, such that the temperature of the catalyst bed could not be controlled. Therefore it was decided to use a diluent for the M_3O_4 (M = Mn, Co and Fe) oxide catalysts, both in the absence and presence of added gold nanoparticles. Prior to further catalysis studies being undertaken, two potential diluents were investigated. These included a silica gel and silicon carbide. As noted above, silica gel was found to be unsuitable as it continuously lost mass with increasing temperature (see Section 4.3.3.1), likely leading to particle size variations and disruption of the catalyst bed. Silicon carbide was chosen as the thermal diluent as it showed no mass loss or phase changes from room temperature to ~900^{o}C, which covered the expected temperature range of the combustion reactions.

Studies of the combustion of isobutane using the M_3O_4 (M = Mn, Co and Fe) oxide catalysts, as both powders and nano-powders, and in the absence and presence of added gold nanoparticles, involved stepping through sequential rises in temperature, allowing equilibration of the system to occur (using a 5-10 minute 'dwell' time), followed by GC analysis of the residual isobutane in the outflow from the catalysis reactor. This generally involved at least three separate GC determinations at each temperature, to ensure that equilibration had been achieved. The data at each temperature were averaged. The temperature was varied from room temperature to those at which the conversion of isobutane was 100%. The oxidation products CO_2, CO and H_2O were not determined, except that at about 20 to 30% conversion of isobutane, the gaseous outflow from the catalyst reactor was sampled using infrared spectroscopy to determine the presence of either CO and/or CO_2. Catalysis studies were made involving variations in the ratio of M_3O_4 oxide catalyst (always

kept at 0.1 g) to SiC diluent, the flow rate and composition of the gas mixture and the addition of gold nanoparticles to the M_3O_4 oxide catalyst. Standard conditions were a 1 mL/min flow of isobutane, 39 mL/min of nitrogen and 10 mL/min oxygen, giving a total flow of 50 mL/min of gas through the reactor. Thus the composition of the gas mixture was 2 vol % isobutane, 20 vol % of oxygen, with the remainder nitrogen. The isobutane:oxygen ratio was 1:10. For complete combustion of isobutane to CO_2 and H_2O, the stoichiometric equation is:

$$2C_4H_{10\,(g)} + 13O_{2\,(g)} \rightarrow 8CO_{2\,(g)} + 10H_2O_{\,(g)} \quad (1)$$

Thus the isobutane:oxygen ratio under the above (standard) conditions was well in excess of the required stoichiometric ratio (1:6½). Variations in the isobutane:oxygen ratio were investigated, as noted above.

Important criteria in the combustion reaction were the temperature at which the reaction began (T_i), the temperature at which 50% conversion ($T_{50\%}$) occurred, and the temperature at which the % conversion of isobutane reached 100% ($T_{100\%}$). Moreover, the % conversion of isobutane at each temperature was converted to a rate, and an Arrhenius plot provided the apparent activation energy (E_{app}). For the Arrhenius plot analysis, data were restricted to a % conversion of >~5%, and a maximum of <~30%, giving a minimum of 4 data points, while at least 5 points were used on a routine basis. Linear regression coefficients were always greater than 0.979 for these analyses.

4.4.1.1 Catalysis using Mn_3O_4 powders and nano-powders

4.4.1.1.1 Dependence on Mn_3O_4:SiC ratio

The effect of varying the Mn_3O_4:SiC ratio was made, using Mn_3O_4 powder, in which the mass of Mn_3O_4 was kept at 0.1 g and the masses of SiC were 0.4, 0.5, 0.7 and 1.0 g. The relevant data are given in Table 8. A typical "S-shaped" reaction profile is shown in Figure

28 for the 0.1/1.0 g Mn_3O_4/SiC study, and the resulting Arrhenius plot is given in Figure 29. These types of plots are typical of all the combustion studies, except where indicated below.

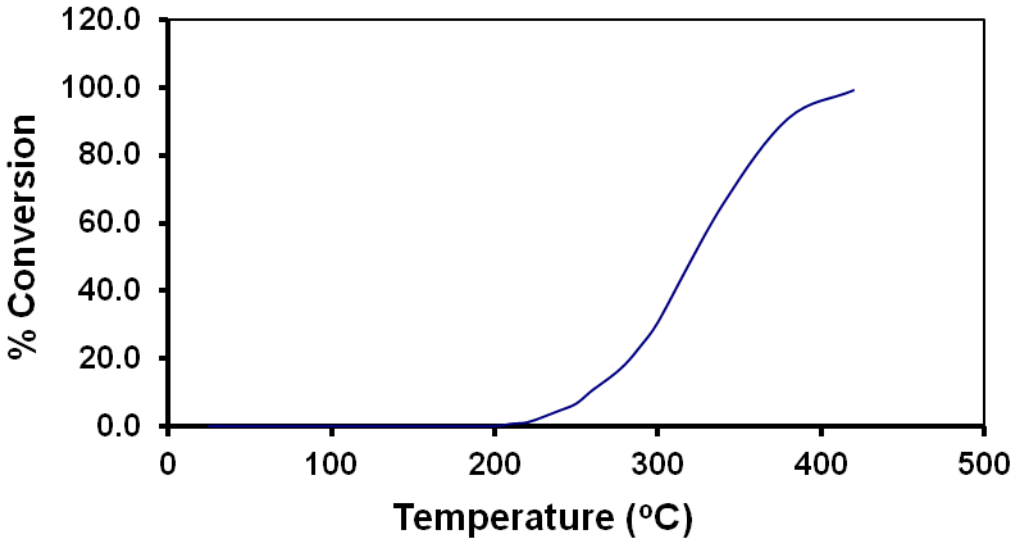

Figure 28. The reaction profile for the complete oxidation of isobutane using Mn_3O_4/SiC (0.1 g/1.0 g); isobutane:oxygen = 1:10; flow rate = 50 mL/min.

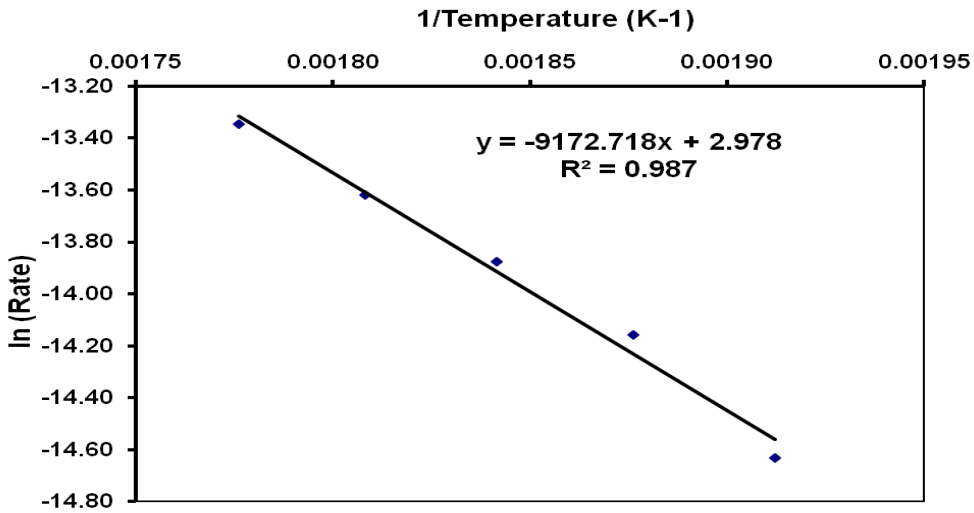

Figure 29. The Arrhenius plot for the oxidation of isobutane using Mn_3O_4/SiC (0.1 g/1.0 g); isobutane:oxygen = 1:10; flow rate = 50 mL/min.

Table 8. Catalysis data for the combustion of isobutane using Mn_3O_4 powder – Mn_3O_4 to SiC dependence: masses of catalyst and SiC, T_i, $T_{50\%}$, $T_{100\%}$ and E_{app} (flow rate = 50 mL/min).

Compound	**Mass of Mn_3O_4 (g)**	**Mass of SiC (g)**	**T_i (^oC)**	**$T_{50\%}$ (^oC)**	**$T_{100\%}$ (^oC)**	**E_{app} (kJ/mol)**
Mn_3O_4 (powder)	0.1	0.4	240	320	450	84(8)
	0.1	0.5	200	310	410	76(6)
	0.1	0.7	200	330	420	82(2)
	0.1	1.0	205	320	420	76(5)

From the results of the increasing amount of SiC to Mn_3O_4, it is apparent that there is little difference between the four studies, showing that addition of SiC has no significant effect above the lowest added amount (0.4 g). The slightly higher T_i, $T_{100\%}$ and E_{app} values for the lowest dilution of Mn_3O_4 with SiC may reflect a small lack of thermal control. Dilution was therefore kept above 0.1 g of Mn_3O_4 to 0.5 g of SiC for the remainder of the studies. The mean apparent activation energy is 80 ± 4 kJ/mol, and excluding the lower dilution study this value is 78 ± 3 kJ/mol. This value is greater than the range of values observed for the combustion of isobutane over palladium and platinum metals, 52 to 56 kJ/mol, but comparable to the value found for nickel metal, 75 kJ/mol [37]. The value for E_{app} found in the present studies is also less than the value observed for the combustion of propane over Mn_3O_4, as expected for an increasing molecular size, which was 84 kJ/mol [38].

4.4.1.1.2 Dependence on flow rate

Studies were also performed using Mn_3O_4 powder, with a constant Mn_3O_4/SiC dilution of 0.1 g/0.5 g. The flow rate data are given in Table 9. There appears to be little dependence on flow rate over the range used in the studies, although the E_{app} value for the lowest flow rate is slightly less than the other values. The $T_{50\%}$, $T_{100\%}$ and E_{app} data for the

two highest flow rates are consistent, and the E_{app} values are in agreement with the values found above. Flow rates were thus kept at 50 mL/min for the present studies.

Table 9. Catalysis data for the combustion of isobutane using Mn_3O_4 powder - flow rate dependence: masses of catalyst and SiC, flow rate, T_i, $T_{50\%}$, $T_{100\%}$ and E_{app}.

Compound	**Mass ratio Mn_3O_4/SiC**	**Flow rate (mL/min)**	**T_i (^oC)**	**$T_{50\%}$ (^oC)**	**$T_{100\%}$ (^oC)**	**E_{app} (kJ/mol)**
Mn_3O_4 (powder)	0.1/0.5	36.6	170	330	400	59(2)
	0.1/0.5	50.0	200	310	410	76(6)
	0.1/0.5	64.1	170	310	410	77(2)

4.4.1.1.3 Dependence on isobutane to oxygen ratio

The effect of varying the isobutane to oxygen ratio was investigated, ranging from as low as 1:6, which is below that required for complete combustion, to 1:15. The data in Table 10 are fairly consistent, particularly the $T_{50\%}$ and E_{app} data. This indicates that there is no dependence on the oxygen concentration for the oxidation reaction, which is consistent with a Mars-van Krevelan mechanism. Interestingly there was no evidence for formation of isobutene or fragment species such as propane and propene in the 1:6 Mn_3O_4:oxygen study, despite the ratio being less than that required for complete combustion to CO_2. The GC capillary column used in these studies was especially chosen such that it was capable of resolving low molecular weight hydrocarbons, and in this case no evidence of other species besides unreacted isobutane was observed. Further discussion of this observation and its relevance to the combustion reaction will be presented below.

Table 10. Catalysis data for the combustion of isobutane using Mn_3O_4 powder – oxygen dependence: masses of catalyst and SiC, flow rates for isobutane (IBU) and oxygen, T_i, $T_{50\%}$, $T_{100\%}$ and E_{app}.

Compound	**Mass ratio Mn_3O_4 /SiC**	**Flow rate 50 (mL/min)**		**T_i (^oC)**	**$T_{50\%}$ (^oC)**	**$T_{100\%}$ (^oC)**	**E_{app} (kJ/mol)**
		IBU	**O_2**				
Mn_3O_4 (powder)	0.1/0.5	1	15	170	310	410	77(3)
	0.1/0.5	1	10	200	310	410	76(6)
	0.1/0.5	1	6	205	340	450	77(4)

4.4.1.1.4 Mn_3O_4 nano-powder

For the Mn_3O_4 nanopowder, the effect of varying the Mn_3O_4:SiC ratio was also made. Again, the mass of Mn_3O_4 was kept at 0.1 g and the masses of SiC were set at 0.4, 0.5 and 1.0 g. The relevant data are given in Table 11. All profiles showed a two-step process, with the discontinuity occurring at ~180^{o}C in each case.

Table 11. Catalysis data for the combustion of isobutane using Mn_3O_4 nano-powder – Mn_3O_4 to SiC dependence: masses of catalyst and SiC, T_i, $T_{50\%}$, $T_{100\%}$ and E_{app} (flow rate = 50 mL/min).

Compound	**Mass of Mn_3O_4 (g)**	**Mass of SiC (g)**	**T_i (^oC)**	**$T_{50\%}$ (^oC)**	**$T_{100\%}$ (^oC)**	**E_{app} (kJ/mol)**
Mn_3O_4 (nano-powder)	0.1	0.4	140	200	225	55(1)
	0.1	0.5	140	195	220	55(3)
	0.1	1.0	120	195	220	43(2)

The profile in the case of the Mn_3O_4:SiC ratio of 0.1:0.5 is shown in Figure 30. The data in Table 11 are for the high temperature stage, while the E_{app} values for the low temperature stage (~120 to 180°C) are ~34 to 48 kJ/mol. For the most dilute Mn_3O_4 to SiC ratio, it is difficult to separate the two stages. At present, it is not known what caused this two-stage process, but it cannot be the thermal process that is observed at 140-200°C for the Mn_3O_4 nanoparticles (see Section 4.3.3.2), as the Mn_3O_4 nano-powder was calcined at 300°C prior to the catalysis studies.

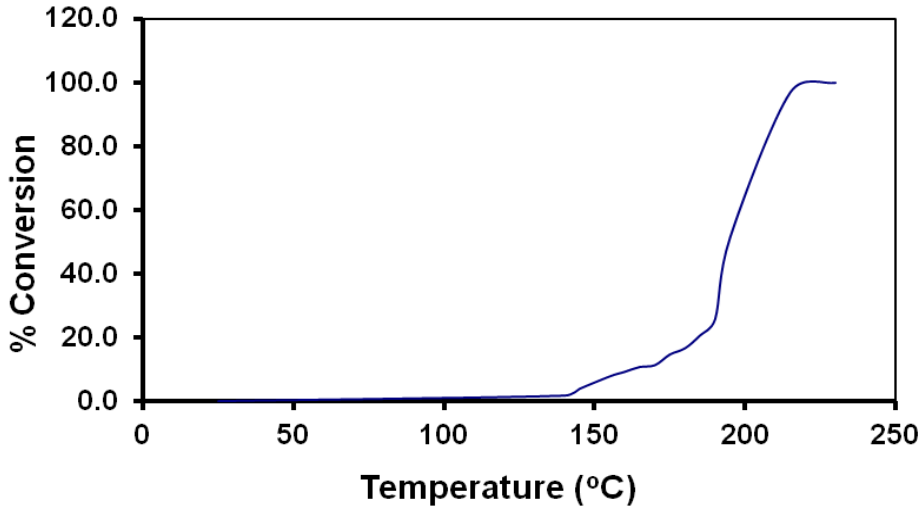

Figure 30. The reaction profile for the combustion of isobutane using Mn_3O_4(nano-powder)/SiC (0.1 g/0.5 g); isobutane:oxygen = 1:10; flow rate = 50 mL/min).

4.4.1.1.5 Catalysis behaviour of Au/Mn_3O_4 powder and Au/Mn_3O_4 nano-powder

Addition of gold nanoparticles to Mn_3O_4 powder caused a significant effect. The data are given in Table 12. Compared to the data in the absence of the added gold nanoparticles, the T_i and $T_{100\%}$ values were all reduced, as was the value of E_{app}. Interestingly, the value of $T_{50\%}$ increased. This was caused by a significant acceleration in the increase of the %

conversion above about 40%. It is likely that a second stage process occurs, and that this is an effect of the size of the gold nanoparticles. As determined above, for the spinel-type M_3O_4 compounds the gold nanoparticles show some aggregation to give particles of about 48-71 nm in size (see Section 4.3.3.2).

For the Mn_3O_4 nano-powder the addition of gold nanoparticles had a detrimental effect on catalyst behaviour. The two-stage process observed for the Mn_3O_4 nano-powder in the absence of gold nanoparticles was still observed, and all parameters T_i, $T_{50\%}$ and $T_{100\%}$, as well as E_{app}, increased in value. For this system, the gold nanoparticles are actually larger than the particles in the Mn_3O_4 nano-powder, which had an average size of ~17 nm (see Section 4.3.3.1). Thus unless gold nanoparticles can be stopped from aggregating, the use of nanopowders in the presence of gold nanoparticles would appear to be ineffective. Reduction in the amount of added gold, using only a 1% loading, showed no improvement in the catalytic behaviour.

Table 12. Catalysis data for the addition of gold nanoparticles to Mn_3O_4 powder and nano-powder: masses of catalyst and SiC, T_i, $T_{50\%}$, $T_{100\%}$ and E_{app} (flow rate = 50 mL/min).

Compound	**Mass ratio of Mn_3O_4/SiC**	**T_i (^oC)**	**$T_{50\%}$ (^oC)**	**$T_{100\%}$ (^oC)**	**E_{app} (kJ/mol)**
Mn_3O_4 powder + Au nanoparticles (5 wt %)	0.1/0.5	180	380	400	54(2)
Mn_3O_4 nano-powder + Au nanoparticles (5 wt %)	0.1/0.5	150	220	260	75(7)
Mn_3O_4 nano-powder + Au nanoparticles (1 wt %)	0.1/0.5	160	235	290	68(6)

4.4.1.2 Catalysis using Co_3O_4 powders and nano-powders

A similar set of studies were performed on Co_3O_4 powder and nano-powder, including the addition of gold nanoparticles, as was performed on the analogous Mn_3O_4 compounds.

4.4.1.2.1 Dependence on Co_3O_4:SiC ratio

The data for the dependence on the Co_3O_4:SiC ratio is given in Table 13. Only a limited study was undertaken. The data for the two dilutions were consistent and gave similar values for all parameters, suggesting little dependence on dilution above a ratio of 0.1/0.5 that had been observed for the studies of Mn_3O_4. The mean E_{app} from the two studies was 97 ± 5 kJ/mol, and is markedly higher than the mean value found for Mn_3O_4 powder.

Table 13. Catalysis data for the combustion of isobutane using Co_3O_4 powder – Co_3O_4 to SiC dependence: masses of catalyst and SiC, T_i, $T_{50\%}$, $T_{100\%}$ and E_{app} (flow rate = 50 mL/min).

Compound	**Mass of Co_3O_4 (g)**	**Mass of SiC (g)**	**T_i (^oC)**	**$T_{50\%}$ (^oC)**	**$T_{100\%}$ (^oC)**	**E_{app} (kJ/mol)**
Co_3O_4 (powder)	0.1	0.5	200	270	340	102(8)
	0.1	1.0	185	270	370	93(3)

4.4.1.2.2 Dependence on flow rate

The flow rate dependence data for Co_3O_4 powder is given in Table 14. Again only a limited study was undertaken, corresponding to the two highest flow rates used in the Mn_3O_4 study that produced the most consistent results. All four parameters agree reasonably well, indicating that a flow rate of 50 mL/min is suitable for combustion studies.

Table 14. Catalysis data for the combustion of isobutane using Co_3O_4 powder - flow rate dependence: masses of catalyst and SiC, flow rate, T_i, $T_{50\%}$, $T_{100\%}$ and E_{app}.

Compound	**Mass ratio Co_3O_4/SiC**	**Flow rate (mL/min)**	**T_i (^oC)**	**$T_{50\%}$ (^oC)**	**$T_{100\%}$ (^oC)**	**E_{app} (kJ/mol)**
Co_3O_4 (powder)	0.1/0.5	50.0	200	270	340	102(8)
	0.1/0.5	64.1	190	290	360	88(4)

4.4.1.2.3 Dependence on isobutane to oxygen ratio

As for the analogous Mn_3O_4 system, the effect of varying the isobutane to oxygen ratio was investigated, as shown in Table 15. The isobutane:oxygen ratio again ranged from 1:6 to 1:15. The data for the two high ratios, 1:10 and 1:15 are consistent, but that of the oxygen deficient ratio gave a low value of E_{app}, although the other parameters showed good agreement. While it is not certain why the E_{app} value is slightly low for the oxygen-deficient study, the other data again indicates that there is no dependence on the oxygen concentration for the oxidation reaction, which is consistent with a Mars-van Krevelan mechanism. There may be a slight dependence on oxygen concentration, but further studies are required to confirm this possibility. As found for the Mn_3O_4 system, there was no evidence of isobutene or fragment species in the 1:6 isobutane:oxygen study.

4.4.1.2.4 Co_3O_4 nano-powder

For the study of the Co_3O_4 nanopowder, the effect of varying the Co_3O_4:SiC ratio was also carried out in a limited study. The mass of Co_3O_4 was set at 0.1 g and the masses of SiC were set at 0.5 and 1.0 g. The catalysis data are given in Table 16.

Table 15. Catalysis data for the combustion of isobutane using Co_3O_4 powder – oxygen dependence: masses of catalyst and SiC, flow rates for isobutane (IBU) and oxygen, T_i, $T_{50\%}$, $T_{100\%}$ and E_{app}.

Compound	**Mass ratio Co_3O_4 /SiC**	**Flow rate 50 (mL/min)**		**T_i (^oC)**	**$T_{50\%}$ (^oC)**	**$T_{100\%}$ (^oC)**	**E_{app} (kJ/mol)**
		IBU	**O_2**				
Co_3O_4 (powder)	0.1/0.5	1	15	180	280	380	97(4)
	0.1/0.5	1	10	200	270	340	102(8)
	0.1/0.5	1	6	190	300	390	71(5)

As found in the study of Mn_3O_4, both profiles showed a two-step process, with the discontinuity now occurring at ~185-190^{o}C in each case. Only E_{app} data could be obtained on the first-stage process, as above the discontinuity the acceleration in the increase of the % conversion was extensive. This behaviour was identical to that found for Mn_3O_4. Again the origin of the two-stage process is uncertain, and further studies are required to resolve this effect. The E_{app} data are for the first stage in the combustion process.

4.4.1.2.5 Catalysis behaviour of Au/Co_3O_4 powder and Au/Co_3O_4 nano-powder

The catalysis data for the addition of gold nanoparticles to both Co_3O_4 powder and nano-powder are given in Table 17. For Co_3O_4 powder, compared to the data in the absence of the added gold nanoparticles, both T_i and E_{app} are lower, but $T_{50\%}$ and $T_{100\%}$ are markedly higher.

Table 16. Catalysis data for the combustion of isobutane using Co_3O_4 nano-powder – Co_3O_4 to SiC dependence: masses of catalyst and SiC, T_i, $T_{50\%}$, $T_{100\%}$ and E_{app} (flow rate = 50 mL/min).

Compound	**Mass of Co_3O_4 (g)**	**Mass of SiC (g)**	**T_i (^oC)**	**$T_{50\%}$ (^oC)**	**$T_{100\%}$ (^oC)**	**E_{app} (kJ/mol)**
Co_3O_4 nano-powder	0.1	0.5	160	~190	195	96(9)
	0.1	1.0	170	~195	200	109(10)

It is not obvious why the % conversion-time profile was so drawn out at higher temperatures, but it is likely attributable to the effect of the gold nanoparticles, which XRD studies indicated were ~48 nm in diameter (see Section 4.3.3.2). However, as found for Mn_3O_4, E_{app} decreased on addition of the gold nanoparticles, although the other catalysis data for addition of gold nanoparticles was less satisfactory. Further investigations of this system are warranted. For the Co_3O_4 nano-powder, the two-stage behaviour was still observed, with the discontinuity between the two stages occurring at ~220^{o}C. The overall catalysis parameters T_i, $T_{50\%}$ and $T_{100\%}$ increased compared to Co_3O_4 in the absence of gold nanoparticles, while E_{app}, which is for the first-stage of the two-stage process, was slightly lower in value. Although the particle sizes for the Co_3O_4 nano-powder were larger than in the Mn_3O_4 nano-powder system, relative to the gold particles, it is again concluded that unless the gold nanoparticles can be stopped from aggregating using the procedure employed in this study for delivering gold nanoparticles, the use of metal-oxide nano-powders with gold nanoparticles provides no advantage.

4.4.1.3 Catalysis using Fe_3O_4 powder

Any catalysis studies on Fe_3O_4 are complicated by the conversion of Fe_3O_4 to Fe_2O_3.

Table 17. Catalysis data for the addition of gold nanoparticles to Co_3O_4 powder and nano-powder: masses of catalyst and SiC, T_i, $T_{50\%}$, $T_{100\%}$ and E_{app} (flow rate = 50 mL/min).

Compound	**Mass ratio of Co_3O_4 /SiC**	**T_i (^oC)**	**$T_{50\%}$ (^oC)**	**$T_{100\%}$ (^oC)**	**E_{app} (kJ/mol)**
Co_3O_4 powder + Au nanoparticles (5 wt %)	0.1/0.5	195	490	600	59(3)
Co_3O_4 nano-powder + Au nanoparticles (5 wt %)	0.1/0.5	180	230	240	71(6)

The TG/DTA and high-temperature X-ray studies have shown that Fe_3O_4 powder converts to Fe_2O_3 above ~240-250^{o}C, while the Fe_3O_4 nano-powder oxidises at even lower temperatures (see Sections 4.3.3.2 and 4.3.4.1). Studies were carried out only on the Fe_3O_4 powder. The data are provided in Table 18, which includes a study, under the same conditions, of Fe_2O_3. It is apparent that under the conditions used in the study, Fe_3O_4 converts fully to Fe_2O_3.

Table 18. Catalysis data for the combustion of isobutane using Fe_3O_4 powder and Fe_2O_3: masses of catalyst and SiC, T_i, $T_{50\%}$, $T_{100\%}$ and E_{app} (isobutane:oxygen = 1:10; flow rate = 50 mL/min).

Compound	**Mass ratio of M_3O_4/SiC**	**T_i (^oC)**	**$T_{50\%}$ (^oC)**	**$T_{100\%}$ (^oC)**	**E_{app} (kJ/mol)**
Fe_3O_4 powder	0.1/0.5	280	390	440	60(3)
Fe_2O_3 powder	0.1/0.5	280	410	450	63(4)

4.4.1.4 The products of reaction

In all of the catalysis studies, the gaseous products were sampled at a % conversion of 20-30% using gas-phase infrared spectroscopy. In all cases the products were found to be essentially CO_2, with a small amount of CO, and presumably water (this was condensed in the ice-cooled liquid-phase collector, and was not determined). The presence of CO was a surprise. The mole ratio of CO_2 to CO varied from 28.4:1 to 11.3:1 in the studies without the added gold nanoparticles, and were slightly higher in the systems with added gold nanoparticles. For example, for Mn_3O_4 powder, with an Mn_3O_4/SiC of 0.1 g /0.5 g, an isobutane:oxygen = 1:10 and a flow rate = 50 mL/min, the CO_2:CO ratio was 28.4:1 in the absence of added gold nanoparticles, and 33.2:1 in the presence of gold nanoparticles. No patterns could be readily established in the present studies with variations in flow rate, isobutane:oxygen ratio, or catalyst type (*i.e.* Mn_3O_4 or Co_3O_4). Presumably there is a minor reaction pathway that leads to the formation of CO, and that with the contact times used in the present studies, which varied from 0.38 to 0.97 s (this is based on the catalyst volume including the SiC diluent), are not sufficient to convert the CO fully to CO_2. Although the CO_2:CO ratios were higher in the presence of gold nanoparticles, and these are known to convert CO to CO_2 [39], it would appear that the contact time was not sufficient to allow such conversion, or that the larger gold particles found in the present combustion studies were not particularly effective in the oxidation of CO to CO_2.

4.5 Conclusions

In this chapter, combustion studies of isobutane using the spinel-type oxides Mn_3O_4 and Co_3O_4 have been performed, using both powders and nano-powders, both in the absence and presence of gold nanoparticles. The Mn_3O_4 and Co_3O_4 have been characterized by TG/DTA, TEM and SEM, X-ray powder diffraction, XPS and surface area measurements. The method of addition of the gold nanoparticles has been less successful in the case of

Mn_3O_4 and Co_3O_4 than for the phosphopolyoxomolybdates studied in Chapter 3. In the present case aggregation of the gold nanoparticles has occurred to give particles of about 48-71 nm, compared to 6.0 nm in the phosphopolyoxomolybdate studies. The reasons for this are presently unknown, some suggestion have been provided above, but the more basic nature of the oxide surface in the M_3O_4 oxides (M = Mn, Co) may play a role. Further studies are required to establish the cause of this phenomenon.

In the absence of gold nanoparticles, the apparent activation energies, E_{app}, of the combustion reactions of isobutane with oxygen under the present experimental conditions were Mn_3O_4, 76 ± 7 kJ/mol, and Co_3O_4, 95 ± 5 kJ/mol. Interestingly, the E_{app} values do not correlate with the standard enthalpies of formation of Mn_3O_4 and Co_3O_4 per metal atom, which are -461.1 and -313.3 kJ/mol [31, 40]. The presence of gold nanoparticles lowered E_{app} for Mn_3O_4 powder to 54 ± 2 kJ/mol, and for Co_3O_4 to 59 ± 3 kJ/mol, although the other catalysis parameters (T_i, $T_{50\%}$, $T_{100\%}$) were generally unfavorable in the case of Co_3O_4. The use of gold nanoparticles delivered by thermolysis of the *n*-hexanethiolate-stabilised gold nanoparticles for the Mn_3O_4 and Co_3O_4 nano-powders was detrimental to their catalytic performance. Alternative approaches of introducing gold nanoparticles onto the surfaces and into the pore structures of these compounds are required. XPS studies showed that Au(I) was also formed in the combustion reactions, and it again likely plays a role in the combustion process. Further, it likely exists as AuO^- [36]. The products of combustion were mainly CO_2 and H_2O, but some CO was also observed.

4.6 References

[1] R.B. Anderson, K.C. Stein, J.J. Feenan, L.J.E. Hofer, Ind. Eng. Chem, 53 (1961) 809.

[2] J.G. Firth, J. Chem. Soc., Faraday Soc, 52 (1966) 2566.

[3] R.E. Roberts, J.B. Roberts, J. Air Pollut. Control Assoc., 26 (1976) 353.

[4] A.E.R. Budd, Environ. Pollut. Manag., (1978) 13.

[5] J.J. Spivey, Ind. Eng. Chem. Res., 26 (1987) 2165.

[6] M.R. Dongworth, A. Melvin, 16th Int. Symp. in Combustion, MIT, (1976) 255.

[7] A. Nishino, Catal. Today, 10 (1991) 107.

[8] S.W. Radcliffe, R.G. Hickman, J. Inst. Fuel, 48 (1975) 208.

[9] D.L. Trimm, C.W. Lam, Chem .Eng. Sci., 35 (1980) 1731.

[10] W.V. Krill, J.P. Kesselring, E.K. Chu, R.M. Kendall, Mech. Eng, 102 (1980) 28.

[11] S.M. DeCorso, S. Mumford, R.V. Carruba, R. Heck, J. Eng. Power, 99 (1977) 159.

[12] W.C. Pfefferle, J. Energy, 2 (1978) 142.

[13] B.E. Enga, D.T. Thompson, Plat. Met. Rev., 23 (1979) 134.

[14] J. Tsuji, K. Ohno, Synthesis, 157 (1969) 1.

[15] J.P. Kesserling, Advanced Combustion Methods, Academic Press, New York, 1986.

[16] M. Haruta, T. Kobayashi, H. Sano, N. Yamada, Chem. Lett., (1987) 405-408.

[17] M. Haruta, Catal. Today, 36 (1997) 153-166.

[18] M. Haruta, Catal. Surveys from Japan, 1 (1997) 61-73.

[19] M. Haruta, N. Yamada, T. Kobayashi, S. Iijima, J. Catal., 115 (1989) 301-309.

[20] N.M. Gupta, A.K. Tripathi, J. Catal, 187 (1999) 343.

[21] P. Graves, C. Johnston, J. Campaniello, Mater. Res. Bull., 23 (1988) 1651-1660.

[22] K.E. Sickafus, J.M. Wills, N.W. Grimes, J. Am. Ceramic Soc., 82 (1999) 3279-3292.

[23] Z. Pan, Patterning and Structural Engineering of Dimensionally Constrained Functional Oxide Nanostructures., in, Northwestern University 2008, pp. 244.

[24] International Centre for Diffraction Data, http://www.icdd.com/.

[25] A.R. Armstrong, P.G. Bruce, Nature, 381 (1996) 499-500.

[26] A. Soldatov, A. Kovtun, A. Bianconi, Physica B: Condensed Matter, 208 (1995) 771-772.

[27] W.S. Kijlstra, J.C.M.L. Daamen, J.M. van de Graaf, B. van der Linden, E.K. Poels, A. Bliek, Appl. Catal. B: Environmental, 7 (1996) 337-357.

[28] Y. Yamashita, K. Mukai, J. Yoshinobu, M. Lippmaa, T. Kinoshita, M. Kawasaki, Surf. Sci., 514 (2002) 54-59.

[29] E. Grootendorst, Y. Verbeek, V. Ponce, J. Catal, 157 (1995) 706.
[30] R.M. Cornell, U. Schwertmann, The Iron Oxides, Wiley-vch Weinheim, Germany, 2003.
[31] Encyclopedia of Chemical Technology/Executive editor, Jacqueline I. Kroschwitz ; editor, Mary Howe-Grant, 4th ed., New York : Wiley, 1991-1998
[32] C.-W. Tanga, Chen-BinWangb, S.-H. Chien, Thermochimica Acta, 473 (2008) 68-73.
[33] X. Li, L. Zhou, J. Gao, H. Miao, H. Zhang, J. Xu, Powder Tech., 190 (2009) 324-326.
[34] NIST; X-ray Photoelectron Spectroscopy Database, Version 3.5; http://srdata.nist.gov/xps/.
[35] M. Oku, K. Hirokawa, S. Ikeda, Journal of Electron Spectroscopy and Related Phenomena, 7 (1975) 465-473.
[36] M. Casaletto, A. Longo, A. Martorana, A. Prestianni, A. Venezia, Surf. Interfac. Anal., 38 (2006) 215-218.
[37] M. Aryafar, F. Zaera, Catal. Lett., 48 (1997) 173-183.
[38] M. Baldi, E. Finocchio, F. Milella, G. Busca, Appl. Catal. B, Environmental, 16 (1998) 43-51.
[39] M. Haruta, Gold Bull., 37 (2004) 27-36.
[40] NIST Chemistry WebBook; NIST Standard Reference Database Number 69, http://webbook.nist.gov/chemistry/.

Chapter 5

Conclusions and Future Studies

5.1 Summary

This present study involved a new approach to the preparation of gold nanoparticles supported on heteropolyoxometalates and metal oxides using *n*-hexanethiolate-stabilised gold nanoparticles as a precursor. The resulting catalysts were used for the partial (*i.e.* selective) and complete heterogeneous oxidation of isobutane. The *n*-hexanethiolate-stabilised gold nanoparticles and catalysts were mixed physically using an *n*-hexane solution. Following adsorption, a thermolysis treatment was then employed to remove the *n*-hexanethiolate ligand, which decomposed at ~220^{o}C, to produce gold nanoparticles loaded on the surfaces and within the pore structures of the catalysts.

n-Hexanethiolate-stabilised gold nanoparticles were synthesised following the two-phase Brust-Schiffrin method [1]. The thiolate-stabilised gold nanoparticles were easily separated out of solution in the form of a black powder and could be stored for long time periods without any agglomeration of the gold nanoparticles. Also, they could be redissolved in different organic solvents and used to deliver known amounts of stabilised gold nanoparticles, such as applied in this study for heterogeneous catalysis. The size and shape of *n*-hexanethiolate-stabilised gold nanoparticles were characterised using a number of techniques. UV-visible spectroscopy and transition electron microscopy (TEM) were employed to estimate the size of the nanoparticles, about 2.5 nm, while X-ray photoelectron spectroscopy was used to establish the electronic valence state of each element.

Phosphopolyoxomolybdates, known to be active in oxidation and oxidative dehydrogenation reactions of, for example methacrolein to methacrylic acid [2], isobutyric acid to methacrylic acid [2], and isobutyraldehyde to both methacrolein and methacrylic acid [3], were employed as catalysts for the partial oxidation of isobutane. Compounds containing the $[PMo_{12}O_{40}]^{3-}$ anion are also known to be effective catalysts for the oxidation/oxidative dehydrogenation of isobutane [4-11]. In addition to $H_3[PMo_{12}O_{40}]$, a number of polyoxometalate salts were synthesised that included the series $Cs_{3-x}H_x[PMo_{12}O_{40}]$ (where x = 0, 0.5, 1 and 2), $Ag_{3-x}H_x[PMo_{12}O_{40}]$ (where x = 0, 1 and 2) and $Cu_{3-2x}H_{2x}[PMo_{12}O_{40}]_2$ (where x = 0, 1 and 2). The catalysts were characterized by IR spectroscopy, SEM, TEM, TG/DTA, X-ray powder diffraction - which was used to estimate the size of the gold nanoparticles using the Scherrer equation (the gold nanoparticles were 6.0 nm in size using the (111) reflection) - and XPS, which was used to establish the oxidation states of gold, molybdenum, and the reducible counter-cations of the heteropolyoxomolybdate catalysts, including examination of the spent catalysts.

The catalysis studies on the series of compounds $Cs_{3-x}H_x[PMo_{12}O_{40}]$ (where x = 0, 0.5, 1 and 2), $Ag_{3-x}H_x[PMo_{12}O_{40}]$ (x = 0, 1 and 2), $Cu_{3-2x}H_{2x}[PMo_{12}O_{40}]_2$ (x = 0, 1 and 2) were studied with and without the addition of gold nanoparticles. The studies on the compounds without gold nanoparticles served to provide a base for an analogous study following addition of gold nanoparticles to the same series of phosphopolyoxomolybdate salts. Higher % conversions and increased % selectivities to the desired products (methacrolein and methacrylic acid) occurred for the H^+-containing salts, and the surface structure, that is, what cations are likely to be encountered by the adsorbed isobutane on the catalyst surface thus play a role. This resulted in different effects for the H^+, Cs^+, Ag^+ and Cu^{2+} salts.

The addition of gold nanoparticles had a significant effect on the % conversion and % selectivities to the products for the selective oxidation of isobutane. The % conversions for $Au_{NPS}/Ag_3[PMo_{12}O_{40}]$ and $Au_{NPS}/Cu_3[PMo_{12}O_{40}]_2$ increased, while that of $Au_{NPS}/Cs_3H_x[PMo_{12}O_{40}]$ decreased. It appears that surface area plays a significant role, which suggests that the % conversion is controlled by an oxidation step. Gold nanoparticles may possibly block the pore structure or simply reduce the surface area. Also, the supported gold nanoparticles affected the % selectivities of the compounds. In some cases, *i.e.* those without H+, the selectivity to CO_2 increased, which suggests that the gold acted to enhance total conversion (*i.e.* oxidation). For $H_3[PMo_{12}O_{40}]$, however, the % conversion and % selectivities to the desired products both increased. XPS investigation of the spent catalysts showed that Au(I) formed in all cases, which suggests that it may play a significant role in the oxidation of isobutane over these types of catalysts. The Au(I) is likely to be present as AuO^-[12]. No evidence for reduction of Ag^+ and Cu^{2+}, was able to be detected by XPS, but this may not be a surprise as Au(I) is strong oxidant. Thus under the catalysis conditions any reduction products, formed through an oxidation-reduction cycle, and involved in the electron transfer process throughout the catalyst bulk as part of the Bulk Catalyst Type-II mechanism, may simply be readily oxidised.

The second part of the present study investigated the spinel-type metal oxides Mn_3O_4, Co_3O_4 and Fe_3O_4, as both powders and nano-powders as catalysts for the complete (combustion) oxidation of isobutane. Again studies were made in the absence and presence of gold nanoparticles. The pure gold nanoparticles were loaded on the oxides using the same approach as described above. XRD analysis using the Scherrer equation gave calculated sizes of the supported gold nanoparticles on Mn_3O_4, Co_3O_4 and Fe_3O_4 nano-powders for the (111) reflection were 48 to 71 nm. The gold nanoparticles had aggregated on the surfaces of the metal oxides and formed much larger particles than found for the supported gold

nanoparticles on the phosphopolyoxomolydbate salts (6.0 nm). Moreover, the supported gold nanoparticles on the Fe_3O_4 surface appeared to form the largest particles (71 nm) compared to Mn_3O_4 and Co_3O_4. In this case aggregation must have occurred because of the oxidation of Fe_3O_4 to Fe_2O_3 during the thermolysis of the *n*-hexanethiolate-stabilised nanoparticles and subsequent calcination at 300^oC. Clearly, transformation of Fe_3O_4 to Fe_2O_3 strongly affected the distribution of the gold nanoparticles on the surface. It is possible that some oxidation of the Mn(II) and Co(II) in the vicinity of the gold nanoparticles could have occurred, leading to surface disruption and aggregation. However, other causes may operate. It is observed that the surface oxygen basicity of the spinel compounds is greater than the very weakly basic surface of the phosphopolyoxomolybdate ion, and this may play a role.

The catalysis studies of on Mn_3O_4 and Co_3O_4 were interpreted in terms of several parameters, including the temperature at which the reaction began (T_i), the temperature at which 50% conversion ($T_{50\%}$) occurred, the temperature at which the 100% conversion was reached ($T_{100\%}$) and the apparent activation energy (E_{app}), which was obtained through an Arrehenius plot. The E_{app} values for oxidation on Mn_3O_4 was 76 ± 7 kJ/mol, and for Co_3O_4 was 95 ± 5 kJ/mol. The Au_{NPS}/Mn_3O_4 and Au_{NPS}/Co_3O_4 catalysts gave lower activation energies. The XPS data showed that Au(I) was present in the spent catalysts, and this species, probably as AuO^-, likely plays a significant role in the oxidation process.

5.2 Future studies

In our future work we plan to expand the investigation of *n*-alkanethiolate stabilised gold nanoparticles for the delivery of gold nanooparticles onto catalyst surfaces and into pore structures and study their effects in both the partial oxidation of isobutane and the complete (combustion) of a series of light hydrocarbons including *n*-butane, *n*-butene, isobutene,

propane and propene, in addition to isobutane. Smaller gold nanoparticles supported on the surface of catalysts will be produced by using other types of stabilisers (long-chain) which will need higher temperatures to decompose. Indeed, the decomposition temperature of *n*-alkanethiolate-stabilised gold nanoparticles increases with an increase in chain length [13]. The expectation is that this will lead to a decrease the agglomeration of the gold nanoparticles on the surface of catalysts, with subsequent effects on catalytic ability. Another possibility is to use a dithiol, *i.e.* HS-R-SH, as a source of stabiliser. This may promote spacing of the gold nanoparticles prior to thermolysis, and lead to smaller gold nanoparticles. Of course, simple studies like optimisation of the loading of the gold nanoparticles, *i.e.* 1, 2.5 and 7.5 mass %, in comparison with the 5 mass % used in the present studies can also be studied.

Another area of exploration is to synthesise other types of metals (Cu, Ag, Pd and Pt) and bimetals (*e.g.* Au/Ag, Pd/Pt and Pt/Pd) as nanoparticles, nano-wires and nano-rods. The literature show that these nano-metals in such forms can be synthesised using various procedures [14-21]. The two-phase transfer synthesis, that was used previous to prepare *n*-hexanethiolate-stabilised Au nanoparticles, is one of the procedures that will be applied to synthesise other types of metals nanoparticles. Moreover, metals (Ag, Cu, Pt and Pd) and bimetals (Ag/Au and Pd/Pt) will be prepared in nano-size in different shapes (particles, wires and rods) to study how differences in shapes, sizes, surfaces all affect catalytic activity.

A number of alternative stabilisers can be employed during the synthesis of nano-metals and bimetals so as to attach to surfaces and ultimately control their sizes and shapes. These include alkylamines [22], aromatic thiols [23, 24], alkanethiols [25], dialkyl disulfides [26], and thiolated cyclodextrin [27] molecules.

The produced nano-metals can be easily stored as solid powders, and that will increase their applications in several research areas including heterogeneous catalysis. The

supported nano-metals and bimetals will likely exhibit promising catalytic properties for the selective oxidation of isobutane and for the oxidation of volatile organic compounds (VOCs), particularly the small molecular weight hydrocarbons indicated above.

The future study will involve two types of oxidation:

5.2.1 Partial oxidation

For future work, different types of phosphopolyoxomolybdates will be employed including $(Pd^{2+})_{3-2x}H_{2x}[PMo_{12}O_{40}]_2$ (x = 0, 1 and 2) and $(Pt^{2+})_{3-2x}H_{2x}[PMo_{12}O_{40}]_2$ (x = 0, 1 and 2), and other potential cations that will have suitable reduction potentials (E^o values) close to the chosen nano-metals (Au, Ag, Pt and Pd). The nano-metal loaded catalysts will be prepared using the same approach used in the present studies.

5.2.2 Complete (combustion) oxidation

The target in this type of oxidation is to examine the effects of supported nano-metals and bimetals on metal oxide surfaces. The metal oxides will include spinel (AB_2O_4) and perovskite (ABO_3) based materials, and other simple oxides such as Fe_2O_3, CuO and NiO. The different oxides will be used to explore the effects of supported nano-metal and bimetal in different shapes (particles, wires and rods) on the oxidation of different hydrocarbons including isobutane, isobutene, *n*-butane, *n*-butene, propane and propene, as indicated above. The nano-metals and bimetals supported on the metal oxides will be obtained using the same procedure that will be used to prepare nano-metals and bimetals supported on the phosphopolyoxomolybdates.

5.3 References

[1] M. Brust, M. Walker, D. Bethell, D.J. Schiffrin, R. Whyman, J. Chem. Soc., Chem. Commun., 1994 (1994) 801-802.

[2] T. Okuhara, N. Mizuno, M. Misono, Adv. Catal., 41 (1996) 113-252.

[3] J. Hu, R. Burns, J. Catal., 195 (2000) 360-375.

[4] N. Mizuno, M. Tateishi, M. Iwamoto, J. Chem. Soc., Chem. Commun., (1994) 1411-1412.

[5] N. Mizuno, M. Tateishi, M. Iwamoto, J. Catal., 163 (1996) 87-94.

[6] F. Cavani, E. Etienne, M. Favaro, A. Galli, F. Trifirò, G. Hecquet, Catal. Lett., 32 (1995) 215-226.

[7] M. Langpape, J.M.M. Millet, U. Oskan, M. Boudeulle, J. Catal., 182 (1999) 148.

[8] J.S. Min, N. Mizuno, Catal. Today, 66 (2001) 47-52.

[9] E. Etienne, F. Cavani, R. Mezzogori, F. Trifirò, G. Calestani, L. Gengembre, M. Guelton, Appl. Catal. A: General, 256 (2003) 275-290.

[10] S.M. Kendell, T.C. Brown, R.C. Burns, Catal. Today, 131 (2008) 526-532.

[11] S. Kendell, T. Brown, Catal. Lett., 141 (2011) 1767-1785.

[12] M. Casaletto, A. Longo, A. Martorana, A. Prestianni, A. Venezia, Surf. Interfac. Anal., 38 (2006) 215-218.

[13] R.H. Terrill, T.A. Postlethwaite, C. Chen, C.D. Poon, A. Terzis, A. Chen, J.E. Hutchison, M.R. Clark, G. Wignall, Journal of the Am. Chem. Soc., 117 (1995) 12537-12548.

[14] A. Mari, P. Imperatori, G. Marchegiani, L. Pilloni, A. Mezzi, S. Kaciulis, C. Cannas, C. Meneghini, S. Mobilio, L. Suber, Langmuir, (2010).

[15] S. Chen, J.M. Sommers, J. Phys. Chem. B, 105 (2001) 8816-8820.

[16] F.P. Zamborini, S.M. Gross, R.W. Murray, Langmuir, 17 (2001) 481-488.

[17] C. Yee, M. Scotti, A. Ulman, H. White, M. Rafailovich, J. Sokolov, Langmuir, 15 (1999) 4314-4316.

[18] S.E. Eklund, D.E. Cliffel, Langmuir, 20 (2004) 6012-6018.

[19] N.N. Kariuki, J. Luo, M.M. Maye, S.A. Hassan, T. Menard, H.R. Naslund, Y. Lin, C. Wang, M.H. Engelhard, C.J. Zhong, Langmuir, 20 (2004) 11240-11246.

[20] B. Lim, J. Wang, P.H.C. Camargo, M. Jiang, M.J. Kim, Y. Xia, Nano lett., 8 (2008) 2535-2540.

[21] A. Gole, C.J. Murphy, Chem. Mater., 16 (2004) 3633-3640.

[22] D.V. Leff, L. Brandt, J.R. Heath, Langmuir, 12 (1996) 4723-4730.
[23] S. Johnson, S. Evans, S. Mahon, A. Ulman, Langmuir, 13 (1997) 51-57.
[24] K. Mayya, V. Patil, M. Sastry, Langmuir, 13 (1997) 3944-3947.
[25] M. Hostetler, J. Wingate, C. Zhong, J. Harris, R. Vachet, M. Clark, J. Londono, S. Green, J. Stokes, G. Wignall, Langmuir, 14 (1998) 17-30.
[26] L.A. Porter Jr, D. Ji, S.L. Westcott, M. Graupe, R.S. Czernuszewicz, N.J. Halas, T.R. Lee, Langmuir, 14 (1998) 7378-7386.
[27] J. Liu, R. Xu, A.E. Kaifer, Langmuir, 14 (1998) 7337-7339.